TEL AVIV UNIVERSITY
RAYMOND AND BEVERLY SACKLER
FACULTY OF EXACT SCIENCES
SCHOOL OF PHYSICS & ASTRONOMY

אוניברסיטת תל-אביב
הפקולטה למדעים מדוייקים
ע"ש ריימונד ובברלי סאקלר
בית הספר לפיסיקה ואסטרונומיה

Study of Neutral and Charged current cross sections at high Q^2 at HERA

Thesis submitted toward the Ph.D. Degree
at Tel Aviv University
School of Physics and Astronomy

by

Arafat Gabareen Mokhtar

January 25, 2006

The research work for this thesis was carried out in the Experimental High Energy Physics Group of the Tel Aviv University under the supervision of Prof. **Halina Abramowicz** and Prof. **Aharon Levy**.

To
Mohammed Abed El Raoof Asaleieh,
a close friend who passed away in a road accident

Abstract

The data of integrated luminosity of 23.8 pb^{-1} collected with the ZEUS detector in 2004 at a centre-of-mass energy of 318 GeV is analysed. The cross section for the charged current deep inelastic scattering in e^+p collisions with longitudinally polarised positron beams is presented. The total and differential charged current (CC) cross sections are presented at two polarisation values, $P = 32.2\%$, and $P = -40.6\%$ in the kinematic region of $Q^2 > 200$ GeV^2. A fit of the Standard Model expectations as a function of polarisation to the measured total CC cross sections yields $\sigma^{CC}(P = -1) = 7.2 \pm 4.0(stat) \,^{+1.1}_{-1.5}(syst)$ pb, consistent with the non-existence of right-handed CC.

The data of integrated luminosity of 116.1 pb^{-1} of e^+p interactions, collected with the ZEUS detector in 1996-2000, is used to extract the value of $\sin^2\theta_W$ by measuring directly the ratio of neutral to charged current total cross section, and assuming well known proton parton density functions. This measurement yields $\sin^2\theta_W = 0.227 \pm 0.013(stat) \,^{+0.008}_{-0.009}(syst)$, a measurement which is consistent with previous results obtained by other experiments.

The data of integrated luminosity of 60.8 pb^{-1} of e^+p, collected with the ZEUS detector in 1999-2000, is used to measure the ratio of d to u quark at three values of x and at $Q^2 = 6400$ GeV^2. This analysis was done under the assumption of well known $\sin^2\theta_W$ and all other Standard Model parameters. The ratio of d to u quarks was found in agreement with the predictions of several parton density functions parameterisations.

Contents

1 Introduction **1**

2 Theoretical framework **6**
2.1 DIS Kinematic variables 6
2.2 Charged current cross section 7
2.3 Neutral current cross section 9
2.4 Parton density functions 11

3 Experimental framework **13**
3.1 HERA 13
3.2 The ZEUS detector 13
3.2.1 Central tracking detector 14
3.2.2 The calorimeter 15
3.2.3 Muon tagging system 17
3.2.4 Luminosity monitor 17
3.3 The HERA and ZEUS upgrade 17
3.3.1 Polarised electron beams 17
3.3.2 Compton scattering 20
3.3.3 The transverse polarimeter 21
3.3.4 The longitudinal polarimeter 22
3.3.5 Polarimeter choice 23
3.3.6 Micro vertex detector (MVD) 23

4 Monte Carlo simulation **26**
4.1 CC signal Monte Carlo 26
4.2 CC characteristics 27
4.3 CC Background simulation 28
4.3.1 Photoproduction 28
4.3.2 Neutral current 28
4.3.3 Di-lepton production 30
4.3.4 W production 30

4.3.5 ZEUS trigger . . . 31
4.3.6 Detector simulation . . . 31

5 Reconstruction of kinematic variables 33
5.1 The electron method . . . 33
5.2 The double angle method . . . 34
5.3 The Jacquet-Blondel method . . . 34
5.4 Hadronic final state energy corrections . . . 35
5.4.1 Energy deposits clustering . . . 35
5.4.2 Back-splash correction . . . 35
5.5 Jet reconstruction . . . 36
5.6 Comparison of reconstruction methods . . . 38

6 Charged current event selections at HERA II 40
6.1 Trigger requirement . . . 40
6.1.1 First level trigger . . . 40
6.1.2 Second level trigger . . . 41
6.1.3 Third level trigger . . . 41
6.2 Background resources . . . 42
6.2.1 Non-ep background . . . 42
6.2.2 ep background . . . 43
6.3 Vertex reconstruction . . . 44
6.4 Pre-selection cuts . . . 46
6.5 Kinematic cuts . . . 48
6.6 High γ_0 event selection . . . 49
6.6.1 Vertex cut . . . 49
6.6.2 P_T cut . . . 49
6.6.3 P'_T cut . . . 49
6.6.4 Tracking requirement . . . 50
6.6.5 Photoproduction background . . . 55
6.7 Low γ_0 event selection . . . 58
6.7.1 Vertex cut . . . 58
6.7.2 P_T and P'_T cuts . . . 59
6.7.3 Halo and cosmic muon rejection . . . 59
6.8 Rejection of NC events . . . 61
6.9 Calorimeter timing cuts . . . 62
6.10 Selection cuts for high and low γ_0 . . . 62
6.11 Visual scanning . . . 64
6.12 Final samples . . . 64
6.13 MC and data comparison . . . 64

7 Cross section **81**
7.1 Binning definitions . . . 81
7.2 Acceptance, purity and efficiency . . . 81
7.3 Cross section measurement . . . 83

8 Systematic uncertainties **88**
8.1 Threshold variation . . . 88
8.2 Energy scale uncertainty . . . 89
8.3 Parton shower scheme . . . 90
8.4 Photoproduction subtraction . . . 90
8.5 Energy leakage . . . 92
8.6 Parton distribution functions . . . 93
8.7 NLO QCD corrections . . . 93
8.8 Luminosity uncertainty . . . 93
8.9 Summary . . . 94

9 Results **96**
9.1 Cross section results . . . 96
9.2 Estimation of $\sigma^{CC}(P=-1)$ . . . 99
9.3 Limit on M_{WR} . . . 102
9.4 Summary . . . 106

10 $\sin^2\theta_W$ extraction from HERA I data **111**
10.1 Introduction . . . 111
10.2 Monte Carlo simulation . . . 115
10.3 Trigger selections . . . 117
10.3.1 Kinematic variables . . . 119
10.3.2 CC trigger . . . 119
10.3.3 NC trigger . . . 119
10.3.4 Background . . . 119
10.4 Events selection . . . 120
10.4.1 CC and NC separation . . . 124
10.4.2 Kinematical range . . . 124
10.5 Monte Carlo and data comparisons . . . 124
10.6 Results . . . 137

11 The $\frac{d}{u}$ ratio **140**
11.1 Introduction . . . 140
11.2 Assumption . . . 141
11.3 Event selection . . . 143
11.4 Kinematic region . . . 143

11.5 Final samples 144
11.6 Monte Carlo and data comparison 145
11.7 $\frac{d}{u}$ extraction 147
11.8 Outlook 149

Appendices **149**

A Figures for systematic uncertainties checks for charged current analysis **152**

Acknowledgement **194**

List of Figures

1.1 Feynman diagrams for the NC (left) and CC (right) interactions at the Born level. 3
1.2 The structure function F_2^{em} versus Q^2 at fixed values of x compared to a fit based on DGLAP evolution equations. . . . 4

2.1 Kinematics of DIS ep interactions (see text for details). 7
2.2 The total CC DIS cross section for $e^{\pm}p$ scattering plotted as a function of the polarisation of the incoming lepton beam, P. 8
2.3 The NC and CC cross sections for $e^{+}p$ and $e^{-}p$ interactions versus Q^2. 10
2.4 The kinematic phase space covered by the data from several experiments including the ZEUS one. 12

3.1 Schematic representation of the HERA accelerator complex at DESY, Hamburg, Germany. 14
3.2 The integrated luminosity delivered by HERA I (left) and HERA II (right) in the various run periods. 15
3.3 A longitudinal cross sectional view of the ZEUS detector. The directions of the incoming beams are shown in the figure. Also the main components of the detector are labelled. 16
3.4 The ZEUS coordinate system. 16
3.5 A schematic diagram of the luminosity monitor. The x axis in bottom of the figure shows the distances of the components relative to the interaction point. 18
3.6 The polarisation, P, versus the time in hours. 19
3.7 Schematic view of HERA II with the location of the spin rotators. 19
3.8 A schematic diagram of the Compton scattering of a laser photon off a beam electron. The scattered photon is the detected in the polarimeter (calorimeter on the figure). 20
3.9 The transformation function $\eta(y)$. 22
3.10 The polarisation distribution as obtained for the ZEUS running period 2003-2004. 24

3.11 A schematic drawing of the MVD along the beam pipe direction (top), and in $r-\phi$ plane (bottom). The FMVD (left-bottom) consists of four double layers, and the BMVD (right-bottom) consists of three double layers. 25

4.1 Diagrams of direct (left) and resolved (right) photoproduction events 29
4.2 The main leading order Feynman diagrams for real $W^{\pm}$ production: $eq \to eW^{\pm}X$. 31

5.1 Schematic representation of the cell island clustering. The larger the zone of the blob the larger the energy deposited in that cell. 36
5.2 A schematic diagram of one jet event, where a proton arrives from the right and collides with an incoming electron from the left. The proton breaks and the remnants scatter with small angles. 38
5.3 The relative deviation of the reconstructed Q^2, x, and y from the true values versus the true values for a) Q^2, b) x, and c) y. The closed circles are obtained by correcting a kinematic variable for the back-splash effect, the open squares show the reconstructed variables using jet/(s) properties, and the open circles without any corrections. 39

6.1 An example of a cosmic muon hitting the detector. 43
6.2 A ZEUS event display of a typical beam-halo muon, overlapped on a regular event. 43
6.3 An event display of a typical beam-gas event as seen in the ZEUS detector. 44
6.4 Distribution of the number of reconstructed secondary vertices, N_{sec}^{vtx}, for LH (a) and RH (b) samples. 45
6.5 The vertex finding efficiency as a function of γ_0, as obtained by the tracking and by the FCAL arrival timing. 47
6.6 The kinematic phase-space of events in the $Q^2 - x$ plane, with lines of constants P_T, γ_0 and y as denoted in the figure. 48
6.7 The z-position of the vertex fitted with the CTD-MVD tracks (high γ_0 events). a) for RH sample and b) for LH sample. The dots stand for the data, the filled histograms denote the MC with Ariadne and the dashed ones denote the MC with MEPS. The dashed filled histograms represent all background contaminations. 50

6.8 (a) ((b)): The P_T distribution of the final LH (RH) high γ_0 sample after all other cuts have been applied. The dots denote the data points, the histogram denotes the MC distribution with Ariadne while the dashed line histogram denotes the MC distribution obtained with MEPS MC. The dashed filled histogram denotes the background contribution from all processes entering the CC sample 51

6.9 (a) ((b)): The P_T' distribution of the final LH (RH) high γ_0 sample after all other cuts have been applied. The dots denote the data points, the filled histogram denotes the MC distribution with Ariadne while the dashed denotes the MC distribution obtained with MEPS MC. The dashed histogram denotes the background contributions from all processes which enter the CC sample. 52

6.10 N_{Good} versus N_{trks} for high γ_0 CC events in data (a) and MC (b). The distribution of the ratio $\frac{(N_{trks}-20)}{N_{Good}}$ for the LH (c) and RH (d) sample is presented. Here all cuts were applied except the tracking cut. 53

6.11 The $|\Delta\phi|$ distributions for the LH (a) and RH (b) for high γ_0 samples after applying all cuts except the $\Delta\phi$ cut. The dots denote the CC data while the filled (dashed) histograms represents the CC MC distributions obtained with ARIADNE (MEPS). The part of the figures to the left of the vertical dotted lines denote the accepted region of events. 54

6.12 (a)- The distribution of P_T/E_T for the final NC high γ_0 sample. b); dots stand for the high γ_0 CC events after applying all cuts except the P_T/E_T cut, while the filled (dashed) histogram is the CC MC with ARIADNE (MEPS). The distribution of P_T/E_T in MC sample of resolved (c) and direct PHP (d), in high γ_0 sample. 56

6.13 Distributions of P_T/E_T in the high γ_0 sample: (a) for the LH events and (b) for the RH events with $P_T < 20$ GeV and (c) and (d) for the events with $20 < P_T < 30$ GeV. All figures above were obtained after applying all cuts except the P_T/E_T cut. The full points denote the CC data, the filled (dotted) histograms denote the CC MC distribution obtained with ARIADNE (MEPS). The dashed histograms show the expectations of the sum of resolved and direct PHP MC. All MC samples were normalised to the data luminosity. The part of the figures to the right of the vertical lines denote the accepted region of events. 57
6.14 The z_{vtx}^{FCAL} distribution for the LH (a) and RH (b) samples. The dots denote the CC data and the filled (dotted) histograms stand for the MC CC events obtained with ARIADNE (MEPS). The filled dashed histograms stand for the contamination background that enter the CC samples. The region between the two vertical lines in each figure represent the accepted region of events. 58
6.15 The distribution of: E_{FCAL}^{EMC}/E_{FCAL} for LH (a) and RH (b) CC samples; E_{FCAL}^{HAC1}/E_{FCAL} for LH (c) and RH (d) CC samples; and E_{FCAL}^{HAC2}/E_{FCAL} for LH (e) and RH (f) CC samples. The full points stand for the CC data and the filled (dotted) histograms represents the CC MC obtained with ARIADNE (MEPS). The parts of the plots a), b), c), and d), to the right of the vertical lines denote the accepted region of events. The part of the plots e) and f) to the left of the vertical lines denote the accepted region of events. The plots in this figure are for events with $\gamma_0 < 0.4$ rad, and were obtained by applying all cuts except the cuts on these quantities and the shower width cuts. 65
6.16 A schematic view of the FCAL as seen from the interaction vertex. The centre of the shower was chosen to be (t^0, m^0), where t^0 and m^0 are the tower and the module of the highest E_T cell. The rings where chosen in steps of one. 66
6.17 The distribution of N_W^t for events with no tracks for LH (a) and RH (b) samples. The distribution of N_W^t for events with at least one track associated with the highest E_T cell for LH (c) and RH (d) samples. The dots stand for the CC data and the filled (dotted) histograms represent the CC MC as obtained with ARIADNE (MEPS). The parts of the plots right of the vertical lines denote the accepted region of events. 67

6.18 The distribution of N_W^m for events with no tracks for LH (a) and RH (b) samples. The distribution of N_W^m for events with at least one track associated with the highest E_T cell for LH (c) and RH (d) samples. The full points stand for the CC data and the filled (dotted) histograms represent the CC MC as obtained with ARIADNE (MEPS). The parts of the plots right of the vertical lines denote the accepted region of events. 68
6.19 The distribution of E_W^t for events with no tracks for LH (a) and RH (b) samples. The distribution of E_W^t for events with at least one track associated with the highest E_T cell for LH (c) and RH (d) samples. The full points stand for the CC data and the filled (dotted) histograms represent the CC MC as obtained with ARIADNE (MEPS). The parts of the plots right of the vertical lines denote the accepted region of events. 69
6.20 The distribution of E_{RSP} for events with no tracks for LH (a) and RH (b) samples. The distribution of E_{RSP} for events with at least one track associated with the highest E_T cell for LH (c) and RH (d) samples. The full points stand for the CC data and the filled (dotted) histograms represent the CC MC as obtained with ARIADNE (MEPS). The parts of the plots (a) and (b) right of the vertical lines denote the accepted region of events. 70
6.21 An example of DIS NC event removed from the CC sample. The transverse momentum of this event is $P_T = 13.5$ GeV. . . 71
6.22 The global calorimeter timing versus the calorimeter energy (a), the BCAL timing versus the BCAL total energy (b), the RCAL timing versus the RCAL total energy (c), and the timing of the upper part of BCAL versus the total energy of the upper half of BCAL (d). In these figures, the tiny dots stand for NC events in the data and the larger filled circles stand for the data CC events. The cuts are represented by the horizontal/ vertical lines. 72
6.23 The timing of the upper RCAL versus the total RCAL energy (a), the upper half FCAL timing versus the total energy in the upper half of FCAL (b), the timing of the lower BCAL half versus the total energy in the lower half of BCAL (c), and the timing of the lower half of RCAL versus the total energy of the lower half of RCAL (d). In these figures, the tiny dots stand for the NC events in the data while the filled larger circles stand for the data CC events. The cuts are represented by the horizontal/ vertical lines. 73

6.24 The P_T/E_T versus P_T for the data (filled circles) and MC (open circles) samples enriched with cosmic and halo muon background events. For the curves description, see the text. . . 74
6.25 The number of BCAL energy deposits versus the fraction of the number of energy deposits in BHAC2 to the total BCAL ones for data and MC expectations. The accepted events are in region to the left of the vertical line or below the horizontal line. 75
6.26 The number of tracks, N^{trks}, versus the number of EMC cells above noise in the BCAL in the data and the MC expectations. The part of the figure to the left of the line denotes the accepted region of events. 76
6.27 An example of an event removed from the final sample after visual scanning. 77
6.28 The kinematic phase-space in the Q^2-x plane for the LH final sample. The closed circles are the high-γ_0 events and the open ones are the low-γ_0. 78
6.29 The kinematic phase-space in the Q^2-x plane for the RH final sample. The closed circles are the high-γ_0 events and the open ones are the low-γ_0. 78
6.30 Shown are the distributions of P_T (a and b), P'_T (c and d), δ (e and f), and P_T/E_T (g and h), for the LH and RH samples as denoted in the figures. The full points stand for the CC data and the filled (dotted) histograms represent the MC expectations as obtained with ARIADNE (MEPS). The contributions from all background processes are shown as the filled dashed histograms. 79
6.31 Shown are the distributions of γ_h (a and b), N_{good} (c and d), z_{vtx}^{trks} (e and f), and z_{vtx}^{FCAL} (g and h), for the LH and RH samples as denoted in the figures. The full points stand for the CC data and the filled (dotted) histograms represent the MC expectations as obtained with ARIADNE (MEPS). The contributions from all background processes are shown as the filled dashed histograms. 80

7.1 The efficiency, purity and the acceptance as a function of Q^2 for LH (open squares) and RH (open circles) samples. 84
7.2 The efficiency, purity and the acceptance as a function of x for LH (open squares) and RH (open circles) samples. 85
7.3 The efficiency, purity and the acceptance as a function of y for LH (open squares) and RH (open circles) samples. 86

9.1 Upper plot: The CC differential cross section as a function of Q^2 for both LH (open squares) and RH (closed circles) samples. The curves represent the SM predictions as obtained with the HECTOR program and for the polarisation values P_{LH} and P_{RH}. Lower plot: The ratio of the measured CC cross section and the SM expectation for $P = 0$ as a function of Q^2, for LH (open squares) and RH (closed circles). The horizontal lines stand for $1 + P_{LH}$ and $1 + P_{RH}$. 97

9.2 Upper plot: The CC differential cross section as a function of x for both LH (open squares) and RH (closed circles) samples. The curves represent the SM predictions as obtained with the HECTOR program and for the polarisation values P_{LH} and P_{RH}. Lower plot: The ratio of the measured CC cross section and the SM expectation for $P = 0$ as a function of x, for LH (open squares) and RH (closed circles). The horizontal lines stand for $1 + P_{LH}$ and $1 + P_{RH}$. 98

9.3 Upper plot: The CC differential cross section as a function of y for both LH (open squares) and RH (closed circles) samples. The curves represent the SM predictions as obtained with the HECTOR program and for the polarisation values P_{LH} and P_{RH}. Lower plot: The ratio of the measured CC cross section and the SM expectation for $P = 0$ as a function of y, for LH (open squares) and RH (closed circles). The horizontal lines stand for $1 + P_{LH}$ and $1 + P_{RH}$. 99

9.4 The CC total cross section as a function of the longitudinal polarisation of the lepton beam. The point which correspond to zero polarisation comes from data collected in the 1999-2000 run period. The line represents the theoretical expectation and the band shows the uncertainty in the cross sections due to the uncertainty in the PDFs (ZEUS-S). 100

9.5 The result of the linear fit (dashed line) to the measurements of CC cross section (data points) as a function of polarisation. The band represents the fit uncertainty. 103

9.6 The variation of the estimate of $\sigma^{CC}(P = -1)$ as a function of the systematic check, denoted by its index as listed in Tables 9.1, 9.2, and 9.3. 104

9.7 The CC cross section assuming RH W only, σ^{CC}_{RH}, as a function of the W mass, M_{WR}. The dotted horizontal line stands for $\sigma^{CC}(P = -1)$ while for the dashed one, three standard deviations were added. 105

10.1 A comparison between the values of $\sin^2\theta_W$ as obtained from NuTeV, LEP, and SLAC with the world average as given by the PDG. 112
10.2 $\sin^2\theta_W$ as a function of M_Z at the Born level (curve) (MS scheme). The data point stands for the measured values of $\sin^2\theta_W$ and M_Z as given in the PDG. The dashed lines show the electroweak radiative correction to the measurement. . . . 114
10.3 Left (Right): The NC to CC ratio in terms of Feynman diagrams at low (medium-high) Q^2. 115
10.4 The theoretical NC to CC total cross sections ratio versus $\sin^2\theta_W$ for $Q^2 \geq 200\,\mathrm{GeV}^2$. The upper plot is for e^+p reactions while the lower one is for e^-p reactions. These values were obtained with HERACLES and the CTEQ5D parton density functions parameterisation. 116
10.5 The relative difference between the ratio of integrated NC to CC cross section obtained at the Born level, R^{Born}, and including the electroweak radiative corrections, R^{Rad}, versus Q^2_{min}, where Q^2_{min} denotes the lower limit of integration for the cross sections. 117
10.6 Upper (lower) figure: example of an CC (NC) event as observed in the ZEUS detector. In the NC event, a scattered electron in the BCAL with matching track in the CTD is observed. The Q^2 for the NC (CC) event is 1245 (3168) GeV^2. . 118
10.7 Flow diagram for selecting the final NC and CC samples. . . . 125
10.8 Comparison between MC and data for the transverse momentum of the hadronic system, P_T, in the NC (upper figures) and CC (lower figures) samples in the three data sets as denoted in the figure. 126
10.9 Comparison between MC and data for the transverse momentum calculated excluding first inner FCAL ring, P'_T, in the NC (upper figures) and CC (lower figures) samples in the three data sets as denoted in the figure. 127
10.10 Comparison between MC and data for Q^2 in the NC (upper figures) and CC (lower figures) samples in the three data sets as denoted in the figure. 128
10.11 Comparison between MC and data for x in the NC (upper figures) and CC (lower figures) samples in the three data sets as denoted in the figure. 129
10.12 Comparison between MC and data for y in the NC (upper figures) and CC (lower figures) samples in the three data sets as denoted in the figure. 130

10.13 Comparison between MC and data for the z-position of the CTD vertex, Z_{vtx}^{trks} in the NC (upper figures) and CC (lower figures) samples in the three data sets as denoted in the figure. 131
10.14 Comparison between MC and data for the z-position of the vertex calculated with the arrival time on the FCAL, Z_{vtx}^{FCAL} in the NC (upper figures) and CC (lower figures) samples in the three data sets as denoted in the figure. 132
10.15 Comparison between MC and data for γ in the NC (upper figures) and CC (lower figures) samples in the three data sets as denoted in the figure. 133
10.16 Comparison between MC and data for the ratio $\frac{P_T}{E_T}$ in the NC (upper figures) and CC (lower figures) samples in the three data sets as denoted in the figure. 134
10.17 Comparison between MC and data for $\Delta\phi$ in the NC (upper figures) and CC (lower figures) samples in the three data sets as denoted in the figure. 135
10.18 Comparison between MC and data for $\frac{N_{trks}-20}{N_{good}}$ in the NC (upper figures) and CC (lower figures) samples in the three data sets as denoted in the figure. 136
10.19 The expected ratio of integrated NC to CC cross section ratio, R, for $Q^2 > 200$ GeV^2 and the CTEQ5D parameterisation of parton distributions, as a function of $\sin^2\theta_W$, given for the experimental conditions relevant to the data sets, 1996-1997 (e^+p), 1998-1999 (e^-p), and 1999-2000 (e^+p). Also shown, as bands, are the results of the measurement with the statistical error. 138

11.1 The $\frac{d}{u}$ ratio as a function of x for $Q^2 = 6400$ GeV^2. The solid (dashed) line corresponds to the parameterisation from CTEQ5M without (with) nuclear corrections. The dotted line represents the result with nuclear corrections and the $\frac{d}{u}$ ratio forced to be 0.2 at $x = 1$. 141
11.2 Upper plot: The fraction of the NC cross section due only to u and d quarks. Lower plot: The fraction of the CC cross section due only to d quarks. 144
11.3 Fig. a) (b)): the kinematical phase-space in $Q^2 - x$ plane for the NC (CC) events, with iso-lines of y, P_T, and γ. 145
11.4 Upper: the P_T (a) and E_T (b) distribution for the final NC sample. Lower: the P_T (c) and E_T (d) distribution for the final CC sample. 146
11.5 The $\frac{P_T}{E_T}$ distribution for the NC (a) and CC (b) final samples. 147

11.6 The kinematic variables, Q^2,x, and y distributions for NC sample are presented in Fig. a), b), and c), respectively. The corresponding distributions for the CC sample are presented in Fig. d), e), and f). 148
11.7 Fig. a) (b)): the energy and the the polar angle of the scattered electron for the final NC sample. 149
11.8 The ratio $\frac{d}{y}$ ratio as a function of x. The dots stand for the extracted $\frac{\bar{d}}{u}$ using the 1999-2000 data, and the curves are the expectations for the parameterisations CTEQ3 DIS, CTEQ3 MS, MRST98 DIS, and MRST98 MS. 151

A.1 The systematic uncertainties (in percentage) in the LH differential cross section versus Q^2 for varying the high γ_0 selection cuts. 154
A.2 The systematic uncertainties (in percentage) in the RH differential cross section versus Q^2 for varying the high γ_0 selection cuts. 155
A.3 The systematic uncertainties (in percentage) in the LH differential cross section versus Q^2 for varying the low γ_0 selection cuts. 156
A.4 The systematic uncertainties (in percentage) in the RH differential cross section versus Q^2 for varying the low γ_0 selection cuts. 157
A.5 The systematic uncertainties (in percentage) in the LH differential cross section versus x for varying the high γ_0 selection cuts. 158
A.6 The systematic uncertainties (in percentage) in the RH differential cross section versus x for varying the high γ_0 selection cuts. 159
A.7 The systematic uncertainties (in percentage) in the LH differential cross section versus x for varying the low γ_0 selection cuts. 160
A.8 The systematic uncertainties (in percentage) in the RH differential cross section versus x for varying the low γ_0 selection cuts. 161
A.9 The systematic uncertainties (in percentage) in the LH differential cross section versus y for varying the high γ_0 selection cuts. 162
A.10 The systematic uncertainties (in percentage) in the RH differential cross section versus y for varying the high γ_0 selection cuts. 163

A.11 The systematic uncertainties (in percentage) in the LH differential cross section versus y for varying the low γ_0 selection cuts. 165
A.12 The systematic uncertainties (in percentage) in the RH differential cross section versus y for varying the low γ_0 selection cuts. 166
A.13 The changes in the LH differential cross section versus Q^2 for the calorimeter energy scale checks. 167
A.14 The changes in the RH differential cross section versus Q^2 for the calorimeter energy scale checks. 168
A.15 The changes in the LH differential cross section versus x for the calorimeter energy scale checks. 169
A.16 The changes in the RH differential cross section versus x for the calorimeter energy scale checks. 170
A.17 The changes in the LH differential cross section versus y for the calorimeter energy scale checks. 171
A.18 The changes in the RH differential cross section versus y for the calorimeter energy scale checks. 172
A.19 The systematic contribution due to using the MEPS MC instead of ARIADNE to the differential cross section versus the kinematic variables, Q^2, x, and y, for LH (figures a, c, and e) and RH (figures b, d, and f). 173
A.20 The distribution of P_T/E_T for events with $\gamma_0 > 0.4$rad and $P_T < 20$GeV for LH (figure a)) and RH (figure b)) sample. The χ^2/ndf distributions versus the parameter α assuming fixed value for the parameter β are given for the LH and RH samples. (figures c) and d) respectively. The χ^2/ndf distributions versus the fit parameter β with fixed value for α for LH and RH samples are shown in figure e) and f), respectively. . . 174
A.21 The systematic uncertainty contribution in the LH and RH cross section (in percentage) measurements, versus the kinematic variables, due to reweighting the MC events which were generated with CTEQ5D to the ZEUS-S NLO QCD PDFs. . . 175
A.22 The systematic uncertainty contributions (in percentage), to the cross section measurements due to the reweighting of the MC events to the NLO QCD corrections. 176
A.23 The systematic uncertainties are compared with the statistical errors in the differential cross sections. The bands represent the statistical errors while the dots are the systematic errors. . 177

List of Tables

4.1 Summary of the CC DIS MC samples used in the CC analysis, generated with the funnel version num02t2.0. N_{gen} denotes the number of generated events in each sample. 27

4.2 The direct and resolved PHP MC samples used in the CC analysis. 29

4.3 Summary of the NC DIS MC samples used in the CC analysis. 29

4.4 List of the di-lepton MC samples used in the CC analysis. . . 30

4.5 List of the W production MC samples used to evaluate the background to the CC sample. 31

6.1 Summary of the timing cuts which are used in this analysis. . 63

8.1 Summary of the description of the energy scale checks implemented in this analysis. 90

8.2 The results of the fits to the P_T/E_T distributions for LH and RH samples. 92

8.3 List of the systematic checks and their description. The index which identifies each source of possible systematic effect is given in the first column. 95

9.1 Variations of the measured cross sections and the resulting estimate of $\sigma^{CC}(P = -1)$ for the systematic checks affecting the high γ_0 sample. 106

9.2 Variations of the measured cross sections and the resulting estimate of $\sigma^{CC}(P = -1)$ for the systematic checks affecting the low γ_0 sample. 106

9.3 Variations of the measured cross sections and the resulting estimate of $\sigma^{CC}(P = -1)$ for the systematic checks affecting the calorimeter energy scale and the analysis details. 107

9.4 The single differential cross sections in bins of Q^2 ($\frac{d\sigma}{dQ^2}$) for e^+p interactions at $P = -40.6\%$. Given in the table are the Q^2 range of the bin, the bin centre (Q_0^2), the number of data events (N_{data}), the estimated number of background events (N_{bg}), the acceptance ($\mathcal{A}$) which results from efficiency (ϵ) and purity ($\mathcal{P}$), and the differential cross section measurement $\frac{d\sigma(e^+p\to\bar{\nu}X)}{dQ^2}$ (SM and measured). 108

9.5 The single differential cross sections in bins of Q^2 ($\frac{d\sigma}{dQ^2}$) for e^+p interactions at $P = +32.2\%$. The notation as in Table 9.4. 108

9.6 The single differential cross sections in bins of x ($\frac{d\sigma}{dx}$) for e^+p interactions at $P = -40.6\%$. Given in the table are the x range of the bin, the bin centre (x_0), the number of data events (N_{data}), the estimated number of background events (N_{bg}), the acceptance ($\mathcal{A}$) which results from efficiency (ϵ) and purity ($\mathcal{P}$), and the differential cross section measurement $\frac{d\sigma(e^+p\to\bar{\nu}X)}{dx}$ (SM and measured). 109

9.7 The single differential cross sections in bins of x ($\frac{d\sigma}{dx}$) for e^+p interactions at $P = +32.2\%$. The notation as in Table 9.6. . . 109

9.8 The single differential cross sections in bins of y ($\frac{d\sigma}{dy}$) for e^+p interactions at $P = -40.6\%$. Given in the table are the y range of the bin, the bin centre (y_0), the number of data events (N_{data}), the estimated number of background events (N_{bg}), the acceptance ($\mathcal{A}$) which results from effecincy (ϵ) and purity ($\mathcal{P}$), and the differential cross section measurement $\frac{d\sigma(e^+p\to\bar{\nu}X)}{dy}$ (SM and measured). 109

9.9 The single differential cross sections in bins of y ($\frac{d\sigma}{dy}$) for e^+p interactions at $P = +32.2\%$. The notation as in Table 9.8. . . 110

10.1 Summary table of the data sample used to extract $\sin^2\theta_W$. . . 113

10.2 The selection cuts implemented in the analysis of e^+p **1996-1997** data. 121

10.3 The selection cuts implemented in the analysis of e^-p **1998-1999** data. 122

10.4 The selection cuts implemented in the analysis of e^+p **1999-2000** data. 123

10.5 The final number of events in the data and in MC in the NC and CC samples in the three data sets. 137

10.6 The determined values of $\sin^2\theta_W$ as obtained from the e^+p (1996-1997 and 1999-2000) and the e^-p (1998-1999) data. . . . 137

11.1 Comparison of the data and MC events for NC and CC samples in three bins of x. Given in the table are the x-range, the bin centre (x_0), the number of NC data events (N^{NC}_{data}), the number of NC MC events (N^{NC}_{MC}), the number of CC data events (N^{CC}_{data}), and number of CC MC events (N^{CC}_{MC}). 150
11.2 The extracted values of $\frac{d}{u}$ from the data, compared to the expectations using the CTEQ3D parameterisation, at the x-bin centre x_0. 150

A.1 Summary of the systematic errors for for the LH and RH $d\sigma/dQ^2$.164
A.2 Summary of the systematic errors for for the LH and RH $d\sigma/dx$.164
A.3 Summary of the systematic errors for for the LH and RH $d\sigma/dy$.164
A.4 The systematic uncertainty contributions (in percentage) in the differential cross section versus Q^2, at $P = -40\%$. 178
A.5 The systematic uncertainty contributions (in percentage) in the differential cross section versus Q^2, at $P = +32\%$. 179
A.6 The systematic uncertainty contributions (in percentage) in the differential cross section versus x, at $P = -40\%$. 180
A.7 The systematic uncertainty contributions (in percentage) in the differential cross section versus x, at $P = +32\%$. 181
A.8 The systematic uncertainty contributions (in percentage) in the differential cross section versus y, at $P = -40\%$. 182
A.9 The systematic uncertainty contributions (in percentage) in the differential cross section versus y, at $P = +32\%$. 183
A.10 The systematic uncertainty contributions (in percentage) in the RH differential cross section versus y. 184

Chapter 1

Introduction

The question of what matter is made off took much of the human attention. This was discussed by the ancient Greeks who classified matter into air, earth, water, and fire. In view of today's particle physicists, the world is built out of six leptons and six quarks [1] and they can be described within the gauge field theory. In addition to gravity, there are three forces; weak, electromagnetic, and strong. The weak and the electromagnetic interactions are unified within the electroweak (EW) theory, as suggested by Glashow, Salam and Weinberg [2–4]. The strong interactions are described by the theory of Quantum Chromodynamics (QCD). The EW theory and QCD are combined in a model called the Standard Model (SM).

The gauge group of the electroweak theory is based on the $SU(2)$ group of weak isospin and the $U(1)$ group of weak hypercharge. The gauge symmetry of electroweak interactions is spontaneously broken around 100 GeV by the Higgs mechanism [5–9] which generates masses for W and Z gauge bosons.

Assuming the simplest Higgs sector, the SM contains, besides fermion masses, quark mixing angles, and the mass of the Higgs scalar, three free parameters in the gauge sector, the values of the gauge couplings, g_1 and g_2, and the Higgs field vacuum expectation value v. These parameters are usually replaced by a set of parameters with closer relation to physical observables. For example, a natural choice in deep inelastic ep scattering is the electromagnetic fine structure constant, α, and the masses of the gauge bosons $W^{\pm}$ and Z. Sometimes, the boson masses are replaced by the Fermi constant, G_μ, and the weak mixing angle, $\sin^2\theta_W$. At the Born level, $\sin^2\theta_W$ is defined as the ratio of gauge couplings, $\sin^2\theta_W = \frac{g_1}{g_2}$, and represents the mixing between the hypercharge current and the third, neutral, component of the weak current.

The proton, as the most stable hadron, was first considered as an elementary particle besides the leptons and the quarks. However, it was found

that the proton is not a point-like particle and therefore has a substructure. Many experiments were built to understand the internal structure of the proton [10–16]. Among these, the hadron electron ring accelerator (HERA) is the first electron proton collider designed to investigate the structure of the proton.

At HERA, a proton beam of energy 920 GeV (820 GeV till 1998) collides with either an electron or a positron [1] beam of energy 27.52 GeV. The interaction between the electron and the proton occurs by exchanging a gauge boson. If the charge of the exchanged boson is neutral, i.e. γ or Z^0, this type of interaction is called neutral current (NC), while if the exchanged boson is charged, i.e. W^+ or W^-, then the interaction is called charged current (CC). The Feynman diagrams for the two processes are shown in Fig. 1.1.

The HERA collider allow the exploration of deep inelastic scattering (DIS) at high values of the negative four-momentum-transfer squared, Q^2. Using the data collected between the years 1994-2000 both the H1 and the ZEUS collaborations have reported measurements of the NC and CC cross sections [17–31]. These measurements were done at an extended kinematic phase-space covered by fixed-target experiments [32] and therefore allow the HERA experiments to probe the electroweak sector of the SM.

Deep inelastic scattering of electrons on protons has been essential to understand the structure of the proton. In the naive quark parton model, the proton is an object which consists of three point-like partons called quarks. In this model the DIS process is the quasi-elastic scattering of the exchanged boson off a single quark in the proton. Fig. 1.2 shows the structure function F_2^{em} measured for NC DIS as a function of Q^2 for different values of x (see sec. 2.1 for kinematics definition). Here F_2^{em} is the electromagnetic part of the structure function F_2^{NC} as described in sec. 2.3. Strong scaling violations are observed, especially at low values of x. This is the manifestation of the presence of a large gluon density in the proton. The observed scaling violations are well reproduced by the DGLAP [33–36] evolution equations of perturbative QCD.

In this thesis we propose to study three subjects, to be described below.

Since 2002, HERA provides longitudinally polarised lepton beam to the colliding experiments and thus polarised lepton-nucleon scattering are performed. This was first used in the 1970s but at Q^2 values of $1 - 5$ GeV^2. A polarised electron beam was used in early measurements of parity violation attributable to the weak neutral current [37, 38]. The SM predicts that NC and CC cross sections depend on the longitudinal polarisation of the incom-

[1] In the following, for simplicity we will denote as electron the charged lepton, independently whether it is an e^+ or an e^-, unless otherwise stated.

ing lepton beam. The absence of right-handed charged currents leads to the conclusion that the CC cross section is a linear function of the polarisation, i.e., the CC cross section of fully left-handed (right-handed) positrons (electrons) on protons vanishes. In this analysis, we measure the total CC cross section at two values of incoming lepton beam polarisations. In addition, using the previous ZEUS result which corresponds to zero polarisation, allows an extrapolation of the CC cross section to fully negative polarisation of the incoming positron beam. In this way, a direct check can be performed whether the right-handed W exists, and thus whether new physics beyond the SM is obtained.

The NC interaction may be either electromagnetic or weak, depending on the scale. The interference between the two processes can be given in terms of $\sin^2\theta_W$. The CC interaction is purely weak and the cross section contains a clear dependence on $\sin^2\theta_W$ via M_W. In this analysis, we extract the value of $\sin^2\theta_W$ from the direct measurement of the NC to the CC cross sections ratio at high Q^2. We believe that some of the systematic uncertainties may cancel out in the ratio and thus better measurement is achieved. This measurement is done under the assumption that the parton density functions (PDFs) are well known.

The PDFs have been given by several parameterisations. It was found that these parameterisations assume different values of d-quark to u-quark at the limit of $x \to 1$ [39,40], where x represents the Bjorken-x (see sec. 2.3). Moreover, the different parameterisations give different $\frac{d}{u}$ for $x > 0.3$. The HERA data can be used to give a first estimate on this ratio in the region $x < 0.7$. We assume that $\sin^2\theta_W$ is well known and use the NC to CC cross sections ratio to constrain the $\frac{d}{u}$ at high x and at $Q^2 \sim M_W^2$.

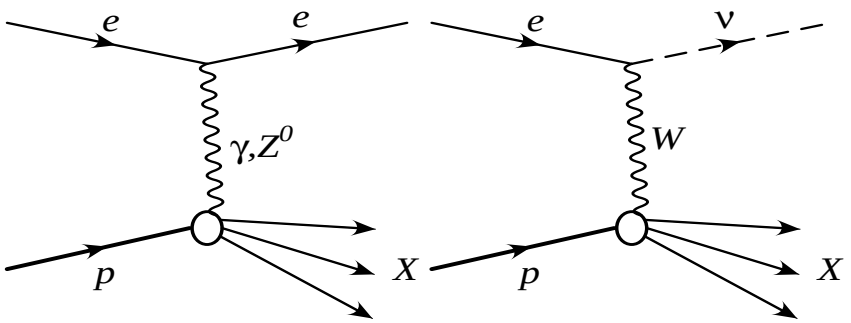

Figure 1.1: Feynman diagrams for the NC (left) and CC (right) interactions at the Born level.

The order of the thesis content is the following:

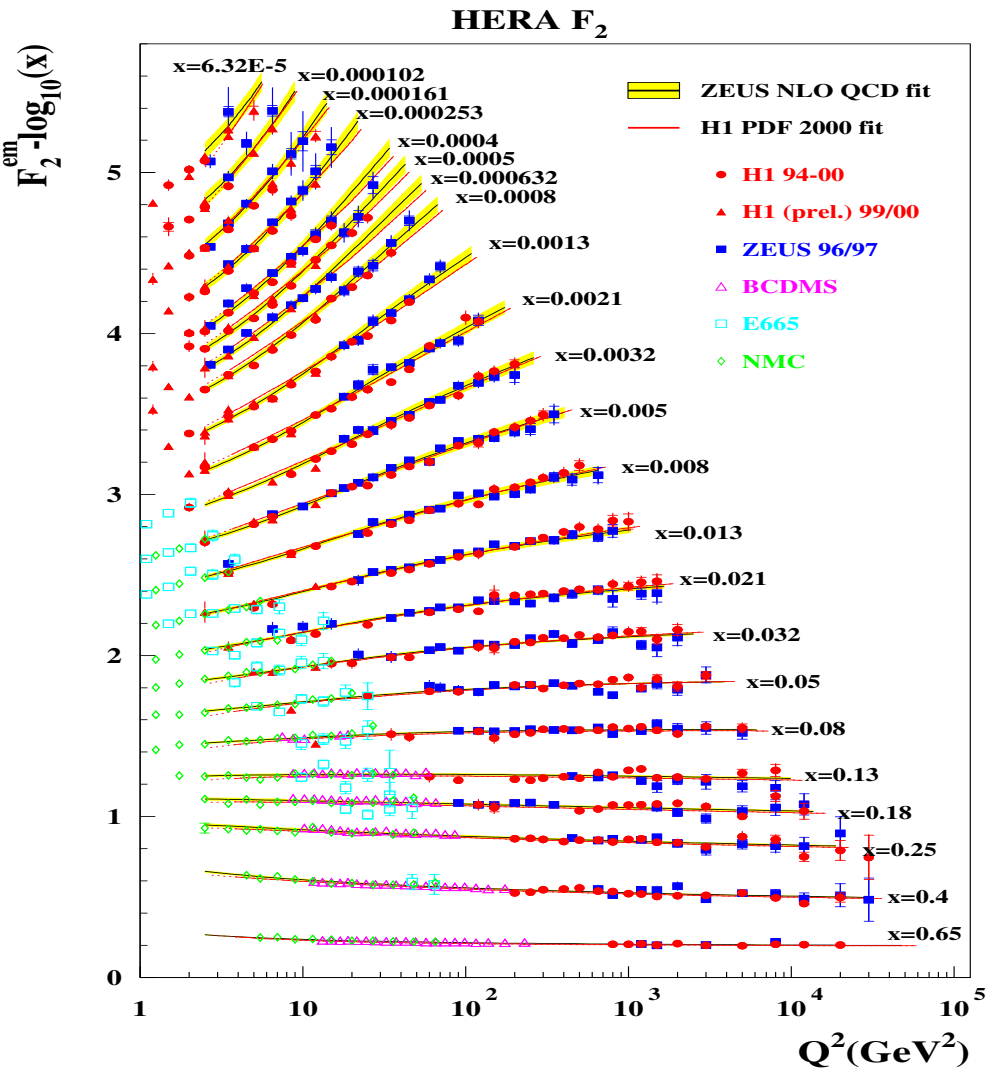

Figure 1.2: The structure function F_2^{em} versus Q^2 at fixed values of x compared to a fit based on DGLAP evolution equations.

In chapter two, the kinematics are introduced and the theoretical framework is discussed.

In chapter third, the experimental framework is introduced with an emphasis on the HERA upgrade project. In addition, the ZEUS detector components used for this analysis are described.

In the four chapter, the description of the Monte Carlo (MC) simulation is discussed. A description of the generation of the MC CC events and the background samples is given.

The reconstruction of the kinematic variables used in this analysis are detailed in chapter five.

The event selection cuts applied for this analysis are detailed in chapter six, where the final right-handed and left-handed CC samples are obtained.

In chapter seven, acceptance, efficiency, purity, the differential and total cross section are defined, described, and determined.

The systematic checks and the systematic uncertainties are discussed in chapter eight.

In chapter nine, the measurements of the CC differential and total cross section at different values of the longitudinal polarisation of the incoming electron beam are presented.

In chapter ten, the extraction of $\sin^2\theta_W$ using the HERA I data with integrated luminosity of $\mathcal{L} \sim 116$ pb^{-1} is presented.

In chapter eleven, the extraction of d to u ratio at three values x and $Q^2 \sim M_W^2$ is described.

Chapter 2

Theoretical framework

2.1 DIS Kinematic variables

At HERA, an incoming electron with four momentum k collides with a proton with four momentum P. The exchanged boson has a momentum q and the scattered lepton polar angle is θ while the scattered angle of the struck quark is γ (see Fig. 2.1). The kinematic variables used in this analysis are defined as

$$
\begin{aligned}
s &= 4E_e E_p \,, && (2.1)\\
Q^2 &= -q^2 \,, \text{where } q = k - k' = P' - P \,, && (2.2)\\
x &= \frac{Q^2}{2P \cdot q} \,, && (2.3)\\
y &= \frac{q \cdot P}{k \cdot P} \,, && (2.4)
\end{aligned}
$$

where $\sqrt{s}$ is the energy in the ep centre of mass, Q^2 is the negative square of the four momentum transfer, x is the Bjorken scaling variable, y is the fractional energy transfer to the proton in the latter rest frame, and k' (P') is the four momentum of the final lepton (hadronic final state). The incoming electron (proton) energy is denoted as E_e (E_p). The kinematic variables, Q^2, x, y, and s, are related by $Q^2 = xys$, when the masses of the particles are neglected. The Q^2 of the interaction characterises how energetic the reaction is and at what scale the proton structure is probed. High Q^2 means that the proton is probed at small distance.

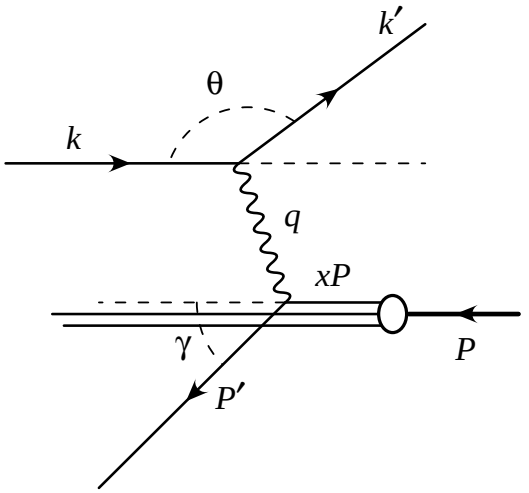

Figure 2.1: Kinematics of DIS ep interactions (see text for details).

2.2 Charged current cross section

The deep inelastic CC cross section for scattering of leptons on protons, $ep \to \nu_e X$, is given by

$$\frac{d^2\sigma^{CC}_{Born}(e^{\pm}p)}{dxdQ^2} = \frac{G_\mu^2}{4\pi x}\left(\frac{M_W^2}{Q^2+M_W^2}\right)^2 \\ [Y_+ F_2^{CC}(x,Q^2) \mp Y_- x F_3^{CC}(x,Q^2)] \cdot (1+P)\,, \tag{2.5}$$

where $Y_\pm = 1 \pm (1-y)^2$. G_μ is the Fermi constant and M_W is the W boson mass. For simplicity, the contribution of the longitudinal structure function is neglected. P is the degree of the longitudinal polarisation of the incoming electron beam and is given by

$$P = \frac{N_+ - N_-}{N_+ + N_-}\,, \tag{2.6}$$

where N_+ (N_-) is the number of electrons parallel (anti parallel) to the electron beam direction. According to eq. (2.5), the fully right (left) handed electron (positron) beam does not interact with the proton beam, i.e. the cross section vanishes due to the absence of right handed W bosons in the SM. In Fig. 2.2 the expectation of the total CC cross section as a function of the polarisation degree, P, is shown for e^+p and e^-p reactions. The data points at $P = 0$ are the measured values using the data with the reactions of non-polarised electrons on protons.

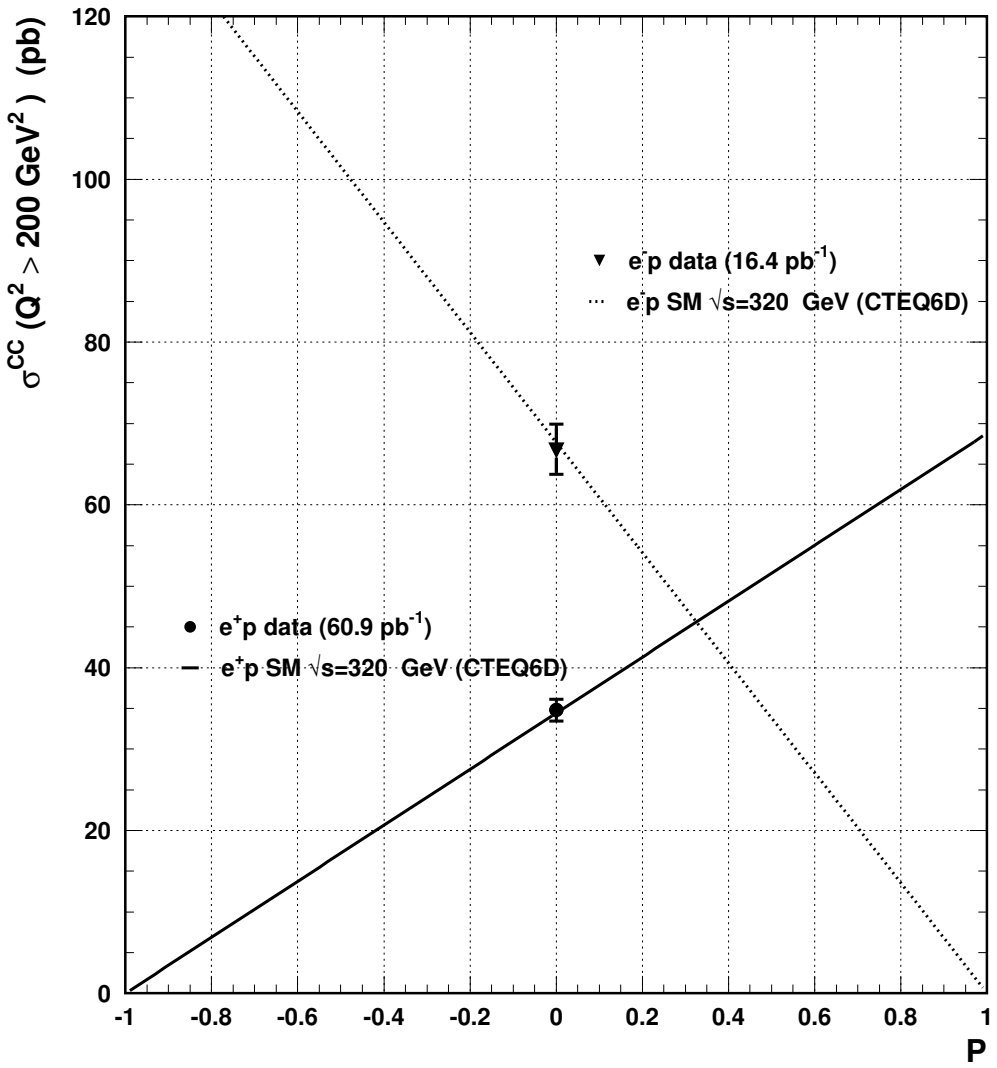

Figure 2.2: The total CC DIS cross section for $e^{\pm}p$ scattering plotted as a function of the polarisation of the incoming lepton beam, P.

In the QCD improved quark-parton model, the structure functions F_2^{CC} and xF_3^{CC} for e^+p are given by

$$F_2^{CC}(x,Q^2) = 2x[d(x,Q^2) + s(x,Q^2) + \bar{u}(x,Q^2) + \bar{c}(x,Q^2)]\,, \qquad (2.7)$$

$$xF_3^{CC}(x,Q^2) = 2x[d(x,Q^2) + s(x,Q^2) - \bar{u}(x,Q^2) - \bar{c}(x,Q^2)]\,, \qquad (2.8)$$

where $q(x,Q^2)$ stands for the appropriate density function for a parton ($q =$

$u, d, s, ...$). Similarly for $e^- p$ scattering

$$F_2^{CC}(x, Q^2) = 2x[u(x, Q^2) + c(x, Q^2) + \bar{d}(x, Q^2) + \bar{s}(x, Q^2)]\,, \tag{2.9}$$

$$xF_3^{CC}(x, Q^2) = 2x[u(x, Q^2) + c(x, Q^2) - \bar{d}(x, Q^2) - \bar{s}(x, Q^2)]\,. \tag{2.10}$$

At high x values, one can safely ignore the sea quarks and assume that the proton is dominated by the valence quarks. Under this assumption, the $e^+ p$ cross section is proportional to $(1-y)^2 d(x, Q^2)$, while the $e^- p$ CC cross section is proportional to $u(x, Q^2)$. Since the u quark dominates in the proton, the $e^- p$ CC cross section is higher than the $e^+ p$ CC cross section (see Fig. 2.3).

2.3 Neutral current cross section

The NC cross section for the reaction $ep \to eX$ can be expressed as

$$\frac{d^2\sigma_{Born}^{NC}(e^{\pm}p)}{dxdQ^2} = \frac{2\pi\alpha^2}{xQ^4}[Y_+ F_2^{NC}(x, Q^2) \mp Y_- xF_3^{NC}(x, Q^2)]\,. \tag{2.11}$$

In the QCD improved quark-parton model, the structure functions F_2^{NC} and xF_3^{NC} are given by

$$F_2^{NC}(x, Q^2) = x\sum_f A_f(Q^2)[q_f(x, Q^2) + \bar{q}_f(x, Q^2)]\,, \tag{2.12}$$

$$xF_3^{NC}(x, Q^2) = x\sum_f B_f(Q^2)[q_f(x, Q^2) - \bar{q}_f(x, Q^2)]\,, \tag{2.13}$$

where $q_f(x, Q^2)$ stands for the appropriate density function for parton f ($f = u, d, s, c, t,$ and b). The factors $A_f(Q^2)$ and $B_f(Q^2)$ are only functions of Q^2,

$$A_f(Q^2) = e_f^2 - 2v_e v_f e_f P_Z + (v_e^2 + a_e^2)P_Z^2\,, \tag{2.14}$$

$$B_f(Q^2) = -2a_e a_f e_f P_Z + 4v_e a_e v_f a_f P_Z^2\,, \tag{2.15}$$

where

$$P_Z = \frac{1}{4\sin^2\theta_W \cos^2\theta_W}\frac{Q^2}{Q^2 + M_Z^2}\,. \tag{2.16}$$

Here, e_f, is the electric charge of the quark, v_e (v_f) and a_e (a_f) are the vector and axial-vector coupling of the electron (quark) to the Z^0, and M_Z is the Z^0 boson mass.

The NC and the CC cross sections for non-polarised electrons with protons were measured at HERA. Fig. 2.3 shows the NC and CC differential cross section, $d\sigma/dQ^2$ as a function of Q^2 for both e^+p and e^-p. The measured cross sections are compared to the SM theoretical expectations. Around $Q^2 \sim 10^4$ GeV^2, the CC and NC cross sections become equal. Since the NC cross section is dominated by electromagnetic component this equality can be interpreted as a manifestation of electroweak unification.

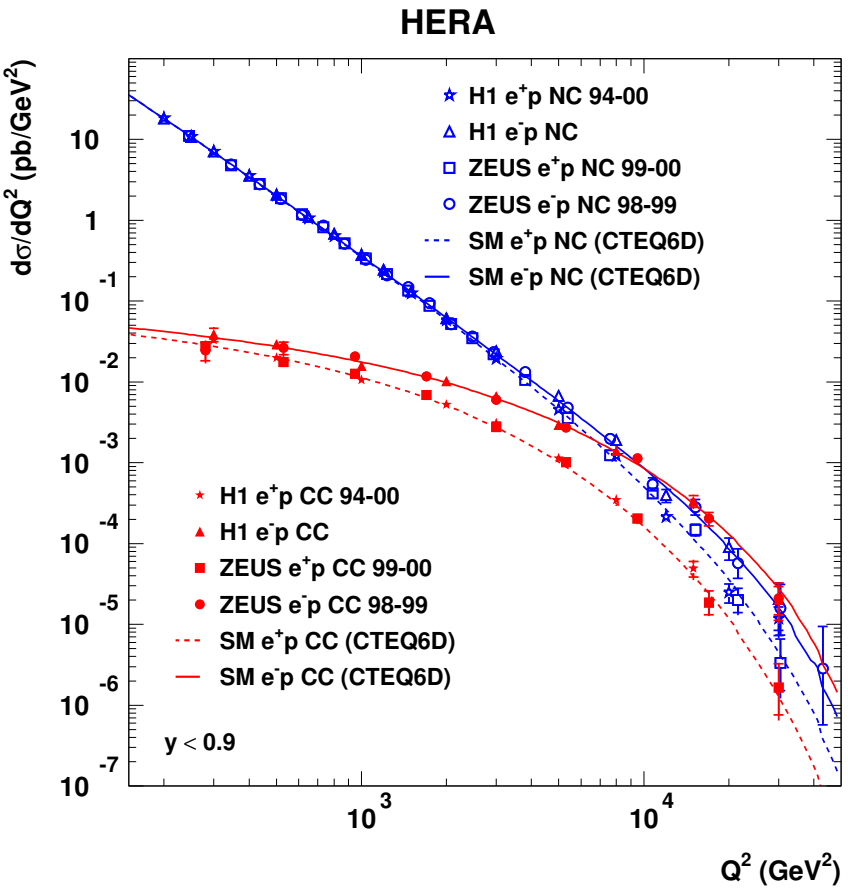

Figure 2.3: The NC and CC cross sections for e^+p and e^-p interactions versus Q^2.

2.4 Parton density functions

A parton density function (PDF) for a particular quark, $q(x, Q^2)$, denotes the probability of finding the quark, with momentum fraction x at a given Q^2. These functions cannot be calculated analytically and therefore global fits to the data sets are implemented to extract the PDFs. The PDFs are parameterised in x at a fixed starting value of Q^2 and can then be evolved using the DGLAP evolution equations.

The ZEUS-S fit [41] are performed on the ZEUS data from the run period 1996-1997, together with fixed-target data, to extract the PDFs. The fixed-target data consist of F_2 measurements from BCDMS [10], NMC [42] and E665 [12], deuterium-target data from NMC and E665 to separate $\bar{u}$ and $\bar{d}$, the ratio F_2^D/F_2^p from NMC which determine the ratio of d to u valence quark, and the structure function xF_3 from the CCFR experiment [43] constraining the valence quarks at high Bjorken x in the range $0.1 < x < 0.65$. The strong coupling constant, α_s, is a free parameter in the fit. The kinematic phase space covered by the above input data is shown in Fig. 2.4. The PDFs u-valence, $xu_v(x)$, d-valence, $xd_v(x)$, total sea, $xS(x)$, $xg(x)$, and the difference between the d and u contribution to the sea, were parameterised at $Q^2 = 7$ GeV^2 using the following expression

$$xf(x) = p_1 x^{p_2}(1-x)^{p_3}(1+P_5 x)\,. \tag{2.17}$$

With these expressions one has 20 parameters. The momentum sum rules fix nine of them and thus 11 free parameters remain.

There are many PDFs parameterisations such as CTEQ6 [44], MRST [45], GRV [46] and others. The MC events used in the analyses of this work were generated with the CTEQ4D [47] and CTEQ5D [48] parameterisations.

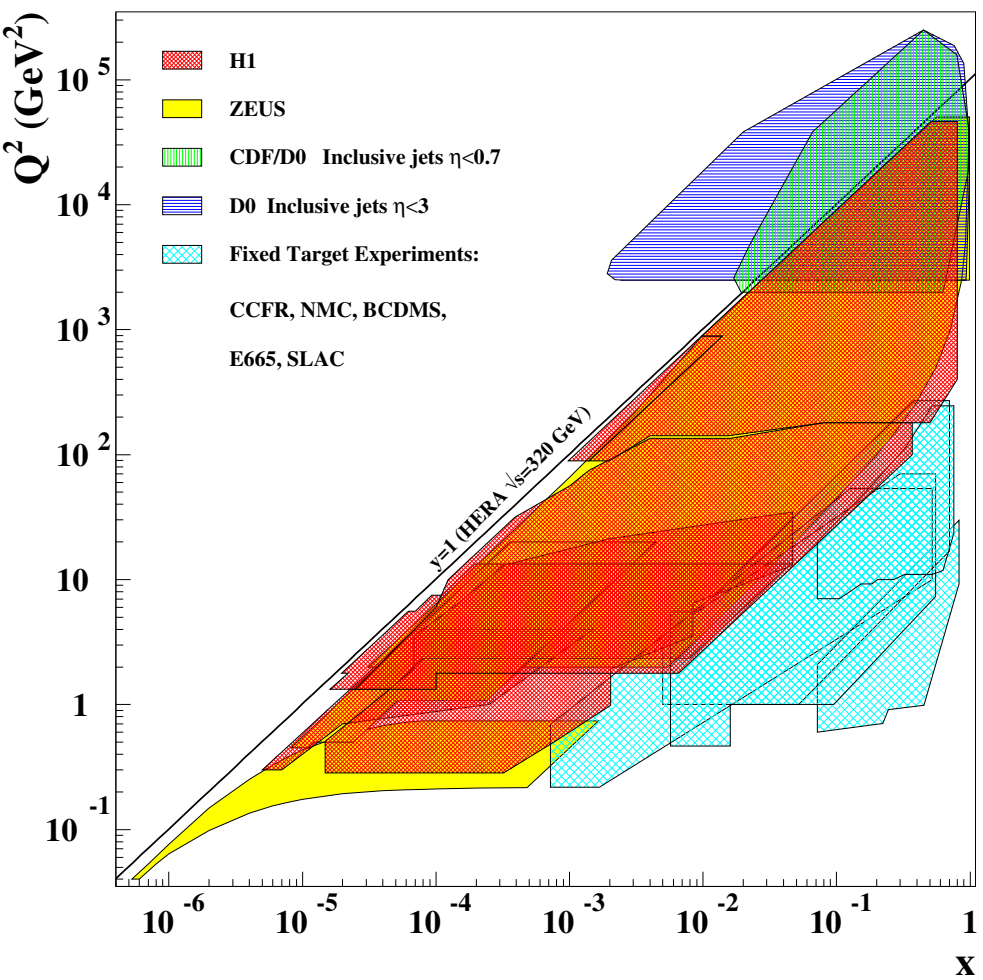

Figure 2.4: The kinematic phase space covered by the data from several experiments including the ZEUS one.

Chapter 3

Experimental framework

3.1 HERA

The Hadron Electron Ring Accelerator, HERA [49], is located at the Deutsches Elektronen Synchrotron (DESY) in Hamburg, Germany. Two collider experiments (H1 [50] and ZEUS [51]) and two fixed target experiments (HERMES [52] and HERA-B [53]) use the beams provided by HERA. The location of the HERA experiments are pointed out in the layout of the accelerator in Fig. 3.1. The electrons are accelerated to an energy of 27.5 GeV and the protons to 920 GeV [1]. The beams are structured over a circumference of 6.3 km into 220 bunches and the time difference between two crossing is 96 ns. For background study purposes, not all bunches are filled. Those that are filled contain $\sim 10^9$ electrons/protons. Fig. 3.2 shows the integrated luminosities delivered by HERA before and after the accelerator upgrade (see sec. 3.3). The integrated luminosity delivered by the accelerator is seen to improve steadily, and so far reached ~ 400 pb^{-1}. As can be seen from this figure, the HERA efficiency in delivering luminosity was increased with time.

3.2 The ZEUS detector

A detailed description of the ZEUS detector can be found elsewhere [51]. A brief outline of the most relevant components for this analysis is given below. The ZEUS detector is located 30 m underground in the south experimental hall of HERA. The weight of the detector is about 3500 tons and it is 12 m in height. ZEUS is a multipurpose solenoid detector with a solid angle coverage of 99.6%. A longitudinal cross sectional view of the detector is shown in

[1] The proton beam energy was 820 GeV until 1998

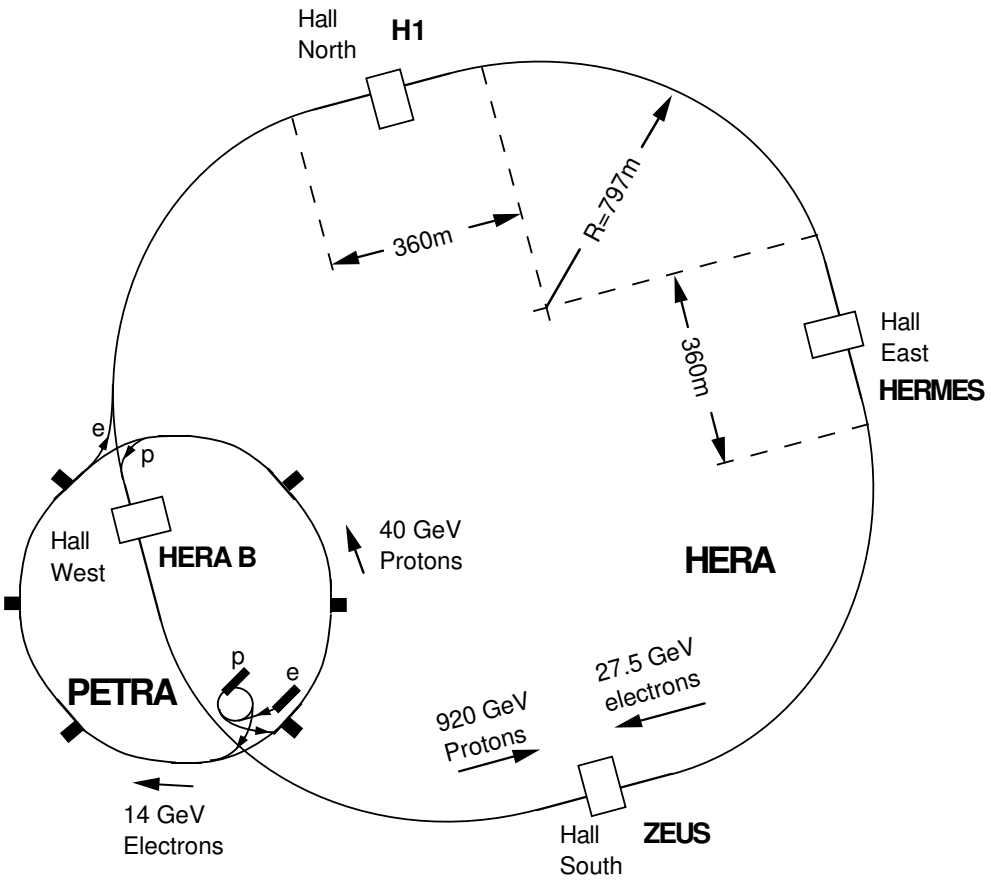

Figure 3.1: Schematic representation of the HERA accelerator complex at DESY, Hamburg, Germany.

Fig. 3.3.

3.2.1 Central tracking detector

Charged particles are tracked in the central tracking detector (CTD) [54–56], which operates in a magnetic field of 1.43 T provided by a thin superconducting solenoid. The CTD consists of 72 cylindrical drift chamber layers, organised in nine superlayers covering the polar angles $(15°, 164°)$. The relative resolution of the transverse-momentum, P_T, for full-length tracks is $\sigma(P_T)/P_T = 0.0058P_T \oplus 0.0014/P_T$, with P_T in GeV. The position of the interaction point along the beam pipe direction can be reconstructed from the hits of the charged particles in the CTD, with a resolution of about 1 cm.

The coordinate system in ZEUS was chosen as a right-handed system,

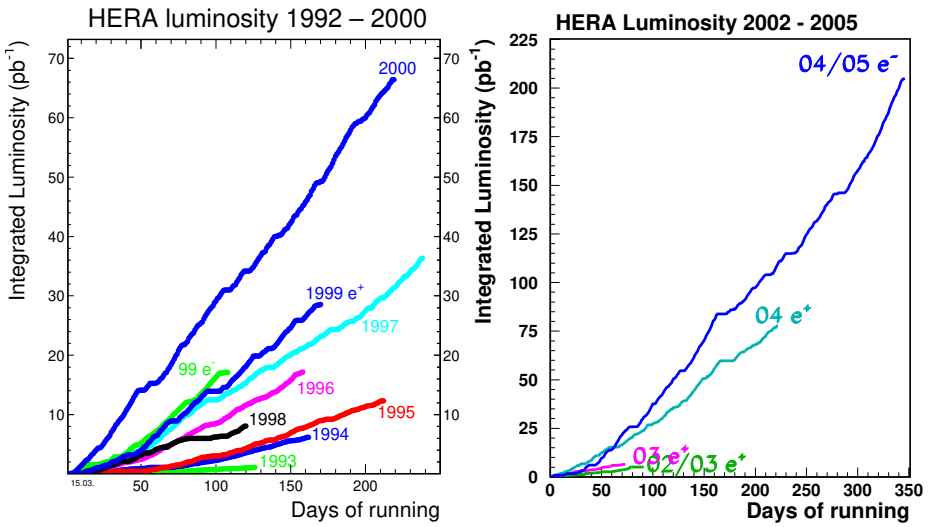

Figure 3.2: The integrated luminosity delivered by HERA I (left) and HERA II (right) in the various run periods.

where the incoming proton travels in the positive z direction, the x-axis is defined to point horizontally toward the centre of HERA, and the y-axis points upward as shown in Fig. 3.4.

3.2.2 The calorimeter

The high-resolution uranium-scintillator calorimeter (CAL) [57–60] consists of three parts: the forward (FCAL), the barrel (BCAL) and the rear (RCAL) calorimeter, covering 99.6% of the solid angle around the interaction point (IP). Each part of the CAL is subdivided transversely into towers and longitudinally into one electromagnetic section (EMC) and either one (in RCAL) or two (in BCAL or FCAL) hadronic sections (HAC). Both EMC and HAC sections are built with cells which are the smallest subdivision of the calorimeter. The energy (E) resolutions, as measured under test-beam conditions, are $\sigma(E)/E = 0.18/\sqrt{E}$ for electrons and $\sigma(E)/E = 0.35/\sqrt{E}$ for hadrons, where E is measured in GeV. For energy deposits exceeding 4.5 GeV, the time resolution is better than 1 ns. The resolution of the interaction vertex position, determined from the arrival time of the signal in the FCAL, is about 10 cm. This is about 10 times larger than the one obtained with the CTD.

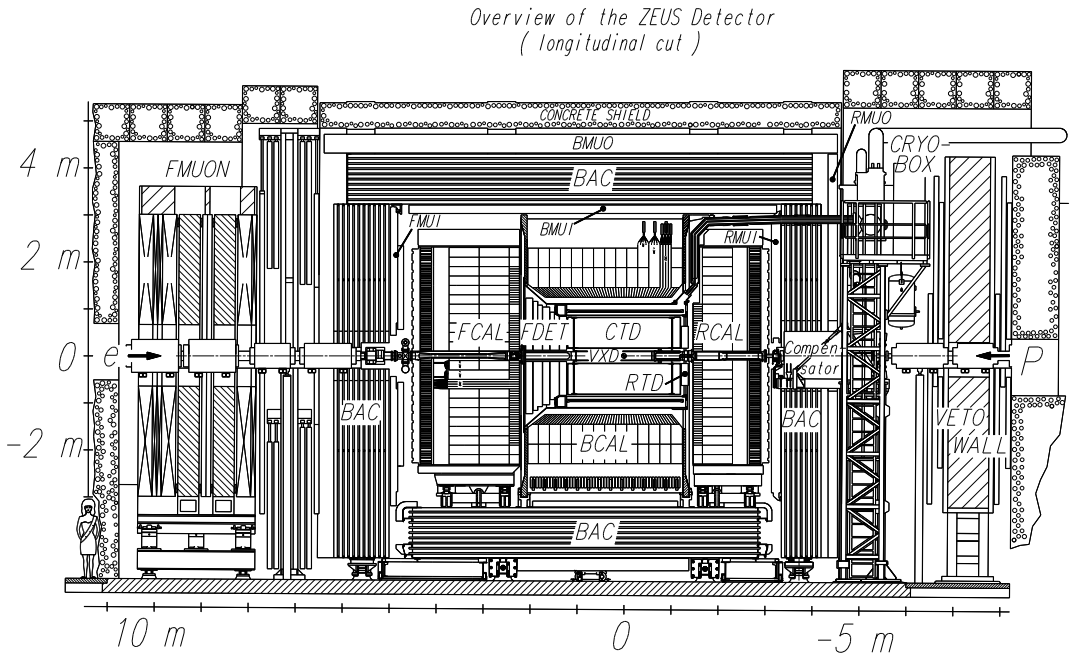

Figure 3.3: A longitudinal cross sectional view of the ZEUS detector. The directions of the incoming beams are shown in the figure. Also the main components of the detector are labelled.

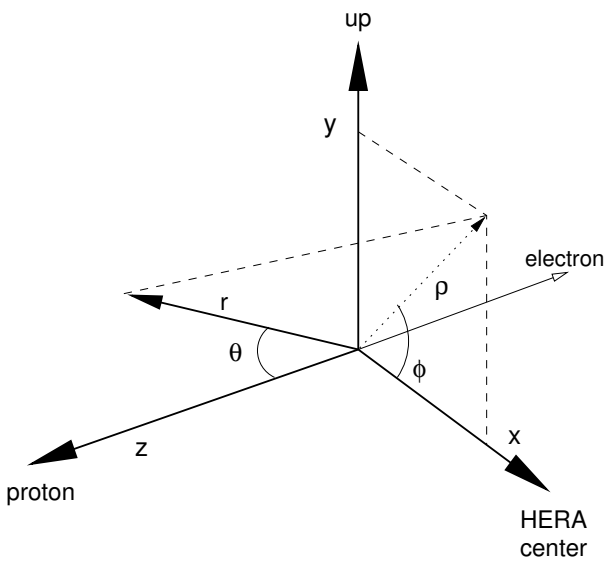

Figure 3.4: The ZEUS coordinate system.

3.2.3 Muon tagging system

The muon tagging system consists of the rear muon chamber (RMUON), barrel muon chamber (BMUON) [61], and the formard muon spectrometer (FMUON) [62]. In this analysis, the muon tagging system in used to reduce the events induces by cosmic-ray or beam halo-muons hitting the detector from outside.

3.2.4 Luminosity monitor

The luminosity was measured using the electromagnetic Bethe-Heitler process $ep \rightarrow e\gamma p$. The luminosity monitoring system consists of a photon detector, which is located -108 m, from the interaction point, as shown in Fig 3.5. The Bethe-Heitler final state particles are emitted at very small angles relative to the incoming electron direction. The photons in this process are travelling anti-parallel to the proton beams and are detected by the photon detector. The luminosity was also measured using a spectrometer system (SPEC) [63]. Thus, two independent luminosity measurements can be performed. In the CC analysis from HERA II, we use the luminosity which was measured with the electron detector. The collected luminosity was measured with 5% uncertainty.

3.3 The HERA and ZEUS upgrade

During the shutdown between the years 2000 to 2002, HERA was upgraded to increase significantly the luminosity and to provide longitudinally polarised lepton beams. So far, the HERA physics was explored mainly at small Q^2 values compared to the scale $Q^2 = M_W^2$. With higher luminosity, the higher Q^2 regime can be explored and thus new important tests of electroweak and strong interaction can be performed. Below, the most relevant upgrades used in this analysis are briefly discussed.

3.3.1 Polarised electron beams

In high energy ring accelerators, electron (positron) beams can become transversely polarised through the emission of synchrotron radiation [64] (Sokolov-Ternov effect). This process involves a small asymmetry in the spin-flip amplitudes, which enhances the population of the spin state anti-parallel (parallel) to the magnetic field in the ring accelerator. The polarisation increases

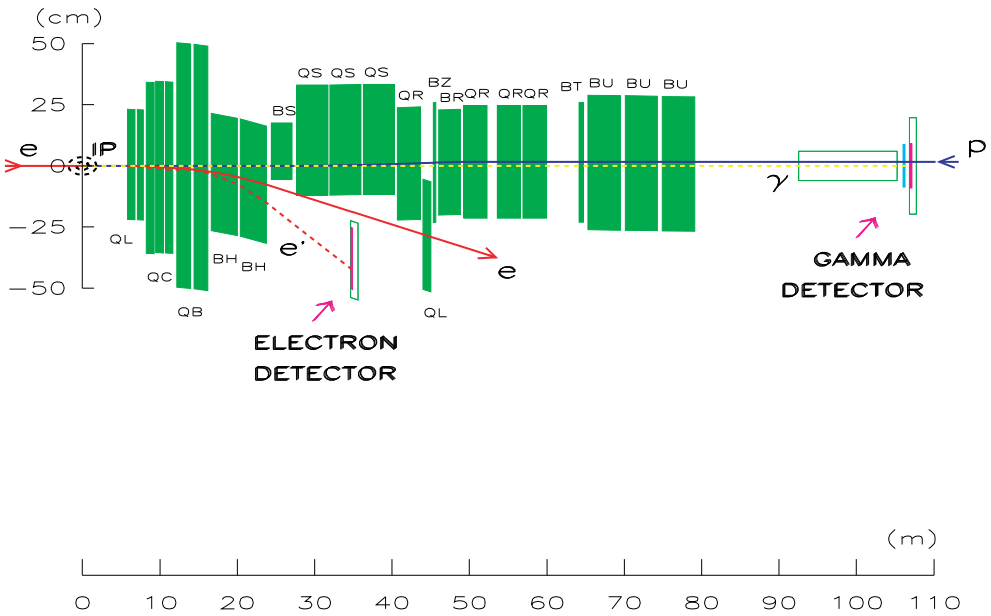

Figure 3.5: A schematic diagram of the luminosity monitor. The x axis in bottom of the figure shows the distances of the components relative to the interaction point.

with time according to

$$P(t) = P_{Max}(1 - e^{-\frac{t}{\tau}}), \tag{3.1}$$

where t is the time, P_{Max} and τ are the maximum polarisation and the build-up time. These constants are characteristic of the ring conditions. The maximum polarisation that can be achieved theoretically, in the absence of depolarisation effects, is $P_{Max} = 0.924$. The build-up time constant, which depends on the bending radius of the rings and the lepton beam energy, is $\tau = 37$ minutes at an electron beam energy of 27.5 GeV. Fig. 3.6 shows the polarisation as a function of time as measured at HERA I, before the upgrade.

At HERA I, two spin rotators around the HERMES experiment were operated to convert the transversely polarised electrons to longitudinally polarised electrons. During the HERA shutdown, another two pairs of spin rotators, around the H1 and ZEUS experiments, were installed. Thus HERA II has now three pairs of spin rotators as shown in Fig. 3.7.

Several known methods to measure the polarisation are used (see for example [65,66]). The most accurate method at high energy is based on Compton scattering of circularly polarised photons from an intense pulsed laser

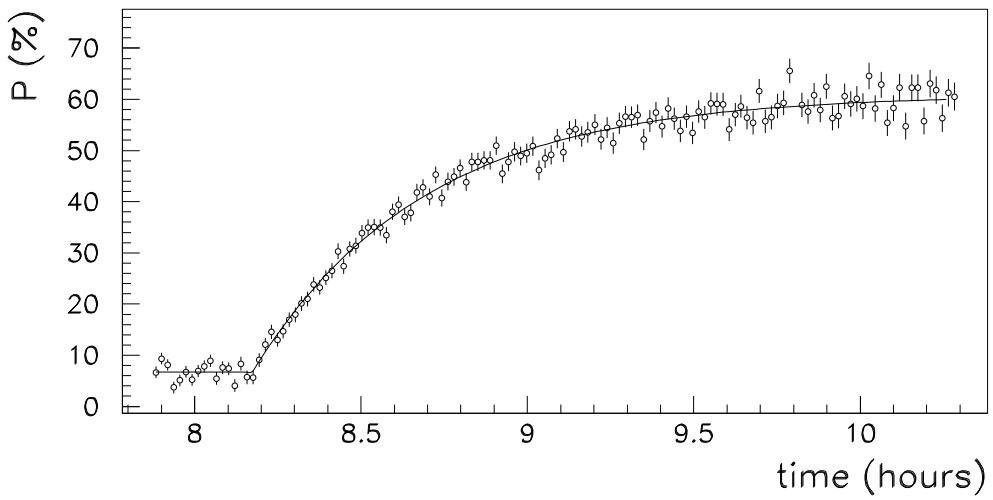

Figure 3.6: The polarisation, P, versus the time in hours.

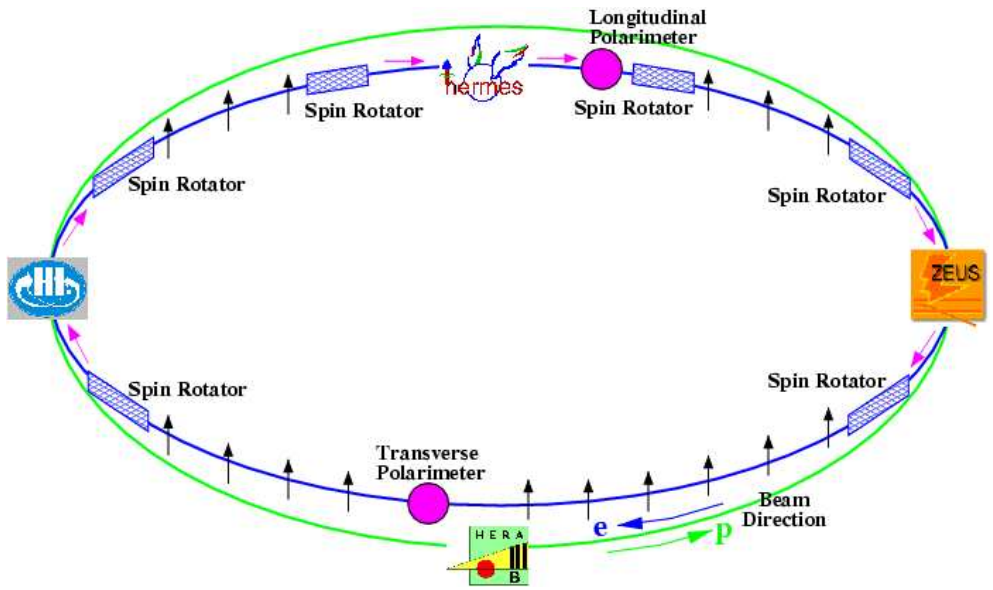

Figure 3.7: Schematic view of HERA II with the location of the spin rotators.

beam. This polarisation method was suggested more than 35 years ago [67] and has been employed at many laboratories [68] to measure transverse polarisation. The Compton scattering has also been employed in linear accelerators [69] to measure the longitudinal polarisation. Recently, NIKHEF [70] and MIT-Bates [71] laboratories have developed Compton polarimeters to

monitor the longitudinal polarisation of the beams in their accelerators. In 1992, a Compton polarimeter has been constructed at DESY to measure the transverse polarisation (TPOL) [66]. Later on, in 1995, the longitudinal Compton polarimeter (LPOL) [72] was added to obtain an independent and more precise polarisation measurement. In 1996, early polarisation measurements from the LPOL were provided to the HERMES experiment. The LPOL is located near the the HERMES hall experiment, and the TPOL is located near the HERA-B hall as shown in Fig. 3.7. The LPOL was in operation at HERA I providing polarisation measurements to HERMES while the TPOL was upgraded during the long HERA shutdown between 2000-2002. Both polarimeters are in use for the HERA II experiments.

3.3.2 Compton scattering

Photons from an intense laser beam collide with $\sim 10^3$ electrons of the $\sim 10^9$ electrons in each bunch of the electron beam. The scattered photons are detected in the detector of the polarimeter which consists of an upper and lower half as shown in Fig. 3.8.

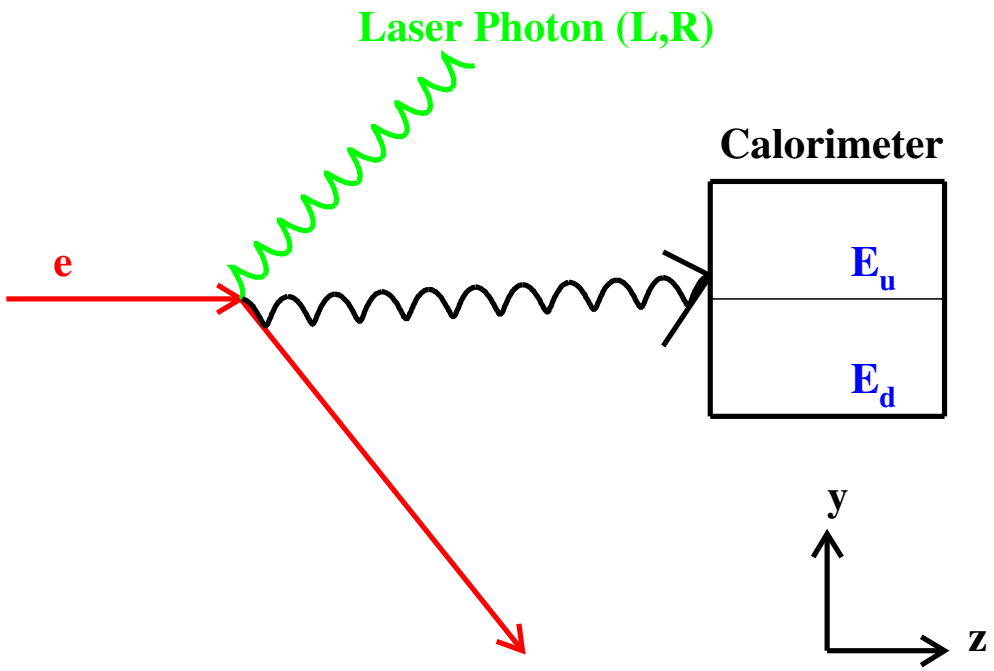

Figure 3.8: A schematic diagram of the Compton scattering of a laser photon off a beam electron. The scattered photon is the detected in the polarimeter (calorimeter on the figure).

The differential cross section for Compton scattering of polarised photons on electrons can be written in the laboratory frame as a function of the initial electron polarisation, P, and the photon polarisation, S, as [66]

$$\frac{d\sigma_C}{d\Omega}(S,P) = \frac{1}{2}r_0^2(\frac{k_f}{k_i})^2[\Sigma_0 + S_1(0)\Sigma_1 + S_3(P_Y\Sigma_{2Y} + P_Z\Sigma_{2Z})]\,, \qquad (3.2)$$

where

$$\begin{aligned}
\Sigma_0 &= (1+\cos^2\theta) + (k_i - k_f)(1-\cos\theta)\,,\\
\Sigma_1 &= \cos 2\phi \sin^2\theta\,,\\
\Sigma_{2Y} &= -k_f \sin\phi \sin\theta(1-\cos\theta)\,,\\
\Sigma_{2Z} &= (1-\cos\theta)(k_f + k_i)\cos\theta\,,
\end{aligned}$$

with S_1 and S_3 the linear and circular components of the initial photon polarisation, and P_y and P_Z the transverse and longitudinal components of the initial electron polarisation. r_0 is the classical electron radius and k_i (k_f)is the initial (final)photon momentum in the rest frame, Σ_0 is the unpolarised cross section, and Σ_1 and Σ_{2Y} depend on the azimuthal scattering angle, ϕ, and are used for the transverse polarisation measurement, and Σ_{2Z} is used for the longitudinal polarisation measurement. The angle θ is defined as the polar angle between the incoming electron direction and the scattered laser photon.

3.3.3 The transverse polarimeter

The transverse polarimeter (TPOL) measures the vertical component of the electron polarisation. The calorimeter of the TPOL is split into two parts, an upper and a lower half. The energy of the incoming photon is the sum of the energies in the two halves, $E_\gamma = E_u + E_d$, and the vertical position is measured using the asymmetry of the energies

$$\eta(y) = \frac{E_u - E_d}{E_u + E_d}\,. \qquad (3.3)$$

The η-to-y transformation is presented in Fig. 3.9. The transverse polarisation component of the electron, P_Y, is measured using the asymmetry of the Compton cross section for scattering of vertically polarised electrons off circularly polarised photons [66]. The polarisation P_Y is obtained, at HERA, from the shift of the mean vertical positions $< y >$ measured with left- and right-circularly polarised light

$$\Delta y(E_\gamma) = \frac{1}{2}(< y >_L - < y >_R) \;=\; P_Y \Delta S_3 \Pi(E_\gamma)\,, \qquad (3.4)$$

where the analysing power, $\Pi(E_\gamma) \leq 200$ μm, depends on the parameters of the Compton cross section, the detector, the electron beam, and is equal to the shift measured when $\Delta S_3 P_Y = 1$, has been derived using the η-to-y transformation. Here ΔS_3 is the difference in the circular polarisation of the laser light. The transformation function $\eta(y)$ is not a linear function

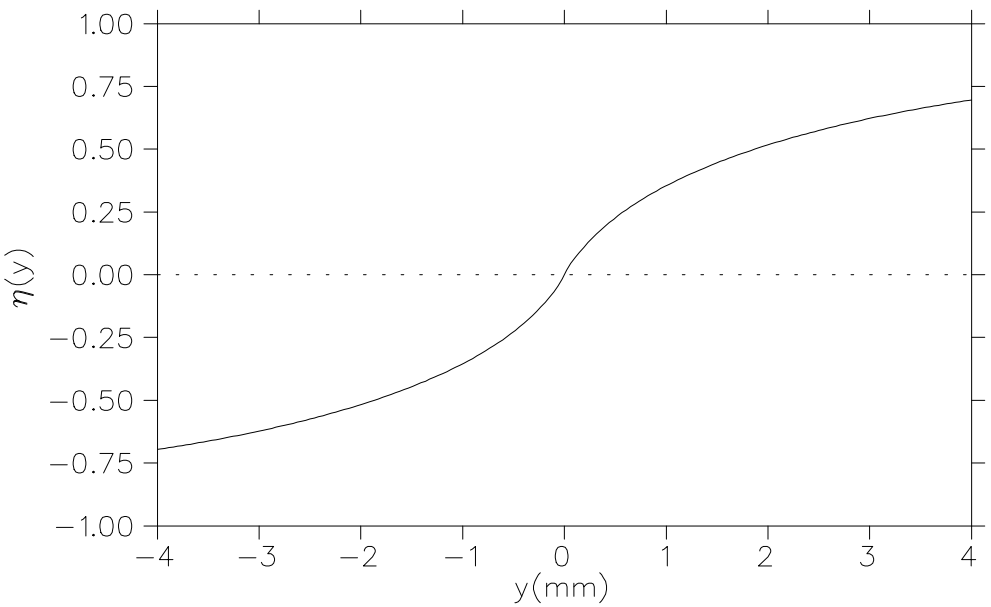

Figure 3.9: The transformation function $\eta(y)$.

of the y-position of the incoming photon as can be seen in Fig. 3.9. However, $\eta(y)$ depends on the properties of the electron beam. The uncertainty in this transformation is among the largest systematic errors for the transverse polarisation measurement [66]. A silicon strip detector was installed in front of the TPOL detector to improve the position sensitivity for calibration purposes.

The statistical error in the transverse polarisation measurement is obtained in one-minute interval and found to be $1-2\%$, depending on whether the measurement is taken at the beginning or towards the end of a fill, where the electron beam currents vary between 10 to 40 μA [72].

3.3.4 The longitudinal polarimeter

The LPOL provides a longitudinal polarisation measurement. The measurement of the longitudinal polarisation, P_Z, is based on large asymmetry in the energy distributions of the scattered photons. The integrals of Σ_1 and Σ_{2Y}

over y are zero, thus the expression of the asymmetry of the energy spectra is given by

$$A(E_\gamma) = \Delta S_3 P_Z \Sigma_{2Z/0} \,. \tag{3.5}$$

The longitudinal polarisation, P_Z, can be obtained from the measurement of the energy asymmetry under reversal of the laser photon helicities using the "single-photon method". However, since the HERMES gas target produces large bremsstrahlung background at the calorimeter of the longitudinal polarimeter, the "multi-photon method" is used. In contrast to the "single-photon method" implemented in the TPOL and where every single photon is analysed individually, the "multi-photon method" measures the total energy deposited in the detector by about 1000 Compton photons per bunch crossing. The pulsed yttrium-aluminium-garnet (YAG) [73] laser is used for this purpose, where 2.3 eV photons are produced with a repetition rate between $0.1 - 100$ Hz and pulse energy from $1 - 250$ mJ. The laser beam is guided with remotely controlled mirrors and lenses in a 72 m long stainless steel vacuum pipe to the $e\gamma$ interaction point.

The back-scattered photons are contained in a narrow cone centred along the initial electron beam direction, and detected in a calorimeter 54 m from the interaction point. It consists of four optically decoupled, radiation hard, $NaBi(WO_4)$ Cerenkov crystals, arranged in a 2×2 array. The energy of the photons is the sum of energies in these crystals.

3.3.5 Polarimeter choice

Since the end of 2003, both TPOL and LPOL are in operation at HERA II. For technical reasons, and because sometimes only one of the two polarimeters provides measurements, the luminosity weighted polarisation for the ZEUS data was calculated using the following algorithm: the polarimeter with the most operation time during a ZEUS run was used, to maximise luminosity; if the two polarimeters have the same time operation, the LPOL measurements are used. In Fig. 3.10 the polarisation distribution is shown for negative (LH) and positive (RH) values. The average of the polarisation in the LH (RH) runs is $P = -40.6\%$ ($P = +32.2\%$). To keep a narrow spread of the LH polarisation values, only runs with $P < -20\%$ were considered.

3.3.6 Micro vertex detector (MVD)

The ZEUS MVD [74, 75] consists of two parts, the barrel and the forward detectors (BMVD and FMVD, respectively) The BMVD covers cylindrically the interaction point and is located in the space between the beam pipe and

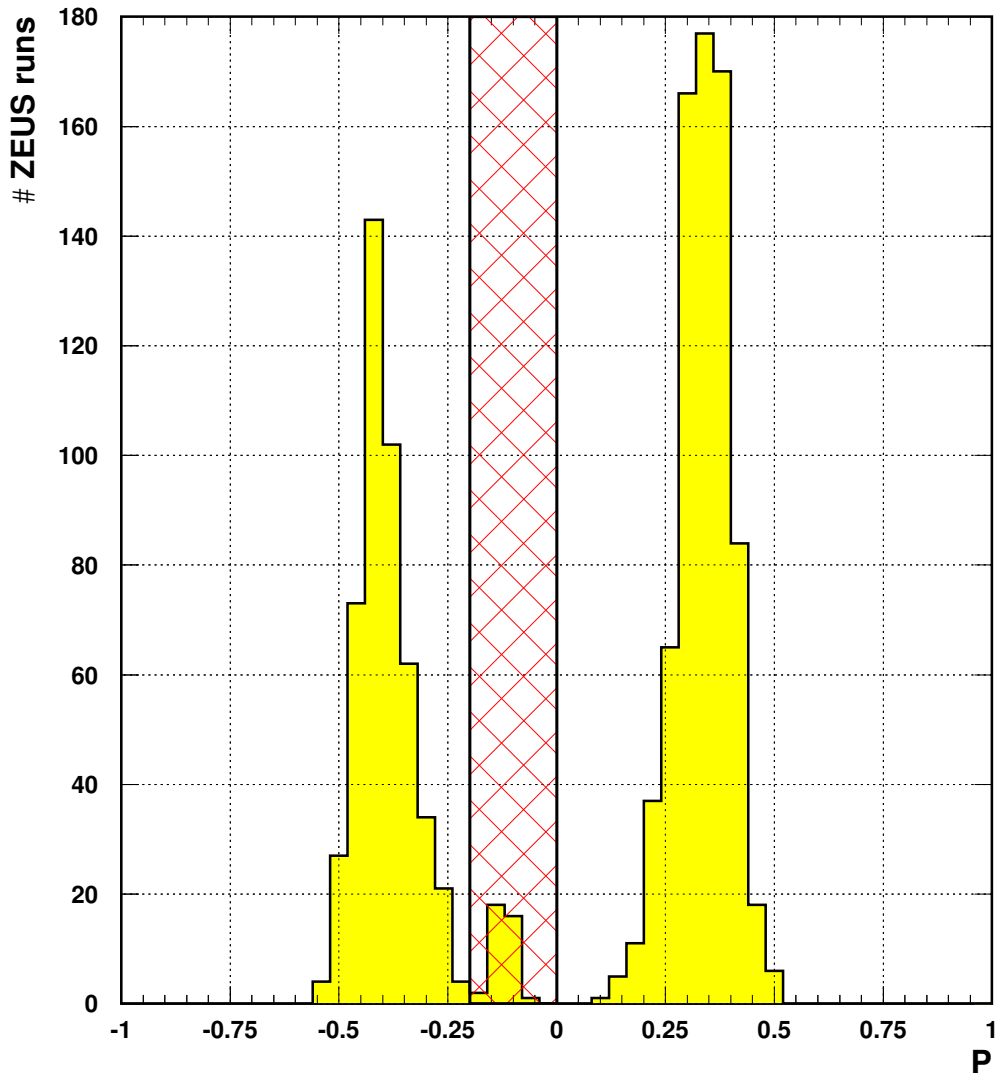

Figure 3.10: The polarisation distribution as obtained for the ZEUS running period 2003-2004.

the inner radius of the CTD. The BMVD is 60 cm long and has a diameter of 31 cm. It covers the polar angles range of $20° - 160°$. The BMVD consists of three double layers of silicon strip detectors which are assembled in planes on concentric cylinders around the nominal interaction point. The shape of the beam pipe was dictated by the presence of high background originating from synchrotron radiation in the horizontal plane. Fig. 3.11 shows a schematic drawing of the MVD along the beam pipe in the z direction and in the $r - \phi$ plane.

The FMVD consists of four wheels around the beam pipe. The locations of these wheels are $z = 31.9,\ 44.9,\ 57.9$ and 72.9 cm away in the forward direction relative to the nominal interaction point. The FMVD sensors have a trapezoidal shape. Two sides are parallel and two are tilted by 13° in opposite direction as shown in Fig. 3.11.

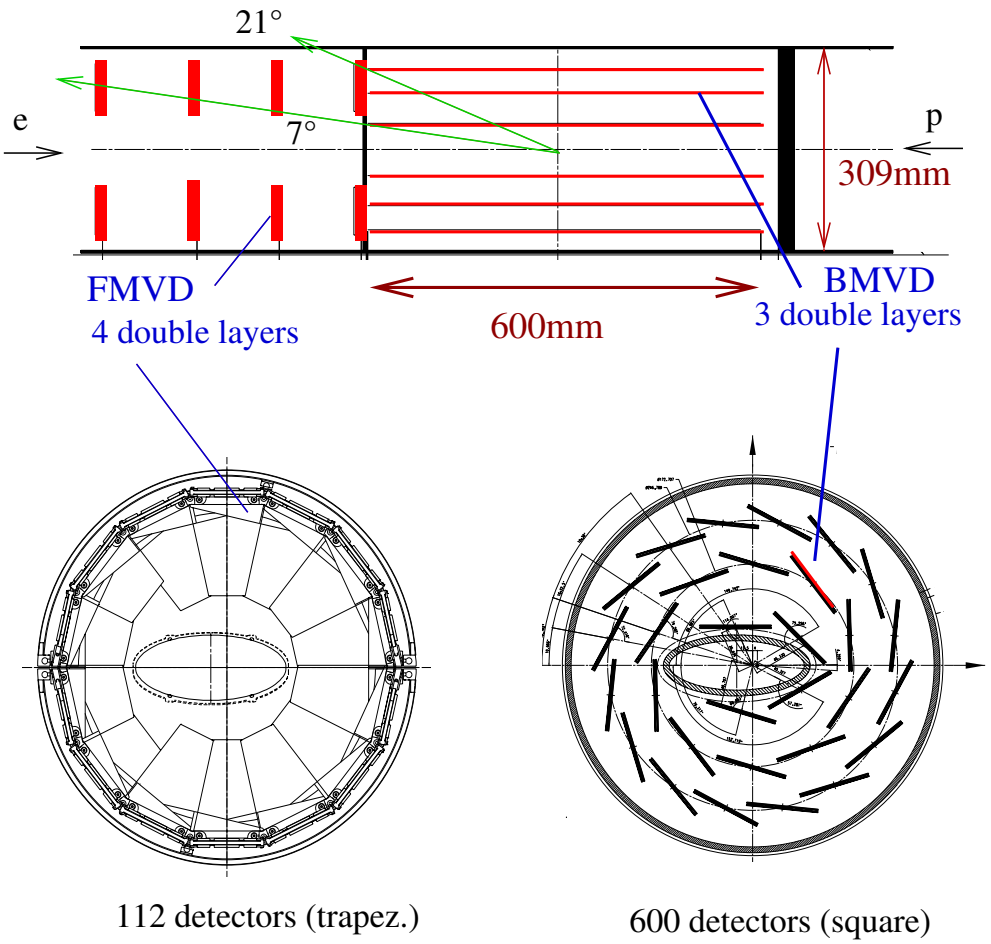

Figure 3.11: A schematic drawing of the MVD along the beam pipe direction (top), and in $r-\phi$ plane (bottom). The FMVD (left-bottom) consists of four double layers, and the BMVD (right-bottom) consists of three double layers.

The tracks in this analysis were reconstructed using the hits created when the final-state particles cross the MVD and CTD. The advantage of using the MVD hits, in addition to the CTD ones, is having a larger number of hits to be fitted for each track. Thus more tracks are reconstructed and the chance to reconstruct the interaction vertex is enhanced.

Chapter 4

Monte Carlo simulation

Monte Carlo (MC) simulations are used to determine the efficiency for selecting events, estimate the *ep* background rates from the known processes which may enter into the CC or NC samples, and to extract the cross section for the full kinematic phase-space. In order to ensure that the statistical uncertainties arising from the MC simulation are negligible, sufficient number of MC events were generated. To compare the data distributions to those obtained by the MC, the MC samples are normalised to the total integrated luminosity of the data.

4.1 CC signal Monte Carlo

Deep inelastic charged current events, including one-loop electroweak radiative corrections, were simulated using the HERACLES 4.6.1 [76] program with DJANGOH 1.1 [77] interfaced to the MC generators that provide hadronisation. HERACLES includes the initial state radiation (ISR), vertex and propagator corrections and two-boson exchange. The ARIADNE 4.10 colour dipole model (CDM) [78] was used for the fragmentation. In this model, the struck quark and the proton remnant are assumed to form a colour dipole that radiates gluons. The emitted gluons can form further colour dipoles. This process continues until all dipoles reach a minimum energy. The CC events were also generated by using the MEPS fragmentation scheme of LEPTO [79]. MEPS describes the hard scatters using the first order matrix elements of processes and soft higher order emissions using parton showers, where the quarks and gluons evolve by successive branchings until all partons reach some minimum energy.

HERACLES calculates electroweak radiative corrections in terms of G_μ and M_Z or M_W, with $\sin^2\theta_W = 1 - M_W^2/M_Z^2$, on top of all the other fermion

MC signal sample	N_{gen}	cross section (pb)
$Q^2 > 10$ GeV^2	13350	44.885
$Q^2 > 100$ GeV^2	11612	39.649
$Q^2 > 5000$ GeV^2	1330	3.2850
$Q^2 > 10000$ GeV^2	1339	0.7062
$Q^2 > 20000$ GeV^2	1432	0.0643

Table 4.1: Summary of the CC DIS MC samples used in the CC analysis, generated with the funnel version num02t2.0. N_{gen} denotes the number of generated events in each sample.

masses and the Higgs mass. The top quark mass is set to 175 GeV, while the Higgs mass is set to 100 GeV. G_μ and M_Z are set to the PDG [80] values. M_W is calculated according to the required $\sin^2\theta_W$ value.

The nominal MC in this analysis is the one generated with ARIADNE. In Table 4.1 a list of the CC MC samples used for the CC analysis from HERA II, is presented. These MC samples were generated with funnel version num02t2.0 [81], taking into account the upgraded ZEUS set-up. Here we note that the MC samples were generated assuming non-polarised incoming lepton beams, and when the comparison between data and MC is shown in the CC analysis, the normalisation of the MC events is multiplied by $1 + P$ where P is the average of the polarisation over all analysed HERA II data runs.

4.2 CC characteristics

The characteristic signature of CC DIS events is missing transverse momentum, $p_{T,miss}$, due to the final state neutrino which escapes detection. In observable quantities, this translates into large measured hadronic transverse momentum, P_T, where $\vec{P}_{T,miss} = -\vec{P}_T$. Therefore, CC events are selected by requiring that candidate events have missing transverse momentum at each level of the trigger. The quantity P_T is calculated from

$$P_T = \sqrt{P_X^2 + P_Y^2}\,, \tag{4.1}$$

with

$$P_X = \sum_i E_i \sin\theta_i \cos\phi_i\,, \tag{4.2}$$

$$P_Y = \sum_i E_i \sin\theta_i \sin\phi_i\,, \tag{4.3}$$

where E_i, θ_i and ϕ_i are the energy, the polar angle and azimuthal angle of a calorimeter energy deposit. The sums run over all deposits in the calorimeter. Another useful variable is the hadronic angle defined as

$$\cos\gamma_h = \frac{P_T^2 - \delta^2}{P_T^2 + \delta^2}\,, \tag{4.4}$$

where

$$\delta = \sum_i (E - P_z)_i = \sum_i E_i(1 - \cos\theta_i)\,. \tag{4.5}$$

Finally, the total transverse energy, E_T, is given by $E_T = \sum_i E_i \sin\theta_i$.

4.3 CC Background simulation

Several physical processes are identified as background sources to the CC DIS signal. To subtract these contributions from the CC signal, events of each background type were generated and put through the detector simulation. The main background sources to the CC signal are detailed below.

4.3.1 Photoproduction

Photoproduction (PHP) events with high transverse momentum P_T jets may fake CC events. In the PHP events, $Q^2 = 0$ GeV^2, the scattered electron escapes through the rear beam pipe. If one of the high P_T jets was partially or fully lost down the beam pipe, or substantial energy from the jet was absorbed in the dead material, a high transverse momentum is measured. Two processes contribute to high P_T jet production in PHP, the so-called direct and resolved PHP processes. In the direct process, the exchanged photon interacts with the proton directly, while in the resolved process the exchanged photon acts as a source of partons for the scattering as shown in Fig. 4.1. Both processes were generated with the HERWIG [82] program.

A large fraction of the PHP events are characterised by low missing transverse momentum P_T which should balance the P_T of the scattered electron. The transverse energy E_T of PHP events is usually high. From previous studies [83] we learn that the PHP events which may enter the CC final sample are found to populate the region of $P_T > 6$ GeV or $E_T > 30$ in the P_T-E_T plane.

4.3.2 Neutral current

The scattered electron in a DIS NC event, balances the hadronic final state and therefore the event has a small transverse momentum. However, if the

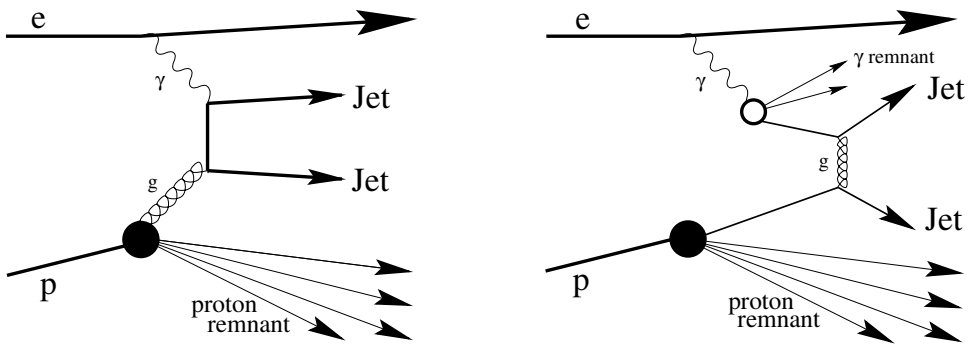

Figure 4.1: Diagrams of direct (left) and resolved (right) photoproduction events

PHP process	N_{gen}	cross section
Direct PHP $E_T > 30$ GeV or $P_T > 6$ GeV	530000	2.83 (nb)
Resolved PHP $E_T > 30$ GeV or $P_T > 6$ GeV	630000	11.9 (nb)

Table 4.2: The direct and resolved PHP MC samples used in the CC analysis.

Process	Q^2 threshold GeV^2	N_{gen}	cross section (pb)
NC	$Q^2 > 4$	100000	322000
NC	$Q^2 > 100$	1000000	8122
NC	$Q^2 > 2500$	24000	58.915
NC	$Q^2 > 20000$	24000	0.3099

Table 4.3: Summary of the NC DIS MC samples used in the CC analysis.

scattered electron is poorly measured in the detector and thus some of the energy-momentum of the scattered electron is lost, this can lead to a high transverse momentum event and then constitute a background to CC signal. In order to evaluate this contamination, NC samples with different Q^2 thresholds were generated with DJANGOH and passed all CC selections described in chapter 6. The NC MC files are listed in Table 4.3. A large number of NC MC events are used to estimate the NC background in the CC sample because a small amount of NC events may have relatively high transverse momentum.

Di-lepton process	N_{gen}	cross section (pb)
$\mu^+\mu^-$ (DIS)	3000	13.00
$\mu^+\mu^-$ (elastic)	3000	10.20
$\mu^+\mu^-$ (quasi-elastic)	3000	4.97
$\tau^+\tau^-$ (DIS)	3000	5.23
$\tau^+\tau^-$ (elastic)	3000	6.35
$\tau^+\tau^-$ (quasi-elastic)	3000	3.56

Table 4.4: List of the di-lepton MC samples used in the CC analysis.

4.3.3 Di-lepton production

Muon pairs can be produced through elastic, quasi-elastic and DIS Bethe-Heitler reactions. The muons energy is not fully absorbed by the calorimeter. Thus, the event may have a high missing transverse momentum and finally enter the CC signal. Similarly τ pairs production can also constitute a background to CC signal, because the τ can decay to a final state neutrino which escapes detection and this may lead to high missing transverse momentum. Electron pairs production event is unlikely to have a high transverse momentum because electrons are fully detected within the calorimeter. All di-leptons production events were generated with the GRAPE [84] generator using the CTEQ5L PDFs parameterisation. The events were generated with a minimum P_T threshold of 5 GeV and at least one of the leptons to have $5^\circ < \theta_\ell < 175^\circ$, where θ_ℓ is the polar angle of one lepton. In Table 4.4 we present all di-lepton production processes which were used in the CC analysis to estimate a possible background contribution.

4.3.4 W production

At HERA, there are two processes contributing to real W boson production, via the NC or via the CC interactions,

$$ep \to eW^{\pm}X \tag{4.6}$$

$$ep \to \nu W^{\pm}X\,, \tag{4.7}$$

where X represents the hadronic final state. The NC cross section is an order of magnitude larger than that of the CC one and therefore, the latter is ignored. In Fig. 4.2, we show the Feynman diagrams of W-production in the neutral current process. The real W in the final state decays into a lepton and a neutrino ($\ell\nu$). Such an event may have a large measured transverse momentum due to the missing transverse momentum of the neutrino.

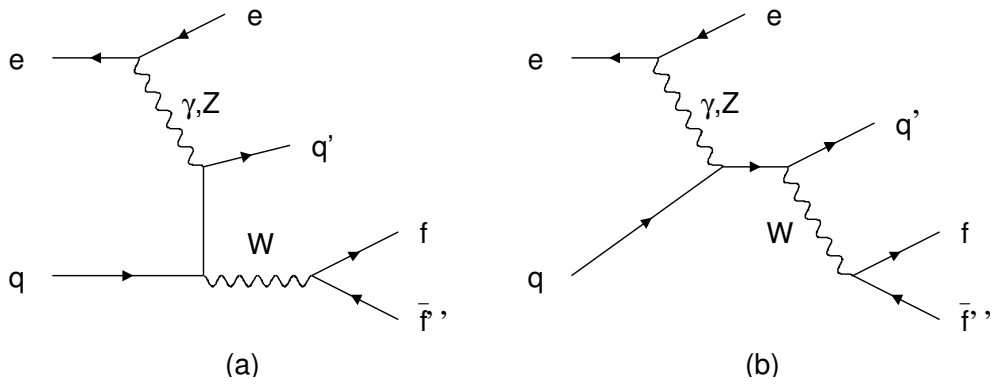

Figure 4.2: The main leading order Feynman diagrams for real $W^{\pm}$ production: $eq \to eW^{\pm}X$.

W production process	N_{gen}	cross section (pb)
$e^+p \to e^+W^+X$ (DIS)	50000	0.1112
$e^+p \to e^+W^+X$ (resolved)	10000	0.0177
$e^+p \to e^+W^-X$ (DIS)	50000	0.0927
$e^+p \to e^+W^-X$ (resolved)	10000	0.0247

Table 4.5: List of the W production MC samples used to evaluate the background to the CC sample.

The MC real W boson productions through the possible modes at HERA were generated using the EPVEC [85] generator, and passed through the detector simulations. In Table 4.5 a list of all W production MC samples used to estimate the background due to the W production processes is presented.

4.3.5 ZEUS trigger

ZEUS has a three-level trigger system [51]. The triggers were designed to select CC and NC events taking into account their characteristics. Detailed description on the CC and NC triggers are discussed in sec. 6.1 and sec. 10.3.3, respectively.

4.3.6 Detector simulation

The MOZART software package provides the detector simulation based on GEANT 3.13 [86]. The ZEUS trigger is simulated by ZCAR for the first and

second levels, and by the ZGANA program for the third level, followed by the ZEUS reconstruction program ZEPHYR.

Chapter 5

Reconstruction of kinematic variables

The kinematic variables for *ep* interactions can be reconstructed by several methods, based on the event characteristics. In order to achieve measurements as accurate as possible, it is important to use the method which gives most precise estimates.

5.1 The electron method

This method requires the final state lepton quantities, such as its energy and position in the CAL to reconstruct the kinematic variables. Since these quantities are not available in the CC case, this method is not relevant for the CC events. However, for DIS NC events this method can be used. The kinematic variables can be expressed as follows:

$$Q_e^2 = 2E_e E'_e(1+\cos\theta)\,, \tag{5.1}$$

$$x_e = \frac{E_e}{E_p}\frac{E'_e(1+\cos\theta)}{2E_e - E'_e(1-\cos\theta)}\,, \tag{5.2}$$

$$y_e = 1 - \frac{E_e}{2E'_e}(1-\cos\theta)\,, \tag{5.3}$$

where the E'_e and θ are the energy and the polar angle of the scattered electron, respectively.

5.2 The double angle method

In this method, the kinematic variables are reconstructed by using the scattered lepton polar angle θ and the hadronic angle γ_h [1] as follows:

$$Q^2_{DA} = 4E_e^2 \frac{\sin\gamma_h(1+\cos\theta)}{\sin\gamma_h + \sin\theta - \sin(\theta+\gamma_h)}, \quad (5.4)$$

$$x_{DA} = \frac{\sin\theta(1-\cos\gamma_h)}{\sin\gamma_h + \sin\theta - \sin(\theta+\gamma_h)}, \quad (5.5)$$

$$y_{DA} = \frac{E_e \sin\gamma_h + \sin\theta + \sin(\theta+\gamma_h)}{E_p \sin\gamma_h + \sin\theta - \sin(\theta+\gamma_h)}. \quad (5.6)$$

This method can be used for NC events but not for CC ones because of the missing information on the scattered lepton.

5.3 The Jacquet-Blondel method

The kinematic variables reconstructed with the Jacquet-Blondel [87] (JB) method are given by

$$y_{JB} = \frac{\delta}{2E_e}, \quad (5.7)$$

$$Q^2_{JB} = \frac{P_T^2}{1-y_{JB}}, \quad (5.8)$$

$$x_{JB} = \frac{Q^2_{JB}}{s y_{JB}}. \quad (5.9)$$

The required informations for the Jacquet-Blondel estimators are based on the hadronic final state which are available in the CC case. In this analysis, we use the Jacquet-Blondel method to reconstruct the kinematic variables.

[1] In the naive Quark Parton Model, γ_h corresponds to the polar angle of the struck quark.

5.4 Hadronic final state energy corrections

The four-momentum of the hadronic final state can be calculated using the calorimeter cell energy deposits

$$E = \sum_i E_i \,, \tag{5.10}$$

$$p_x = \sum_i E_i \cos\theta_i \cos\phi_i \,, \tag{5.11}$$

$$p_y = \sum_i E_i \cos\theta_i \sin\phi_i \,, \tag{5.12}$$

$$p_z = \sum_i E_i \sin\theta_i \,, \tag{5.13}$$

where the sums run over all the calorimeter cells, and for the i^{th} cell E_i, θ_i and ϕ_i are the energy, the polar and azimuthal angles with respect to the measured position of the interaction vertex.

There are several effects, which generate corrections to the measured energy on calorimeter-cell base.

5.4.1 Energy deposits clustering

Typical showers due to single particles consists of several detector cells in the ZEUS calorimeter. The idea of the clustering algorithm is to merge these cells into one object called island [88]. Since the electromagnetic showers differ from the hadronic ones, the formed clusters can be classified. Clustering leads to a better determination of the kinematic variables.

The algorithm of clustering is built of two steps. First, cells within a calorimeter part and type e.g. BEMC or FHAC, are grouped around the highest energy cells. This way, 2D-islands are created around the cell with the maximum energy as described in Fig. 5.1. Second, these islands are combined to 3D cone-islands according to a probability function which depends on the angular separation. The 3D cone-islands are referred to in this analysis as "islands". The position of the island is reconstructed by logarithmically weighting the position of all cells in the particular island where the energy of the cell is the weight.

5.4.2 Back-splash correction

When a high energy shower jet hits the calorimeter, some of the particles back-scatter and are detected away from the original jet direction (albedo

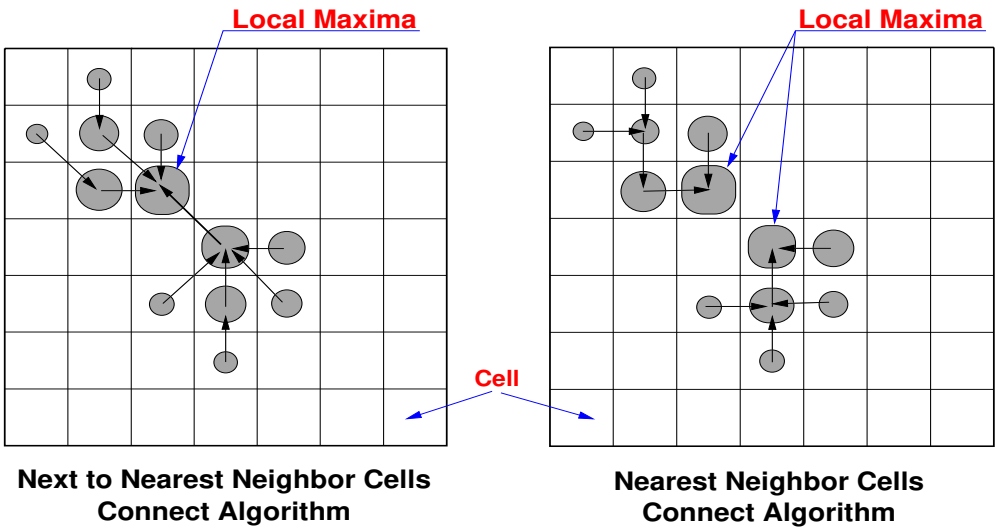

Figure 5.1: Schematic representation of the cell island clustering. The larger the zone of the blob the larger the energy deposited in that cell.

effect). In this case, the energy deposits due to the back-scattered particles cause an over-estimation of the value of γ. A method to remove these deposits is described in [89]. This method removes low energy islands with energy $E_{island} < 3$ GeV if the event has a hadronic angle greater than a threshold, γ_{max}, which is itself a function of the hadronic angle and is derived from a fit to NC MC.

5.5 Jet reconstruction

At high Q^2 events, a proton collides with an electron, a final state lepton with an energy of E' is scattered with a polar angle θ, and one (or more) hadronic jet with energy of E_j containing a large number of particles is produced. A schematic diagram of a one jet event is shown in Fig 5.2. The four-momentum of the event is extracted from the islands, which give better estimations for the kinematic variables than the cells. However, because of the albedo effect, some islands do not belong to the jet direction and therefore distort the kinematic variable. In order to avoid this problem, one can extract the four-momentum of the event from the jets of the event. The Q^2 is given by

$$Q^2 = 2E_e E'(1 + \cos\theta)\,, \tag{5.14}$$

(5.15)

and since the final state lepton quantities are not measurable, this formula can not be used to reconstruct Q^2. However, the non-measurable quantities of the scattered lepton can be given in terms of hadronic variables and known quantities. For example, the transverse momentum of the final state lepton is equal to the hadronic final state transverse momentum

$$P_T^\ell = P_T^{had} \quad \rightarrow \quad E' = \frac{P_T^{had}}{\sin\theta}\,, \tag{5.16}$$

where P_T^{had} is the transverse momentum of the hadronic system and is given by

$$P_T^{had} = \sqrt{\left(\sum_i (p_x^i)^{had}\right)^2 + \left(\sum_i (p_y^i)^{had}\right)^2}\,, \tag{5.17}$$

where $(p_x^i)^{had}$ and $(p_y^i)^{had}$ are the x and y-component of the momentum of a hadronic energy deposit. From the energy-momentum conservation the following relation is obtained

$$\sum_i \delta_i^{had} + E'(1-\cos\theta) = 2E_e\,, \tag{5.18}$$

where δ_i^{had} is δ of the i^{th} hadronic energy deposit. Using eq. (5.16) and eq. (5.18) leads to the following relation:

$$\frac{\sin\theta}{1-\cos\theta} = \frac{P_T^{had}}{2E_e - \sum_i \delta_i^{had}}\,, \tag{5.19}$$

and therefore

$$Q^2 = \frac{2E_e (P_T^{had})^2}{2E_e - \sum_i \delta_i^{had}}\,. \tag{5.20}$$

The kinematic variables x and y can be derived in a similar way

$$x = \frac{E_j}{E_p}\frac{1+\cos\theta_j}{2 - \frac{E_j}{E_e}(1-\cos\theta_j)}\,, \tag{5.21}$$

$$y = \frac{\sum_i \delta_i^{had}}{2E_e}\,, \tag{5.22}$$

where θ_j is the polar angle of the jet.

The majority of the events have one jet and the number of the two-jets events is proportional to $\sim \alpha_s$, and three-jets events to $\sim \alpha_s^2$, etc.

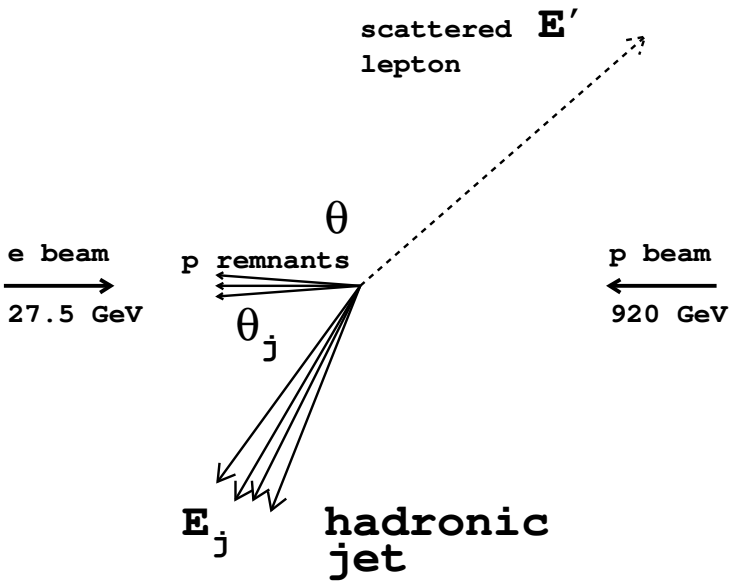

Figure 5.2: A schematic diagram of one jet event, where a proton arrives from the right and collides with an incoming electron from the left. The proton breaks and the remnants scatter with small angles.

5.6 Comparison of reconstruction methods

In Fig. 5.3 we show $\frac{Q^2_{rec}-Q^2_{true}}{Q^2_{true}}$, $\frac{x_{rec}-x_{true}}{x_{true}}$, and $\frac{y_{rec}-y_{true}}{y_{true}}$ for MC CC events. Here the subscript "rec" denotes the reconstructed value of a kinematic variable. The reconstructed values were obtained once with the correction due to the back-splash and once using the jets. As we see from these figures, both the back-splash correction and the jets give good estimation to the reconstructed values. Although at low y values a better estimation is given by the jet method compared to that given by the back-splash correction, this improvement is not significant. In this analysis, we use the back-splash correction method to reconstruct the kinematic variables.

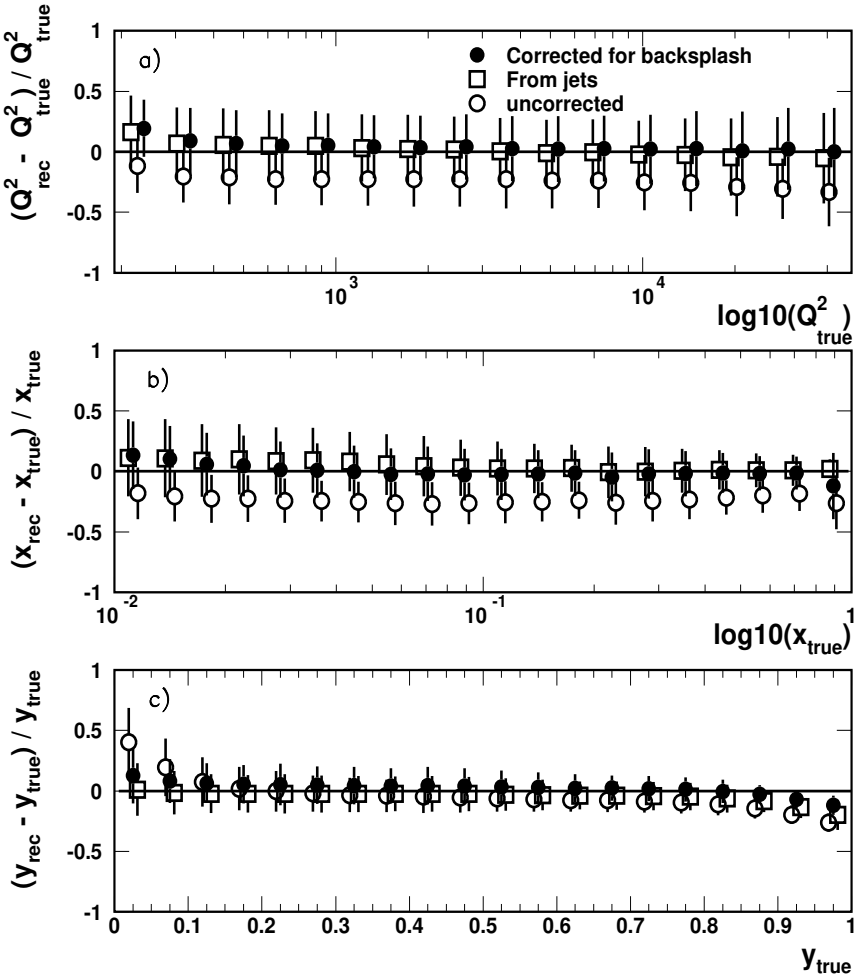

Figure 5.3: The relative deviation of the reconstructed Q^2, x, and y from the true values versus the true values for a) Q^2, b) x, and c) y. The closed circles are obtained by correcting a kinematic variable for the back-splash effect, the open squares show the reconstructed variables using jet/(s) properties, and the open circles without any corrections.

Chapter 6

Charged current event selections at HERA II

6.1 Trigger requirement

Special triggers were designed to select CC events taking in account the characteristics of this type of events. The characteristics of CC events are the base for designing the event selection rules at the triggering level as well as in the offline analysis.

6.1.1 First level trigger

At the first level trigger (FLT), events are selected by using the information on the energy, transverse energy and the transverse momentum of the events as they are measured by the ZEUS calorimeter. Generally, the events are triggered with low thresholds on these quantities if there is a coincidence with CTD-MVD tracks which fit the interaction point, while higher thresholds are required if the event has no CTD-MVD track candidates. The required subtrigger FLT slots and their logic are as follows:

slot39 or slot40 or slot41 or slot43 or slot44 or slot60 ,

where each slot has the following meaning

- slot39: The energy in the EMC section of the BCAL associated with the scattered electron, B^e_{EMC}, exceeds a threshold of 3.4 GeV, and has a good associated track (See sec. 6.6.4 for definition of "good" track).
- slot40: In this slot we require $E_{EMC} > 25$ GeV, where E_{EMC} is the energy in the electromagnetic sections of the calorimeter.

- slot41: A minimum transverse energy of the event of $E_T > 30$ GeV is required.

- slot43: $E_T > 11.5$ GeV and at least one track ($N_{trks} \geq 1$) is required.

- slot44: $B_{EMC} > 9.7$ GeV and isolated scattered electron in the BCAL, where B_{EMC} is the energy in the BCAL EMC section.

- slot60: This slot is the main FLT slot to select CC events and requires ($P_T \geq 5$ GeV and $E''_T \geq 5$ GeV and $N_{trks} \geq 1$) or ($P_T \geq 8$ GeV and ($N_{trks} \geq 1$ or $E_{FCAL} \geq 11$GeV)), where E''_T is the transverse energy calculated outside the most inner first two rings in the FCAL, E_{FCAL} is the total energy in the FCAL, and N_{trks} is the total number of CTD-MVD tracks. The tracks have to point to the nominal interaction vertex.

6.1.2 Second level trigger

The timing of each cell in the calorimeter is set to zero for an interaction that occurs at the nominal vertex, i.e. $(0, 0, 0)$. At the second level trigger (SLT), the timing information is used to reject events inconsistent with the bunch-crossing time. Also the topology of the calorimeter energy deposits is used to reject background events. In particular, a tighter cut of 6 GeV (9 GeV for events without any CTD track) is required on the missing transverse momentum, because the resolution of this variable is better at the SLT level than at the FLT one. The slot "EXO_SLT_4" is required in the second level trigger and its logic is,
($|t_G| \leq 7$ ns and
(($P_T \geq 6$ GeV) and $E''_T \geq 6$ GeV and $N^{good}_{trk} \geq 1$) or ($P_T \geq 9$ GeV and $E'_T \geq 8$ GeV and $E_{FCAL} \geq 20$ GeV)),
where $|t_G|$ is the average calorimeter timing, E'_T is the transverse energy calculated outside the FCAL most inner ring.

6.1.3 Third level trigger

At the third level trigger (TLT), tighter timing cuts in addition to algorithms to remove proton-gas interaction events are applied. CC candidates are required to satisfy "EXO_TLT_2" or "EXO_TLT_6" subtriggers. The logic of "EXO_TLT_2" can be expressed as follows:

$$P_T \geq 6 \text{ GeV and } N^{good}_{trk} \geq 1$$
$$\text{and } |z_{vtx}| \leq 60 \text{ cm and } |t_U - t_D| \leq 8 \text{ ns},$$

where z_{vtx}^{trks} denotes the z-position of the interaction point measured by the CTD-MVD. t_U and t_D are the timing averages of the upper and lower half of the calorimeter. The timing requirement removes cosmic muon events. The logic of "EXO_TLT_6" is as follows:

$$\begin{gathered}\text{EXO_SLT_4 and } |t_U - t_D| \leq 8 \text{ ns} \\ \text{and } P_T \geq 8 \text{ GeV} \\ \text{and } (E_{FCAL} \geq 10 \text{ GeV or } N_{trk}^{good} \geq 1) \quad .\end{gathered}$$

6.2 Background resources

The background which may contribute to the DIS CC can be split into two categories, non-*ep* interactions and *ep* interactions. The non-*ep* interactions occur when the proton does not collide with the electron but with the beam-gas. This happens when the electron bunch is empty. The *ep* interaction events are physical events of *ep* collision but not DIS CC.

6.2.1 Non-*ep* background

There are three background sources of non-*ep* background.
• Cosmic muons are produced in the upper atmosphere. These muons may stop in the calorimeter/detector or lose locally a catastrophic amount of energy, leading to events with missing transverse momentum. Fig. 6.1 shows an example of a cosmic muon event which leaves a high transverse momentum.
• Halo muons are muons produced in the collision between protons and residual gas in the beam pipe or between protons in the halo of the beam with material upstream of the detector. These muons travel parallel to the proton beam, can traverse the veto wall and then the RCAL, and if the energy is high, they can traverse the BCAL and the FCAL and deposit a trail of energy in the calorimeter, increasing the missing transverse momentum. Fig. 6.2 shows an example of a halo muon event traversing the full calorimeter.
• Beam gas events, in which the proton interacts with residual gas in the beam pipe. These events typically have high track multiplicity and high activity in the calorimeter. Such beam-gas events deposit energies close to the forward beam pipe, mostly in the inner first rings in the FCAL. Generally, these events have a small P_T imbalance. If, however, the final state is mismeasured in the calorimeter, it fakes a large missing transverse momentum and therefore contributes to the CC sample. In order to reduce the amount of these events, one needs to remove events where most of the energy is in the innermost ring. A typical beam gas event is shown in Fig. 6.3 as observed in the ZEUS detector.

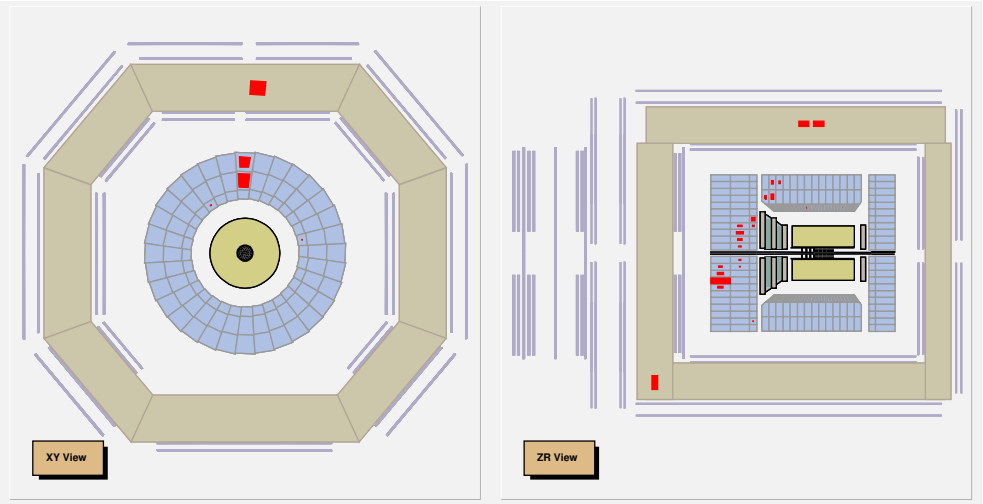

Figure 6.1: An example of a cosmic muon hitting the detector.

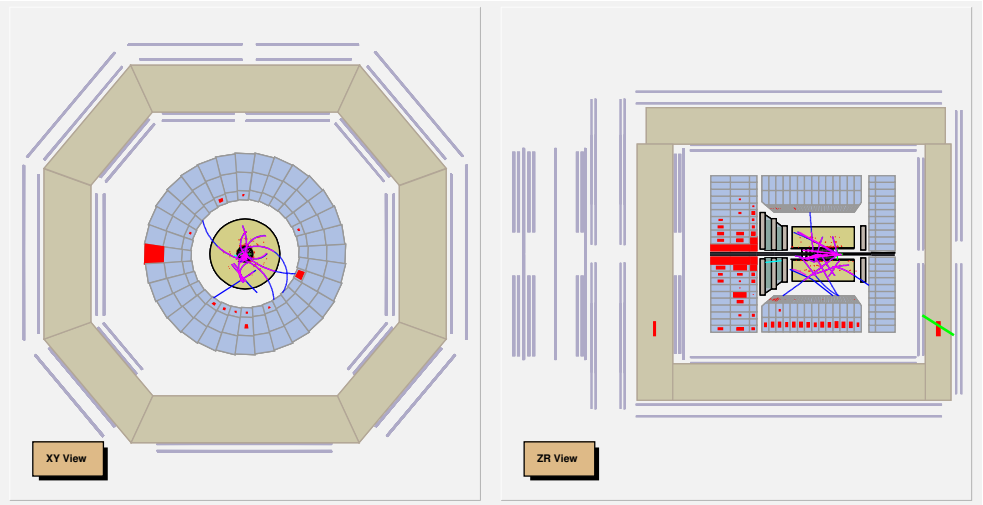

Figure 6.2: A ZEUS event display of a typical beam-halo muon, overlapped on a regular event.

6.2.2 *ep* background

The *ep* background events are events due to processes other than CC, which lead to missing transverse momentum, either because of missing neutrinos or due to fluctuations in the final state. The amount of contamination from these events can be estimated by using the respective MC samples. The main

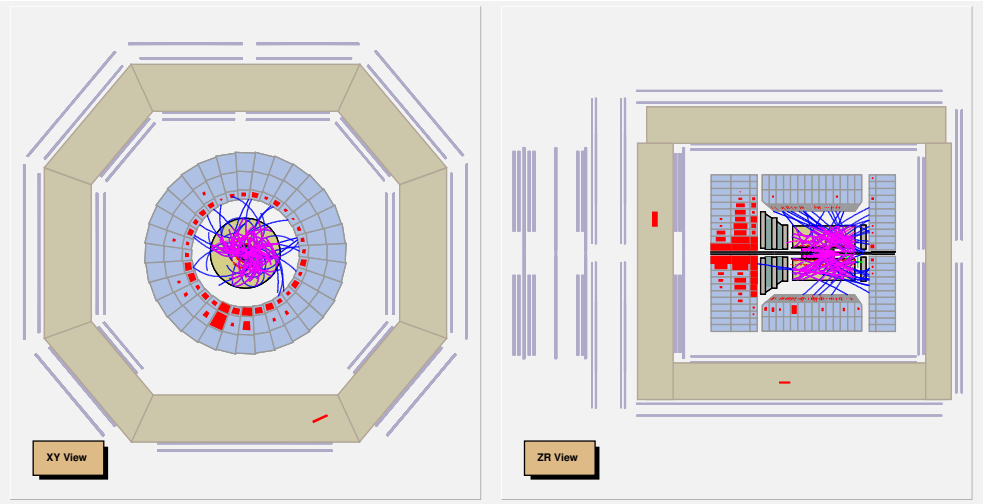

Figure 6.3: An event display of a typical beam-gas event as seen in the ZEUS detector.

sources of this background are:

- hard photoproduction events, which have missing transverse momentum because part of the hadronic final state is lost down one of the beam pipe holes or in cracks between calorimeter sections. The hard photoproduction cross section is much higher than the DIS CC cross section and thus the contamination may be sizable.

- poorly measured neutral current DIS events, where the electron or the hadronic jet hits a crack between the calorimeter sections, or part of the hadronic jet is lost down the beam pipe, and as a result a high transverse momentum imbalance is created.

- Di-lepton production via the Bethe-Heitler process and single $W^{\pm}$ production. The W decays into $\ell\nu$ and the momentum of the lepton, ℓ, is not correctly measured in the calorimeter. This may lead to high missing transverse momentum.

6.3 Vertex reconstruction

The tracks within the CTD-MVD geometrical acceptance can be reconstructed with the CTD-MVD tracking informations. Reconstructed tracks are fitted to provide a primary vertex and possibly secondary vertices. The

primary vertex is constrained to lie on the beam line. Further details about the fitting method can be found in [90]. When the hadronic jet travels in the beam pipe, it may interact with the gas and produce many tracks which fit a secondary vertex. In this case the fitted primary vertex will be biased with respect to the real interaction vertex. The objective of the multi-vertex fitting is to provide a better measurement of the interaction vertex. Fig. 6.4 shows the distribution of the number of secondary vertices for LH and RH samples. The MC simulation properly reproduces these distributions. The

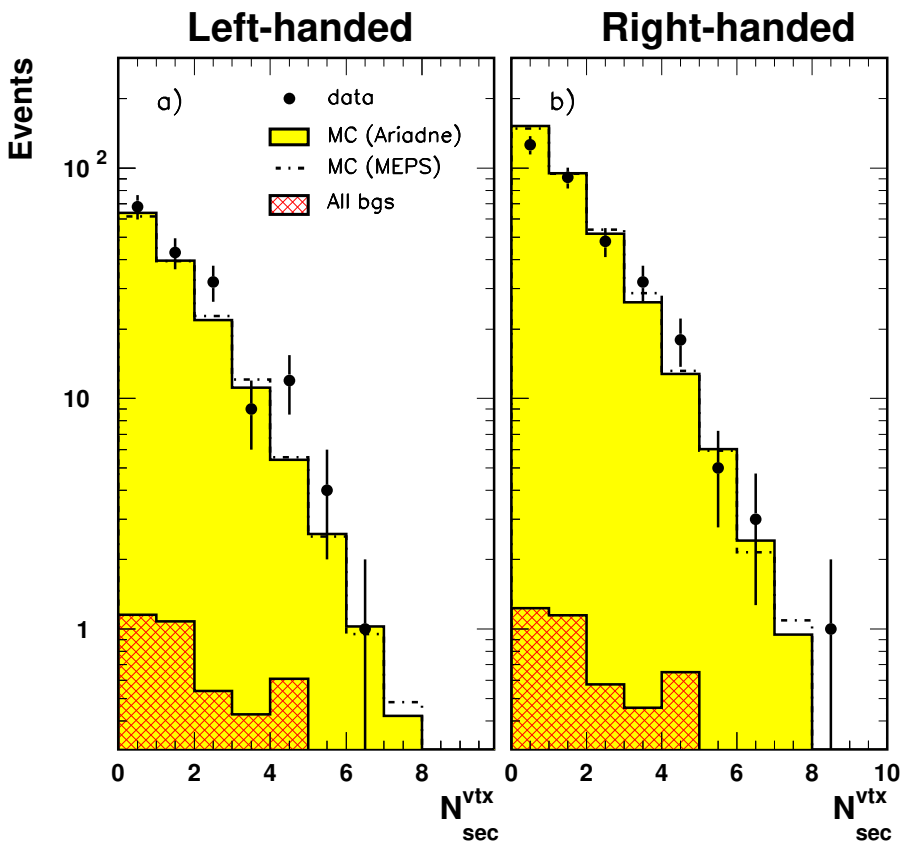

Figure 6.4: Distribution of the number of reconstructed secondary vertices, N^{vtx}_{sec}, for LH (a) and RH (b) samples.

resolution of the z-position of the primary vertex fitted with the CTD-MVD tracks for CC events is about 1 cm. The resolution is smaller (~ 0.15 cm) in case of NC. For high-Q^2 NC events, the scattered electron track is perpendicular to the beam line and thus improves the quality of the vertex fit.

The efficiency of the CTD-MVD to reconstruct the vertex decreases when the current jet is boosted toward the forward region, i.e. γ_h is small. This

is because most of the tracks are produced at low polar angles and no CTD-MVD information is available. However, if the energy deposited in the CAL (mostly the FCAL) is large enough, the vertex can be reconstructed from the arrival time to the CAL [91]. The resolution of the vertex from timing is about 9 cm to be compared with 1 cm resolution for the vertex from tracking. Because of the large difference in the resolution, which also affects the resolution of the kinematical variables, the two classes of events are treated separately. The efficiency of the CTD vertex reconstruction as a function of γ_0 is shown in Fig. 6.5. Here γ_0 is the γ angle calculated assuming the nominal position of the interaction point

$$\cos\gamma_0 \equiv \frac{P_{T,0}^2 - \delta_0^2}{P_{T,0}^2 + \delta_0^2}\,, \tag{6.1}$$

where $P_{T,0}$ and δ_0 are P_T and δ calculated assuming the vertex at $(0,0,0)$. As can be seen, the efficiency drops markedly for $\gamma_0 \leq 0.3$. Since the z-position of the vertex is spread over a relatively wide range, γ_0 and γ may be different. In fact, γ_0 is a calculation and the event topology depends on γ and not γ_0. On the other hand, the determination of γ requires a known vertex position. To tackle this puzzle, we decide to use the FCAL timing vertex for events with $\gamma_0 < 0.4$ rad and the CTD-MVD vertex if $\gamma_0 > 0.4$ rad.

The events with small values of γ are experimentally challenging because most of the produced hadrons lie close to the forward beam pipe and there is no CTD or MVD information available. These events tend to populate the high x region in the kinematic phase space as shown in Fig. 6.6, where iso-lines of P_T, γ, and y are drawn.

Another reason to classify events in low γ_0 ($\gamma_0 \leq 0.4$) and high γ_0 ($\gamma_0 \geq 0.4$) samples is the different type of background affecting the two samples. The low γ_0 sample is more affected by photoproduction and beam-gas interactions than the high γ_0 sample. Therefore, the selection cuts on the low γ_0 events are more restrictive than for high γ_0.

6.4 Pre-selection cuts

From all the triggered events, only events which pass the CC trigger requirement (see sec. 6.1) and pass the following condition

$$P_T > 10\ \text{GeV}\,, \tag{6.2}$$
$$P_T' > 9\ \text{GeV}\,, \tag{6.3}$$
$$Q^2 > 180\ \text{GeV}^2\,, \tag{6.4}$$
$$|z_{vtx}| < 100\ \text{cm}\,, \tag{6.5}$$

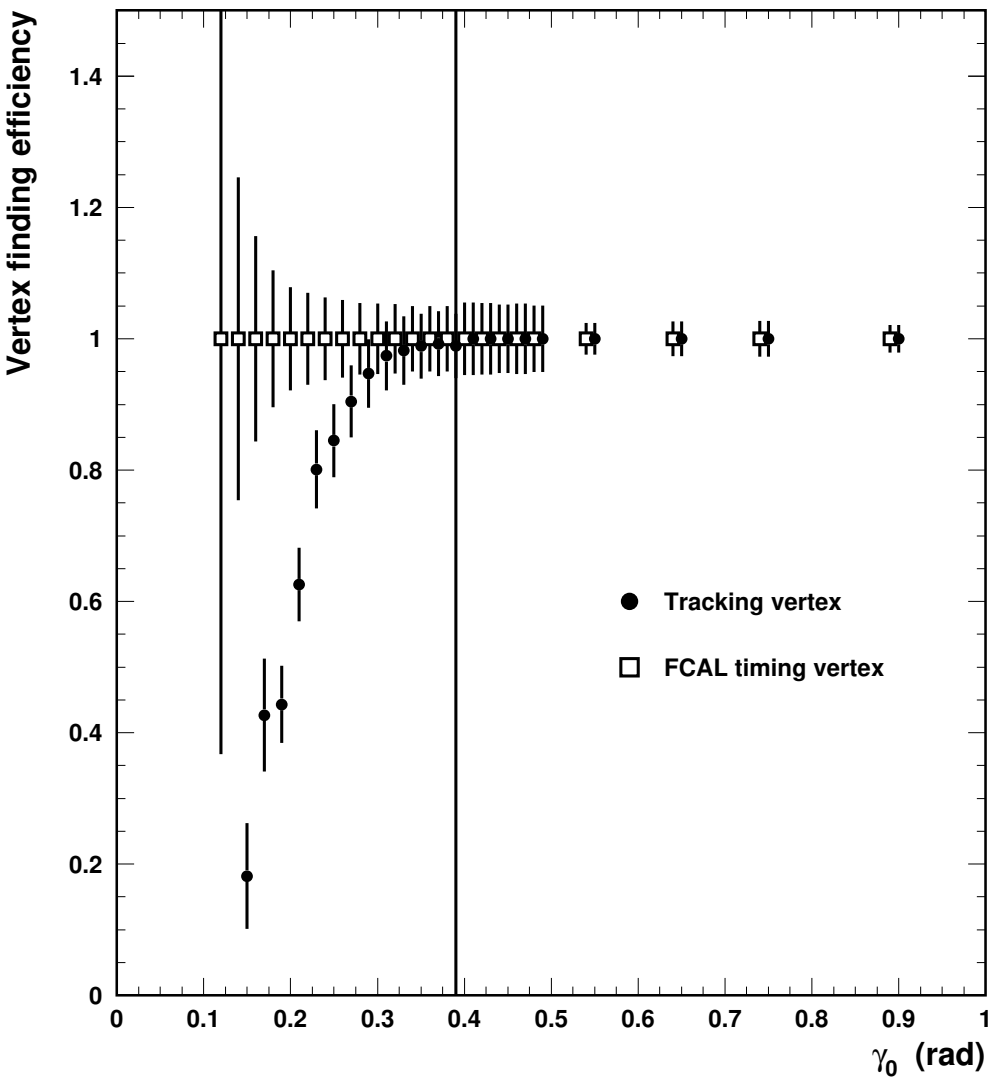

Figure 6.5: The vertex finding efficiency as a function of γ_0, as obtained by the tracking and by the FCAL arrival timing.

were accepted. Here $|z_{vtx}|$ is defined as the z-position of the CTD-MVD vertex if $\gamma_0 > 0.4$ and of FCAL-timing if $\gamma_0 < 0.4$. These selection cuts are applied in the online selections and used to reduce the background events. Tighter thresholds on these quantities and further cuts are applied in the offline analysis.

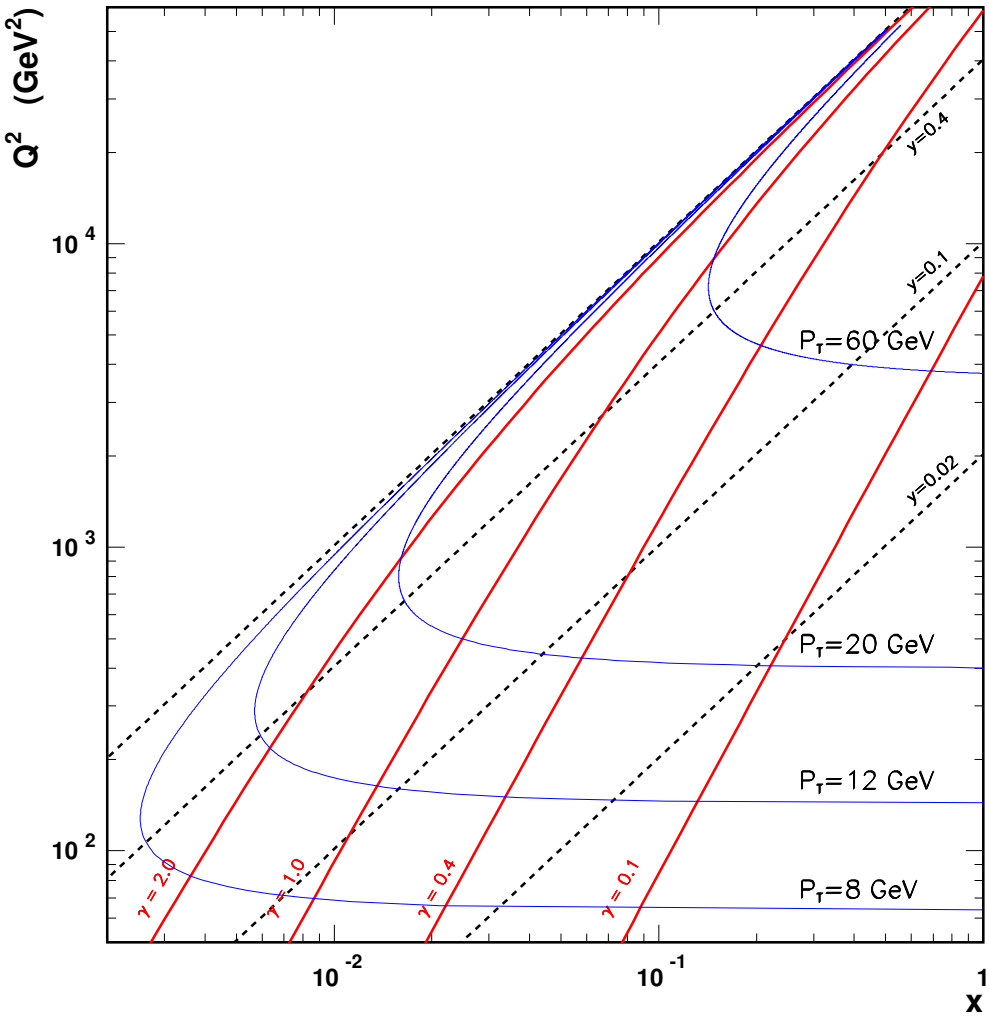

Figure 6.6: The kinematic phase-space of events in the $Q^2 - x$ plane, with lines of constants P_T, γ_0 and y as denoted in the figure.

6.5 Kinematic cuts

The kinematical range was chosen such as to make the background contributions as small as possible, and to have a good resolution in the Jacquet-Blondel estimators [87]. The kinematical region in the offline analysis is restricted to

$$Q^2 \geq 200 \text{ GeV}^2 , \tag{6.6}$$

$$y \leq 0.9 . \tag{6.7}$$

The y cut is introduced because the Q^2 resolution degrades as $y \to 1$,

$$\frac{\Delta Q^2}{Q^2} = \sqrt{4(\frac{\Delta P_T}{P_T})^2 + (\frac{\Delta y}{1-y})^2}\,. \tag{6.8}$$

6.6 High γ_0 event selection

6.6.1 Vertex cut

The longitudinal length of the proton bunch is ~ 11 cm, while the electron bunch length is ~ 10 cm. Thus, the z-coordinate of the interaction point is distributed around the nominal interaction point with $\sigma \sim 11$ cm. In order to select the events which are consistent with the ep collisions we require

$$|z_{vtx}^{trks}| \leq 50 \text{ cm}\,, \tag{6.9}$$

where $|z_{vtx}^{trks}|$ is the z-position of the ep interaction vertex fitted with the CTD-MVD tracks. This cut reduces the non-ep background events and ensures that events have been well reconstructed. Fig. 6.7 shows the distribution of the z_{vtx}^{trks} for LH and RH samples. The MC properly reproduces the data in the accepted regions.

6.6.2 P_T cut

The undetected neutrino carries a transverse momentum which balances the transverse momentum of the hadronic final state. However, since the neutrino escapes detection, the full event is characterised by a relatively high transverse momentum. In this analysis, we require

$$P_T > 12 \text{ GeV}\,. \tag{6.10}$$

Fig. 6.8 shows the comparison of the P_T distribution in data and MC for LH and RH CC events. The MC properly reproduces the data.

6.6.3 P_T' cut

P_T' is the transverse momentum of the event calculated excluding the energy deposited in cells closest to the first inner ring of the FCAL beam hole. We require

$$P_T' \geq 10 \text{ GeV}\,. \tag{6.11}$$

This cut is effective in removing possible proton beam-gas events, which deposit little energy at higher angles. Fig. 6.9 shows the P_T' distribution of

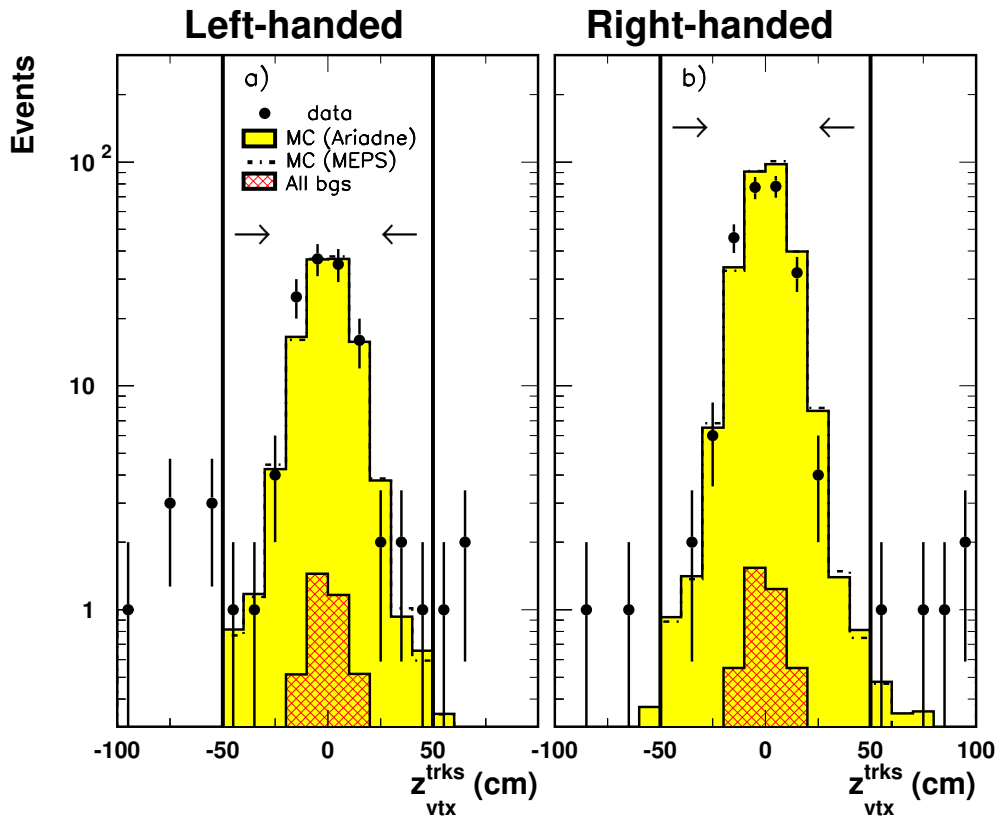

Figure 6.7: The z-position of the vertex fitted with the CTD-MVD tracks (high γ_0 events). a) for RH sample and b) for LH sample. The dots stand for the data, the filled histograms denote the MC with Ariadne and the dashed ones denote the MC with MEPS. The dashed filled histograms represent all background contaminations.

both LH and RH samples after applying all cuts except the cut on P_T'. The MC well reproduces the data.

6.6.4 Tracking requirement

In the high γ_0 sample, where the hadronic final state travels through the CTD-MVD, we require

$$N_{Good} \geq 1\,, \tag{6.12}$$

where N_{Good} denotes the number of good tracks that satisfy the following:

- the track is fitted to the primary vertex,
- the track is in the CTD-MVD acceptance, i.e. $15^\circ \leq \theta_{trk} \leq 164^\circ$.

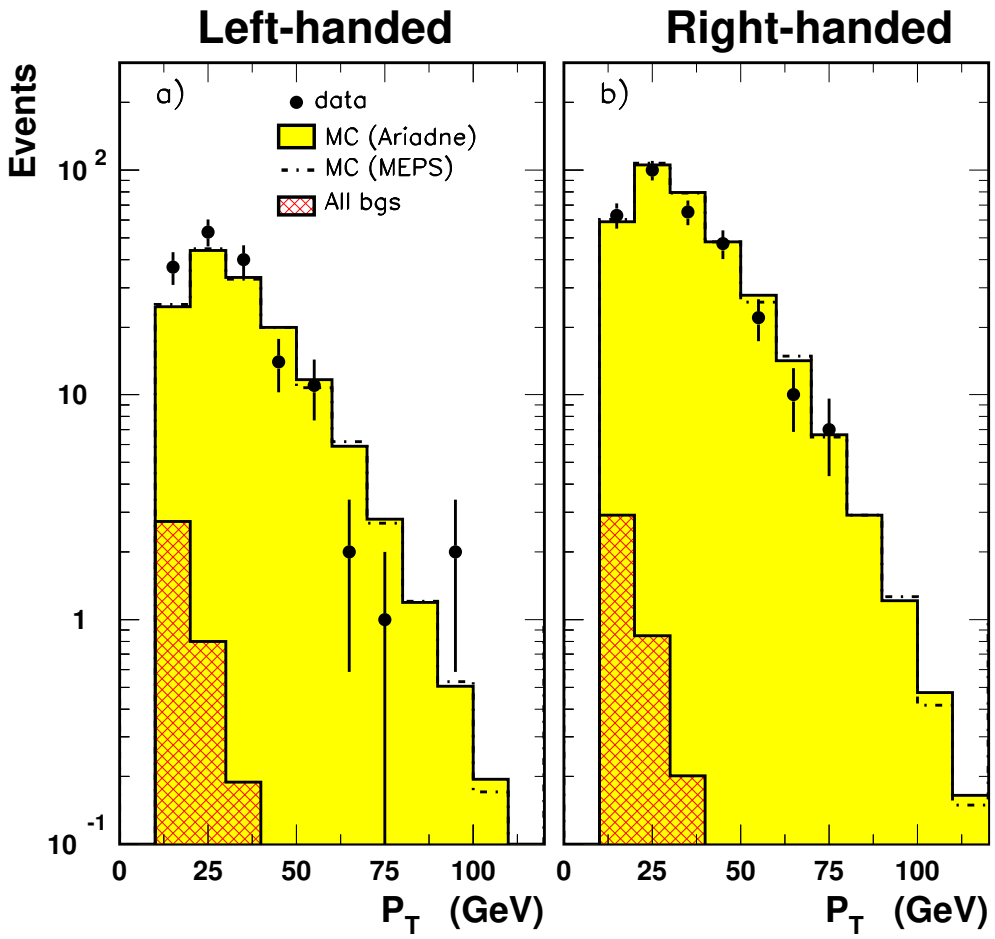

Figure 6.8: (a) ((b)): The P_T distribution of the final LH (RH) high γ_0 sample after all other cuts have been applied. The dots denote the data points, the histogram denotes the MC distribution with Ariadne while the dashed line histogram denotes the MC distribution obtained with MEPS MC. The dashed filled histogram denotes the background contribution from all processes entering the CC sample

- the transverse momentum of the track exceeds 200 MeV.

The contamination of the proton beam-gas events can be reduced by requiring that

$$N_{Good} \geq \frac{1}{4}(N^{trks} - 20)\,, \tag{6.13}$$

where N^{trks} is the total number of tracks found by the CTD-MVD. Proton beam-gas events are characterised by a high number of poor quality

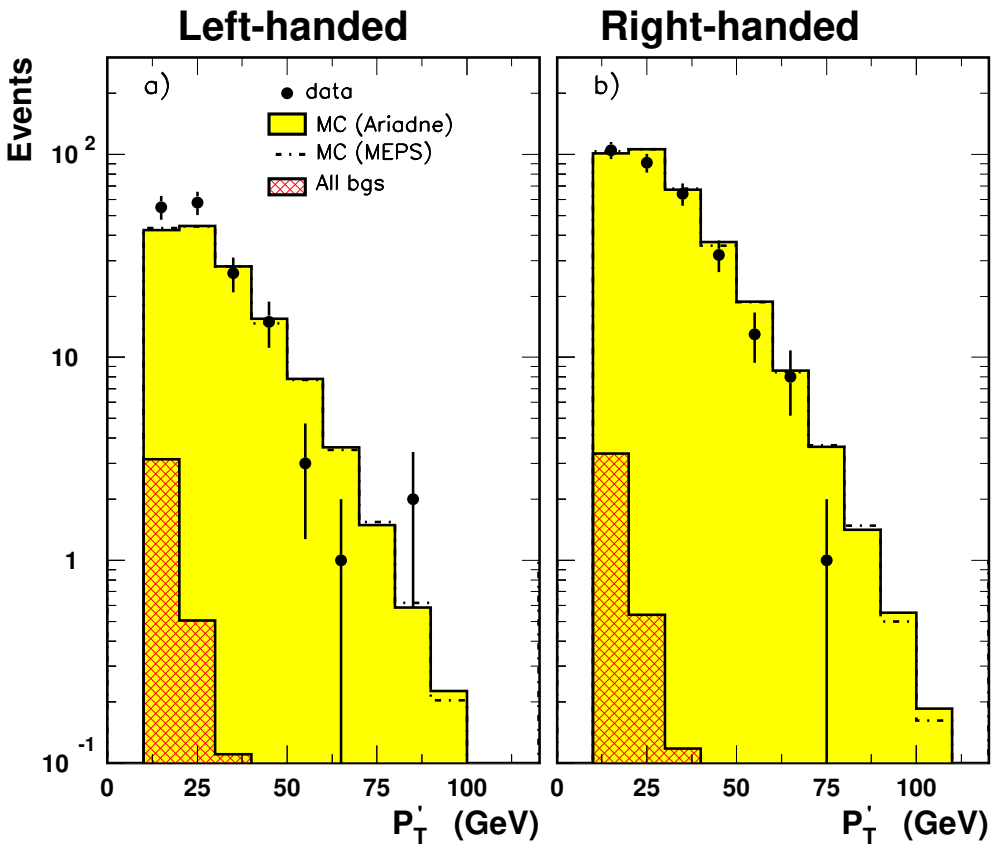

Figure 6.9: (a) ((b)): The P'_T distribution of the final LH (RH) high γ_0 sample after all other cuts have been applied. The dots denote the data points, the filled histogram denotes the MC distribution with Ariadne while the dashed denotes the MC distribution obtained with MEPS MC. The dashed histogram denotes the background contributions from all processes which enter the CC sample.

tracks [92]. Fig. 6.10 shows the distributions of the number of good tracks versus the total number of tracks in data (Fig. 6.10 a) and MC (Fig. 6.10 b). In the previous analysis [83, 92–95] the data distributions were not well simulated by the MC and the above cut was introduced. In this analysis we do not have enough statistics and therefore we keep the conventional cut on N_{Good} versus N^{trks}. The distribution of $\frac{N^{trks}-20}{N_{Good}}$ is shown for the LH and RH samples in Fig. 6.10 c and Fig. 6.10 d. A good agreement between the MC and data is observed in the accepted region.

The P_T direction can be calculated by either the CTD-MVD tracks or by the CAL energy deposits. These two angles should be very similar. The

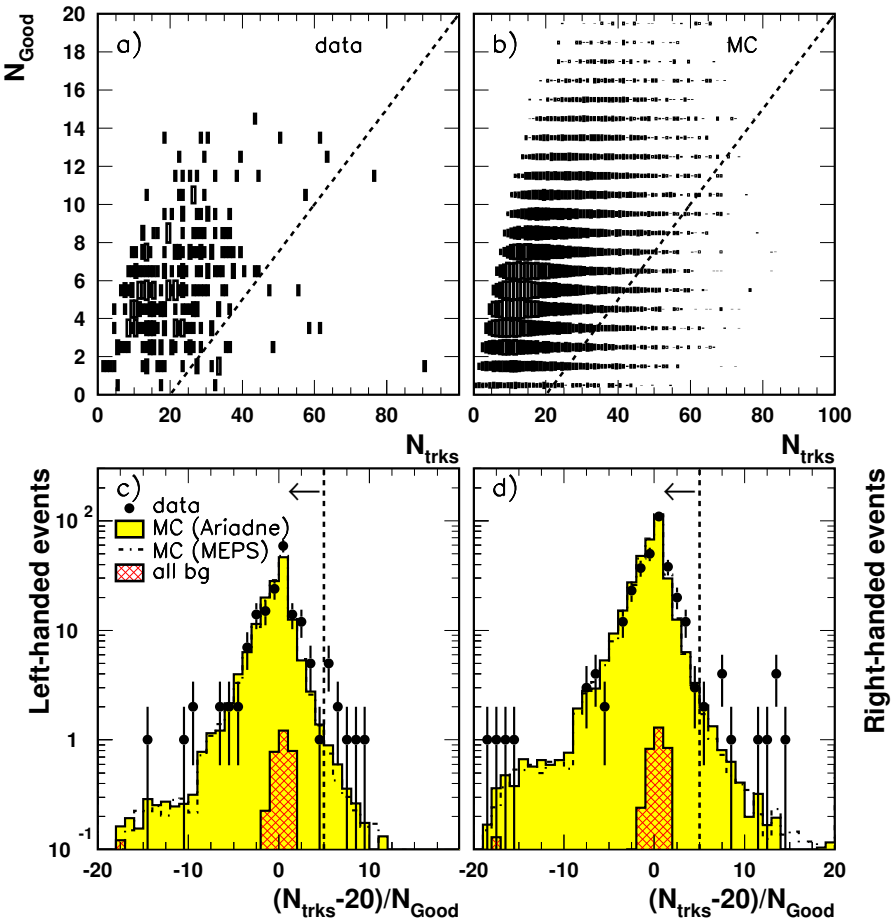

Figure 6.10: N_{Good} versus N_{trks} for high γ_0 CC events in data (a) and MC (b). The distribution of the ratio $\frac{(N_{trks}-20)}{N_{Good}}$ for the LH (c) and RH (d) sample is presented. Here all cuts were applied except the tracking cut.

difference of the two azimuthal angles is denoted as $\Delta\Phi_{trks-CAL}$. Only tracks with $15^\circ \leq \theta_{trk} \leq 164^\circ$ are used for the $\Delta\Phi_{trks-CAL}$ calculations. The requirement is that

$$\Delta\Phi_{trks-CAL} \leq \begin{cases} 1.0 \text{ rad} & \text{if } P_T \leq 30 \text{ GeV}, \\ 2.0 \text{ rad} & \text{if } P_T > 30 \text{ GeV}. \end{cases} \tag{6.14}$$

Also here we keep the conventional cut as proposed in the previous analysis [83, 92–95]. This cut is effective in removing halo muons and cosmic muon

events because in this type of events a large P_T is measured in the CAL while a small P_T is measured by the CTD-MVD because of the requirement of at least on good track for high γ_0 events. In addition, this cut removes some photoproduction and NC-DIS background in which a P_T arises from a poor energy measurement in the CAL. This is the reason why a tighter threshold was imposed on the events with a lower P_T.

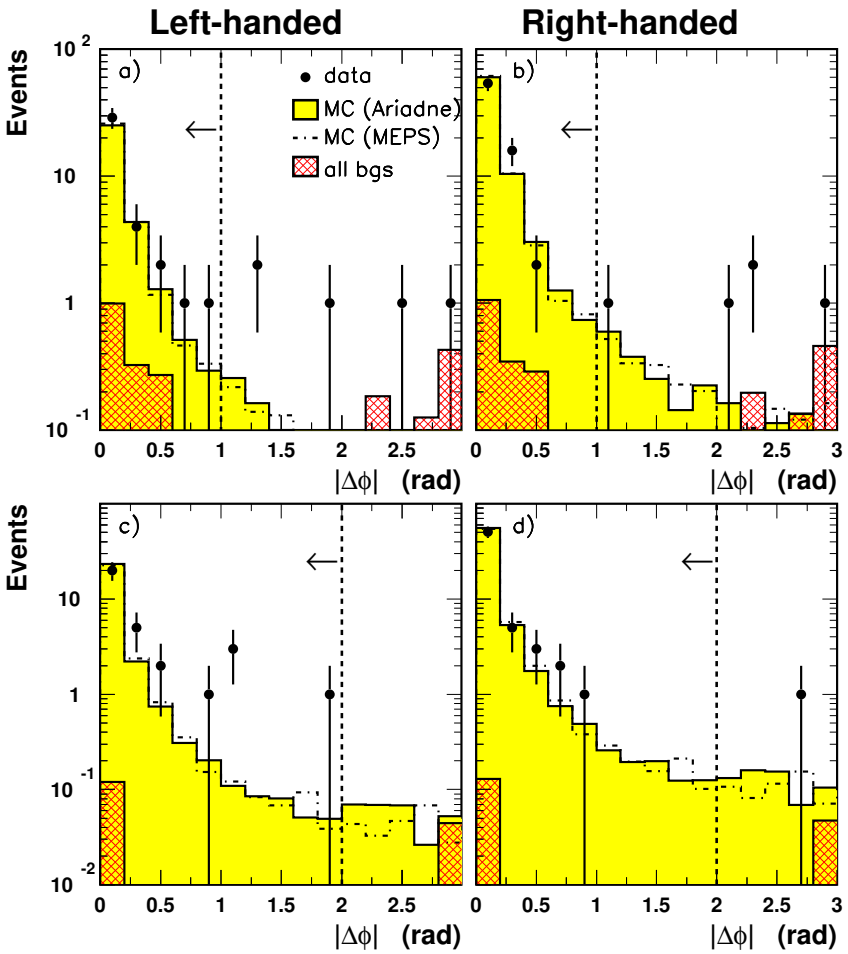

Figure 6.11: The $|\Delta\phi|$ distributions for the LH (a) and RH (b) for high γ_0 samples after applying all cuts except the $\Delta\phi$ cut. The dots denote the CC data while the filled (dashed) histograms represents the CC MC distributions obtained with ARIADNE (MEPS). The part of the figures to the left of the vertical dotted lines denote the accepted region of events.

6.6.5 Photoproduction background

For DIS events, the values of P_T and E_T of the hadronic final state are very close ($P_T \sim E_T$), while in photoproduction events, the value of E_T is larger than P_T. In photoproduction events, the scattered electron travels down the beam pipe in the negative z-direction and thus has a small transverse momentum which balances the hadronic transverse momentum. The PHP cross section is much higher than the CC cross section and thus some PHP events may fake high transverse momentum and enter the CC sample. The PHP contamination in the CC sample drops rapidly with increasing P_T. To reject photoproduction events we require

$$P_T/E_T > \begin{cases} 0.55 & \text{if } P_T < 20 \text{ GeV}\,, \\ 0.40 & \text{if } 20 < P_T < 30 \text{ GeV}\,. \end{cases} \tag{6.15}$$

For $P_T \geq 30$ GeV, the photoproduction background was found to be negligible.

In Fig. 6.12 (a) the P_T/E_T of the hadronic final state for a NC sample is shown. A clear peak is observed at values of $P_T/E_T \approx 0.8$ with a tail extending towards low values. The comparison of the P_T/E_T distribution of the high γ_0 CC events in the data and in the MC is shown in Fig. 6.12 (b). The distribution of P_T/E_T from the resolved and direct photoproduction MC before applying the P_T/E_T cuts are presented in Fig. 6.12 (c) and Fig. 6.12 (d). These figures were obtained after applying all selection cuts except those on the P_T/E_T. The CC MC does not describe the CC data at low values of P_T/E_T, and the expectations from the resolved and the direct PHP MC are not negligible.

The distribution of P_T/E_T for events with $P_T < 20$ GeV for LH and RH samples are presented in Fig. 6.13(a) and Fig. 6.13(b), respectively. The distribution of P_T/E_T for events with $20 < P_T < 30$ GeV for the LH and RH samples are shown in Fig. 6.13(c) and Fig. 6.13(d), respectively. Fig. 6.13 (a), Fig. 6.13 (b), Fig. 6.13 (c), and Fig. 6.13 (d) were obtained before the cut on P_T/E_T was applied. According to Fig. 6.13, tighter P_T/E_T cut is needed for small P_T events, to reduce the PHP contaminations.

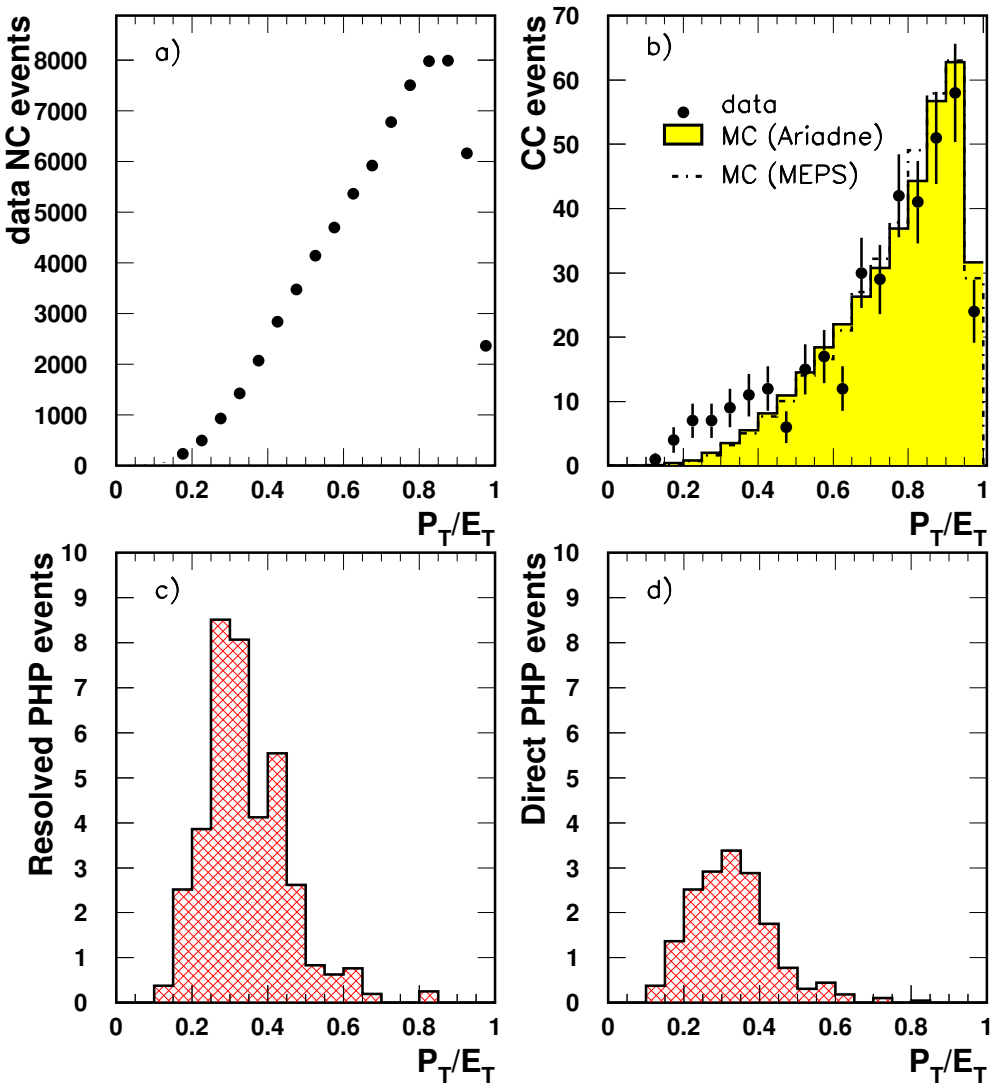

Figure 6.12: (a)- The distribution of P_T/E_T for the final NC high γ_0 sample. b); dots stand for the high γ_0 CC events after applying all cuts except the P_T/E_T cut, while the filled (dashed) histogram is the CC MC with ARIADNE (MEPS). The distribution of P_T/E_T in MC sample of resolved (c) and direct PHP (d), in high γ_0 sample.

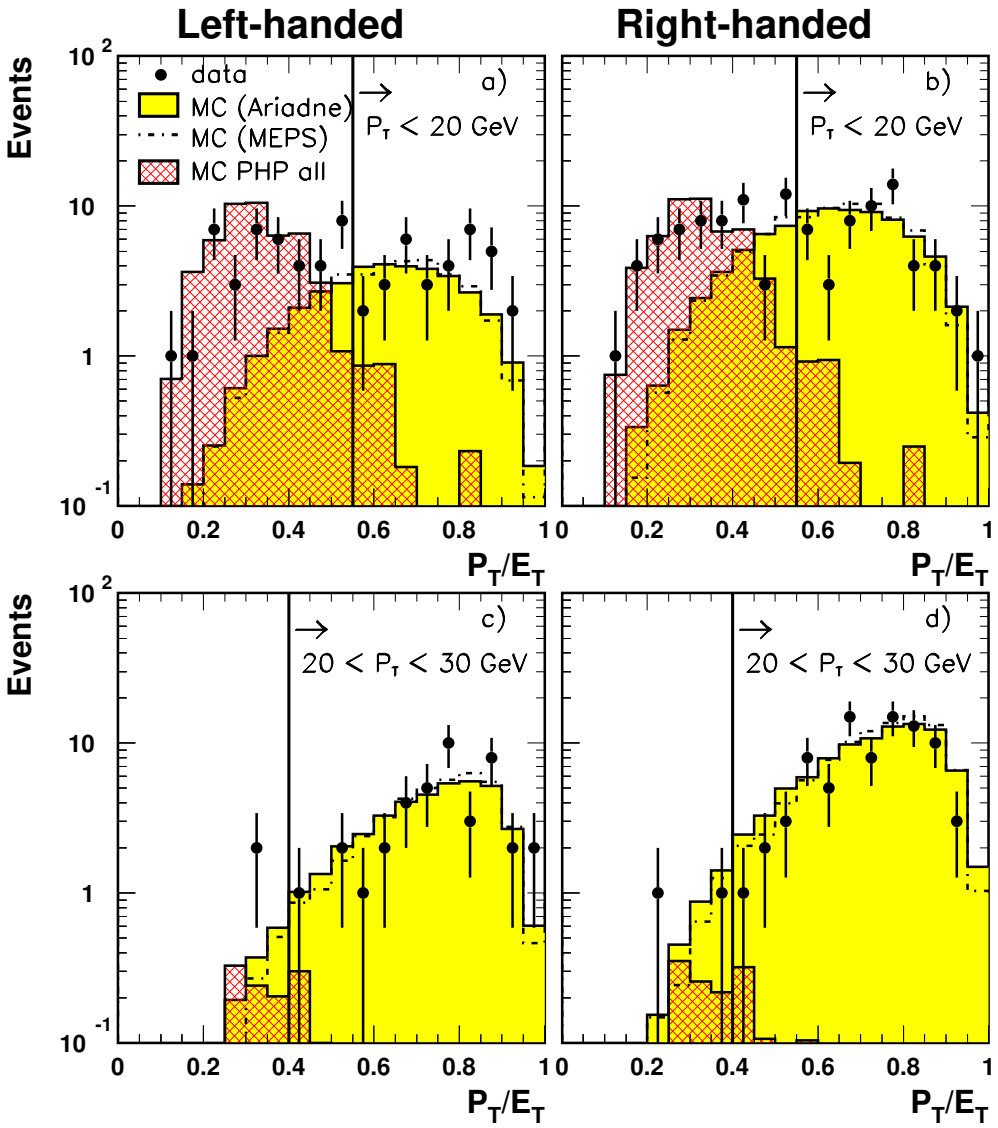

Figure 6.13: Distributions of P_T/E_T in the high γ_0 sample: (a) for the LH events and (b) for the RH events with $P_T < 20$ GeV and (c) and (d) for the events with $20 < P_T < 30$ GeV. All figures above were obtained after applying all cuts except the P_T/E_T cut. The full points denote the CC data, the filled (dotted) histograms denote the CC MC distribution obtained with ARIADNE (MEPS). The dashed histograms show the expectations of the sum of resolved and direct PHP MC. All MC samples were normalised to the data luminosity. The part of the figures to the right of the vertical lines denote the accepted region of events.

6.7 Low γ_0 event selection

6.7.1 Vertex cut

As was explained in sec 6.3, for low γ_0 events the z-component of the interaction point is reconstructed by the arrival time of the energy deposits in the FCAL. Fig. 6.14 shows the comparison between z_{vtx}^{FCAL} distribution in data and MC for the final CC sample. The MC expectation reproduces well the data points.

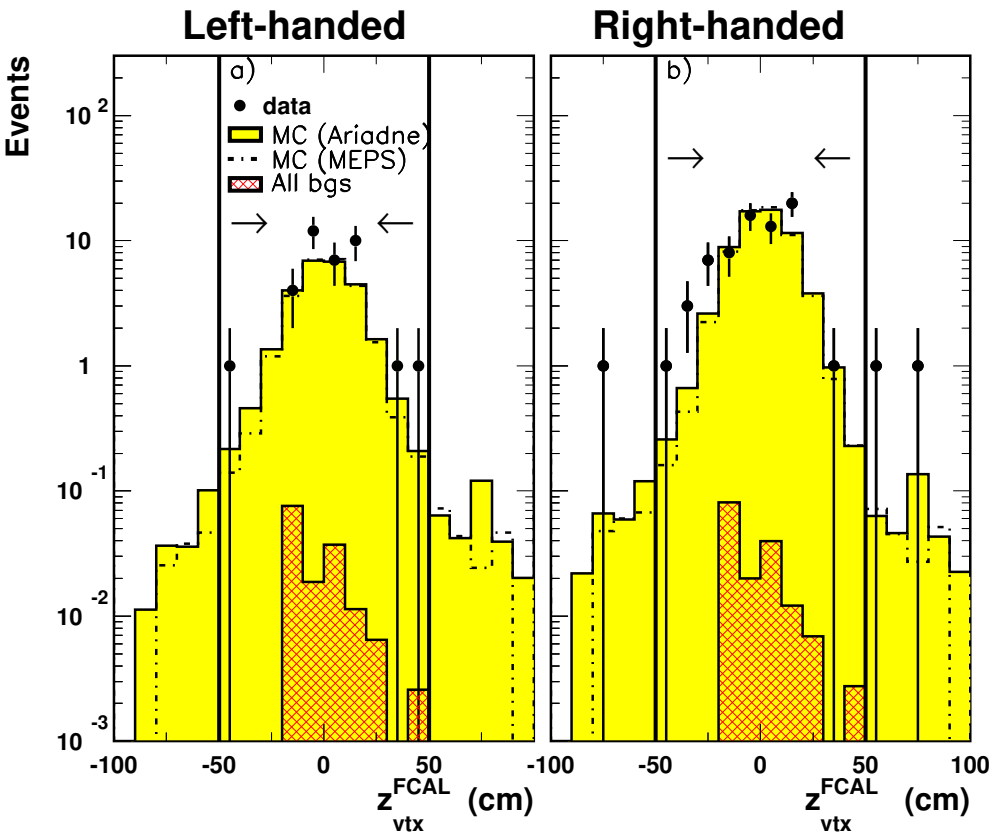

Figure 6.14: The z_{vtx}^{FCAL} distribution for the LH (a) and RH (b) samples. The dots denote the CC data and the filled (dotted) histograms stand for the MC CC events obtained with ARIADNE (MEPS). The filled dashed histograms stand for the contamination background that enter the CC samples. The region between the two vertical lines in each figure represent the accepted region of events.

6.7.2 P_T and P'_T cuts

Since the photoproduction background is higher in the low γ_0 sample, the threshold on the P_T cut was increased to reduce the photoproduction contamination and was set to

$$P_T > 14 \text{ GeV}\,. \tag{6.16}$$

Also, to reduce possible proton beam-gas contamination, the threshold on P'_T was increased to

$$P'_T > 12 \text{ GeV}\,. \tag{6.17}$$

6.7.3 Halo and cosmic muon rejection

The low γ_0 sample is more affected by halo and cosmic muon backgrounds than the high γ_0 sample because the tracking information is not available in the low γ_0 sample. Fig. 6.15 shows the comparison between the data and the MC for the distributions of the energy fraction of each FCAL section to the total energy in the FCAL, i.e. E^{EMC}_{FCAL}/E_{FCAL}, E^{HAC1}_{FCAL}/E_{FCAL}, and E^{HAC2}_{FCAL}/E_{FCAL}, where E_{FCAL} is the total energy in the FCAL, E^{EMC}_{FCAL} is the energy in the EMC section of the FCAL and E^{HAC1}_{FCAL} (E^{HAC2}_{FCAL}) is the energy in the HAC1 (HAC2) FCAL section. The plots in Fig. 6.15 were obtained after applying all the selection cuts except those designed to remove backgrounds of the type of cosmic/halo muon events. The data seem to include a large number of events with almost zero energy in the FCAL EMC section. This can occur when a cosmic muon hit perpendicularly one of the HAC FCAL sections and left no energy deposit in the EMC section. Such an event may fake high transverse momentum and thus enter the CC sample. Similarly, a muon can hit perpendicularly the FCAL EMC section without crossing the EMC. In order to reduce the contamination from these backgrounds, we propose to require

$$\frac{E^{EMC}_{FCAL}}{E_{FCAL}} \geq 0.1\,, \tag{6.18}$$

$$\frac{E^{HAC1}_{FCAL}}{E_{FCAL}} \geq 0.1\,, \tag{6.19}$$

$$\frac{E^{HAC2}_{FCAL}}{E_{FCAL}} \leq 0.3\,. \tag{6.20}$$

In addition, For events with no CTD-MVD tracks, we require

$$N^{BRMU}_{trks} = 0\,, \tag{6.21}$$

where N_{trks}^{BRMU} is the number of reconstructed tracks in the BMUON and RMUON. The muon rejection cuts are not 100% efficient in removing all cosmic/halo muon background. The CC sample, after applying the above cuts, still contains some background events, especially halo-muon events, where the muon had catastrophic energy loss in the FCAL. Such an event can be removed by observing that the calorimeter shower is very narrow as opposed to a typical hadronic shower accompanying a CC event. In the following we describe an algorithm used to reduce the remaining cosmic/halo muon in the CC sample.

- This algorithm works only if the cell with the highest E_T value is located in the FCAL.
- The centre of the shower is defined as the position of the cell with the highest E_T cell in the FCAL, in terms of modules and towers (t^0, m^0), where t^0 (m^0) is the tower (module) number of the highest E_T cell.
- We draw rings around the centre of the shower in steps of one unit in towers and modules. See Fig. 6.16
- We define:
$$R(t,m) = \sqrt{(t^i - t^0)^2 + (m^i - m^0)^2}\,, \tag{6.22}$$
where the superscript i runs over all cells in a particular event.
- To find the shower radius, we sum the energies of those cells in each ring for which the energy is higher than 100 MeV [1]. If the energy in the R_i ring is zero, the radius of the shower is set to R_{i-1}.
- At this stage, we concentrate on the cells within the shower radius and we define:
$$N_W^t \equiv \max|t^i - t^0| \tag{6.23}$$
$$N_W^m \equiv \max|m^i - m^0| \tag{6.24}$$
$$E_W^t = \sum_i E_T^i \sqrt{(t^i - t^0)^2 + (m^i - m^0)^2} \tag{6.25}$$
where i runs over the cells within the shower radius R_{i-1}, and E_T^i is the transverse energy of the ith cell within the shower radius R_{i-1}. Only events which satisfy the following requirements are accepted as CC events
$$N_W^t > \begin{cases} 1 & \text{if } N_{trks} \geq 1, \\ 2 & \text{if } N_{trks} = 0, \end{cases} \tag{6.26}$$

[1] If the energy is less than 100 MeV, the cell is treated as a noisy cell.

$$N_W^m > \begin{cases} 1 & \text{if } N_{trks} \geq 1, \\ 2 & \text{if } N_{trks} = 0, \end{cases} \tag{6.27}$$

$$E_W^t > \begin{cases} 6 \text{ GeV} & \text{if } N_{trks} \geq 1, \\ 10 \text{ GeV} & \text{if } N_{trks} = 0, \end{cases} \tag{6.28}$$

- A halo muon usually loses some energy in the RCAL before arriving to the FCAL. We require therefore that the energy in RCAL, E_{RSP}, within the radius of 30 cm around the RCAL cell, which has the mirror position like the FCAL highest E_T cell, be less than 0.1 GeV if no CTD-MVD tracks were found.

$$E_{RSP} \equiv \sum_{\sqrt{(x^i-x^0)^2+(y^i-y^0)^2}<30 \text{ cm}}^{i} E^i < 0.1 \text{ GeV if } N_{trks}^F = 0\,, \tag{6.29}$$

  where x^i and y^i are the x and y position of the i-th RCAL cell. x^0 and y^0 stand for the position of the highest FCAL E_T cell. N_{trks}^F is the number of tracks which have a closest approach distance of less than 40 cm to the FCAL highest E_T cell and fit the tracking vertex.

6.8 Rejection of NC events

In DIS NC events, the scattered electron is detected and balances the hadronic final state. These events are therefore characterised by a low transverse momentum imbalance. However, if part of the hadronic jet is lost, for example having a very low polar angle, then such an event may be measured with higher P_T. The particles which escape detection though the forward beampipe have a relatively small $E - P_z$. This indicates that NC background events in the CC sample are mainly with high γ_0 . The Sinistra [96] finder was used to find the scattered electron. An event was rejected from the CC sample, if it satisfied the following selection cuts:

- at least one candidate found with Sinistra with probability exceeding 90%,
- $E_e \geq 4$ GeV, where E_e is the scattered electron energy,
- the electron cluster was isolated, that is $E^{cone} - E_e < 5$ GeV, where E^{cone} is the total energy deposited in the scattered electron cone,

- $P_T \leq 30$ GeV,
- $\delta \geq 30$ GeV,
- for electrons within the CTD-MVD acceptance, with $15^\circ \leq \theta_e \leq 164^\circ$, we require that $\frac{P_e}{E_e} > 0.25$, where P_e is the momentum of scattered electron as measured with the CTD-MVD,
- for electron with $\theta_e < 15^\circ$, the momentum of the electron as measured in the calorimeter should exceed 20 GeV.

Fig. 6.21 shows an example of DIS NC event removed with the above selection cuts. In this event, the scattered electron hits the BCAL and the track was measured with the CTD-MVD.

6.9 Calorimeter timing cuts

The timing in the calorimeter was designed such that for a collision at the nominal vertex, all energy deposits hit the calorimeter at time zero. When the electron or the proton beam has some lateness, the interaction point is boosted either to the rear direction or to the forward direction, depending on which beam was delayed. The boost on the interaction point from the nominal causes shifts on the arrival timings in the calorimeter up to 8 ns. The background due to cosmic muon and halo muon events can be reduced significantly by timing requirements. The NC sample, where the scattered electron is seen in the calorimeter and therefore the contributions from cosmic and halo muon events are negligible, can help in tuning the timing cuts. In order to treat the NC sample the same way as the CC one, the scattered electron was removed for the timing calculations. In Fig. 6.22 and Fig. 6.23 the global timing of the full calorimeter, BCAL, RCAL, upper BCAL, upper RCAL , lower FCAL, lower BCAL and lower RCAL is presented for NC and CC samples. Since the NC are constrained by the presence of the scattered electron, the NC sample is unlikely to have background from cosmic/halo muon events. By looking at the timings in the NC and the CC, we remove all events in the CC sample that have timing which is inconsistent with the NC one. Table 6.9 summarises the timing cuts which are used to get the final sample. Events that pass these cuts were rejected.

6.10 Selection cuts for high and low γ_0

The events that imposed the selection cuts discussed above were visually scanned using the ZEUS events display called ZEVIS [97]. It was found that

	timing cut	Energy threshold
Global CAL	$t > 4$ ns **or** $t < -6.5$ ns	$E > 20$ GeV
BCAL	$\|t\| > 5$ ns	$E > 4$ GeV
RCAL	$\|t\| > 5$ ns	$E > 3$ GeV
Upper BCAL	$t > 6$ ns **or** $t < -5$ ns	$E > 6$ GeV
Upper RCAL	$t < -6$ ns	$E > 2$ GeV
Lower FCAL	$t > 5$ ns **or** $t < -6$ ns	$E > 110$ GeV
Lower BCAL	$\|t\| > 5$ ns	$E > 3$ GeV
Lower RCAL	$t < -5$ ns	$E > 2$ GeV

Table 6.1: Summary of the timing cuts which are used in this analysis.

a large number of possible overlap CC events with cosmic/halo muon remain in both LH and RH CC samples. To reduce the number of these events we require

$$\frac{P_T}{E_T} < 0.98(\frac{P_T}{13})^{0.017}\,, \tag{6.30}$$

and

$$\frac{P_T}{E_T} < 0.997\,. \tag{6.31}$$

In Fig. 6.24, the P_T/E_T versus P_T is shown for data and MC CC samples enriched with halo and cosmic muons background events by removing the selection cuts described in sec. 6.7.3. The events which do not satisfy eq. (6.30) are likely to be background (see curve in Fig. 6.24).

Since halo muons travel in parallel to the proton beam, the energy deposits caused by them in the calorimeter are usually located in the same x and y coordinates, i.e. a straight line in the z-direction. In addition, the number of the energy deposits due to the halo muon events is relatively large if they hit the calorimeter in the BCAL. Fig. 6.25 shows the number of BCAL energy deposits versus the fraction of the number of energy deposits in the HAC2 section of the BCAL to all number of BCAL energy deposits in data compared to the MC expectations for CC events. We require

$$\frac{NBHAC2}{NBCAL} < 0.35 \;\text{ if }\; NBCAL > 19\,. \tag{6.32}$$

Similar cuts on the number of energy deposits of the EMC and HAC1 sections can be introduced.

As mentioned above, a halo muon that crosses the BCAL creates relatively large number of energy deposits. The large number of BCAL energy deposits can be obtained when an event with large multiplicity is observed. Fig. 6.26

shows the total number of tracks versus the number of EMC energy deposits in the BCAL, for data compared to the MC expectations. To reduce the halo muon backgrounds, we require

$$N^{trks} > \frac{1}{2} NBEMC - 30\,, \tag{6.33}$$

where $NBEMC$ is the number of EMC energy deposits in the BCAL.

6.11 Visual scanning

After applying all selection cuts, the events were visually scanned. There were still seven (eight) LH (RH) events identified as halo/cosmic muon events. These 15 events were removed from the final samples. An example of such an event is shown in Fig. 6.27, where a cosmic muon hit the calorimeter from outside, simultaneously with an ep interaction.

6.12 Final samples

The final CC data sample contains 160 LH and 314 RH events. The polarisation average of the LH (RH) data sample is -0.406 ± 0.011 (0.322 ± 0.009). The MC final sample, polarisation weighted, contains 144 LH and 345 RH events. The LH (RH) events in the final samples populate the kinematic phase-space as shown in Fig. 6.28 (Fig. 6.29).

6.13 MC and data comparison

In this section, the MC final sample is compared to the final data sample. In Fig. 6.30, the comparison of the distributions of P_T, P'_T, δ, and P_T/E_T is shown. Good agreement between data and MC is observed in all variables. In Fig. 6.31, the comparison of the distributions of γ_h, N_{good}, z_{vtx}^{trks}, and z_{vtx}^{FCAL} are presented. Also here the MC reproduces all distributions.

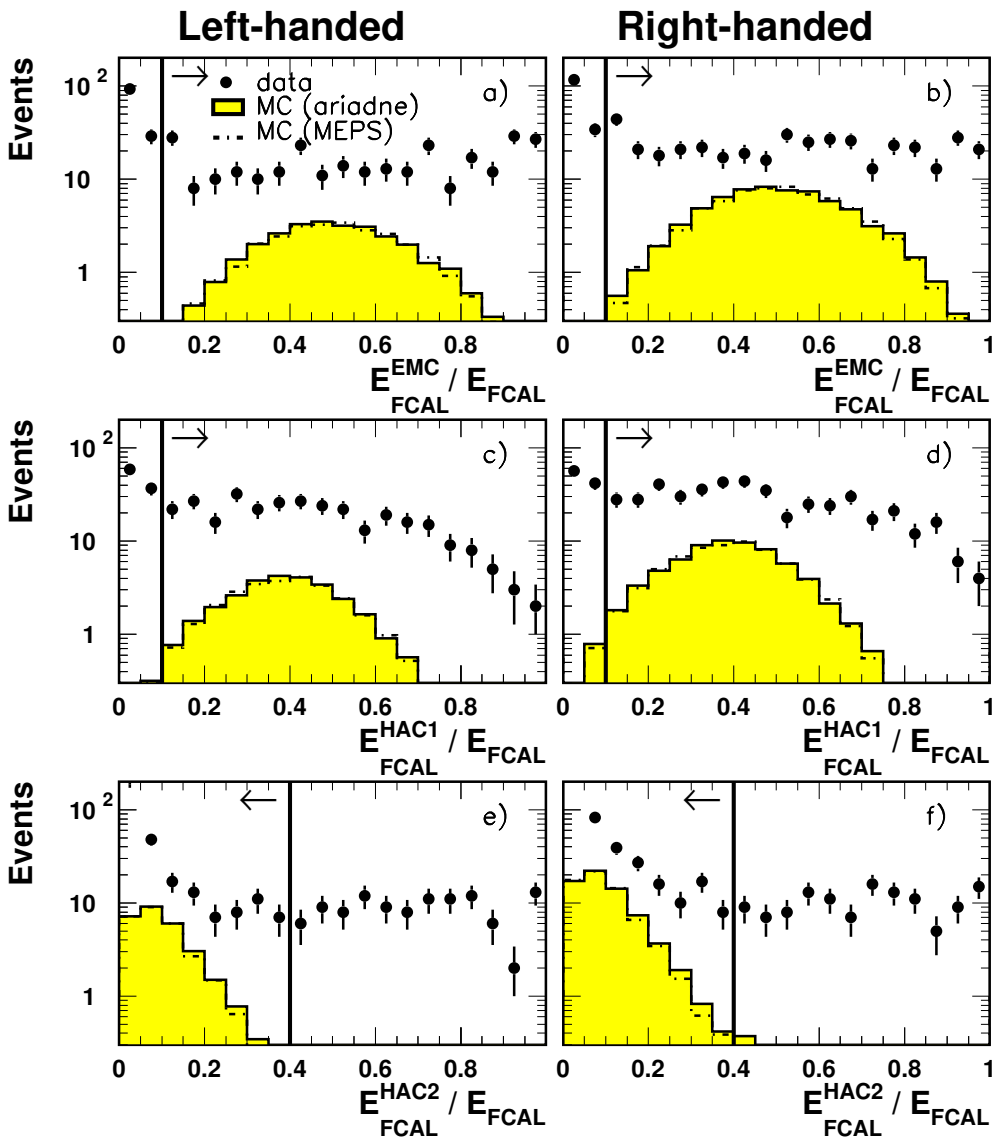

Figure 6.15: The distribution of: E^{EMC}_{FCAL}/E_{FCAL} for LH (a) and RH (b) CC samples; E^{HAC1}_{FCAL}/E_{FCAL} for LH (c) and RH (d) CC samples; and E^{HAC2}_{FCAL}/E_{FCAL} for LH (e) and RH (f) CC samples. The full points stand for the CC data and the filled (dotted) histograms represents the CC MC obtained with ARIADNE (MEPS). The parts of the plots a), b), c), and d), to the right of the vertical lines denote the accepted region of events. The part of the plots e) and f) to the left of the vertical lines denote the accepted region of events. The plots in this figure are for events with $\gamma_0 < 0.4$ rad, and were obtained by applying all cuts except the cuts on these quantities and the shower width cuts.

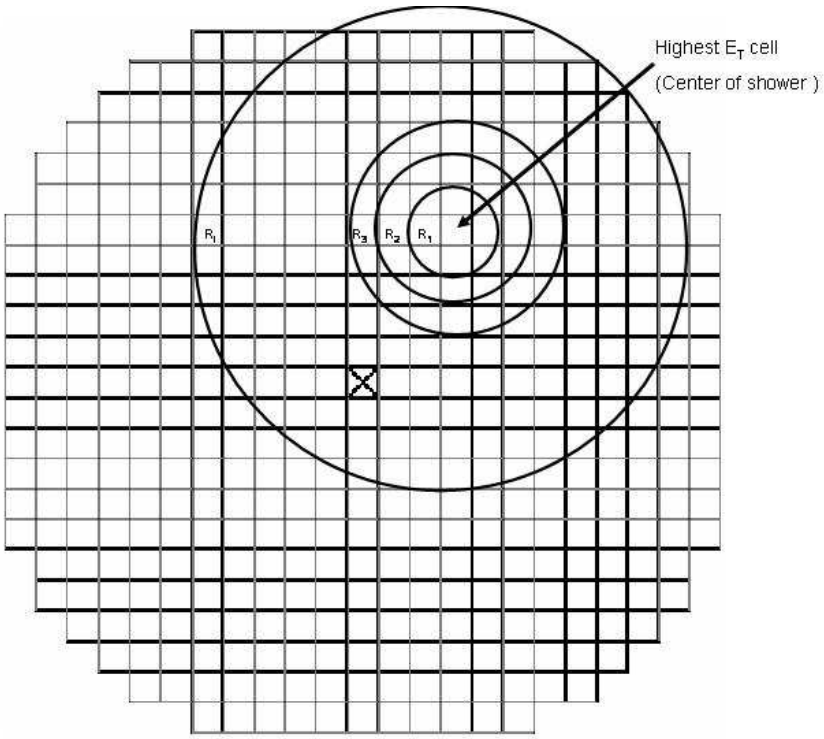

Figure 6.16: A schematic view of the FCAL as seen from the interaction vertex. The centre of the shower was chosen to be (t^0, m^0), where t^0 and m^0 are the tower and the module of the highest E_T cell. The rings where chosen in steps of one.

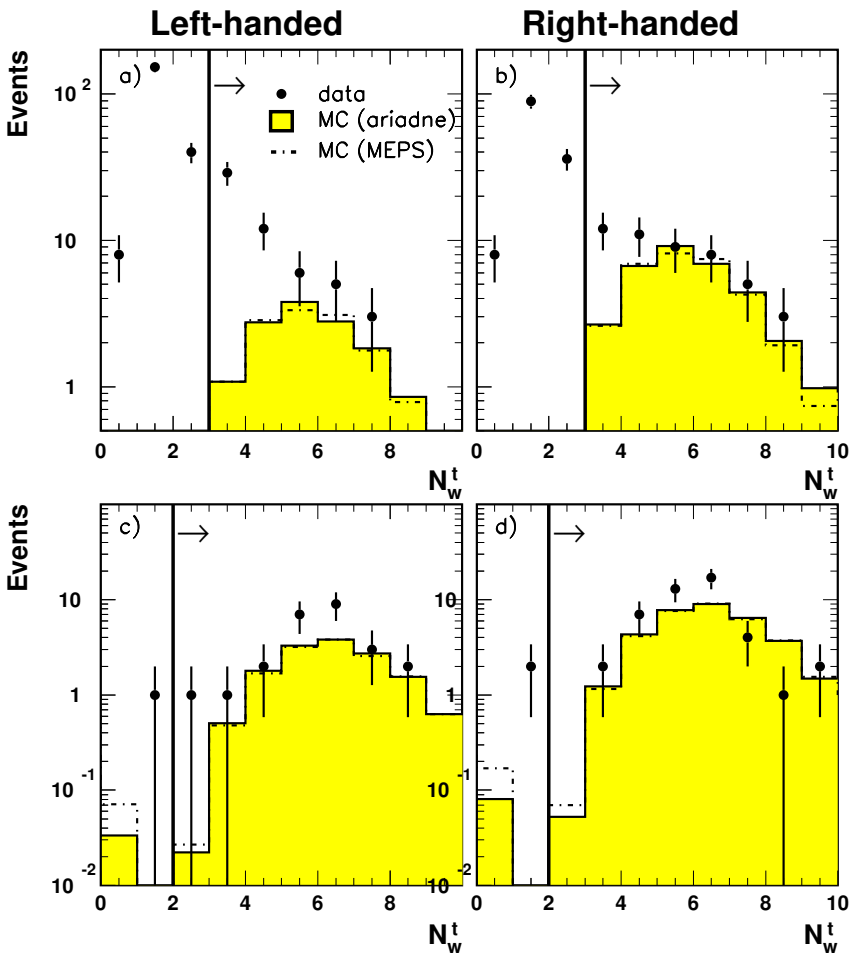

Figure 6.17: The distribution of N_W^t for events with no tracks for LH (a) and RH (b) samples. The distribution of N_W^t for events with at least one track associated with the highest E_T cell for LH (c) and RH (d) samples. The dots stand for the CC data and the filled (dotted) histograms represent the CC MC as obtained with ARIADNE (MEPS). The parts of the plots right of the vertical lines denote the accepted region of events.

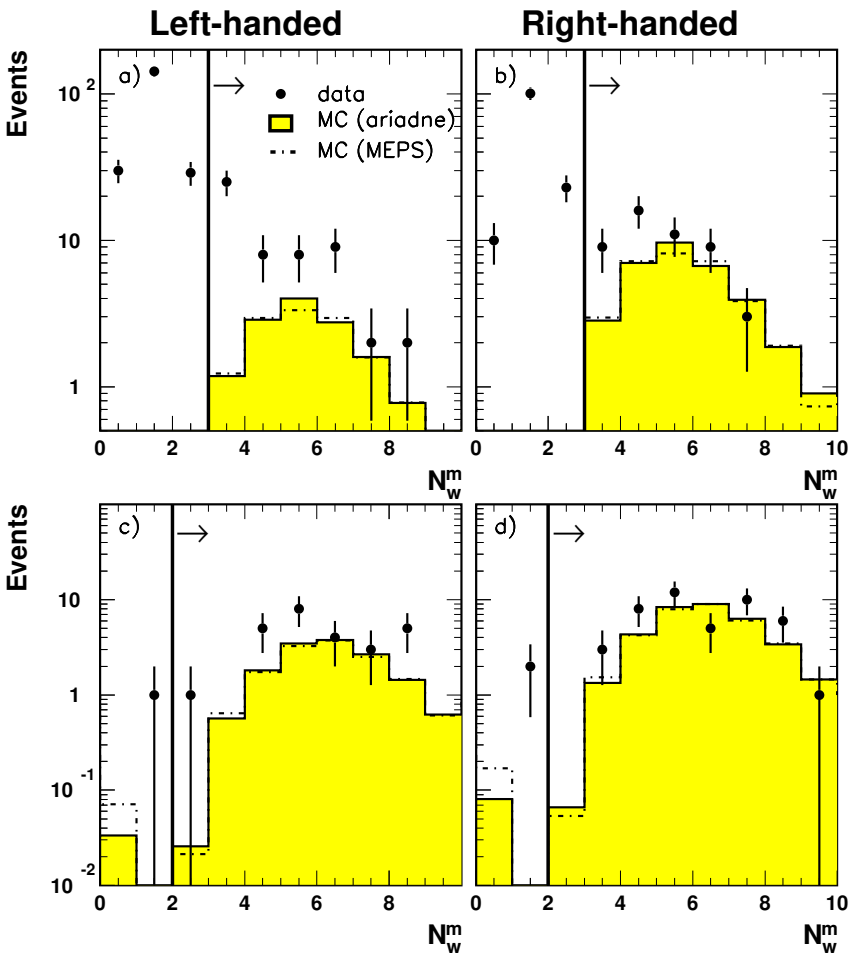

Figure 6.18: The distribution of N_W^m for events with no tracks for LH (a) and RH (b) samples. The distribution of N_W^m for events with at least one track associated with the highest E_T cell for LH (c) and RH (d) samples. The full points stand for the CC data and the filled (dotted) histograms represent the CC MC as obtained with ARIADNE (MEPS). The parts of the plots right of the vertical lines denote the accepted region of events.

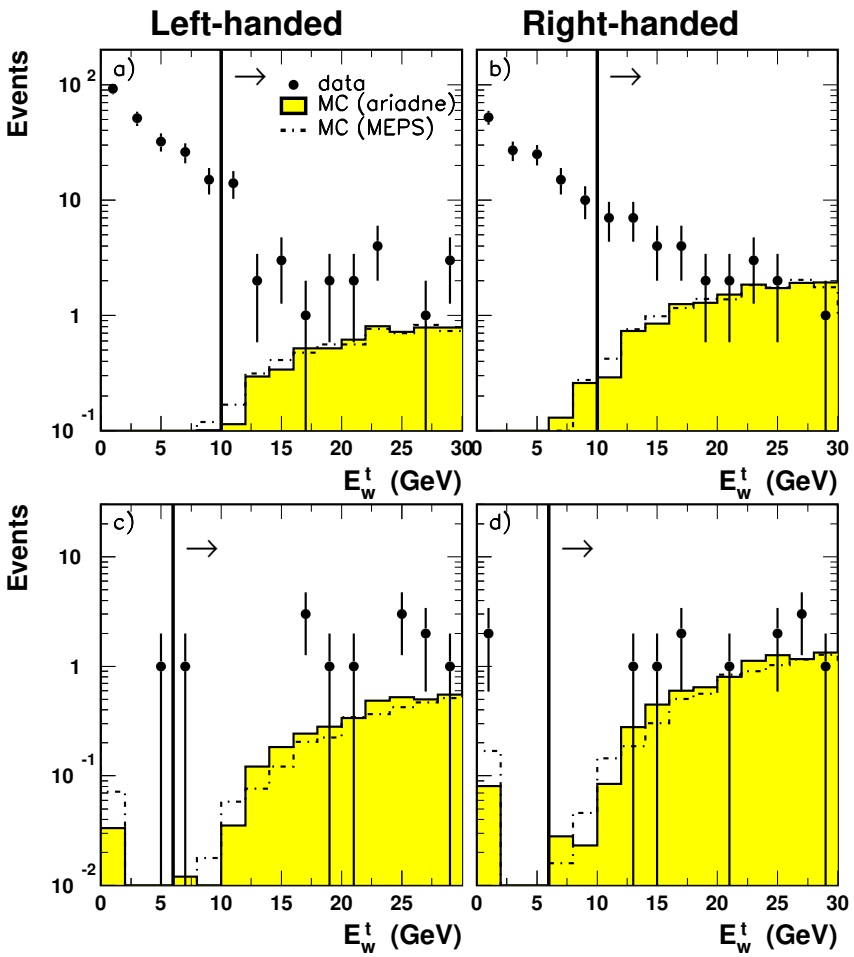

Figure 6.19: The distribution of E_W^t for events with no tracks for LH (a) and RH (b) samples. The distribution of E_W^t for events with at least one track associated with the highest E_T cell for LH (c) and RH (d) samples. The full points stand for the CC data and the filled (dotted) histograms represent the CC MC as obtained with ARIADNE (MEPS). The parts of the plots right of the vertical lines denote the accepted region of events.

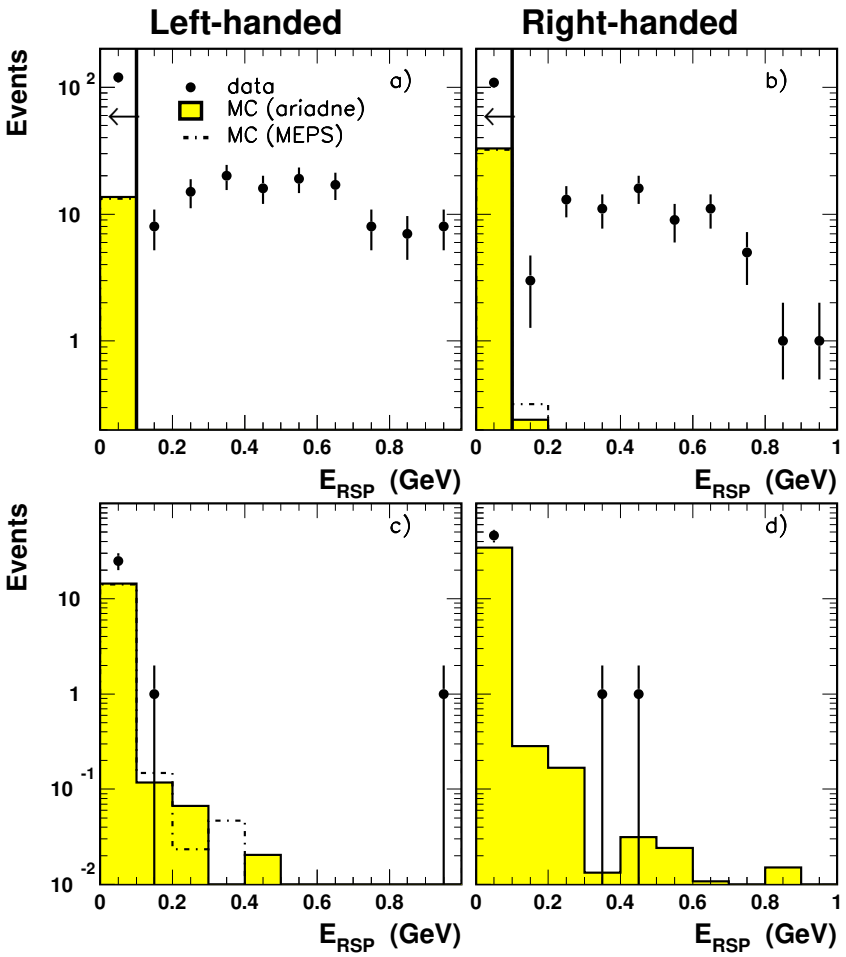

Figure 6.20: The distribution of E_{RSP} for events with no tracks for LH (a) and RH (b) samples. The distribution of E_{RSP} for events with at least one track associated with the highest E_T cell for LH (c) and RH (d) samples. The full points stand for the CC data and the filled (dotted) histograms represent the CC MC as obtained with ARIADNE (MEPS). The parts of the plots (a) and (b) right of the vertical lines denote the accepted region of events.

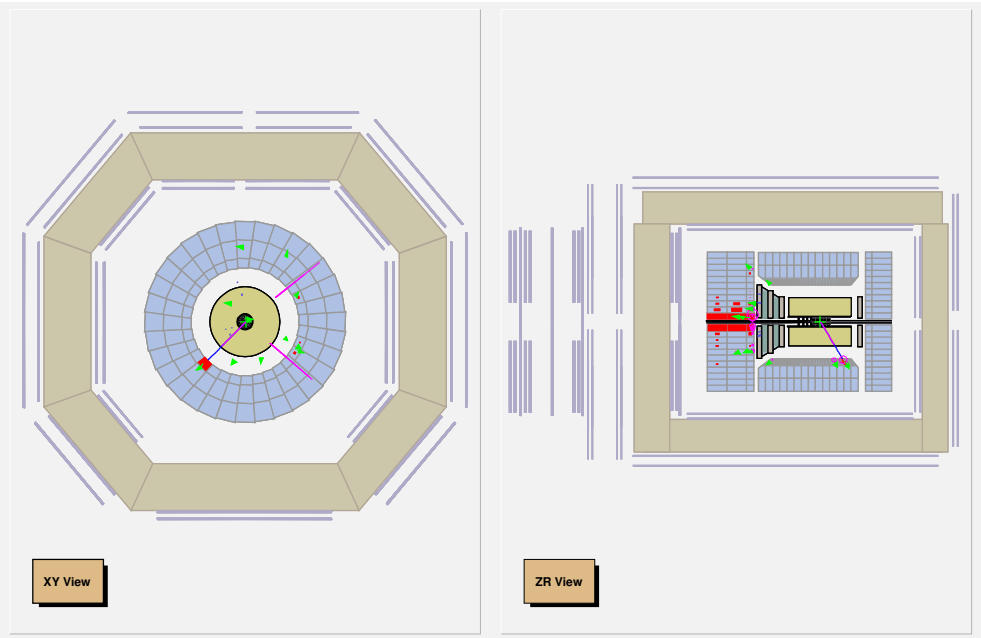

Figure 6.21: An example of DIS NC event removed from the CC sample. The transverse momentum of this event is $P_T = 13.5$ GeV.

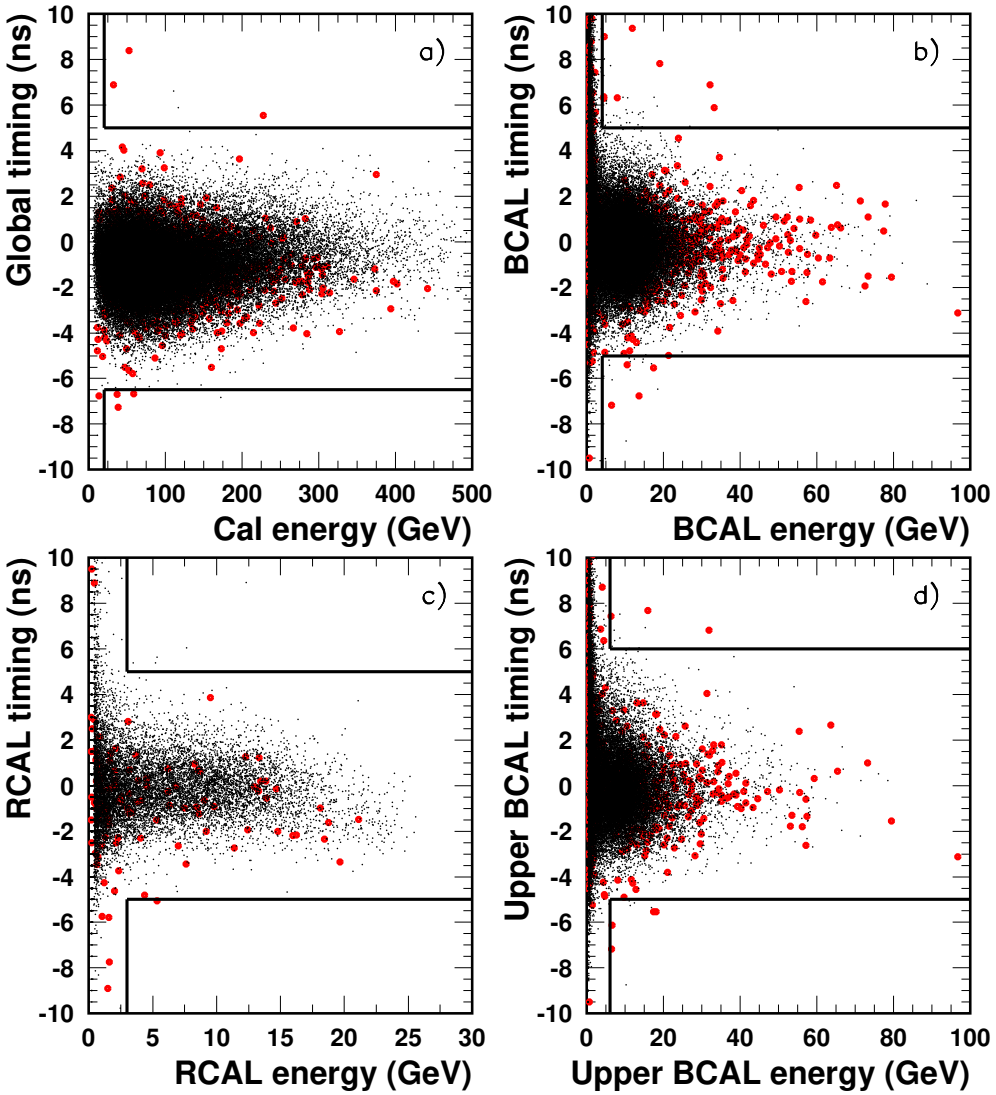

Figure 6.22: The global calorimeter timing versus the calorimeter energy (a), the BCAL timing versus the BCAL total energy (b), the RCAL timing versus the RCAL total energy (c), and the timing of the upper part of BCAL versus the total energy of the upper half of BCAL (d). In these figures, the tiny dots stand for NC events in the data and the larger filled circles stand for the data CC events. The cuts are represented by the horizontal/ vertical lines.

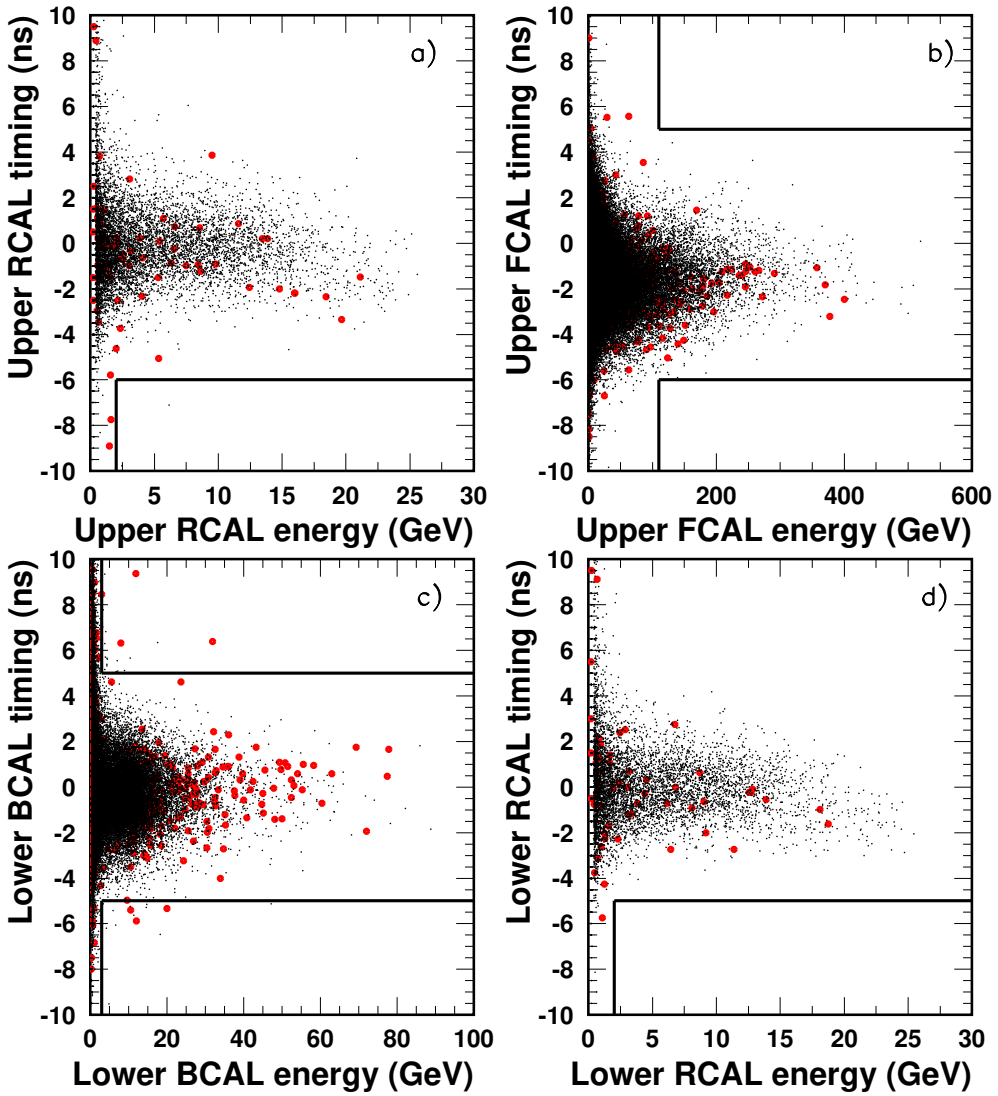

Figure 6.23: The timing of the upper RCAL versus the total RCAL energy (a), the upper half FCAL timing versus the total energy in the upper half of FCAL (b), the timing of the lower BCAL half versus the total energy in the lower half of BCAL (c), and the timing of the lower half of RCAL versus the total energy of the lower half of RCAL (d). In these figures, the tiny dots stand for the NC events in the data while the filled larger circles stand for the data CC events. The cuts are represented by the horizontal/ vertical lines.

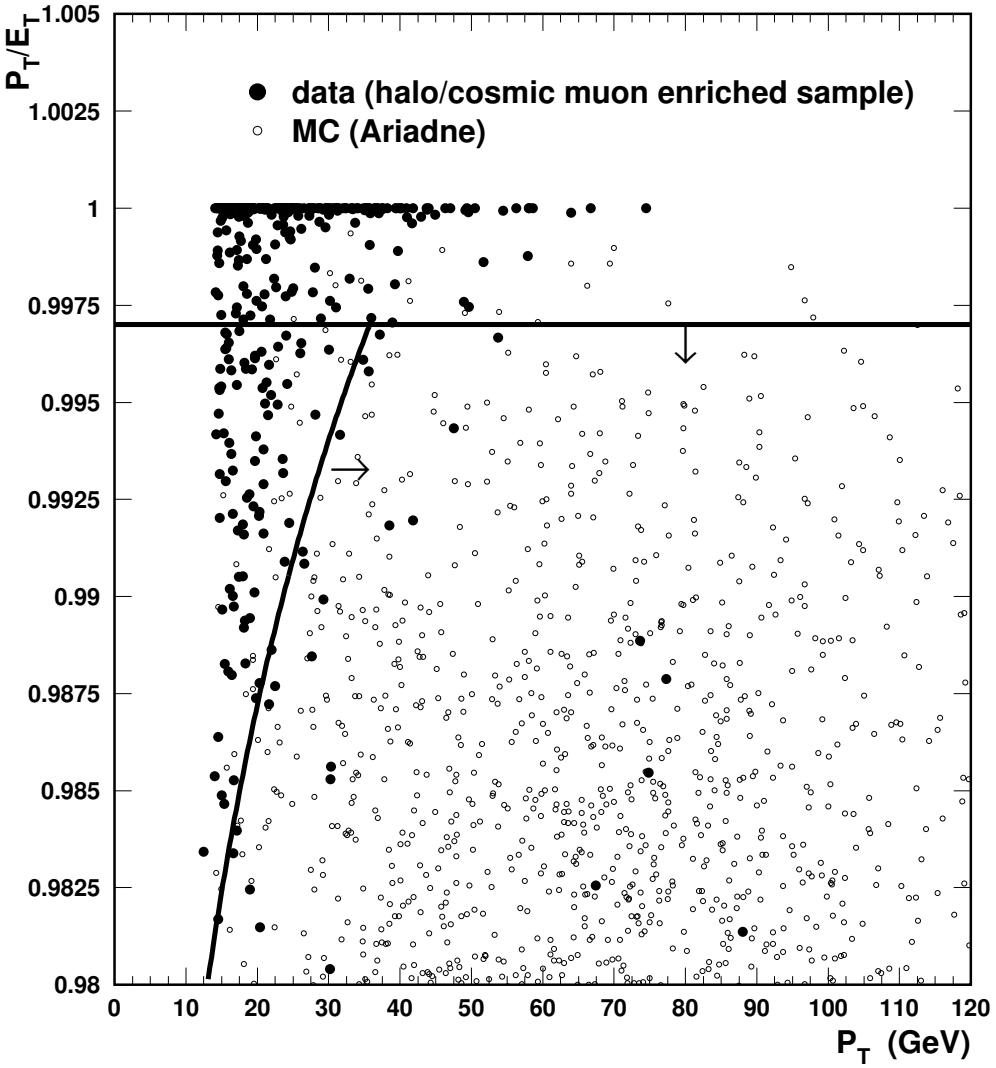

Figure 6.24: The P_T/E_T versus P_T for the data (filled circles) and MC (open circles) samples enriched with cosmic and halo muon background events. For the curves description, see the text.

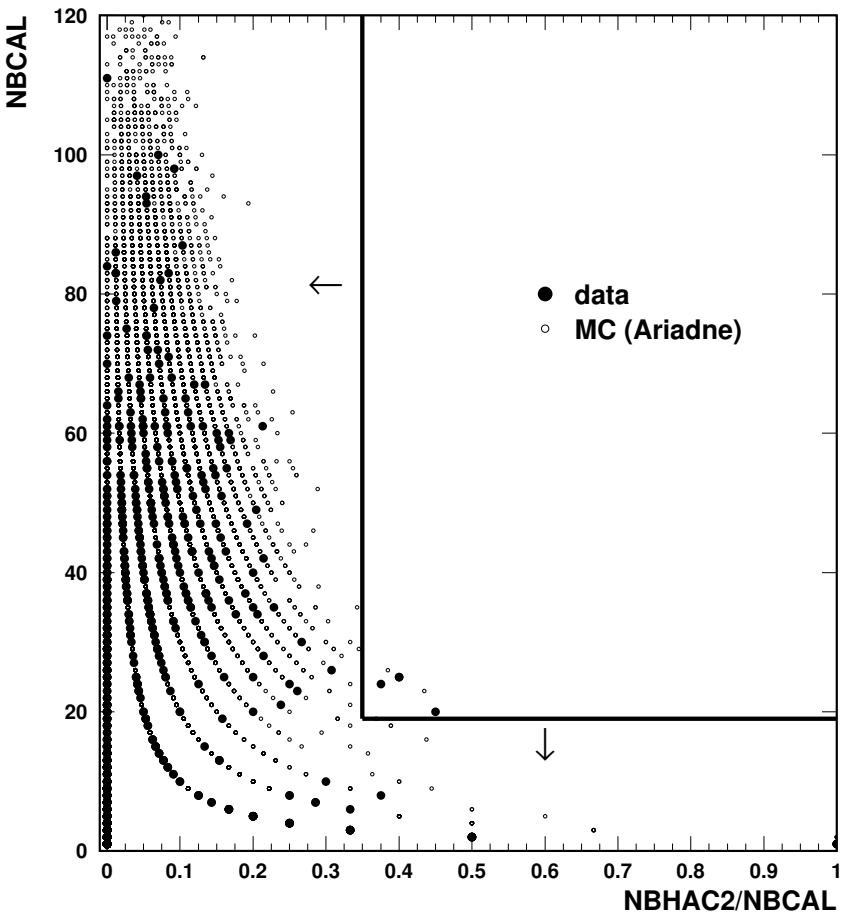

Figure 6.25: The number of BCAL energy deposits versus the fraction of the number of energy deposits in BHAC2 to the total BCAL ones for data and MC expectations. The accepted events are in region to the left of the vertical line or below the horizontal line.

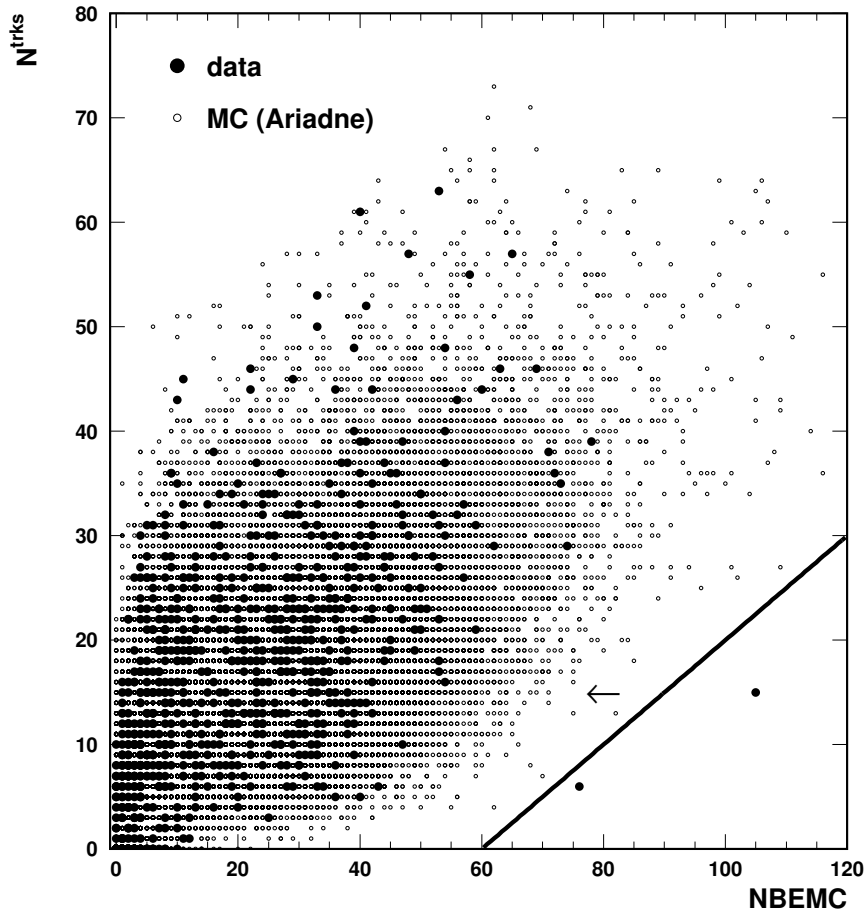

Figure 6.26: The number of tracks, N^{trks}, versus the number of EMC cells above noise in the BCAL in the data and the MC expectations. The part of the figure to the left of the line denotes the accepted region of events.

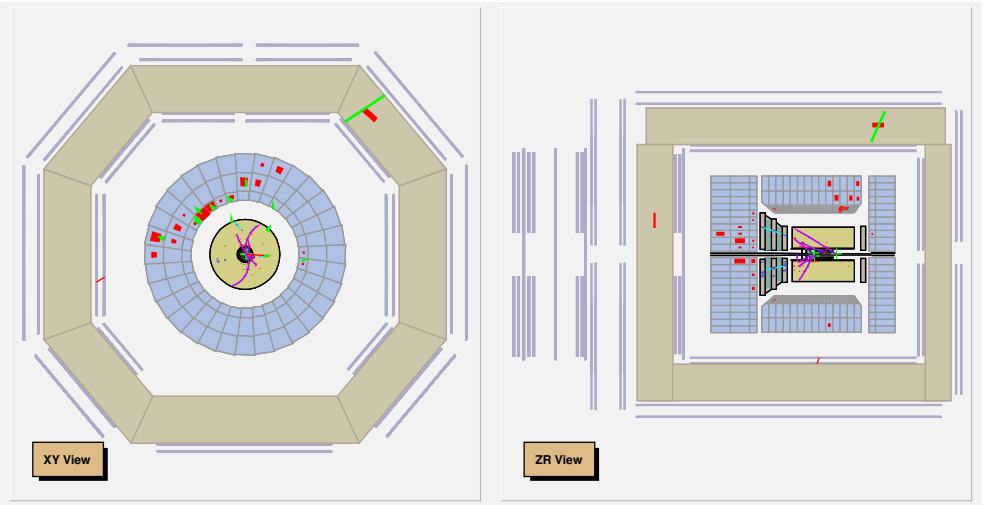

Figure 6.27: An example of an event removed from the final sample after visual scanning.

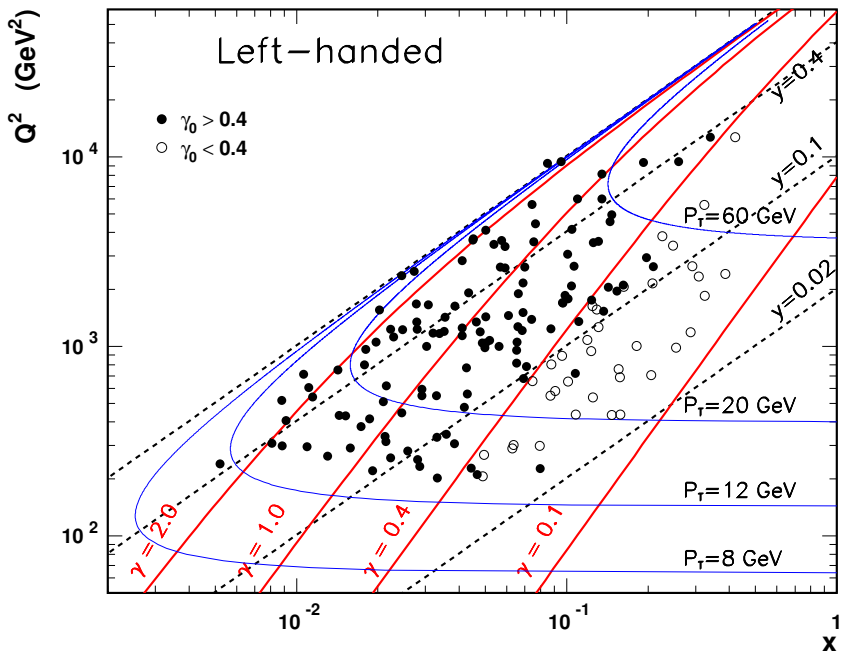

Figure 6.28: The kinematic phase-space in the Q^2-x plane for the LH final sample. The closed circles are the high-γ_0 events and the open ones are the low-γ_0.

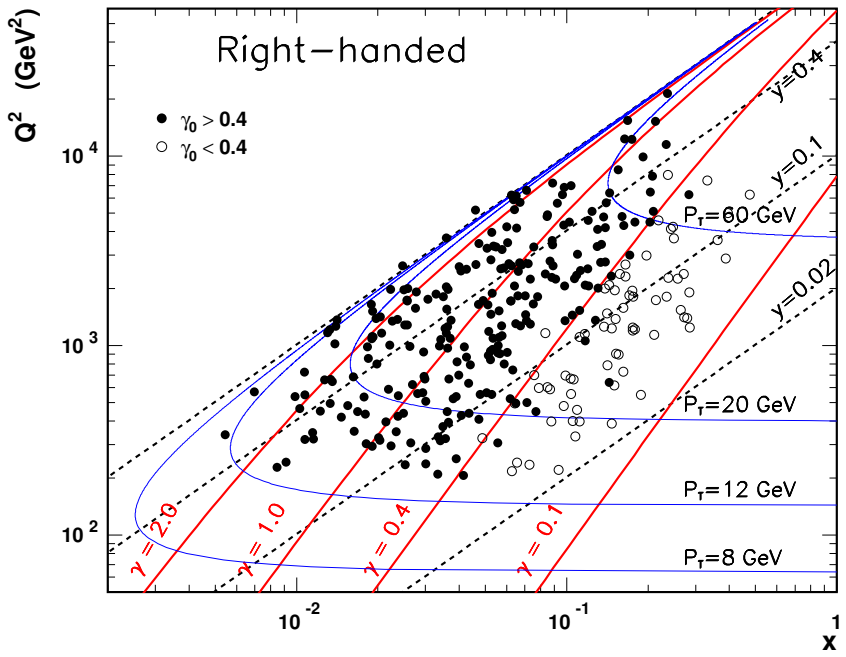

Figure 6.29: The kinematic phase-space in the Q^2-x plane for the RH final sample. The closed circles are the high-γ_0 events and the open ones are the low-γ_0.

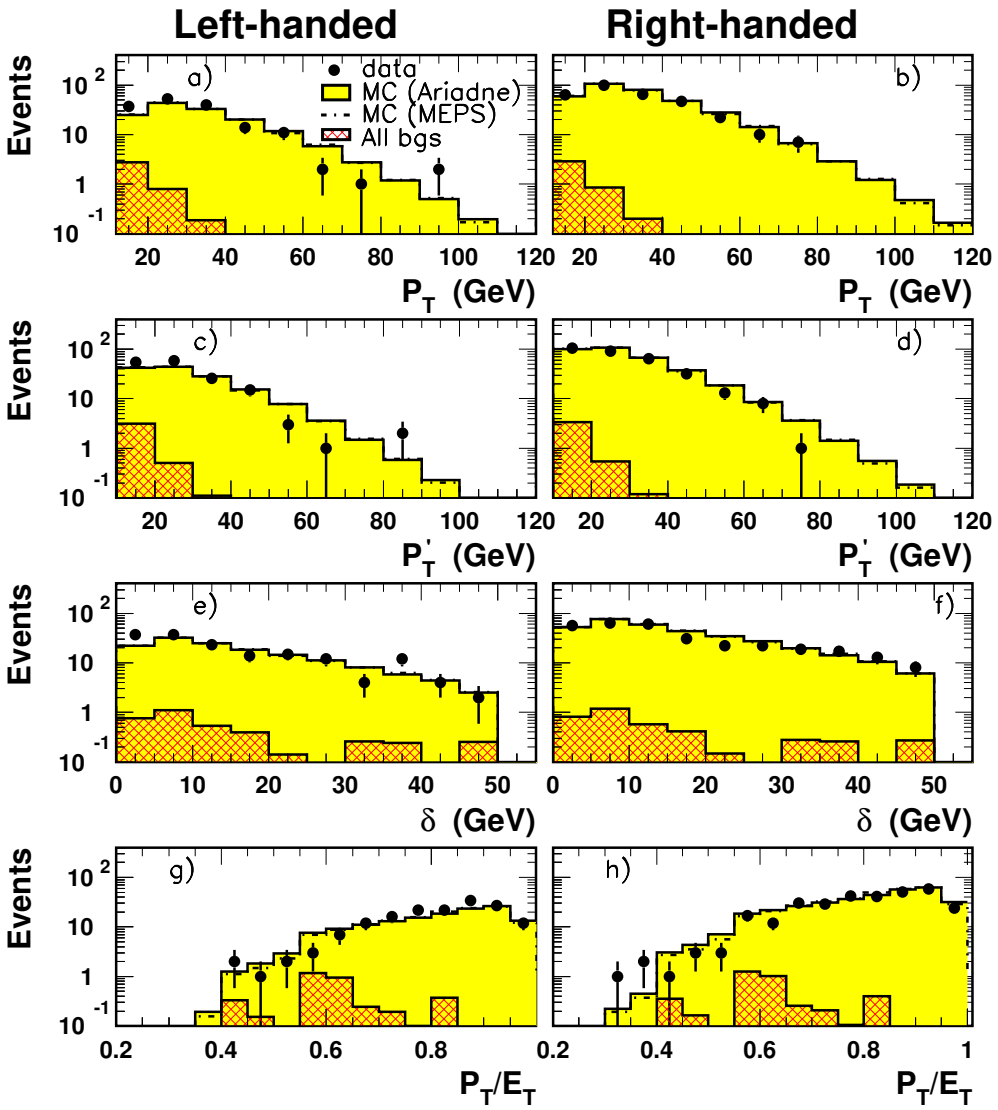

Figure 6.30: Shown are the distributions of P_T (a and b), P_T' (c and d), δ (e and f), and P_T/E_T (g and h), for the LH and RH samples as denoted in the figures. The full points stand for the CC data and the filled (dotted) histograms represent the MC expectations as obtained with ARIADNE (MEPS). The contributions from all background processes are shown as the filled dashed histograms.

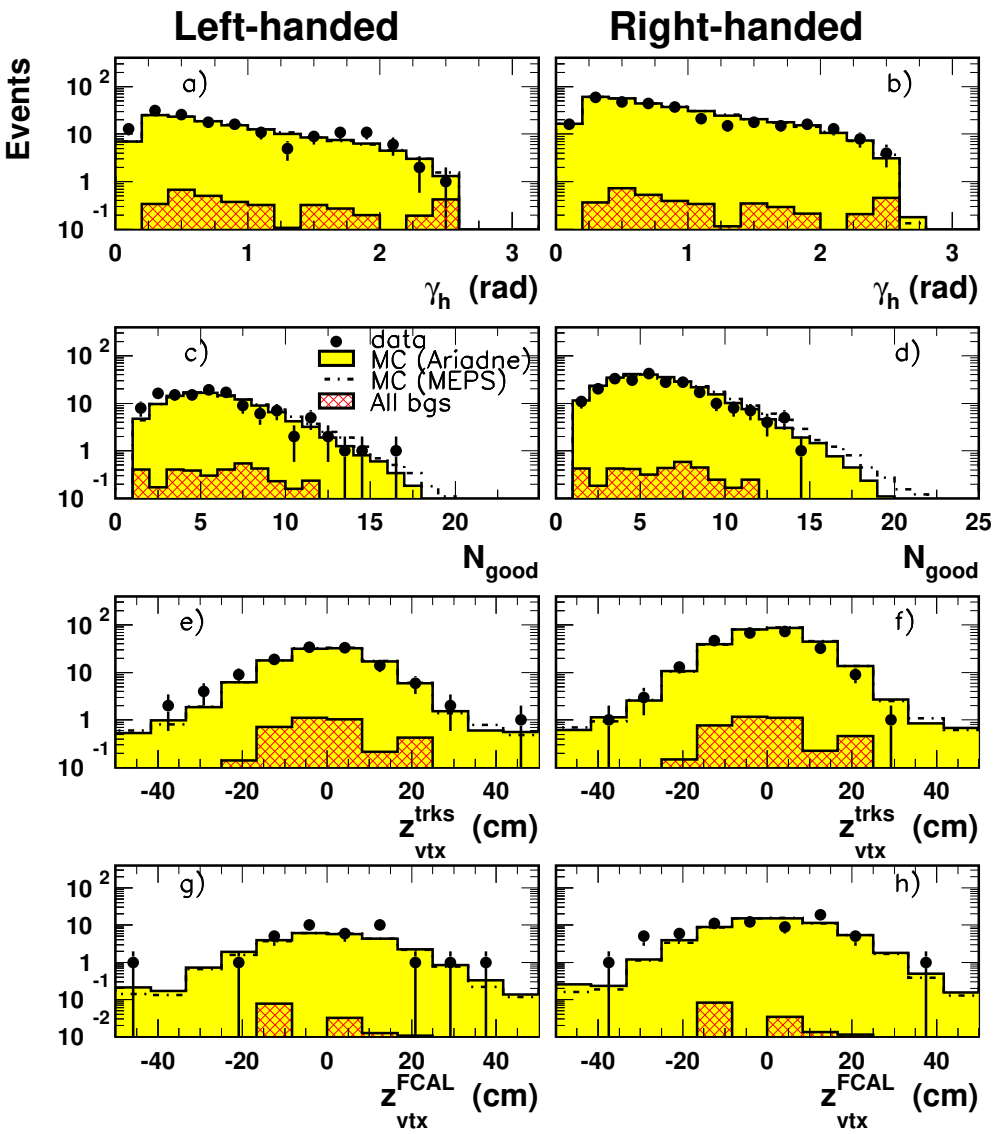

Figure 6.31: Shown are the distributions of γ_h (a and b), N_{good} (c and d), z_{vtx}^{trks} (e and f), and z_{vtx}^{FCAL} (g and h), for the LH and RH samples as denoted in the figures. The full points stand for the CC data and the filled (dotted) histograms represent the MC expectations as obtained with ARIADNE (MEPS). The contributions from all background processes are shown as the filled dashed histograms.

Chapter 7

Cross section

The CC cross section as a function of Q^2, x and y were measured using the events which passed the selection cuts described in chapter 6. In this chapter, the differential and total cross sections are presented for both LH and RH samples.

7.1 Binning definitions

The binning was the same as the one used for the data of HERA I [29]. For $d\sigma/dQ^2$ measurements, nine bins were considered between the $Q^2 = 200$ GeV^2 and $Q^2 = 60000$ GeV^2. For $d\sigma/dx$ measurements, seven bins were chosen from 0.01 to 1., and for $d\sigma/dy$ seven bins were taken, starting from 0 to 0.9. These bins are presented in the Tables 9.5-9.8.

7.2 Acceptance, purity and efficiency

The number of events reconstructed in each bin in Q^2, x and y has to be corrected for the detector acceptance. The acceptance, $\mathcal{A}$, efficiency, ε, and purity, $\mathcal{P}$ are defined as follows

$$\mathcal{A} \equiv \frac{N_1^i + N_3^i}{N_1^i + N_2^i}, \tag{7.1}$$

$$\varepsilon \equiv \frac{N_1^i}{N_1^i + N_2^i}, \tag{7.2}$$

$$\mathcal{P} \equiv \frac{N_1^i}{N_1^i + N_3^i}, \tag{7.3}$$

where

- $N_1^i \equiv$ The number of events generated and reconstructed in bin i.
- $N_2^i \equiv$ The number of events generated in bin i but not reconstructed in it.
- $N_3^i \equiv$ The number of events generated outside of bin i, but reconstructed in bin i.

The number of events reconstructed in a bin is the total number of events that pass the whole selection cuts described in chapter 6, and are binned according to the measured Q^2, x and y values. The number of events generated in a bin is the number of MC events which were generated in the specific kinematical region and binned according to the generated hadronic values of Q^2, x and y.

The quantities, N_1^i, N_2^i, and N_3^i are independent and therefore the statistical uncertainties in the acceptance, efficiency, and purity are given by:

$$\Delta\mathcal{A} = \frac{1}{(N_1^i + N_2^i)^2} \sqrt{((N_2^i - N_3^i)\sigma_{N_1^i})^2 + ((N_1^i + N_3^i)\sigma_{N_2^i})^2 + ((N_1^i + N_2^i)\sigma_{N_3^i})^2}\,, \tag{7.4}$$

$$\Delta\varepsilon = \frac{1}{(N_1^i + N_2^i)^2}\sqrt{(N_2^i\sigma_{N_1^i})^2 + (N_1^i\sigma_{N_2^i})^2}\,, \tag{7.5}$$

$$\Delta\mathcal{P} = \frac{1}{(N_3^i + N_1^i)^2}\sqrt{(N_1^i\sigma_{N_3^i})^2 + (N_1^i\sigma_{N_3^i})^2}\,, \tag{7.6}$$

where $\sigma_{N_{1,2,3}^i}$ stands for the statistical uncertainty of N_1^i, N_2^i, and N_3^i, respectively.

The acceptance reflects the detector geometrical acceptance. Higher acceptance in a bin will give rise to a small correction to the measured cross section and the systematic uncertainty from MC simulation is expected to be small. The efficiency and purity in a bin characterise the effect of migration and the resolution of a kinematical variable. The efficiency measures the fraction of events generated in a bin that are also measured in the same bin. Higher values of efficiency in a bin mean that the migration in that bin are small, and that the selection cuts are not rejecting a high percentage of events in that bin. High purity means that a small number of events measured in the bin come from neighbouring bins.

Fig. 7.1 shows the efficiency, purity and acceptance versus Q^2 for both LH and RH samples. The purity is more than 60% except at the highest Q^2

bin. This is due to the steep fall-off of the cross section in the high Q^2 region, resulting a migration of events from lower Q^2 regions. The acceptance increases with Q^2 and becomes flatter at high values of Q^2. The small difference between the LH and RH efficiency, purity, and acceptance values are due to the differences in the trigger requirements which were slightly changed during the data taking. Fig. 7.2 shows the efficiency, purity and acceptance versus x for both LH and RH. The acceptance in x is relatively small at low and high x because it is rare to find events with low x (restriction on the kinematic phase-space), while at high x, the acceptance is small due to tight selection cuts in the low γ_0 sample. Similar plots are shown in Fig. 7.3 for y. Also here, the acceptance at low y values i.e. low γ_0 is relatively small due to the tight cuts.

7.3 Cross section measurement

The measured cross section is given by

$$\sigma_{meas}^{data} = \frac{N_{meas}^{data} - N_{meas}^{bkg}}{\mathcal{L}\mathcal{A}}\,, \tag{7.7}$$

where N_{meas}^{data} is the number of data events found in the bin, N_{meas}^{bkg} is the number of expected background events, $\mathcal{L}$ is the integrated luminosity and $\mathcal{A}$ is the acceptance. The Born cross section is defined as follows

$$\sigma_{Born}^{data} = \mathcal{C}_{rad} \cdot \sigma_{meas}^{data}\,, \tag{7.8}$$

where $\mathcal{C}_{rad}$ is the radiative correction factor, which is given by

$$\mathcal{C}_{rad} = \frac{\sigma_{Born}^{theory}}{\sigma_{RAD}^{theory}}\,, \tag{7.9}$$

where σ_{Born}^{theory} is the Born cross section as given from the theoretical calculations, and σ_{meas}^{MC} is the corresponding cross section modified by radiative effects. When we combine the above relations we find that the total cross section at the Born level can be expressed as

$$\sigma_{Born}^{data} = \frac{N_{meas}^{data} - N_{meas}^{bkg}}{N_{meas}^{MC}} \cdot \sigma_{Born}^{theory}\,, \tag{7.10}$$

where N_{meas}^{MC} is the number of MC events reweighted to the integrated luminosity. In order to extract the differential cross section, a bin centre correction

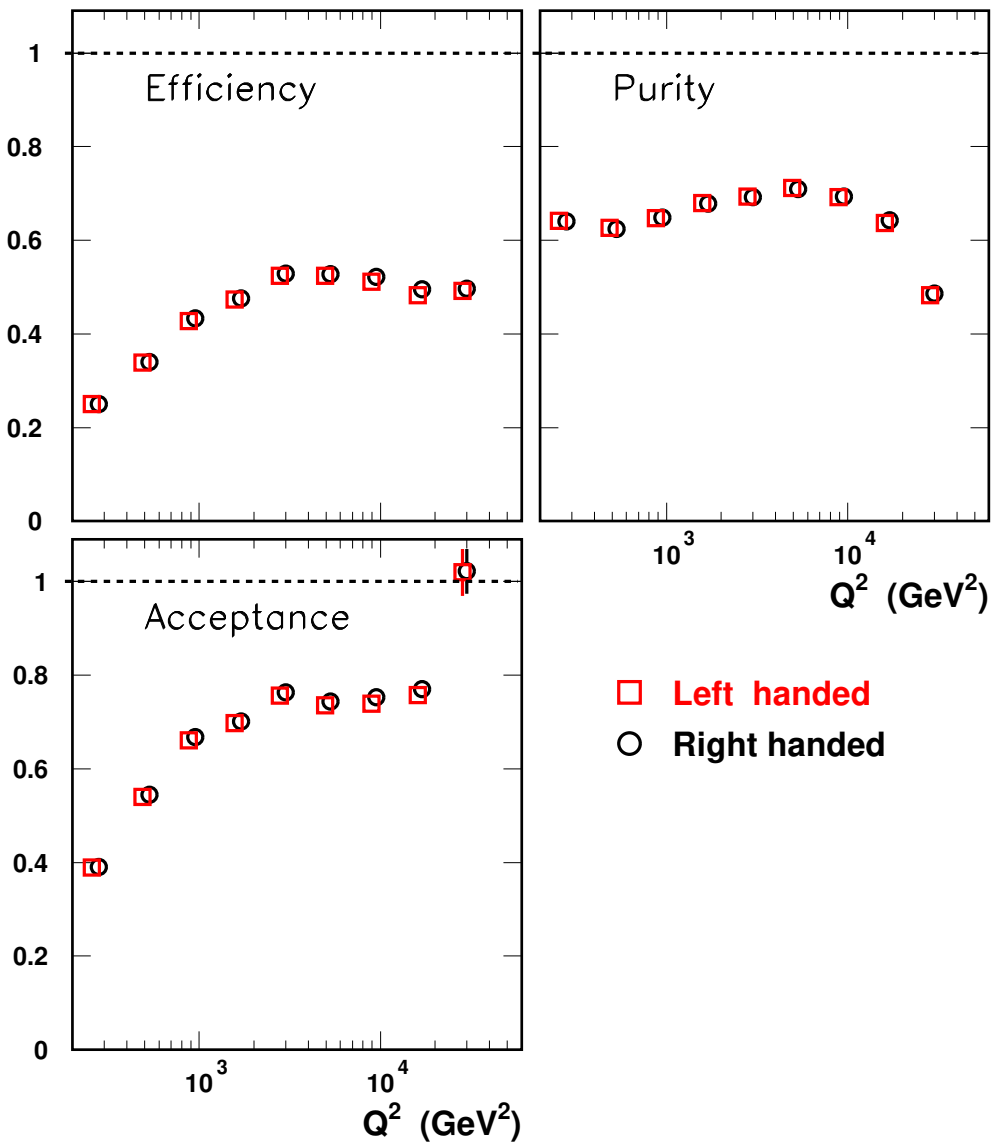

Figure 7.1: The efficiency, purity and the acceptance as a function of Q^2 for LH (open squares) and RH (open circles) samples.

factor, $\mathcal{C}_{bin}$, is defined to convert the cross section integrated over a bin into a differential cross section quoted at a particular point,

$$\mathcal{C}_{bin} = \frac{\left(\frac{d\sigma^{theory}_{Born}}{dQ^2}\right)\Big|_{Q^2_0}}{\sigma^{theory}_{Born}}. \tag{7.11}$$

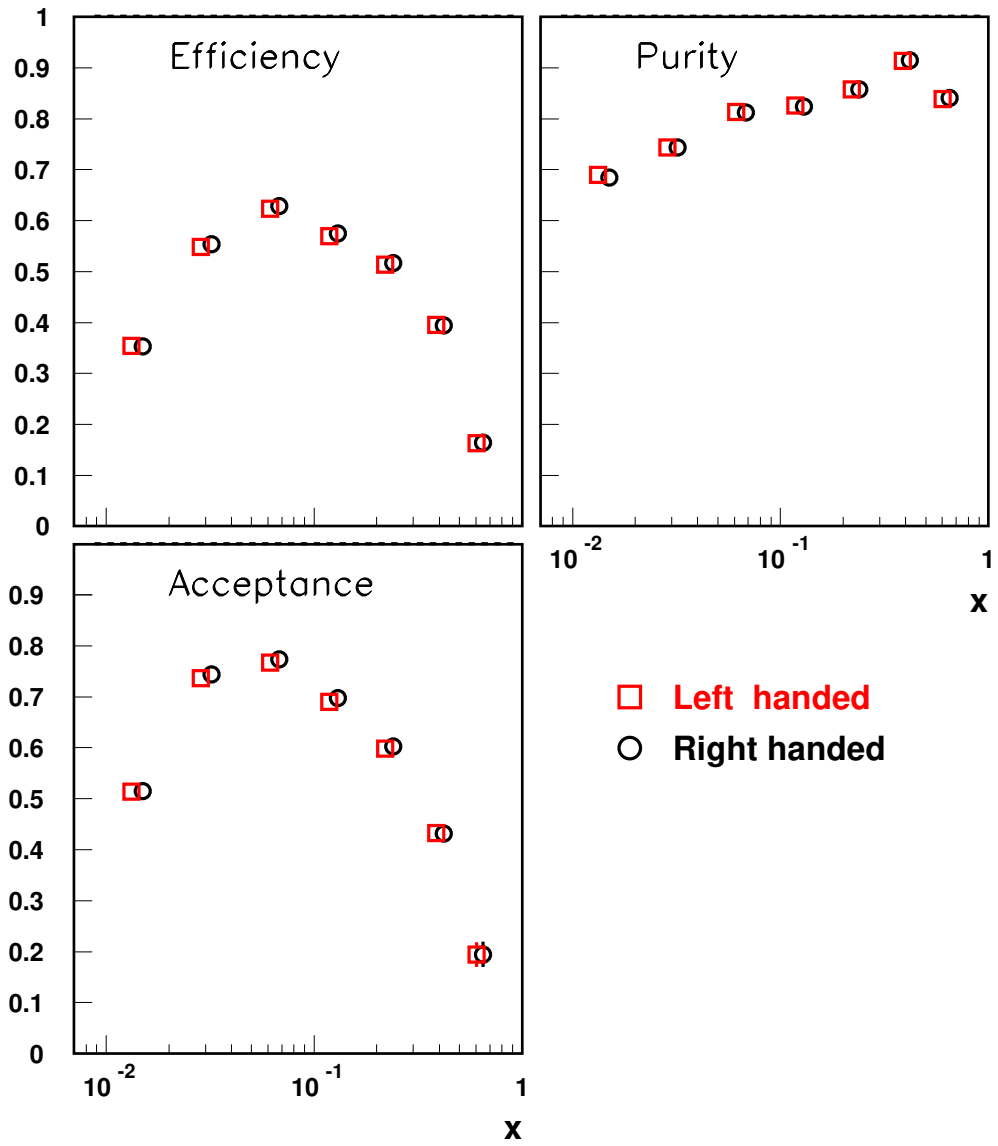

Figure 7.2: The efficiency, purity and the acceptance as a function of x for LH (open squares) and RH (open circles) samples.

For example, the differential Born cross section at a particular value of Q^2 in a bin is given by

$$\left.\frac{d\sigma^{data}_{Born}}{dQ^2}\right|_{Q^2_0} = \frac{N^{data}_{meas} - N^{bkg}_{meas}}{N^{MC}_{meas}} \cdot \left.\frac{d\sigma^{theory}_{Born}}{dQ^2}\right|_{Q^2_0}, \tag{7.12}$$

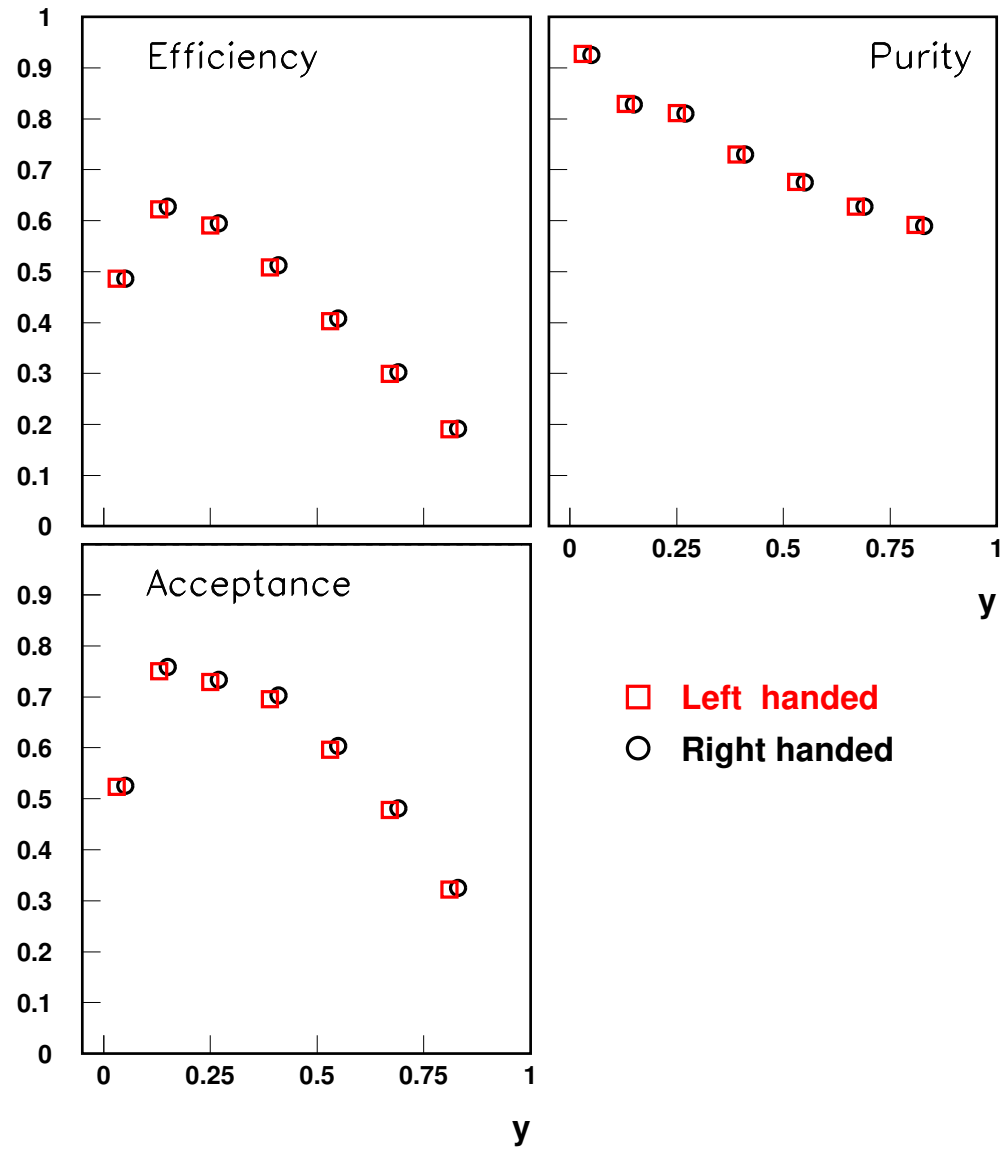

Figure 7.3: The efficiency, purity and the acceptance as a function of y for LH (open squares) and RH (open circles) samples.

where Q_0^2 is some point in the Q^2 bin in which data and MC events are counted. The total statistical error of the cross section has two contributions, one from the number of data events and another, usually smaller, from MC statistics. The statistical error assigned to the number of data events is $\sqrt{N_{meas}^{data}}$ for bins with at least 12 events. For bins with smaller number of events, a 67% confidence interval is calculated using the Poisson statistics,

and the boundaries of this confidence interval are taken as the statistical uncertainty. The total number of MC events which enter in the cross section calculations is the sum of the weights of all events, i.e. $N^{MC}_{meas} = \sum_i \omega_i$, and their statistical error is $\sqrt{\sum_i \omega_i^2}$. Thus, the total statistical error on the cross section can be expressed as

$$\Delta(\frac{d\sigma^{data}_{Born}}{dQ^2}) = (1+P)\cdot$$
$$\sqrt{(\frac{\Delta N^{data}_{meas}}{N^{MC}_{meas}})^2 + (\frac{\Delta N^{bkg}_{meas}}{N^{MC}_{meas}})^2 + (\frac{\Delta N^{MC}_{meas}(N^{data}_{meas}-N^{bkg}_{meas})}{(N^{MC}_{meas})^2})^2} \cdot \frac{d\sigma^{theory}_{Born}}{dQ^2}\,, \qquad (7.13)$$

where ΔN^{data}_{meas}, ΔN^{bkg}_{meas} and ΔN^{MC}_{meas} are the statistical uncertainty from the number of data events, background MC events, and signal MC events, respectively, P is the degree of the longitudinal polarisation. The main contribution to the statistical errors in this analysis is due to the number of data events.

Chapter 8

Systematic uncertainties

The systematic uncertainties were estimated by varying the thresholds of selection cuts or changing the analysis details such as using different MC simulation or using different PDF parameterisations. The nominal cross section (σ_0) is defined as the cross section obtained with the nominal selection cuts described in chapter 6. While varying the thresholds or the analysis details, we repeat the analysis and obtain cross section (σ_i), where i stands for a particular systematic check. The values of σ_i may be slightly different from the nominal cross section. For each check i, we calculate $\Delta_i = \sigma_i - \sigma_0$. The total positive (negative) systematic uncertainty ($\delta^{+(-)}$) is obtained as $\delta^{+(-)} = \sqrt{\sum_i (\Delta_i)^2}$, where the sum runs over all positive (negative) contributions.

8.1 Threshold variation

The thresholds of the selection cuts were varied to examine the stability of the cross section measurements. The selection thresholds for a given cut were varied by an amount comparable with the resolution of the variable. Moreover, the thresholds were varied by such an amount that the efficiency remained good and the background contamination was not significantly increased. Most of the threshold variations change the cross section up to a few percent, except for some few bins where the changes exceed $10 - 20\%$. Typically, the thresholds of the selection cuts were varied up and down by $\pm 10\%$. Their influence can be significant if the MC does not behave like the data around the region of the cut. The uncertainty on the cross section was obtained by determining the cross section with the modified selection cuts and then subtracting the nominal cross section. The systematic uncertainties are graphically presented in appendix A (Fig. A.1-Fig. A.12). These figures show the variation (in percentage) of the differential cross sections for LH

and RH samples. The thresholds for both high and low γ_0 selection cuts were varied independently.

8.2 Energy scale uncertainty

An important systematic uncertainty is due to the energy scale of the calorimeter. The energy scale has a direct effect on the reconstruction of the event kinematic variables and therefore, biases on the cross section can be observed. This effect can be relatively large at high Q^2 due to the steeply falling of the cross section.

Detailed studies [29] on the calorimeter energy scale have been done at ZEUS. The energy scale and the associated systematic uncertainty of the energy scale were determined, using the DIS NC sample by comparing the hadronic transverse momentum, $P_{T,h}$, to $P_{T,DA}$, and $P_{T,e}$, where $P_{T,DA} = \sqrt{Q^2_{DA}(1-y_{DA})}$ is the transverse momentum calculated within the double angle method and $P_{T,e}$ is the transverse momentum of the scattered electron. The difference between the real detector response and the simulation can be extracted from the comparison between the ratio of $P_{T,DA}$ and $P_{T,h}$, between data and MC.

The uncertainty in the hadronic energy scale was determined to be 2% for the RCAL and 1% in both FCAL and BCAL [29]. The following checks on the calorimeter energy uncertainty were implemented to obtain the systematic uncertainty in the cross section

- varying the energy scale of the calorimeter sections by 2% for the RCAL and 1% for both FCAL and BCAL [29]. This induces small shifts of the Jacquet-Blondel estimators of the kinematic variables. The variation of the energy scale, up and down by these amounts, of each calorimeter section gives systematic uncertainty on the total measured energy.

- the effect of the energy scale on the measurement of γ_h was obtained by increasing (decreasing) the FCAL and RCAL energy scales together while the BCAL energy scale was decreased (increased).

- the cross section sensitivity depends on the fraction of the energy deposits in the EMC and HAC sections. The sensitivity was determined by increasing the energy measured in the EMC section of the calorimeter by 2% and decreasing the energy measured in the HAC section by 2%, and vice-versa. These checks were done separately for each calorimeter section.

check number	description
1	RHAC +2%, BHAC +1%, FHAC +1%
2	RHAC −2%, BHAC −1%, FHAC −1%
3	RHAC +2%, BHAC −1%, FHAC +1%
4	RHAC −2%, BHAC +1%, FHAC −1%
5	RHAC −2%, REMC +2%
6	RHAC +2%, REMC −2%
7	BHAC −2%, BEMC +2%
8	BHAC +2%, BEMC −2%
9	FHAC −2%, FEMC +2%
10	FHAC +2%, FEMC −2%

Table 8.1: Summary of the description of the energy scale checks implemented in this analysis.

In total, by varying the calibration in different parts of the calorimeters independently, 10 checks were implemented as listed in Table 8.1. The results are shown in Figs. A.13-A.18 in appendix A.

8.3 Parton shower scheme

As mentioned in sec 4.1, the nominal MC simulation used in this study was chosen as the one generated with the colour dipole model, CDM, as implemented in the ARIADNE program. The matrix element parton shower (MEPS) model as implemented in the LEPTO program is an alternative model to simulate the QCD cascade. These two models describe well the high-Q^2 DIS data [98].

In Fig. A.19, in appendix A, the systematic contributions to the differential cross section due to the use of the MEPS MC instead of ARIADNE are presented. The changes in the integrated cross sections are negligible (below 1%). The $d\sigma/dx$ measurement is affected by at most 3%, while in $d\sigma/dy$ and $d\sigma/dQ^2$ the uncertainty may rise to 5%.

8.4 Photoproduction subtraction

The uncertainties in the normalisation or shapes of the direct and resolved PHP contribution can bias the cross section measurements. The PHP background is expected mainly at low values of P_T. Since the threshold cuts are

tighter for events with $\gamma_0 < 0.4$ rad than those with $\gamma_0 > 0.4$ rad, we do not expect a significant PHP contribution for the low γ_0 sample. Here we concentrate on the PHP contribution for high γ_0 events. In Fig. A.20 we show the P_T/E_T distributions for LH and RH samples where only events with $P_T < 20$ GeV and $\gamma_0 > 0.4$ rad are selected. In addition, the P_T/E_T selection cut was removed to enrich the PHP sample.

The uncertainty in the normalisation of the direct and resolved PHP events was obtained by a χ^2 fit to the total P_T/E_T distribution with the following function:

$$N_{MC} = \alpha(\beta r^i_{Dir} + (1-\beta) r^i_{Res}) + N_{CC} + N_{others} \tag{8.1}$$

where

- r^i_{Dir} is the fraction of direct PHP events in bin i from the total direct PHP sample, $r^i_{Dir} = N^i_{Dir} / \sum_i N^i_{Dir}$,
- r^i_{Res} is the fraction of resolved PHP events in bin i from the total resolved PHP sample, $r^i_{Res} = N^i_{Res} / \sum_i N^i_{Res}$,
- α is the sum of all PHP events ($\sum_i (N^i_{Dir} + N^i_{Res})$),
- β is the fraction of direct PHP events of the total number of PHP events,
- N_{CC} is the number of MC CC events,
- N_{others} is the sum of MC events from other background processes (NC, W-production, and di-lepton production).

The fit parameters, α and β, are extracted by minimising the χ^2 function

$$\chi^2 = \sum_i \frac{(N^i_{data} - N^i_{MC})^2}{(\delta N^i_{data})^2 + (\delta N^i_{MC})^2} \,, \tag{8.2}$$

where N^i_{data} is the number of data events in bin i, and N^i_{MC} is the sum of the number of events from MC CC and all background MC events in the same bin. δN^i_{data} (δN^i_{MC}) stands for the statistical error on N^i_{data} (N^i_{MC}).

The χ^2 function in eq. (8.2) contains two parameters and we propose to find the parameters in the following way: First, a fit was performed to determine α assuming a fixed value for β ($\beta = 0.84$). The fit was done in the full $0 < P_T/E_T \leq 1$ range. The results of the fits for α parameter in the LH and RH are shown in Fig. A.20 (c) and (d), respectively. The expected number of PHP (direct and resolved) events is 18.8 ± 5.4 and 25.5 ± 7.0 for

sample	free parameter	α	β	χ^2/ndf
LH	α	18.8 ± 5.4	0.841	0.85
LH	β	18.8	1.5 ± 1.0	0.82
RH	α	25.5 ± 7.0	0.841	1.75
RH	β	25.5	1.5 ± 0.5	2.35

Table 8.2: The results of the fits to the P_T/E_T distributions for LH and RH samples.

LH and RH, respectively. When we fix α to these values and let β free and minimise χ^2 then we obtain the results which are given in Fig. A.20, for LH and RH. The fit results are summarised in Table 8.2.

The fit leads to a 30% uncertainty in α (see Fig. A.20) for both LH and RH samples. The uncertainties in the cross sections, due to α, were obtained by changing the value of α by $\pm 30\%$. The fit leads to $\sim$ 70% ($\sim$ 30%) uncertainty in β for the LH (RH) sample. The β uncertainties are translated into cross sections uncertainties by

$$\delta^{\pm} = \alpha \left[\pm \Delta\beta \frac{r^i_{Dir}}{\sum r^i_{Dir}} \pm \Delta\beta \frac{r^i_{res}}{\sum^i_{res}} \right] . \tag{8.3}$$

The systematic uncertainties are typically less than 1% except for the first bin in Q^2, where $\sim$ 2% ($\sim$ 1.5%) difference in the cross sections were found in the LH (RH) sample. The total cross sections are not sensitive to the variation of β and therefore the quoted systematic error due to varying β is zero. The systematic uncertainties due to varying α were found as $\pm 0.5\%$ for the LH sample and $\pm 0.23\%$ for the RH sample.

8.5 Energy leakage

To measure the kinematic variables with high accuracy, the hadronic final state should be fully contained within the CAL. Events with an energy leakage from the CAL to the backing calorimeter, (BAC), have been observed in the ZEUS detector. It was found that 4% of the accepted events have a measurable energy leakage in the BAC. The average energy fraction in the BAC is 5%. The fraction of events with leakage and the average amount of leakage were well modelled by the MC simulation and therefore had no effect on the cross section measurements [94].

8.6 Parton distribution functions

The PDFs are essential ingredients for calculating the cross sections in the MC generators. They influence the distribution of events in the x, Q^2 plane as well as the hadronic final state. The PDFs can be given by several parameterisations. The MC events used in unfolding the cross section were generated with the CTEQ5D PDFs. Alternatively, the ZEUS-S NLO QCD PDFs, obtained by fitting the NC ZEUS data [1], were used. The difference between the cross section assuming CTEQ5D and assuming ZEUS-S was treated as a systematic uncertainty. In the total cross sections, for LH and RH, the effect is below 1% and well within the statistical fluctuations. Few percent effects are observed in the differential cross sections at the low Q^2, low x , and high y regions, as shown in Fig. A.21.

8.7 NLO QCD corrections

The DJANGOH program calculates the CC cross section in leading order (LO) in QCD, i.e. $F_L = 0$ and with LO xF_3. The contribution of F_L becomes non-negligible at higher values of y and may exceed 10% [99]. This implies a change in the y distribution of events in the MC. If the MC events are reweighted to fit the cross section calculated with NLO corrections, the extracted cross section in the data changes by 2% in the highest y bin as shown in Fig. A.22. The total cross section is not affected.

8.8 Luminosity uncertainty

During the 2003-2004 run period, the systematic uncertainty quoted for the luminosity measurement is

$$\left(\frac{\Delta\mathcal{L}}{\mathcal{L}}\right)_{sys} = 5\%\,, \tag{8.4}$$

and it affects the uncertainty in the normalisation of the cross sections. In the analysis presented here this uncertainty is included in the systematic error.

[1] Note that no CC data is included in the fit

8.9 Summary

The list of all checks is presented in Table 8.3. The corresponding systematic uncertainties in the differential cross section measurements, $d\sigma/dQ^2$, $d\sigma/dx$, and $d\sigma/dy$ are presented graphically in Figs. A.1-A.12 and summarised in Tables A.1-A.3.

The systematic uncertainty in the LH and RH $d\sigma/dQ^2$ are presented in Table A.4 and Table A.5, respectively, and the systematic contributions for $d\sigma/dx$ and $d\sigma/dy$ are presented in Tables A.6-A.9, respectively. The sum of all systematical uncertainties, added in quadrature, are given at the bottom of the tables.

The systematic uncertainties to the LH and RH total cross sections are presented in Table A.10. The largest contribution is due to the luminosity uncertainty. The total systematic uncertainties are given at the bottom of the table.

In Fig. A.23, the total systematic uncertainties for $d\sigma/dQ^2$, $d\sigma/dx$, and $d\sigma/dy$ are compared to the statistical errors in the differential cross sections. The statistical errors are larger than the systematic ones except in the lowest x bin of the RH sample.

Index	description
1	nominal
2	$P_T > 13.2$ GeV
3	$P_T > 10.8$ GeV
4	$P'_T > 11$ GeV
5	$P'_T > 9$ GeV
6	$z_{vtx}^{CTD} < 55$
7	$z_{vtx}^{CTD} < 45$
8	$P_T/E_T > 0.44$ for $20 < P_T < 30$ GeV
9	$P_T/E_T > 0.36$ for $20 < P_T < 30$ GeV
10	$P_T/E_T > 0.605$ for $P_T < 20$ GeV
11	$P_T/E_T > 0.495$ for $P_T < 20$ GeV
12	P_T box $22 - 33$
13	P_T box $18 - 27$
14	$N_{good} > 0.2(N^{trks} - 20)$
15	$N_{good} > 0.3(N^{trks} - 20)$
16	$N_{good} > 0.25(N^{trks} - 22)$
17	$N_{good} > 0.25(N^{trks} - 18)$
18	$\Delta\phi < 2.2$ rad if $P_T > 30$ GeV
19	$\Delta\phi < 1.8$ rad if $P_T > 30$ GeV
20	$\Delta\phi < 1.1$ rad if $P_T < 30$ GeV
21	$\Delta\phi < 0.9$ rad if $P_T < 30$ GeV
22	$\Delta\phi < 1(2)$ rad if $P_T < (>)33$ GeV
23	$\Delta\phi < 1(2)$ rad if $P_T < (>)27$ GeV
24	good track def. $P_T > 250$ MeV
25	good track def. $17^\circ < theta > 164^\circ$
26	$P_T > 15.4$ GeV
27	$P_T > 12.6$ GeV
28	$P'_T > 13.2$ GeV
29	$P'_T > 10.8$ GeV
30	$z_{vtx}^{FCAL} < 55$ cm
31	$z_{vtx}^{FCAL} < 45$ cm

Index	description
32	$P_T/E_T < 0.66$ for $P_T < 30$ GeV
33	$P_T/E_T < 0.54$ for $P_T < 30$ GeV
34	$P_T/E_T < 0.6$ for $P_T < 33$ GeV
35	$P_T/E_T < 0.5$ for $P_T < 27$ GeV
36	$FEMC/FCAL > 0.11$
37	$FEMC/FCAL > 0.09$
38	$FHAC1/FCAL > 0.11$
39	$FHAC1/FCAL > 0.09$
40	$FHAC2/FCAL < 0.33$
41	$FHAC2/FCAL < 0.27$
42	RHAC +2%, BHAC +1%, FHAC +1%
43	RHAC -2%, BHAC -1%, FHAC -1%
44	RHAC +2%, BHAC -1%, FHAC +1%
45	RHAC -2%, BHAC +1%, FHAC -1%
46	RHAC -2%, REMC +2%
47	RHAC +2%, REMC -2%
48	BHAC -2%, BEMC +2%
49	BHAC +2%, BEMC -2%
50	FHAC -2%, FEMC +2%
51	FHAC +2%, FEMC -2%
52	MEPS +
53	MEPS −
54	PDFs
55	F_L
56	PHP subtraction $\alpha + 20\%$
57	PHP subtraction $\alpha - 20\%$
58	PHP subtraction $\beta + 20\%$
59	PHP subtraction $\beta - 20\%$
60	Luminosity +5%
61	Luminosity −5%

Table 8.3: List of the systematic checks and their description. The index which identifies each source of possible systematic effect is given in the first column.

Chapter 9

Results

9.1 Cross section results

The single differential CC cross sections, for the LH and RH samples, as a function of Q^2, x, and y, are presented in Fig. 9.1, Fig. 9.2 and Fig. 9.3, respectively. In each figure, the measured cross section is compared to the SM prediction, calculated using the HECTOR program with the ZEUS-S PDFs and the appropriate polarisation factor $(1 + P)$. P is the luminosity weighted polarisation, which is

$$P_{LH} \equiv P = -0.406 \ \pm \ 0.011\,, \tag{9.1}$$

for the LH sample and

$$P_{RH} \equiv P = +0.322 \ \pm \ 0.009\,, \tag{9.2}$$

for the RH sample. Good agreement between the data and the SM predictions is observed. The lower plot in each figure, presents the ratio of the measured cross section to the SM prediction obtained with the HECTOR program assuming $P = 0$. As expected, the ratio for the RH sample is larger than for the LH, and the departure from unity is fully accounted for by the beam polarisation. The total LH CC cross section measured at $P = P_{LH}$ comes out to be

$$\sigma^{CC}(P = P_{LH}) = 23.11 \pm 1.89\ (\text{stat})^{+1.38}_{-1.41}\ (\text{syst})\,, \tag{9.3}$$

and the total RH CC cross section at $P = P_{RH}$ is

$$\sigma^{CC}(P = P_{RH}) = 42.66 \pm 2.45\ (\text{stat})^{+2.28}_{-2.27}\ (\text{syst})\,. \tag{9.4}$$

In Fig. 9.4 the total CC cross section versus P is shown. The measurement corresponding to $P = 0$ was obtained at HERA I for e^+p interactions with

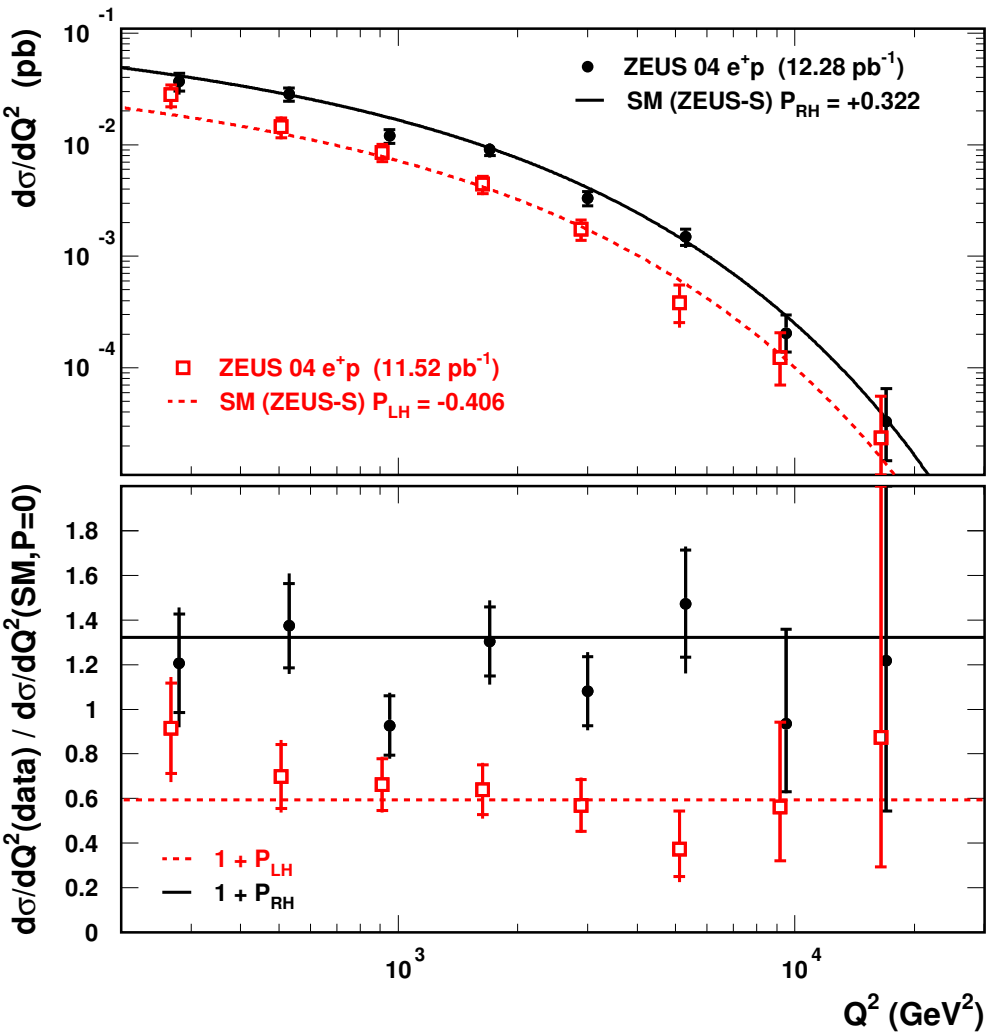

Figure 9.1: Upper plot: The CC differential cross section as a function of Q^2 for both LH (open squares) and RH (closed circles) samples. The curves represent the SM predictions as obtained with the HECTOR program and for the polarisation values P_{LH} and P_{RH}. Lower plot: The ratio of the measured CC cross section and the SM expectation for $P = 0$ as a function of Q^2, for LH (open squares) and RH (closed circles). The horizontal lines stand for $1 + P_{LH}$ and $1 + P_{RH}$.

$\mathcal{L} = 60.9$ pb^{-1} [30]. The results are compared to the expectations in Fig. 9.4. The value of $\sigma^{CC}(0)$ was calculated with the HECTOR program, using the ZEUS-S PDFs. The band accompanying the theoretical expectation represents the uncertainty in the ZEUS-S PDFs. Within statistical errors, a good

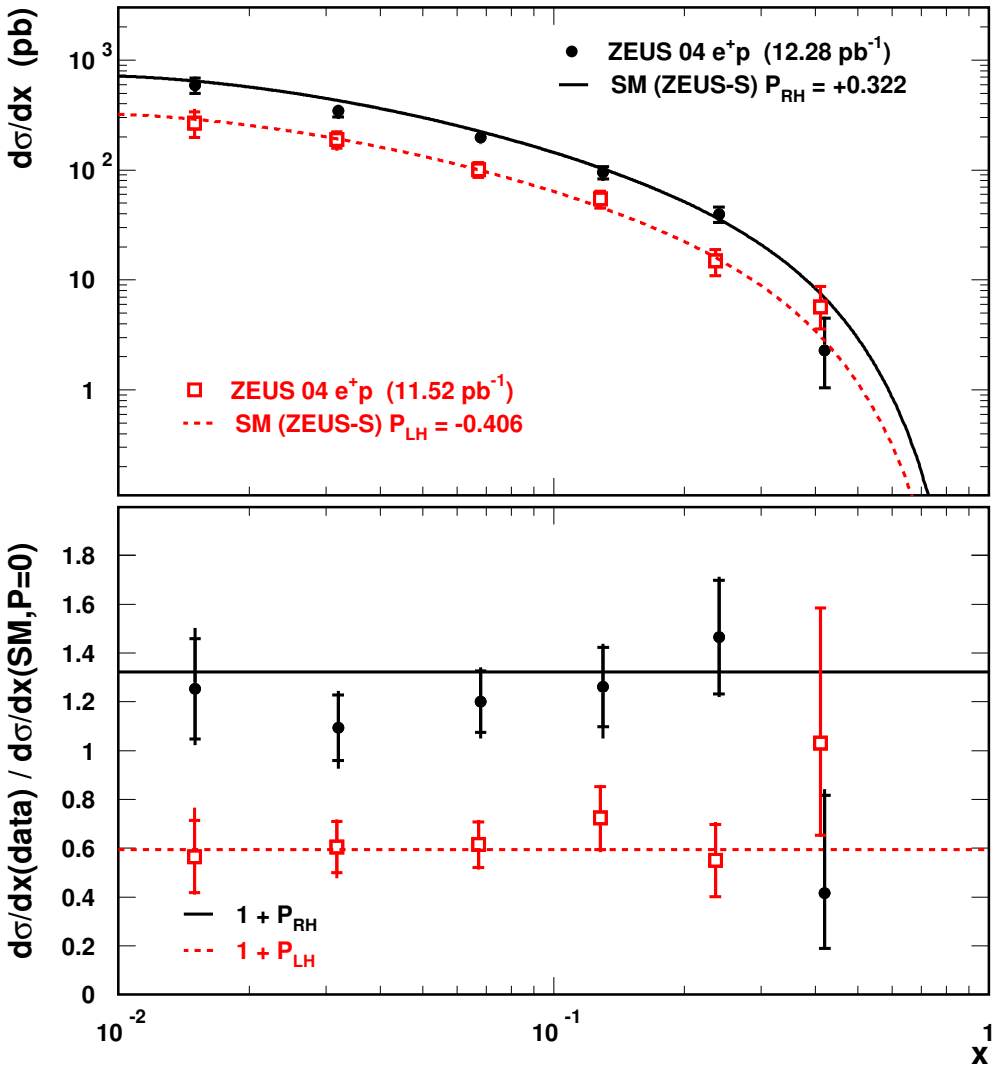

Figure 9.2: Upper plot: The CC differential cross section as a function of x for both LH (open squares) and RH (closed circles) samples. The curves represent the SM predictions as obtained with the HECTOR program and for the polarisation values P_{LH} and P_{RH}. Lower plot: The ratio of the measured CC cross section and the SM expectation for $P = 0$ as a function of x, for LH (open squares) and RH (closed circles). The horizontal lines stand for $1 + P_{LH}$ and $1 + P_{RH}$.

agreement between the measurements and the SM expectations is observed.

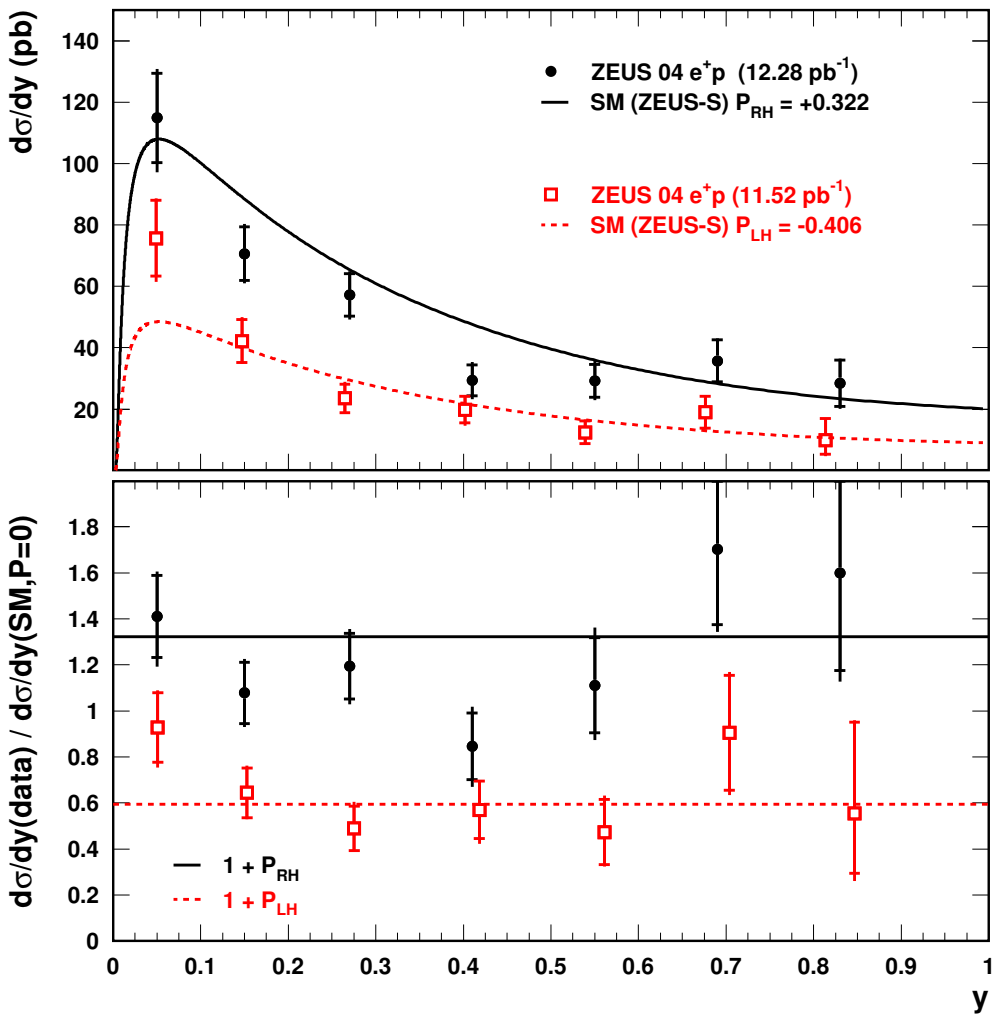

Figure 9.3: Upper plot: The CC differential cross section as a function of y for both LH (open squares) and RH (closed circles) samples. The curves represent the SM predictions as obtained with the HECTOR program and for the polarisation values P_{LH} and P_{RH}. Lower plot: The ratio of the measured CC cross section and the SM expectation for $P = 0$ as a function of y, for LH (open squares) and RH (closed circles). The horizontal lines stand for $1 + P_{LH}$ and $1 + P_{RH}$.

9.2 Estimation of $\sigma^{CC}(P = -1)$

A linear fit, $\sigma^{CC}(P) = a \cdot P + b$, was used to extrapolate the CC cross section to $P = -1$. To obtain a correct estimate of the fit parameters, the error of

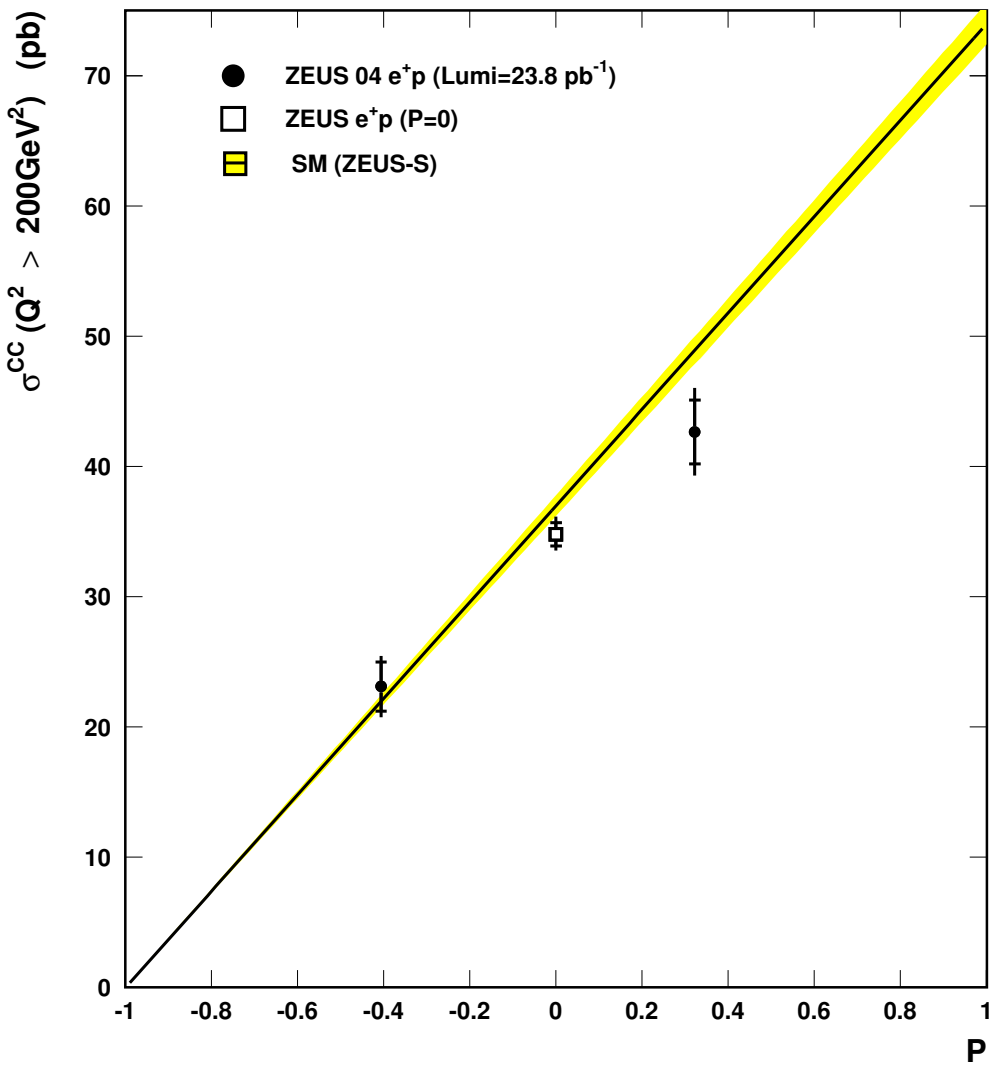

Figure 9.4: The CC total cross section as a function of the longitudinal polarisation of the lepton beam. The point which correspond to zero polarisation comes from data collected in the 1999-2000 run period. The line represents the theoretical expectation and the band shows the uncertainty in the cross sections due to the uncertainty in the PDFs (ZEUS-S).

the CC cross section should be taken into account as well as the error on the polarisation measurement. The fit was done using the method suggested by H. Abramowicz and A. Caldwell [100] where the uncertainties in both x and

y were taken into account. The χ^2 of the fit is defined as follows

$$\chi^2 = \sum_i (h_i)^2 \,, \tag{9.5}$$

with

$$h_i^2 = \frac{(a \cdot P + b - \sigma_i^{CC})^2 \cos^2(\tan^{-1}(a\frac{\Delta P_i}{\Delta \sigma_i^{CC}}))}{(\Delta \sigma_i^{CC})^2} \,, \tag{9.6}$$

and where σ_i^{CC} is the CC cross section, $\Delta\sigma_i^{CC}$ is the statistical uncertainty of the CC cross section, and ΔP_i is the polarisation uncertainty.

The best parameters of the fit performed by MINUIT [101] were

$$\begin{aligned} a &= 27.43 \pm 4.08 \,, & (9.7)\\ b &= 34.61 \pm 0.78 \,, & (9.8)\\ cov(a,b) &= 0.59 \,, & (9.9)\\ \chi^2/ndf &= 0.2 \,, & (9.10) \end{aligned}$$

where $cov(a,b)$ is the covariance between a and b, and ndf is the number of degrees of freedom. The extrapolated cross section at $P = -1$ is given by $\sigma^{CC}(P=-1) = -a + b$, and was found to be

$$\sigma^{CC}(P=-1) = 7.2 \pm 4.0(stat) \text{ pb} \,. \tag{9.11}$$

In Fig. 9.5 the result of the fit is presented together with the 1σ uncertainty band.

The cross sections are slightly changed when the analysis details are varied (see sec. 8). For the sake of completeness, the fit was repeated for every systematic check, as shown in Tables 9.1, Table 9.2, and Table 9.3. The error bars in Fig. 9.6 represent the uncertainty on the cross section at $P = -1$ for each of the fits. The variation in the $\sigma^{CC}(P=-1)$ leads to an estimate of the systematic uncertainty and the final result is then

$$\sigma^{CC}(P=-1) = 7.2 \pm 4.0(stat)^{+1.1}_{-1.5}(syst) \text{ pb} \,. \tag{9.12}$$

Within errors the $\sigma^{CC}(P=-1)$ value is consistent with zero as expected in the SM.

9.3 Limit on M_{WR}

An exercise to put a limit on the mass of the RH W, M_{WR}, was attempted. The CC cross section assuming only RH W, $\frac{d\sigma^{CC}_{RHW}(e^+p)}{dxdQ^2}$, is given by [102]

$$\frac{d\sigma^{CC}_{RHW}(e^+p)}{dxdQ^2} = \frac{G_\mu}{\pi}\frac{M^4_{WR}}{(M^2_{WR}+Q^2)^2} \cdot(\bar{u}(x,Q^2)+\bar{c}(x,Q^2)+(1-y)^2(d(x,Q^2)+s(x,Q^2)))\,. \tag{9.13}$$

In Fig. 9.7, σ^{CC}_{RH} as a function of the RH W mass is shown. The vertical line shows the limit on M_{WR} which is

$$M_{WR} > 110 \text{ GeV}\,, \tag{9.14}$$

for a 97% confidence level (about three standard deviations). This limit is in an agreement with the other limit obtained [103] at the TEVATRON [104].

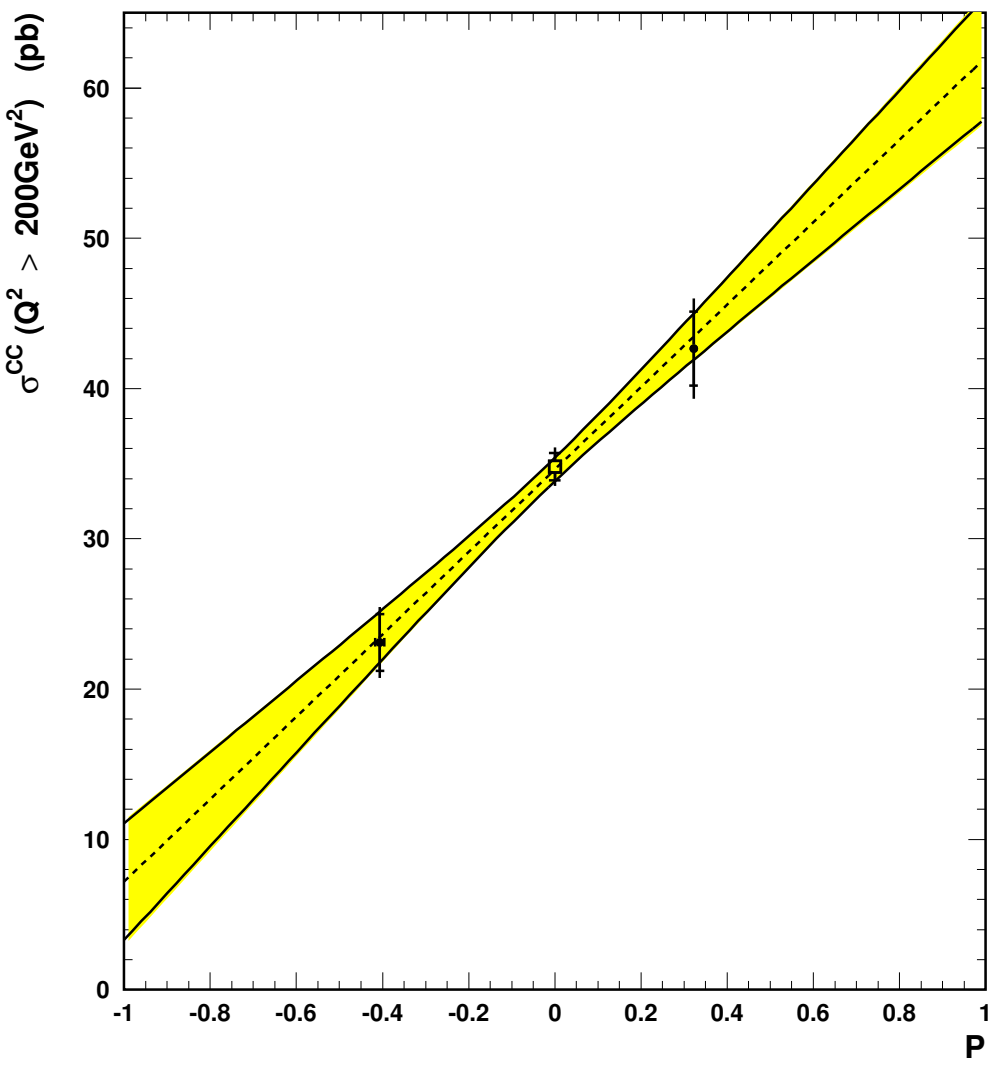

Figure 9.5: The result of the linear fit (dashed line) to the measurements of CC cross section (data points) as a function of polarisation. The band represents the fit uncertainty.

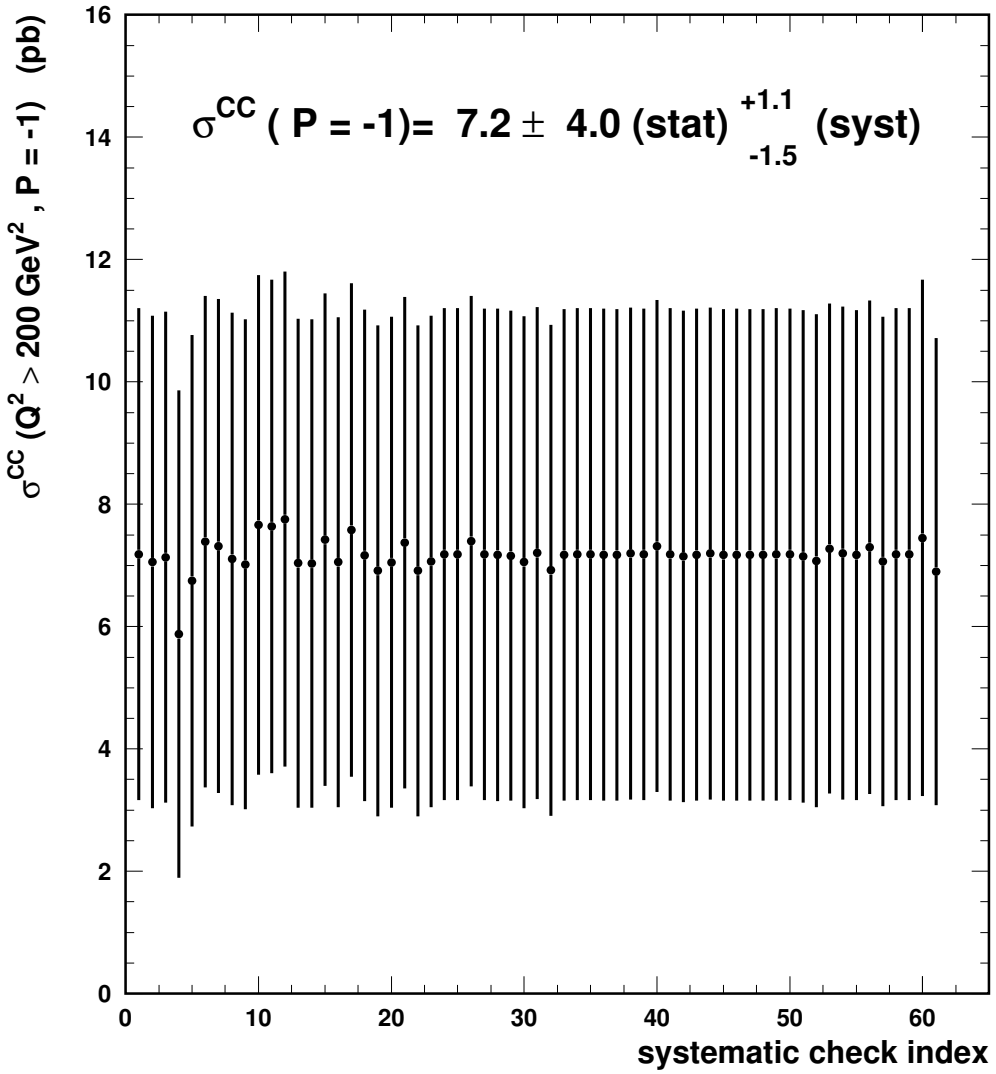

Figure 9.6: The variation of the estimate of $\sigma^{CC}(P = -1)$ as a function of the systematic check, denoted by its index as listed in Tables 9.1, 9.2, and 9.3.

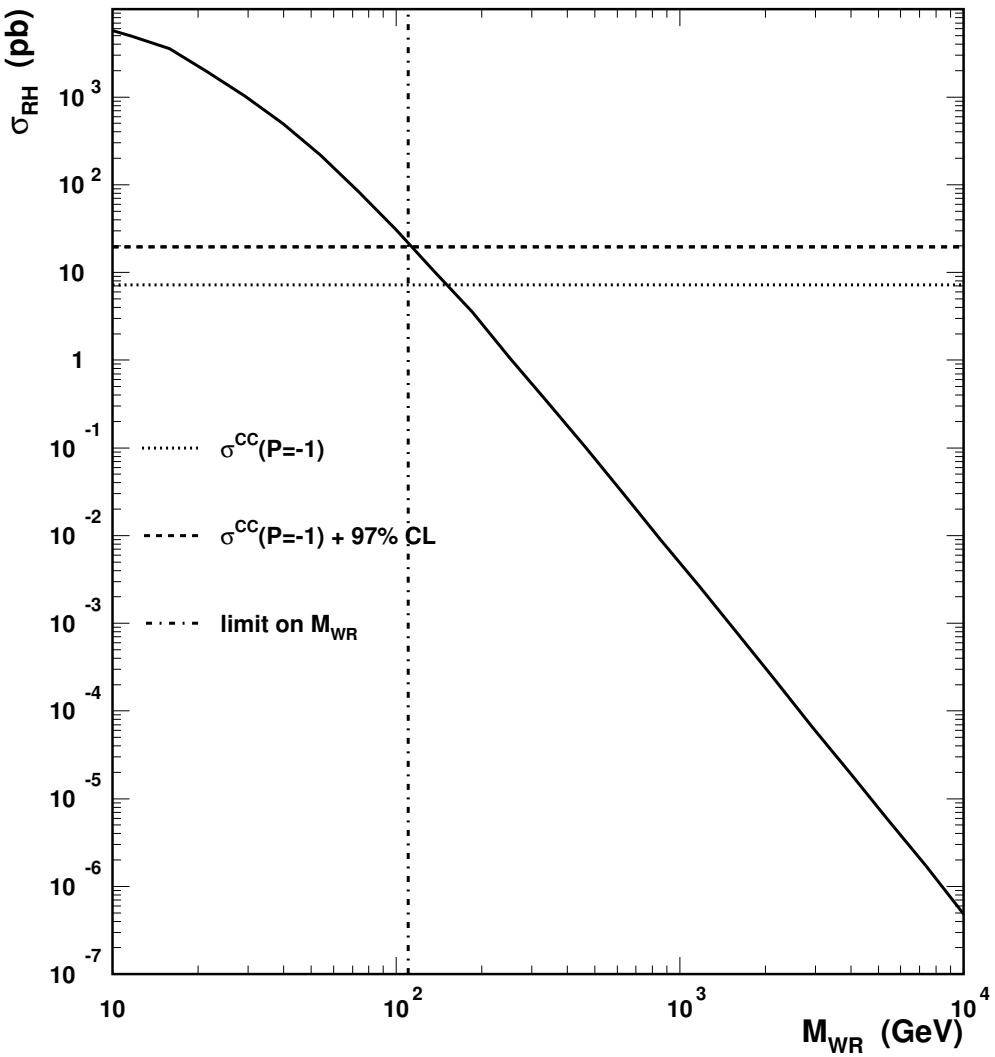

Figure 9.7: The CC cross section assuming RH W only, σ^{CC}_{RH}, as a function of the W mass, M_{WR}. The dotted horizontal line stands for $\sigma^{CC}(P = -1)$ while for the dashed one, three standard deviations were added.

index	description	$\sigma(P=-40.6\%)$ (pb)	$\sigma(P=+32.2\%)$ (pb)	$\sigma(P=-1)$ (pb)
1	nominal	23.11 ± 1.89	42.66 ± 2.45	7.18 ± 4.02
2	$P_T > 13.2$ GeV	23.03 ± 1.90	42.64 ± 2.46	7.05 ± 4.03
3	$P_T > 10.8$ GeV	23.03 ± 1.89	42.55 ± 2.45	7.13 ± 4.01
4	$P'_T > 11$ GeV	22.39 ± 1.87	42.64 ± 2.46	5.87 ± 3.98
5	$P'_T > 9$ GeV	22.97 ± 1.89	42.87 ± 2.46	6.75 ± 4.01
6	$z_{vtx}^{CTD} < 55$	23.19 ± 1.89	42.59 ± 2.45	7.39 ± 4.02
7	$z_{vtx}^{CTD} < 45$	23.23 ± 1.90	42.76 ± 2.46	7.32 ± 4.03
8	$P_T/E_T > 0.44$ for $20 < P_T < 30$ GeV	23.14 ± 1.90	42.81 ± 2.46	7.11 ± 4.03
9	$P_T/E_T > 0.36$ for $20 < P_T < 30$ GeV	23.00 ± 1.89	42.62 ± 2.45	7.02 ± 4.01
10	$P_T/E_T > 0.605$ for $P_T < 20$ GeV	23.54 ± 1.93	43.01 ± 2.49	7.66 ± 4.09
11	$P_T/E_T > 0.495$ for $P_T < 20$ GeV	23.62 ± 1.91	43.21 ± 2.45	7.64 ± 4.04
12	P_T box $22-33$	23.40 ± 1.91	42.61 ± 2.46	7.75 ± 4.05
13	P_T box $18-27$	23.10 ± 1.88	42.81 ± 2.44	7.04 ± 4.00
14	$N_{good} > 0.2(N^{trks} - 20)$	23.03 ± 1.88	42.67 ± 2.44	7.03 ± 3.99
15	$N_{good} > 0.3(N^{trks} - 20)$	23.03 ± 1.90	42.22 ± 2.45	7.42 ± 4.02
16	$N_{good} > 0.25(N^{trks} - 22)$	23.10 ± 1.89	42.79 ± 2.45	7.05 ± 4.01
17	$N_{good} > 0.25(N^{trks} - 18)$	23.17 ± 1.90	42.33 ± 2.46	7.58 ± 4.03
18	$\Delta\phi < 2.2$ rad if $P_T > 30$ GeV	23.09 ± 1.89	42.64 ± 2.45	7.16 ± 4.01
19	$\Delta\phi < 1.8$ rad if $P_T > 30$ GeV	22.97 ± 1.89	42.68 ± 2.46	6.91 ± 4.01
20	$\Delta\phi < 1.1$ rad if $P_T < 30$ GeV	23.07 ± 1.89	42.73 ± 2.45	7.05 ± 4.01
21	$\Delta\phi < 0.9$ rad if $P_T < 30$ GeV	23.22 ± 1.89	42.67 ± 2.45	7.37 ± 4.02
22	$\Delta\phi < 1(2)$ rad if $P_T < (>)33$ GeV	22.98 ± 1.89	42.70 ± 2.46	6.91 ± 4.01
23	$\Delta\phi < 1(2)$ rad if $P_T < (>)27$ GeV	23.09 ± 1.89	42.76 ± 2.46	7.06 ± 4.02
24	good track def. $P_T > 250$ MeV	23.11 ± 1.89	42.66 ± 2.45	7.18 ± 4.02
25	good track def. $17^\circ < theta > 164^\circ$	23.11 ± 1.89	42.66 ± 2.45	7.18 ± 4.02

Table 9.1: Variations of the measured cross sections and the resulting estimate of $\sigma^{CC}(P=-1)$ for the systematic checks affecting the high γ_0 sample.

index	description	$\sigma(P=-40.6\%)$ (pb)	$\sigma(P=+32.2\%)$ (pb)	$\sigma(P=-1)$ (pb)
26	$P_T > 15.4$ GeV	23.02 ± 1.89	42.22 ± 2.44	7.40 ± 4.01
27	$P_T > 12.6$ GeV	23.11 ± 1.89	42.66 ± 2.45	7.18 ± 4.02
28	$P'_T > 13.2$ GeV	23.09 ± 1.90	42.63 ± 2.46	7.17 ± 4.03
29	$P'_T > 10.8$ GeV	23.02 ± 1.89	42.50 ± 2.45	7.16 ± 4.00
30	$z_{vtx}^{FCAL} < 55$ cm	23.10 ± 1.89	42.79 ± 2.46	7.05 ± 4.02
31	$z_{vtx}^{FCAL} < 45$ cm	23.13 ± 1.89	42.68 ± 2.46	7.20 ± 4.02
32	$P_T/E_T < 0.66$ for $P_T < 30$ GeV	22.98 ± 1.89	42.69 ± 2.46	6.92 ± 4.01
33	$P_T/E_T < 0.54$ for $P_T < 30$ GeV	23.10 ± 1.89	42.65 ± 2.45	7.17 ± 4.02
34	$P_T/E_T < 0.6$ for $P_T < 33$ GeV	23.11 ± 1.89	42.66 ± 2.45	7.18 ± 4.02
35	$P_T/E_T < 0.5$ for $P_T < 27$ GeV	23.11 ± 1.89	42.66 ± 2.45	7.18 ± 4.02
36	$FEMC/FCAL > 0.11$	23.11 ± 1.89	42.67 ± 2.45	7.18 ± 4.02
37	$FEMC/FCAL > 0.09$	23.10 ± 1.89	42.65 ± 2.45	7.17 ± 4.02
38	$FHAC1/FCAL > 0.11$	23.13 ± 1.89	42.69 ± 2.46	7.19 ± 4.02
39	$FHAC1/FCAL > 0.09$	23.10 ± 1.89	42.64 ± 2.45	7.18 ± 4.02
40	$FHAC2/FCAL < 0.33$	23.21 ± 1.90	42.72 ± 2.45	7.31 ± 4.02
41	$FHAC2/FCAL < 0.27$	23.16 ± 1.90	42.77 ± 2.46	7.18 ± 4.03
42	RHAC +2%, BHAC +1%, FHAC +1%	23.06 ± 1.89	42.60 ± 2.45	7.15 ± 4.02
43	RHAC -2%, BHAC -1%, FHAC -1%	23.11 ± 1.89	42.67 ± 2.45	7.18 ± 4.02

Table 9.2: Variations of the measured cross sections and the resulting estimate of $\sigma^{CC}(P=-1)$ for the systematic checks affecting the low γ_0 sample.

The test

9.4 Summary

The differential CC cross sections in different bins of Q^2, x, and y are summarised in Tables 9.4, 9.6, 9.8 for the LH sample, respectively, and in Tables 9.5, 9.7, 9.9 for the RH sample, respectively.

index	description	$\sigma(P=-40.6\%)$ (pb)	$\sigma(P=+32.2\%)$ (pb)	$\sigma(P=-1)$ (pb)
44	RHAC +2%, BHAC -1%, FHAC +1%	23.13 ± 1.89	42.69 ± 2.46	7.19 ± 4.02
45	RHAC -2%, BHAC +1%, FHAC -1%	23.08 ± 1.89	42.61 ± 2.45	7.17 ± 4.01
46	RHAC -2%, REMC +2%	23.11 ± 1.89	42.67 ± 2.45	7.18 ± 4.02
47	RHAC +2%, REMC -2%	23.10 ± 1.89	42.65 ± 2.45	7.17 ± 4.02
48	BHAC -2%, BEMC +2%	23.09 ± 1.89	42.63 ± 2.45	7.17 ± 4.01
49	BHAC +2%, BEMC -2%	23.13 ± 1.90	42.71 ± 2.46	7.18 ± 4.02
50	FHAC -2%, FEMC +2%	23.10 ± 1.89	42.64 ± 2.45	7.18 ± 4.02
51	FHAC +2%, FEMC -2%	23.08 ± 1.90	42.64 ± 2.46	7.15 ± 4.02
52	MEPS +	23.15 ± 1.90	42.87 ± 2.47	7.07 ± 4.03
53	MEPS −	23.06 ± 1.89	42.45 ± 2.44	7.28 ± 4.01
54	PDFs	23.17 ± 1.90	42.77 ± 2.46	7.20 ± 4.03
55	F_L	23.05 ± 1.89	42.55 ± 2.45	7.17 ± 4.01
56	PHP subtraction $\alpha + 20\%$	23.22 ± 1.90	42.76 ± 2.46	7.30 ± 4.03
57	PHP subtraction $\alpha - 20\%$	23.00 ± 1.88	42.56 ± 2.45	7.07 ± 4.00
58	PHP subtraction $\beta + 20\%$	23.11 ± 1.89	42.66 ± 2.45	7.18 ± 4.02
59	PHP subtraction $\beta - 20\%$	23.11 ± 1.89	42.66 ± 2.45	7.18 ± 4.02
60	Luminosity +5%	24.26 ± 1.99	44.79 ± 2.58	7.45 ± 4.22
61	Luminosity −5%	21.95 ± 1.80	40.53 ± 2.33	6.90 ± 3.81

Table 9.3: Variations of the measured cross sections and the resulting estimate of $\sigma^{CC}(P=-1)$ for the systematic checks affecting the calorimeter energy scale and the analysis details.

The measurement of the CC cross sections obtained with a longitudinally polarised lepton beam, for $Q^2 > 200$ GeV^2 and at a centre of mass energy of 318 GeV, were found to agree with the expectations of the SM, both in the shapes of the Q^2, x, and y distributions and in the behaviour of the total cross section. The linear dependence of the cross section on polarisation allows to derive an estimate of the CC cross section for $P = -1$, which is found to be consistent with zero, as expected in the SM.

Q^2 range (GeV^2)	Q_0^2 (GeV^2)	N data	N bg	ϵ	$\mathcal{P}$	$\mathcal{A}$	$\frac{d\sigma(e^+p\to\bar{\nu}X)}{dQ^2}$ ($\frac{\text{pb}}{\text{GeV}^2}$)	
							SM	measured
$200-400$	280	26	2.01	0.25	0.64	0.39	$1.82\cdot10^{-2}$	$2.81^{+0.62\ +0.35}_{-0.62\ -0.40}\cdot10^{-2}$
$400-711$	530	27	1.04	0.34	0.63	0.54	$1.23\cdot10^{-2}$	$1.45^{+0.29\ +0.17}_{-0.29\ -0.15}\cdot10^{-2}$
$711-1265$	950	34	0.54	0.43	0.65	0.66	$7.66\cdot10^{-3}$	$8.56^{+1.50\ +0.55}_{-1.50\ -0.65}\cdot10^{-3}$
$1265-2249$	1700	33	0.08	0.47	0.68	0.70	$4.12\cdot10^{-3}$	$4.43^{+0.77\ +0.34}_{-0.77\ -0.43}\cdot10^{-3}$
$2249-4000$	3000	24	0.02	0.52	0.69	0.76	$1.82\cdot10^{-3}$	$1.75^{+0.36\ +0.14}_{-0.36\ -0.12}\cdot10^{-3}$
$4000-7113$	5300	9	0.06	0.52	0.71	0.74	$6.05\cdot10^{-4}$	$3.81^{+1.74\ +0.21}_{-1.25\ -0.85}\cdot10^{-4}$
$7113-12649$	9500	5	0.01	0.51	0.69	0.74	$1.30\cdot10^{-4}$	$1.23^{+0.83\ +0.07}_{-0.53\ -0.08}\cdot10^{-4}$
$12649-22494$	17000	2	0.04	0.48	0.64	0.76	$1.61\cdot10^{-5}$	$2.37^{+3.17\ +0.21}_{-1.57\ -0.16}\cdot10^{-5}$
$22494-60000$	30000	0	0.02	0.49	0.48	1.02	$8.77\cdot10^{-7}$	–

Table 9.4: The single differential cross sections in bins of Q^2 ($\frac{d\sigma}{dQ^2}$) for e^+p interactions at $P=-40.6\%$. Given in the table are the Q^2 range of the bin, the bin centre (Q_0^2), the number of data events (N_{data}), the estimated number of background events (N_{bg}), the acceptance ($\mathcal{A}$) which results from efficiency (ϵ) and purity ($\mathcal{P}$), and the differential cross section measurement $\frac{d\sigma(e^+p\to\bar{\nu}X)}{dQ^2}$ (SM and measured).

Q^2 range (GeV^2)	Q_0^2 (GeV^2)	N data	N bg	ϵ	$\mathcal{P}$	$\mathcal{A}$	$\frac{d\sigma(e^+p\to\bar{\nu}X)}{dQ^2}$ ($\frac{\text{pb}}{\text{GeV}^2}$)	
							SM	measured
$200-400$	280	36	2.14	0.25	0.64	0.39	$4.06\cdot10^{-2}$	$3.70^{+0.68\ +0.37}_{-0.68\ -0.57}\cdot10^{-2}$
$400-711$	530	56	1.11	0.34	0.62	0.55	$2.74\cdot10^{-2}$	$2.84^{+0.39\ +0.29}_{-0.39\ -0.22}\cdot10^{-2}$
$711-1265$	950	51	0.58	0.43	0.65	0.67	$1.71\cdot10^{-2}$	$1.20^{+0.17\ +0.08}_{-0.17\ -0.09}\cdot10^{-2}$
$1265-2249$	1700	72	0.09	0.48	0.68	0.70	$9.17\cdot10^{-3}$	$9.04^{+1.07\ +0.71}_{-1.07\ -0.81}\cdot10^{-3}$
$2249-4000$	3000	49	0.02	0.53	0.69	0.76	$4.05\cdot10^{-3}$	$3.31^{+0.47\ +0.26}_{-0.47\ -0.25}\cdot10^{-3}$
$4000-7113$	5300	38	0.06	0.53	0.71	0.74	$1.35\cdot10^{-3}$	$1.50^{+0.24\ +0.09}_{-0.24\ -0.20}\cdot10^{-3}$
$7113-12649$	9500	9	0.01	0.52	0.69	0.75	$2.90\cdot10^{-4}$	$2.05^{+0.93\ +0.12}_{-0.67\ -0.12}\cdot10^{-4}$
$12649-22494$	17000	3	0.04	0.49	0.64	0.77	$3.58\cdot10^{-5}$	$3.29^{+3.24\ +0.28}_{-1.82\ -0.21}\cdot10^{-5}$
$22494-60000$	30000	0	0.02	0.50	0.49	1.02	$1.95\cdot10^{-6}$	–

Table 9.5: The single differential cross sections in bins of Q^2 ($\frac{d\sigma}{dQ^2}$) for e^+p interactions at $P=+32.2\%$. The notation as in Table 9.4.

x range	x_0	N data	N bg	ϵ	$\mathcal{P}$	$\mathcal{A}$	$\frac{d\sigma(e^+p\to\bar{\nu}X)}{dx}$ (pb)	
							SM	measured
$0.010-0.022$	0.015	18	1.28	0.35	0.69	0.51	$2.80\cdot10^{+2}$	$2.67^{+0.70\ +0.64}_{-0.70\ -0.24}\cdot10^{+2}$
$0.022-0.046$	0.032	37	1.30	0.55	0.74	0.74	$1.87\cdot10^{+2}$	$1.90^{+0.33\ +0.14}_{-0.33\ -0.23}\cdot10^{+2}$
$0.046-0.100$	0.068	45	0.51	0.62	0.81	0.77	$9.75\cdot10^{+1}$	$1.01^{+0.15\ +0.06}_{-0.15\ -0.07}\cdot10^{+2}$
$0.100-0.178$	0.130	32	0.10	0.57	0.83	0.69	$4.48\cdot10^{+1}$	$5.46^{+0.97\ +0.30}_{-0.97\ -0.40}\cdot10^{+1}$
$0.178-0.316$	0.240	14	0.05	0.51	0.86	0.60	$1.61\cdot10^{+1}$	$1.49^{+0.40\ +0.16}_{-0.40\ -0.08}\cdot10^{+1}$
$0.316-0.562$	0.420	7	0.00	0.40	0.91	0.43	$3.27\cdot10^{0}$	$5.69^{+3.05\ +0.41}_{-2.09\ -0.35}\cdot10^{0}$
$0.562-1.000$	0.650	0	0.00	0.16	0.84	0.19	$2.24\cdot10^{-1}$	–

Table 9.6: The single differential cross sections in bins of x ($\frac{d\sigma}{dx}$) for e^+p interactions at $P=-40.6\%$. Given in the table are the x range of the bin, the bin centre (x_0), the number of data events (N_{data}), the estimated number of background events (N_{bg}), the acceptance ($\mathcal{A}$) which results from efficiency (ϵ) and purity ($\mathcal{P}$), and the differential cross section measurement $\frac{d\sigma(e^+p\to\bar{\nu}X)}{dx}$ (SM and measured).

x range	x_0	N^{data} data	N^{bg} bg	ϵ	$\mathcal{P}$	$\mathcal{A}$	$\frac{d\sigma(e^+p\to\bar{\nu}X)}{dx}$ (pb)	
							SM	measured
$0.010-0.022$	0.015	41	1.37	0.35	0.68	0.52	$6.24\cdot10^{+2}$	$5.92^{+0.97\ +0.66}_{-0.97\ -0.51}\cdot10^{+2}$
$0.022-0.046$	0.032	71	1.38	0.55	0.74	0.74	$4.17\cdot10^{+2}$	$3.45^{+0.42\ +0.23}_{-0.42\ -0.31}\cdot10^{+2}$
$0.046-0.100$	0.068	94	0.55	0.63	0.81	0.77	$2.17\cdot10^{+2}$	$1.97^{+0.21\ +0.10}_{-0.21\ -0.14}\cdot10^{+2}$
$0.100-0.178$	0.130	60	0.11	0.57	0.82	0.70	$9.98\cdot10^{+1}$	$9.52^{+1.23\ +0.53}_{-1.23\ -1.02}\cdot10^{+1}$
$0.178-0.316$	0.240	40	0.05	0.52	0.86	0.60	$3.58\cdot10^{+1}$	$3.97^{+0.63\ +0.23}_{-0.63\ -0.22}\cdot10^{+1}$
$0.316-0.562$	0.420	3	0.00	0.39	0.91	0.43	$7.29\cdot10^{0}$	$2.29^{+2.22\ +0.78}_{-1.24\ -0.15}\cdot10^{0}$
$0.562-1.000$	0.650	0	0.00	0.16	0.84	0.19	$4.98\cdot10^{-1}$	–

Table 9.7: The single differential cross sections in bins of x ($\frac{d\sigma}{dx}$) for e^+p interactions at $P=+32.2\%$. The notation as in Table 9.6.

y range	y_0	N^{data} data	N^{bg} bg	ϵ	$\mathcal{P}$	$\mathcal{A}$	$\frac{d\sigma(e^+p\to\bar{\nu}X)}{dy}$ (pb)	
							SM	measured
$0.000-0.100$	0.051	41	1.15	0.49	0.93	0.52	$4.84\cdot10^{+1}$	$7.57^{+1.23\ +0.43}_{-1.23\ -0.72}\cdot10^{+1}$
$0.100-0.200$	0.153	38	0.74	0.62	0.83	0.75	$3.89\cdot10^{+1}$	$4.22^{+0.70\ +0.32}_{-0.70\ -0.25}\cdot10^{+1}$
$0.200-0.340$	0.275	28	0.76	0.59	0.81	0.73	$2.84\cdot10^{+1}$	$2.35^{+0.46\ +0.29}_{-0.46\ -0.16}\cdot10^{+1}$
$0.340-0.480$	0.418	22	0.32	0.51	0.73	0.70	$2.06\cdot10^{+1}$	$1.98^{+0.43\ +0.13}_{-0.43\ -0.28}\cdot10^{+1}$
$0.480-0.620$	0.561	12	0.28	0.40	0.68	0.60	$1.56\cdot10^{+1}$	$1.24^{+0.37\ +0.19}_{-0.37\ -0.12}\cdot10^{+1}$
$0.620-0.760$	0.704	14	0.29	0.30	0.63	0.48	$1.25\cdot10^{+1}$	$1.90^{+0.52\ +0.18}_{-0.52\ -0.23}\cdot10^{+1}$
$0.760-0.900$	0.847	5	0.26	0.19	0.59	0.32	$1.06\cdot10^{+1}$	$9.85^{+7.07\ +1.49}_{-4.59\ -2.42}\cdot10^{0}$

Table 9.8: The single differential cross sections in bins of y ($\frac{d\sigma}{dy}$) for e^+p interactions at $P=-40.6\%$. Given in the table are the y range of the bin, the bin centre (y_0), the number of data events (N_{data}), the estimated number of background events (N_{bg}), the acceptance ($\mathcal{A}$) which results from effecincy (ϵ) and purity ($\mathcal{P}$), and the differential cross section measurement $\frac{d\sigma(e^+p\to\bar{\nu}X)}{dy}$ (SM and measured).

y range	y_0	N^{data} data	N^{bg} bg	ϵ	$\mathcal{P}$	$\mathcal{A}$	$\frac{d\sigma(e^+p\to\bar{\nu}X)}{dy}$ (pb)	
							SM	measured
$0.000-0.100$	0.051	66	1.23	0.49	0.93	0.53	$1.08\cdot10^{+2}$	$1.15^{+0.15\ +0.06}_{-0.15\ -0.10}\cdot10^{+2}$
$0.100-0.200$	0.153	68	0.79	0.63	0.83	0.76	$8.66\cdot10^{+1}$	$7.06^{+0.87\ +0.42}_{-0.87\ -0.42}\cdot10^{+1}$
$0.200-0.340$	0.275	72	0.81	0.59	0.81	0.73	$6.33\cdot10^{+1}$	$5.72^{+0.69\ +0.35}_{-0.69\ -0.41}\cdot10^{+1}$
$0.340-0.480$	0.418	35	0.35	0.51	0.73	0.70	$4.59\cdot10^{+1}$	$2.94^{+0.50\ +0.32}_{-0.50\ -0.35}\cdot10^{+1}$
$0.480-0.620$	0.561	30	0.30	0.41	0.68	0.60	$3.47\cdot10^{+1}$	$2.92^{+0.54\ +0.37}_{-0.54\ -0.31}\cdot10^{+1}$
$0.620-0.760$	0.704	28	0.31	0.30	0.63	0.48	$2.77\cdot10^{+1}$	$3.57^{+0.69\ +0.26}_{-0.69\ -0.31}\cdot10^{+1}$
$0.760-0.900$	0.847	15	0.28	0.19	0.59	0.32	$2.35\cdot10^{+1}$	$2.85^{+0.76\ +0.27}_{-0.76\ -0.37}\cdot10^{+1}$

Table 9.9: The single differential cross sections in bins of y ($\frac{d\sigma}{dy}$) for e^+p interactions at $P=+32.2\%$. The notation as in Table 9.8.

Chapter 10

$\sin^2\theta_W$ extraction from HERA I data

10.1 Introduction

At present, the parameters of the SM, excluding the quark masses, are known with high precision. However, the determination of these parameters is affected by radiative corrections, which in turn are sensitive to the content of the theory. The NC and CC DIS cross sections also depend on the SM parameters. Since in the kinematics of HERA these parameters are probed in a different region of phase space than all the previous measurements, it is of interest to extract them from the HERA data. For example the CC cross section at large Q^2 is sensitive to the mass of the W boson. An extraction of M_W from the CC data was attempted in the 1996-1997 run period [105], and the value was found to be in agreement with that of other experiments. While the statistical uncertainty is small, the uncertainties of the PDFs cause the systematic error to be large. The dependence on the PDFs and on the absolute normalisation can be avoided to a large extend by using the ratio of NC to CC cross sections. This ratio is best expressed in terms of $\sin^2\theta_W = 1 - \frac{M_W^2}{M_Z^2}$, α, and G_μ.

The parameters α and G_μ were measured with high precision [106, 107]. Also $\sin^2\theta_W$ was measured in many reactions and precise values were obtained [108]. In general, very good agreement between various measurements is obtained after correcting for higher order electroweak radiative effects. The most precise values for $\sin^2\theta_W$ are obtained at the e^+e^- colliders LEP and SLC [109, 110] and in νN scattering in the NuTeV experiment [111]. However, a 2.3σ difference between values measured in e^+e^- and νN interactions was found as shown in Fig. 10.1. This difference attracted much of atten-

tion [112]. The main reason for this interest is that electroweak radiative corrections affect differently the e^+e^- measurements and the νN measurement. This could be a hint for a new "content" of the theory which has not yet been included in the calculations. In this chapter an attempt is

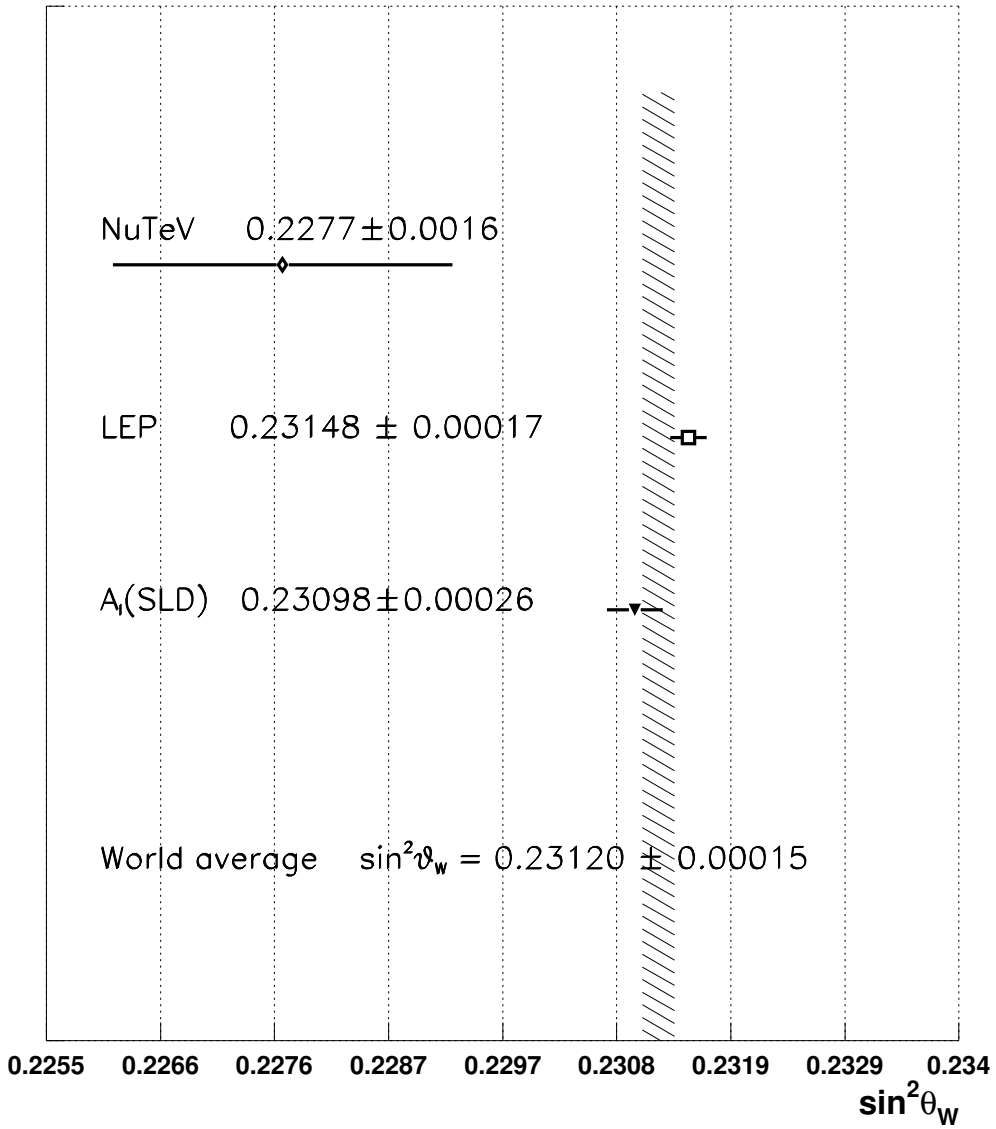

Figure 10.1: A comparison between the values of $\sin^2\theta_W$ as obtained from NuTeV, LEP, and SLAC with the world average as given by the PDG.

presented to extract the value of $\sin^2\theta_W(M_Z^2)$ from DIS NC and CC cross sections measured for $Q^2 > 200$ GeV^2 from the high statistics samples based

Year	Collision type	$\sqrt{s}$ (GeV)	$\mathcal{L}$ (pb^{-1})
1996-1997	e^+p	300	38.61
1998-1999	e^-p	318	16.67
1999-2000	e^+p	318	60.80

Table 10.1: Summary table of the data sample used to extract $\sin^2\theta_W$.

on 99.41 pb^{-1} of e^+p interactions and 16.67 pb^{-1} of e^-p interactions, all of which were collected between 1996 and 2000, as shown in Table 10.1.

The parameters of the SM used in this analysis are α, G_μ and $\sin^2\theta_W$, where $\sin^2\theta_W$ is defined in the on-mass-shell renormalisation scheme to be [113]

$$\sin^2\theta_W = 1 - \frac{M_W^2}{\rho_0 M_Z^2}\,. \tag{10.1}$$

The parameter ρ_0 is assumed to be $\rho_0 = 1$, as in the minimal standard model with a Higgs doublet. At the Born level of the SM, M_W and M_Z can be expressed in terms of α, G_μ and $\sin^2\theta_W$,

$$M_W^2 = \frac{\pi\alpha}{\sqrt{2}\sin^2\theta_W G_\mu}\,, \tag{10.2}$$

$$M_Z^2 = \frac{M_W^2}{1-\sin^2\theta_W}\,. \tag{10.3}$$

The dependence of $\sin^2\theta_W$ on M_Z at the Born level is shown in Fig. 10.2. Also shown is a point in the $\sin^2\theta_W$ and M_Z plane which corresponds to the world average [80]. The difference between the curve and the point at the appropriate M_Z is due to electroweak radiative corrections.

The $\sin^2\theta_W$ dependence in the CC and NC cross sections can be obtained by writing their cross sections in terms of α, G_μ and $\sin^2\theta_W$, using equations (10.1) and (10.2). In case of the CC cross section, only the propagator introduces the dependence on $\sin^2\theta_W$. Therefore, at low Q^2, $Q^2 << M_W^2$ the CC cross section is almost $\sin^2\theta_W$ independent. For NC, the electromagnetic process is the dominant one. In the medium Q^2 range, the dependence on $\sin^2\theta_W$ comes from the interference between the γ and Z^0 exchanges. The region of Q^2 where Z^0 dominates can be ignored within the present Q^2 range of this measurement. The ratio of NC to CC cross section in terms of scattering matrix at low and medium-high Q^2 range is shown in Fig. 10.3.

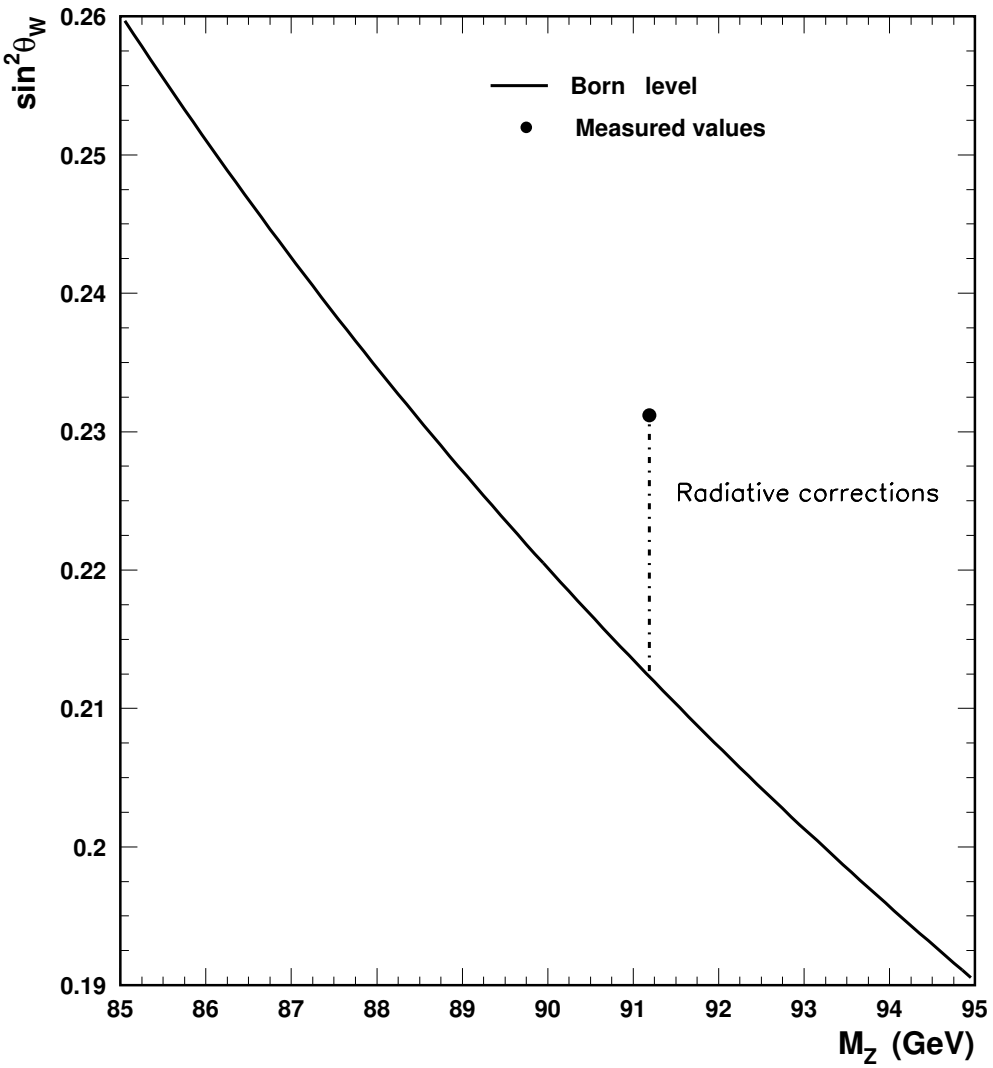

Figure 10.2: $\sin^2\theta_W$ as a function of M_Z at the Born level (curve) (MS scheme). The data point stands for the measured values of $\sin^2\theta_W$ and M_Z as given in the PDG. The dashed lines show the electroweak radiative correction to the measurement.

The ratio of the integrated NC to CC cross sections ratio is defined as

$$R \equiv \frac{\int\int dxdQ^2 \frac{d^2\sigma^{NC}}{dxdQ^2}}{\int\int dxdQ^2 \frac{d^2\sigma^{CC}}{dxdQ^2}}. \tag{10.4}$$

The dependence of R, calculated including radiative corrections, on $\sin^2\theta_W$ for $e^{\pm}p$ is shown in Fig. 10.4 for a lower limit of integration of $Q^2 = 200$ GeV^2.

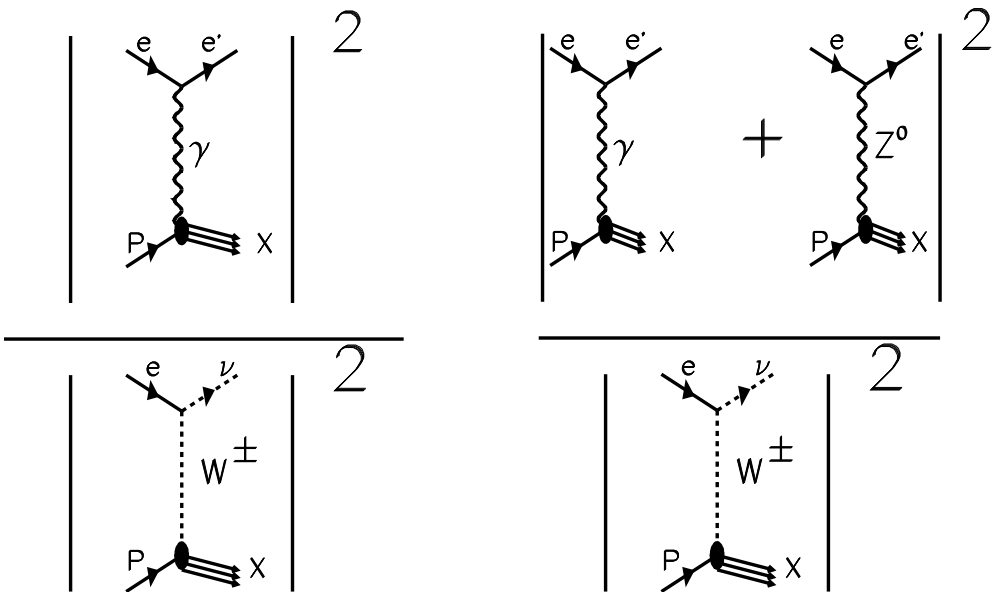

Figure 10.3: Left (Right): The NC to CC ratio in terms of Feynman diagrams at low (medium-high) Q^2.

A clear dependence of the ratio on $\sin^2\theta_W$ is observed.

The physical NC and CC cross sections are affected by the electroweak radiative processes which are dominated by QED corrections that amount to $20 - 50$ % [114–116]. Fig. 10.5 shows the difference in the value of R calculated at the Born level, R_{Born}, and R calculated including one-loop electroweak radiative corrections, R_{Rad}, as a function of the lower limit of Q^2 used in the integrals of equation (10.4). These corrections are about 6 % for Q^2 up to 1000 GeV^2, and increase for $Q^2 \geq 1000$ GeV^2 to 18 % in the highest Q^2 range. The electroweak radiative corrections include the correction due to the renormalisation of M_W and M_Z, where for example

$$M_W^2 = \frac{\pi\alpha}{\sqrt{2}\sin^2\theta_W G_\mu}\frac{1}{1-\Delta r(\alpha, M_W, M_Z, M_H, m_t)}\,, \tag{10.5}$$

where Δr depends on the content of the theory.

10.2 Monte Carlo simulation

CC and NC events including radiative effects are simulated using the HERACLES 4.6.1 [76] program with the DJANGO 1.1 [77] interface to the QCD final state generators. In HERACLES, electroweak corrections are calculated

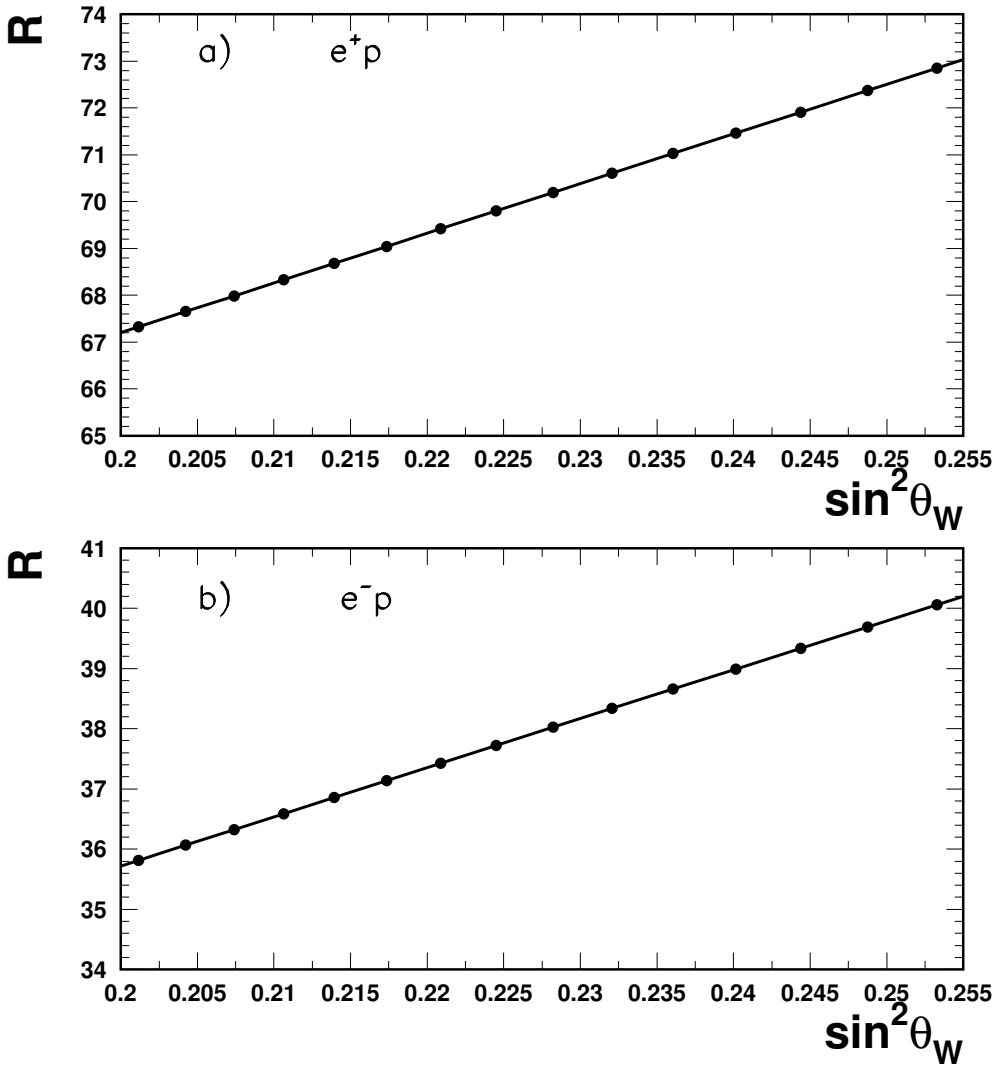

Figure 10.4: The theoretical NC to CC total cross sections ratio versus $\sin^2\theta_W$ for $Q^2 \geq 200$ GeV^2. The upper plot is for e^+p reactions while the lower one is for e^-p reactions. These values were obtained with HERACLES and the CTEQ5D parton density functions parameterisation.

to one-loop. The QCD cascade and the hadronic final state are simulated using the colour-dipole model of ARIADNE [78]. This program uses the Lund string model of JETSET 7.4 [117–119] for hadronisation. The events were generated using the CTEQ-5D [48] PDF's.

HERACLES calculates electroweak radiative corrections in terms of G_μ and M_Z or M_W, with $\sin^2\theta_W = 1 - M_W^2/M_Z^2$ on top of all the other fermion

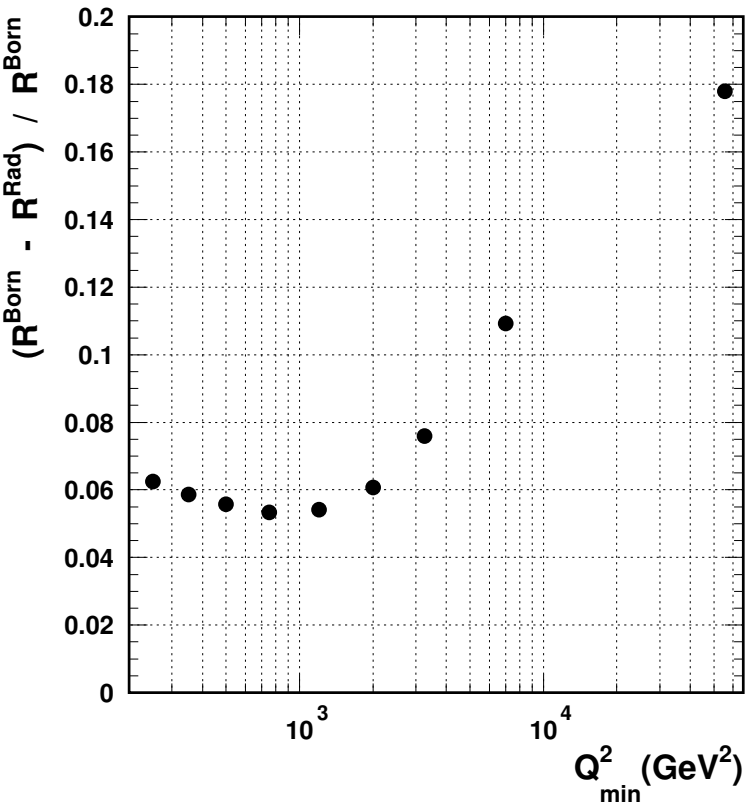

Figure 10.5: The relative difference between the ratio of integrated NC to CC cross section obtained at the Born level, R^{Born}, and including the electroweak radiative corrections, R^{Rad}, versus Q^2_{min}, where Q^2_{min} denotes the lower limit of integration for the cross sections.

masses and the Higgs mass. The top quark mass is set to 175 GeV, while the Higgs mass is set to 100 GeV. G_μ and M_Z are set to the PDG [80] values. M_W is calculated according to the required $\sin^2\theta_W$ value.

10.3 Trigger selections

As was mentioned in earlier chapters, ZEUS has a three-level trigger system. The triggers were designed to select CC and NC events taking into account their characteristics. The characteristics are the base for designing the event selection rules at the triggering level as well as in the offline analysis. The characteristics of a CC event were described in sec. 4.2. The characteristic

signature of NC DIS events is the presence of the scattered electron in the calorimeter. In addition, for NC DIS events the reconstructed δ is expected to be equal to 55 GeV (twice the incoming electron energy). Typical CC and NC events observed in the ZEUS detector are shown in Fig. 10.6

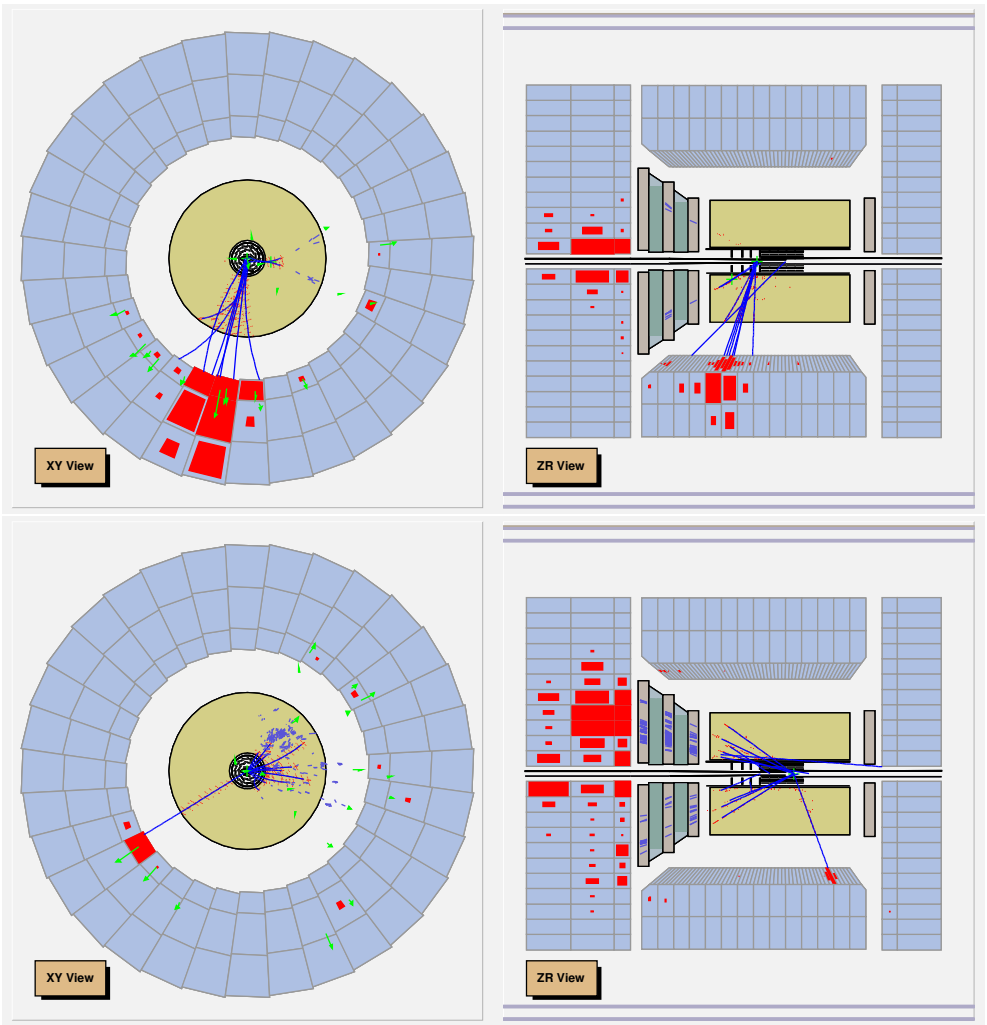

Figure 10.6: Upper (lower) figure: example of an CC (NC) event as observed in the ZEUS detector. In the NC event, a scattered electron in the BCAL with matching track in the CTD is observed. The Q^2 for the NC (CC) event is 1245 (3168) GeV^2.

10.3.1 Kinematic variables

To avoid extra systematic effects, the kinematic variables of both NC and CC events are calculated using their hadronic final states. Thus, the Jacquet-Blondel method is used to determine the kinematic variables of both NC and CC events.

10.3.2 CC trigger

The CC trigger was described in sec. 6.1.

10.3.3 NC trigger

The NC first-level trigger requires

- a total electromagnetic energy of at least 3.4 GeV in the EMC cells of the RCAL;
- or 4.8 GeV in the EMC cells of the BCAL and a good track (a track which has a transverse momentum that exceeds 200 MeV and is associated with the vertex);
- or an isolated energy deposit of at least 2 GeV in the EMC section of the RCAL;
- or 15 GeV summed over the entire EMC cells of the CAL;
- or $E_T'' \geq 12$ GeV and a good track, where E_T'' is the total transverse energy excluding the two inner rings of FCAL, nearest to the forward beam-pipe.

At the second-level trigger, we require that $\delta + 2E_\gamma \geq 29$ GeV, where E_γ is the photon energy measured in the luminosity monitor, and the calorimeter timing of the event is consistent with an *ep* interaction.

At the third-level trigger, events are fully reconstructed on a computer farm. The main requirement at this level, related to this analysis, is the presence of the scattered electron in the CAL by using an electron finder.

10.3.4 Background

As in the CC analysis, the main sources of background come from high-E_T photoproduction events, which mimic CC events. The energy that escapes detection can lead to significant missing transverse momentum. Beam-halo

muon events, cosmic ray events and beam-gas interactions can also cause substantial apparent imbalance in the transverse momentum and so constitute other sources of background. The requirement of a scattered electron and $\delta \approx 55$ GeV, leads to a very clean NC sample at high Q^2.

10.4 Events selection

The event selection follows closely the CC events described in chapter 6 [1]. In order to treat the CC and NC events the same way, the candidates of the two types are selected by requiring a large hadronic final state P_T and a reconstructed event vertex consistent with an ep interaction. The tracks in this analysis were reconstructed using the CTD only, and the reconstructed vertex was obtained by fitting these tracks for events with $\gamma_0 > 0.4$ rad, while the vertex for events with $\gamma_0 < 0.4$ rad was calculated using the FCAL arrival timing. In the standard reconstruction, in case of NC events, in addition to the hadronic final state tracks also the scattered electron tracks is used to reconstruct the CTD vertex. Therefore, for high Q^2 events where the electron is perpendicular to the beam line the resolution of the CTD vertex is much higher than for CC events. For the purpose of this analysis, the electron track was removed.

Also in this analysis, the events are classified according to the value of γ_0. The selection cuts for events with $\gamma_0 > 0.4$ rad and $\gamma_0 < 0.4$ rad for the three data sets $1996-1997$, $1998-1999$, and $1999-2000$ are summarised in Tab. 10.2, Tab. 10.3, and Tab. 10.4, respectively. The selection cuts for the different data sets can be slightly different because the beam-condition and the background were not the same during the run periods. Thus tighter thresholds and extra selection cuts may be used to reduce the background as far as possible.

[1] For rejection of cosmic and halo muons, the MUFFIN program [120] was used. This program was not available after the 2000 running period.

selection	high γ_0 selection ($\gamma_0 > 0.4$ rad)	low γ_0 selection ($\gamma_0 < 0.4$ rad)
Trigger	NC or CC DST bit trigger	
Kinematic region	$Q^2 > 200$ GeV^2 && $y < 0.9$	
Vertex requirement	$\lvert z_{vtx}^{trks}\rvert < 50$ cm	$\lvert z_{vtx}^{FCAL}\rvert < 50$ cm
P_T requirement	$P_T > 12$ GeV $P'_T > 10$ GeV	$P_T > 14$ GeV $P'_T > 12$ GeV
$\frac{P_T}{E_T}$ requirements	$\frac{P_T}{E_T} > \begin{cases} 0.55 & \text{if } P_T < 20 \text{ GeV} \\ 0.40 & \text{if } 20 < P_T < 30 \text{ GeV} \end{cases}$	$\frac{P_T}{E_T} > 0.6$ if $P_T < 30$ GeV
Tracking requirements	$N_{good} \geq 1$ $N_{good} > \frac{1}{4}(N^{trks} - 20)$ $\Delta\Phi_{trks-CAL} < \begin{cases} 1 \text{ rad} & \text{if } P_T < 20 \text{ GeV} \\ 2 \text{ rad} & \text{if } P_T > 20 \text{ GeV} \end{cases}$	
Background rejection		$\frac{E_{FCAL}^{EMC}}{E_{FCAL}} \geq 0.1$ && $\frac{E_{FCAL}^{HAC1}}{E_{FCAL}} \geq 0.1$ && $\frac{E_{FCAL}^{HAC2}}{E_{FCAL}} \leq 0.3$ $N_{trks}^{BRMU} = 0$ if $N^{trks} = 0$ $N_w^t > 1(2)$ if $N_F^{trks} \geq 1(=0)$ $N_w^m > 1(2)$ if $N_F^{trks} \geq 1(=0)$ $E_w^T > 6(10)$ if $N_F^{trks} \geq 1(=0)$ $E_{RSP} < 0.1$ GeV if $N_F^{trks} = 0$

Table 10.2: The selection cuts implemented in the analysis of e^+p **1996-1997** data.

selection	high γ_0 selection ($\gamma_0 > 0.4$ rad)	low γ_0 selection ($\gamma_0 < 0.4$ rad)
Trigger	NC or CC DST bit trigger	
Kinematic region	$Q^2 > 200$ GeV^2 && $y < 0.9$	
Vertex requirement	$\lvert z_{vtx}^{trks}\rvert < 50$ cm	$\lvert z_{vtx}^{FCAL}\rvert < 50$ cm
P_T requirement	$P_T > 12$ GeV $P'_T > 10$ GeV	$P_T > 25$ GeV $P'_T > 25$ GeV
$\frac{P_T}{E_T}$ requirements	$\frac{P_T}{E_T} > \begin{cases} 0.55 & \text{if } P_T < 20 \text{ GeV} \\ 0.40 & \text{if } 20 < P_T < 30 \text{ GeV} \end{cases}$	$\frac{P_T}{E_T} > 0.6$ if $P_T < 30$ GeV
Tracking requirements	$N_{good} \geq 1$ $N_{good} > \frac{1}{4}(N^{trks} - 20)$ $\Delta\Phi_{trks-CAL} < 0.5$ rad	
BCAL energy	$\frac{E_{BHAC}}{E_{BCAL}} < 0.9$ for $E_{BCAL} > 2$ GeV	
Background rejection		$\frac{E_{FCAL}^{EMC}}{E_{FCAL}} \geq 0.1$ && $\frac{E_{FCAL}^{HAC1}}{E_{FCAL}} \geq 0.1$ && $\frac{E_{FCAL}^{HAC2}}{E_{FCAL}} \leq 0.3$ $N_{trks}^{BRMU} = 0$ if $N^{trks} = 0$ $N_w^t > 1(2)$ if $N_F^{trks} \geq 1(=0)$ $N_w^m > 1(2)$ if $N_F^{trks} \geq 1(=0)$ $E_w^T > 6(10)$ if $N_F^{trks} \geq 1(=0)$ $E_{RSP} < 0.1$ GeV if $N_F^{trks} = 0$

Table 10.3: The selection cuts implemented in the analysis of e^-p **1998-1999** data.

selection	high γ_0 selection ($\gamma_0 > 0.4$ rad)	low γ_0 selection ($\gamma_0 < 0.4$ rad)
Trigger	NC or CC DST bit trigger	
Kinematic region	$Q^2 > 200$ GeV^2 && $y < 0.9$	
Vertex requirement	$\lvert z_{vtx}^{trks}\rvert < 50$ cm	$\lvert z_{vtx}^{FCAL}\rvert < 50$ cm
P_T requirement	$P_T > 12$ GeV $P'_T > 10$ GeV	$P_T > 14$ GeV $P'_T > 12$ GeV
$\frac{P_T}{E_T}$ requirements	$\frac{P_T}{E_T} > \begin{cases} 0.65 & \text{if } P_T < 20 \text{ GeV} \\ 0.40 & \text{if } 20 < P_T < 30 \text{ GeV} \end{cases}$	$\frac{P_T}{E_T} > 0.6$ if $P_T < 30$ GeV
Tracking requirements	$N_{good} \geq 1$ $N_{good} > \frac{1}{4}(N^{trks} - 20)$ $\Delta\Phi_{trks-CAL} < \begin{cases} .5 \text{ rad} & \text{if } P_T < 20 \text{ GeV} \\ 2. \text{ rad} & \text{if } P_T > 20 \text{ GeV} \end{cases}$	
Background rejection		$\frac{E_{FCAL}^{EMC}}{E_{FCAL}} \geq 0.1$ && $\frac{E_{FCAL}^{HAC1}}{E_{FCAL}} \geq 0.1$ && $\frac{E_{FCAL}^{HAC2}}{E_{FCAL}} \leq 0.3$ $N_{trks}^{BRMU} = 0$ if $N^{trks} = 0$ $N_w^t > 1(2)$ if $N_F^{trks} \geq 1(=0)$ $N_w^m > 1(2)$ if $N_F^{trks} \geq 1(=0)$ $E_w^T > 6(10)$ if $N_F^{trks} \geq 1(=0)$ $E_{RSP} < 0.1$ GeV if $N_F^{trks} = 0$

Table 10.4: The selection cuts implemented in the analysis of e^+p **1999-2000** data.

10.4.1 CC and NC separation

The event samples, after the offline cuts described in the Tab. 10.2, Tab. 10.3, and Tab. 10.4, consist of CC and NC events. The identification of the scattered electron is done by using the so-called **EM** algorithm which combines information from the energy deposits in the calorimeter with tracks measured in the CTD. A NC event is defined as one that satisfies the following criteria:

- at least one scattered electron candidate with a minimum energy of 10 GeV. The energy requirement is needed to ensure high purity;
- the scattered electron cluster within the CTD acceptance has to be matched to a track with a momentum of at least 5 GeV;
- to reduce background, only isolated electrons were selected by requiring that less than 5 GeV be deposited in calorimeter cells, not associated with the final state scattered electron, inside an $\eta - \phi$ cone of radius $R_{cone} = \sqrt{(\Delta\phi)^2 + (\Delta\eta)^2} = 0.8$ centred on the electron, where $\Delta\phi$ (in radians) is the azimuthal angle between CAL energy-deposit and the scattered electron and $\Delta\eta$ is the difference in pseudorapidity between the scattered electron and energy deposit [121, 122].

Note that events in which a non-isolated electron was found, are treated as if no electron was identified. All events which are not flagged as NC events are called CC events. A schematic diagram which describes the procedure of getting the final CC and NC samples is shown in Fig. 10.7. The purities of the CC and NC final samples are very high. For example, among 1474 CC events scanned in the 1999-2000 data, only two NC events were identified as CC events.

10.4.2 Kinematical range

As in the earlier analysis, the kinematical range was chosen such as to make the background contributions as small as possible, and to make the Jacquet-Blondel estimators give good resolution. The kinematical region is restricted to

$$Q^2 \geq 200 \text{ GeV}^2 \text{ and } y \leq 0.9\,.$$

10.5 Monte Carlo and data comparisons

A comparison between data and MC for the 1996-2000 sub-samples are shown in Fig. 10.8-10.18. The comparison is shown for the most relevant variables

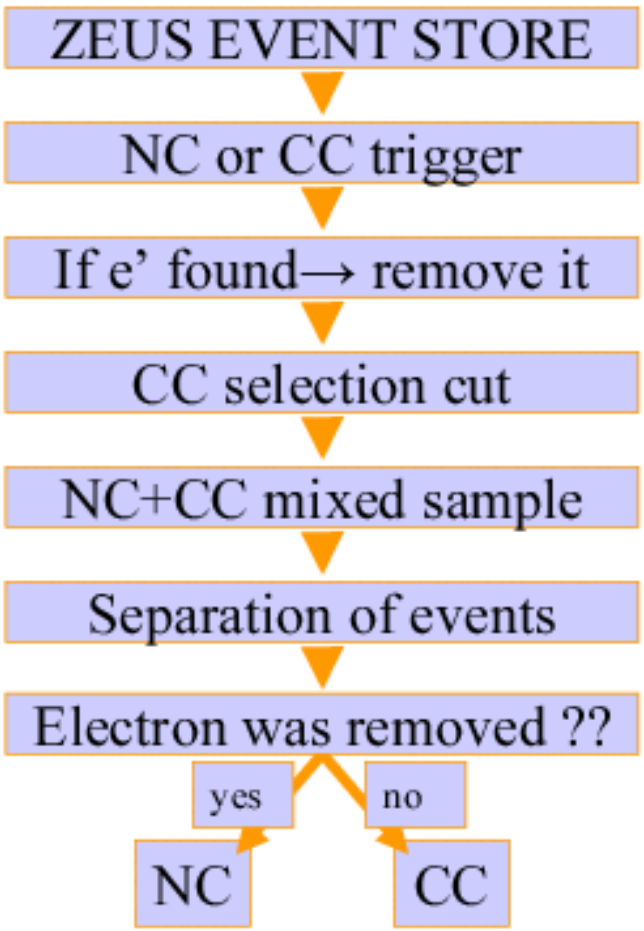

Figure 10.7: Flow diagram for selecting the final NC and CC samples.

which affect directly the data selection. A good agreement between data and MC is observed for all variables.

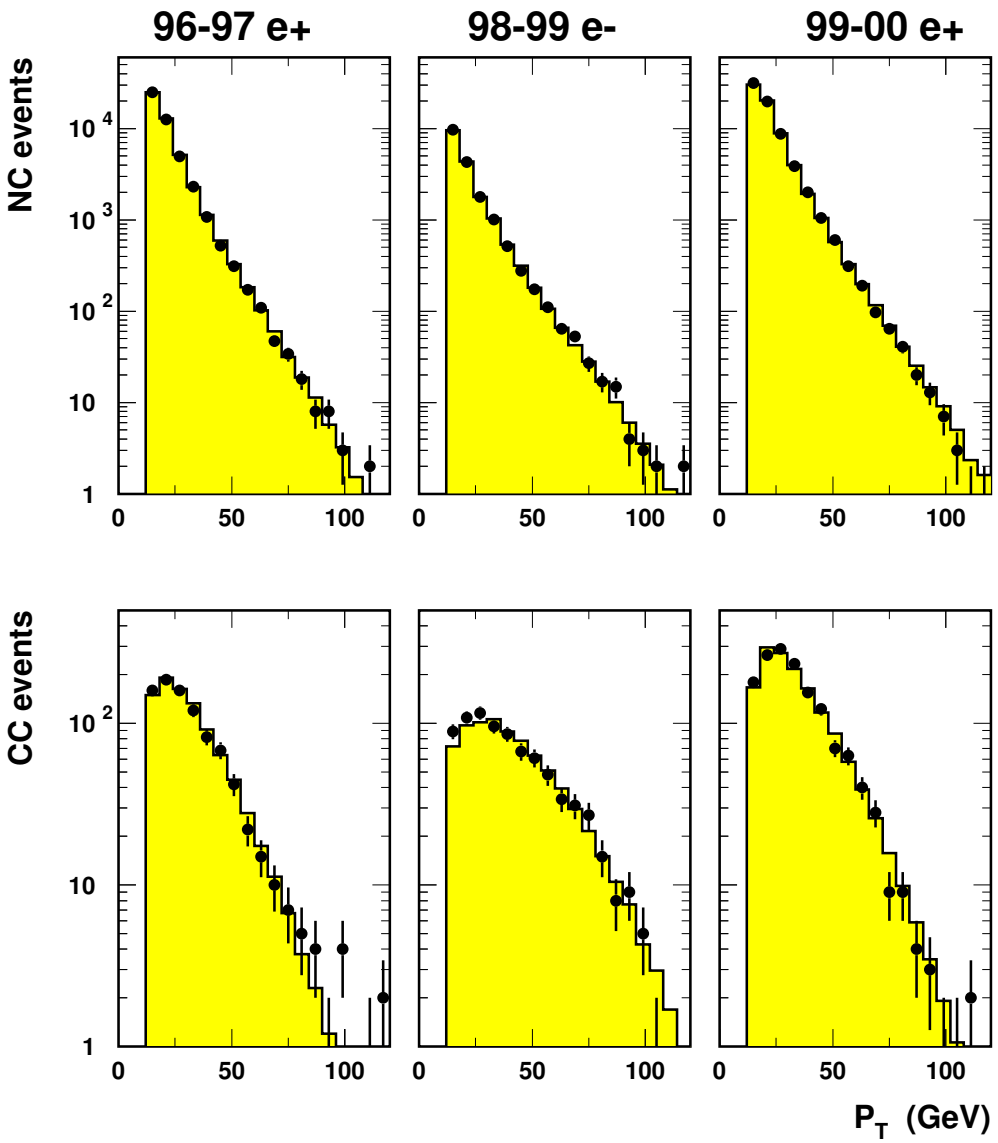

Figure 10.8: Comparison between MC and data for the transverse momentum of the hadronic system, P_T, in the NC (upper figures) and CC (lower figures) samples in the three data sets as denoted in the figure.

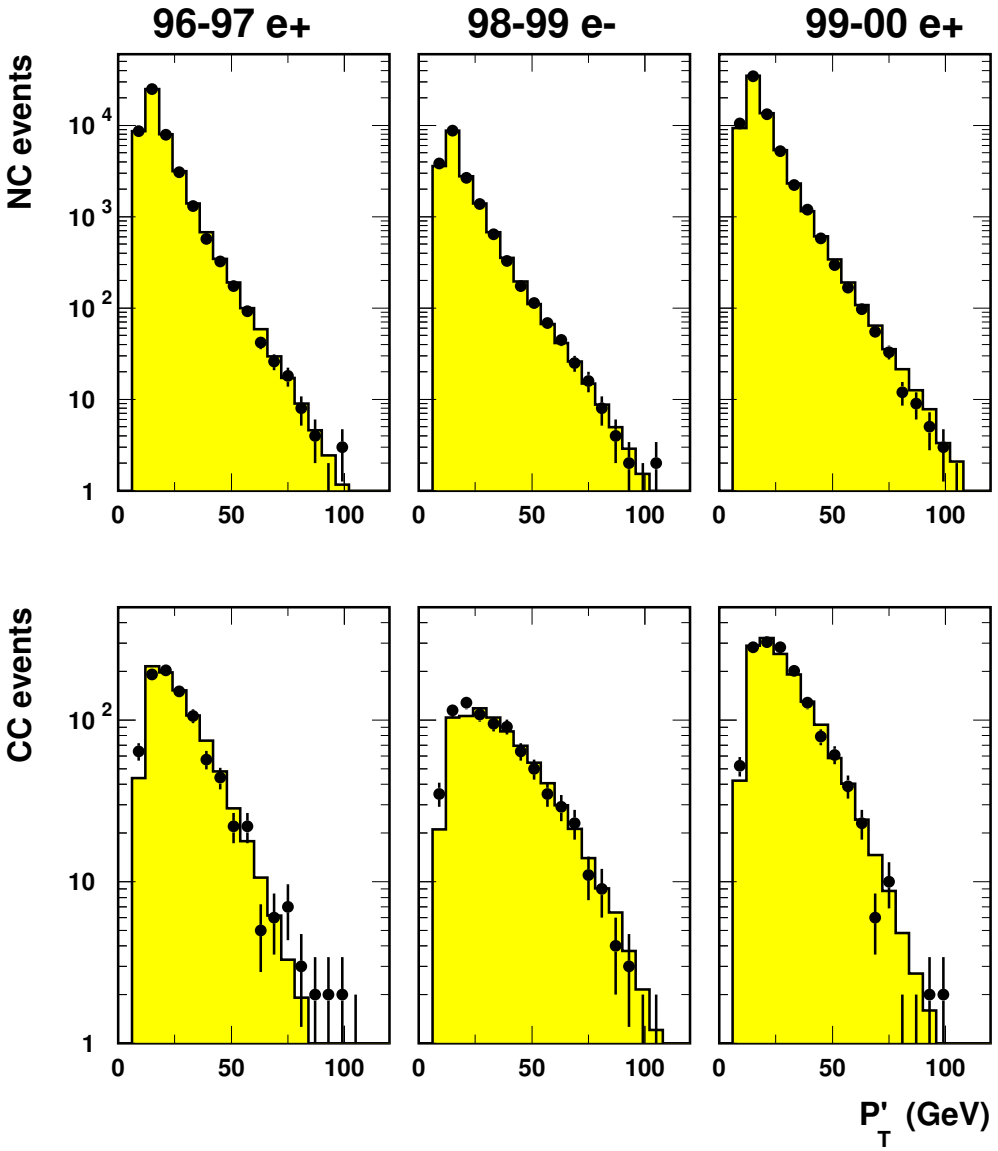

Figure 10.9: Comparison between MC and data for the transverse momentum calculated excluding first inner FCAL ring, P'_T, in the NC (upper figures) and CC (lower figures) samples in the three data sets as denoted in the figure.

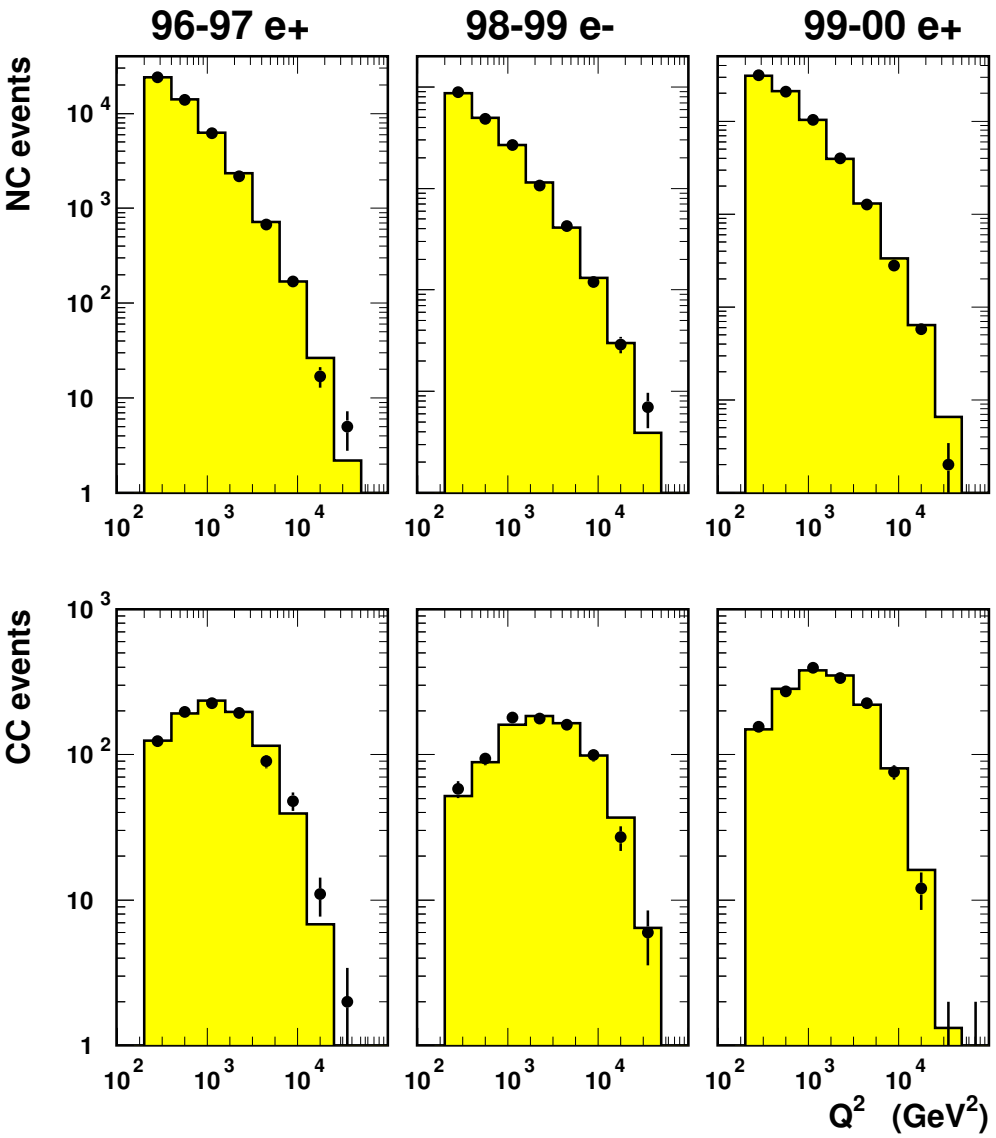

Figure 10.10: Comparison between MC and data for Q^2 in the NC (upper figures) and CC (lower figures) samples in the three data sets as denoted in the figure.

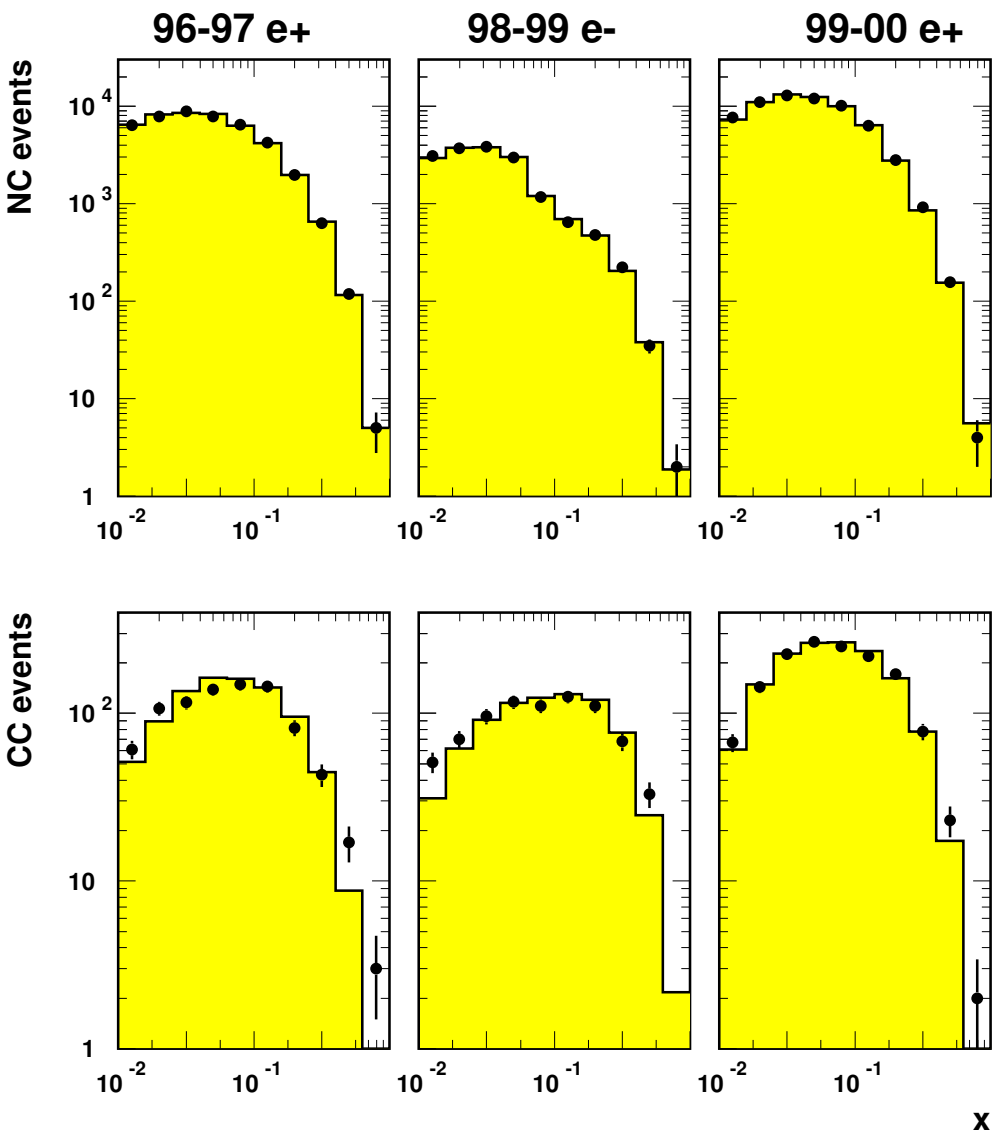

Figure 10.11: Comparison between MC and data for x in the NC (upper figures) and CC (lower figures) samples in the three data sets as denoted in the figure.

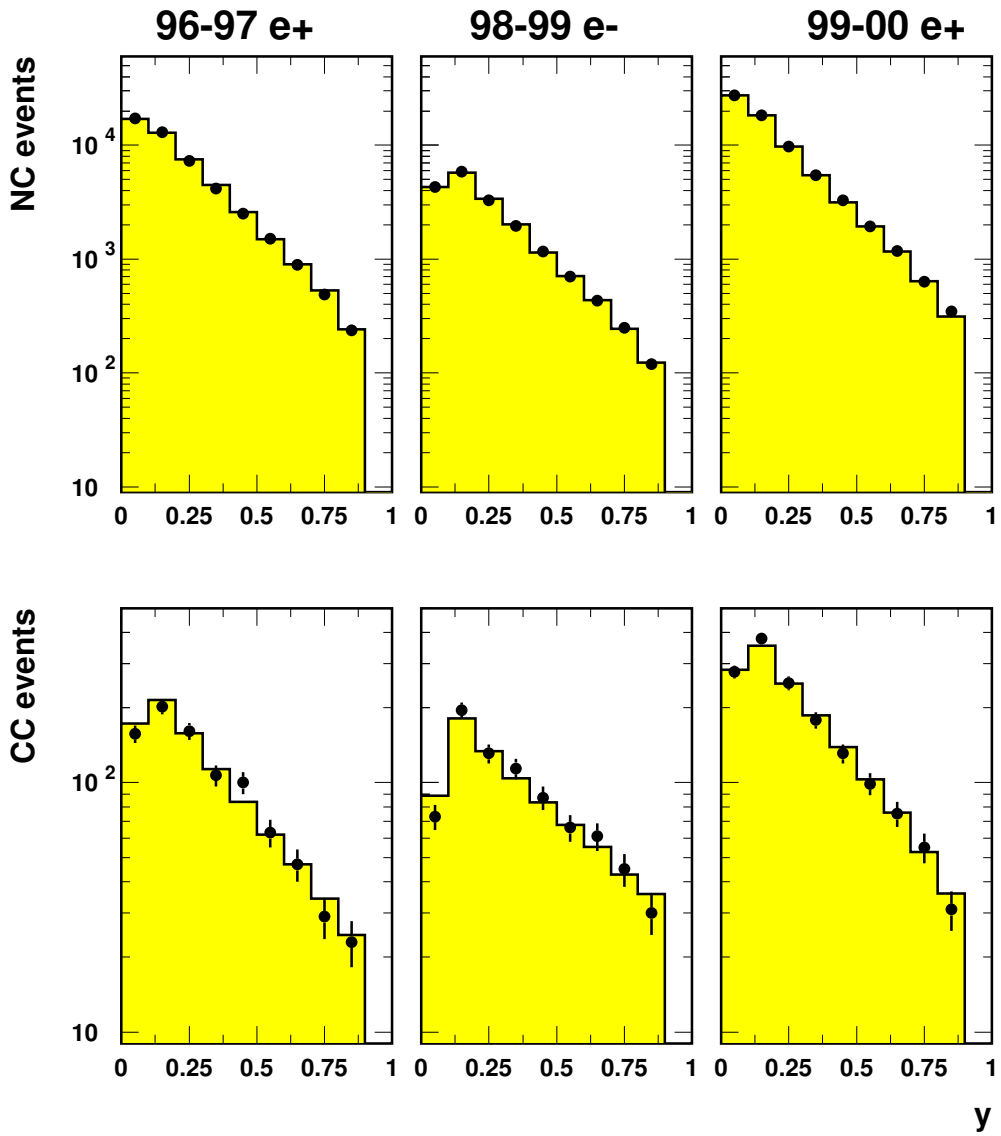

Figure 10.12: Comparison between MC and data for y in the NC (upper figures) and CC (lower figures) samples in the three data sets as denoted in the figure.

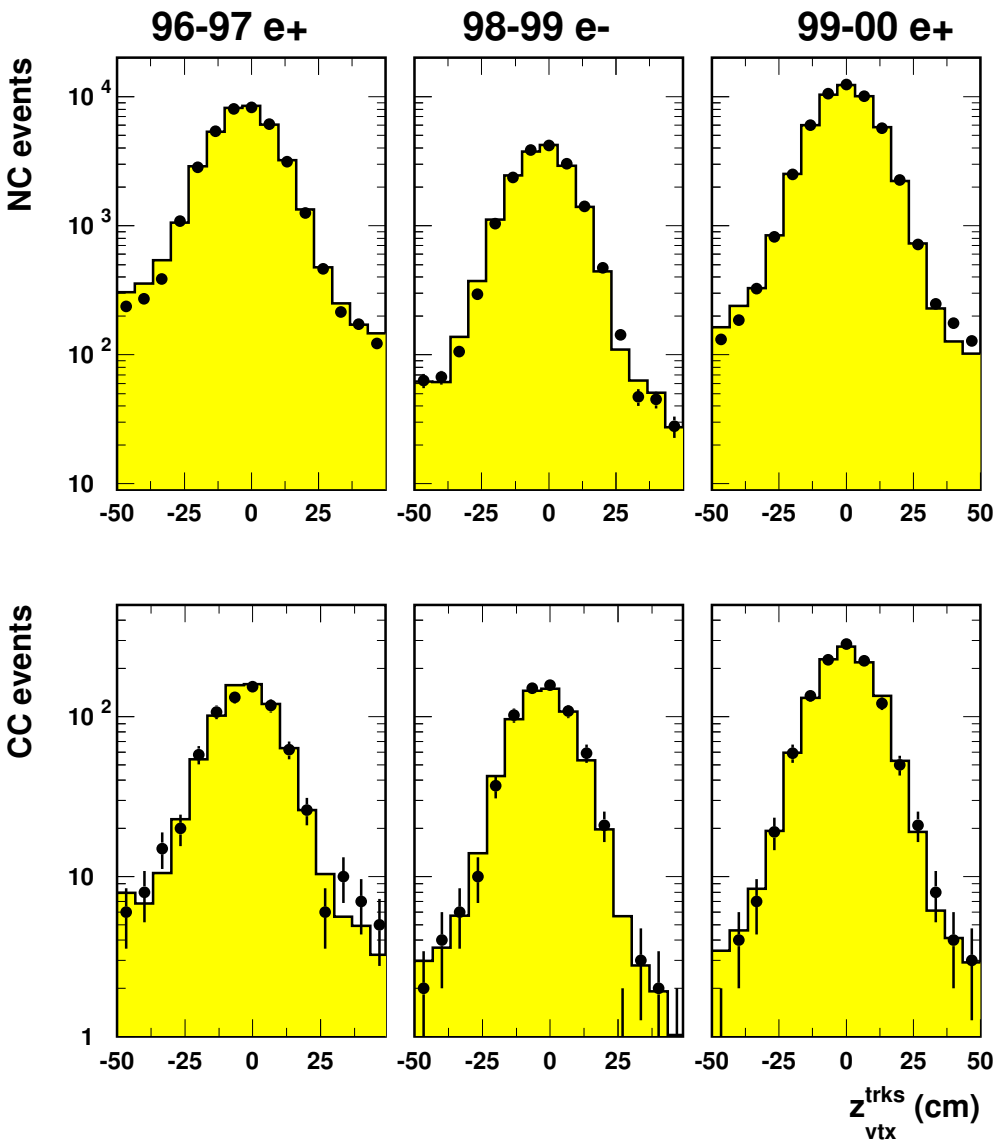

Figure 10.13: Comparison between MC and data for the z-position of the CTD vertex, Z_{vtx}^{trks} in the NC (upper figures) and CC (lower figures) samples in the three data sets as denoted in the figure.

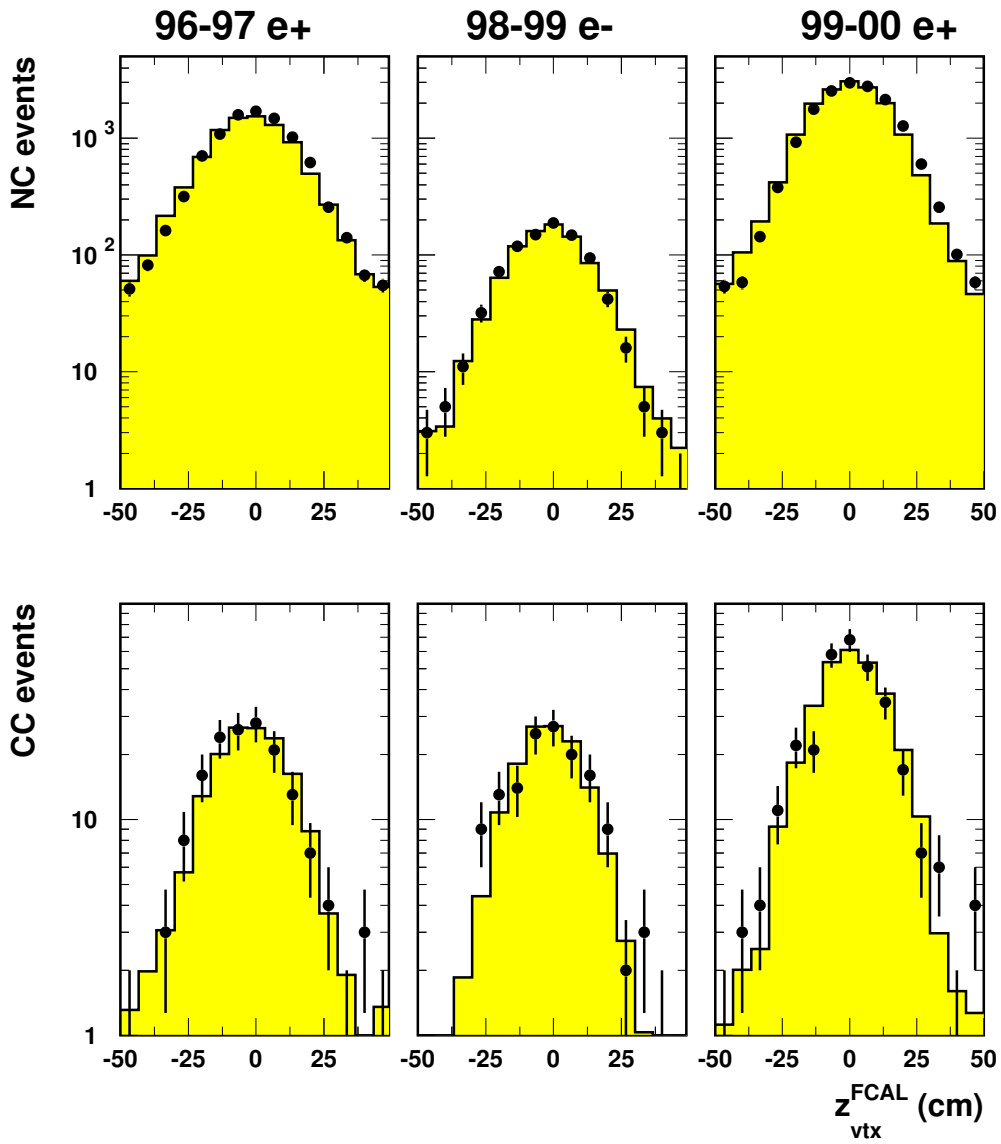

Figure 10.14: Comparison between MC and data for the z-position of the vertex calculated with the arrival time on the FCAL, Z_{vtx}^{FCAL} in the NC (upper figures) and CC (lower figures) samples in the three data sets as denoted in the figure.

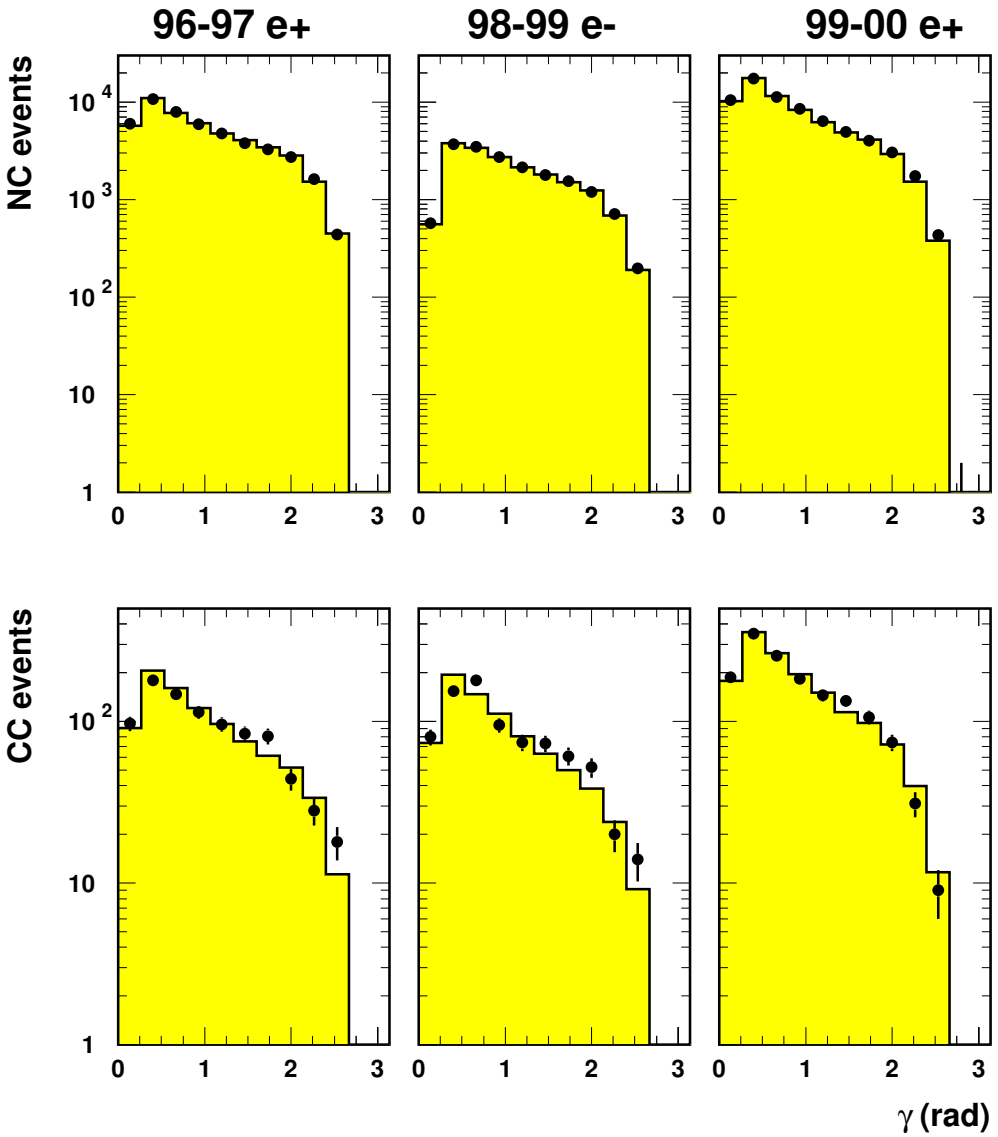

Figure 10.15: Comparison between MC and data for γ in the NC (upper figures) and CC (lower figures) samples in the three data sets as denoted in the figure.

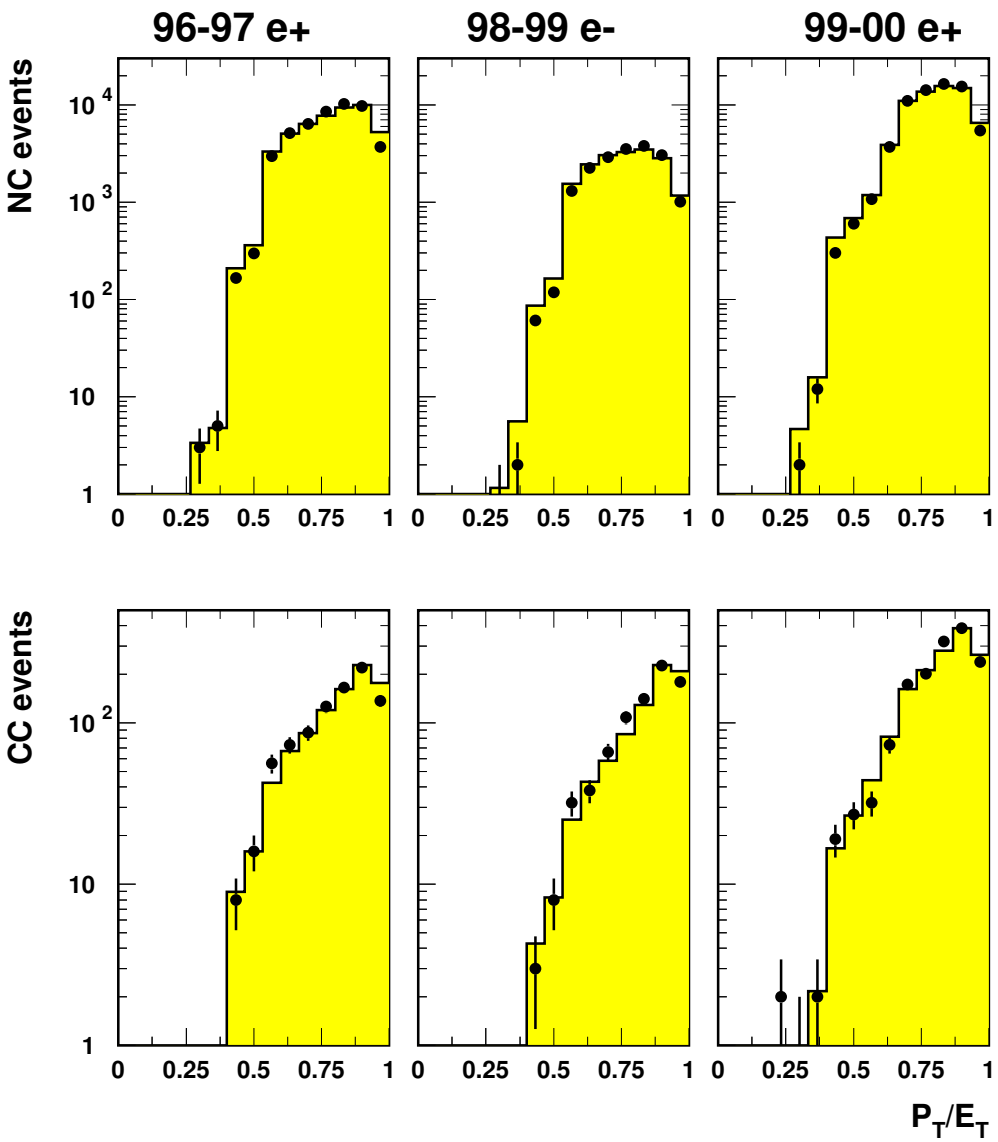

Figure 10.16: Comparison between MC and data for the ratio $\frac{P_T}{E_T}$ in the NC (upper figures) and CC (lower figures) samples in the three data sets as denoted in the figure.

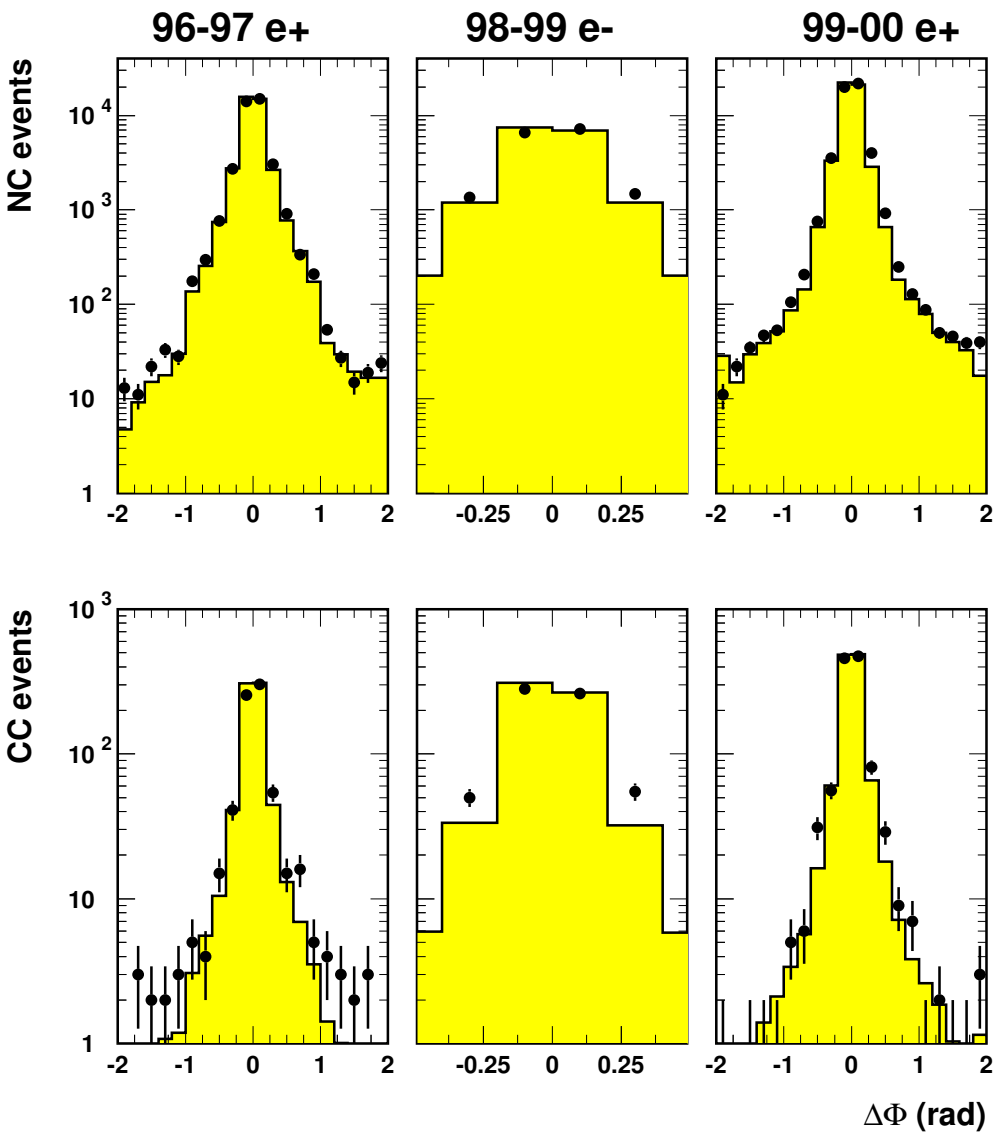

Figure 10.17: Comparison between MC and data for $\Delta\phi$ in the NC (upper figures) and CC (lower figures) samples in the three data sets as denoted in the figure.

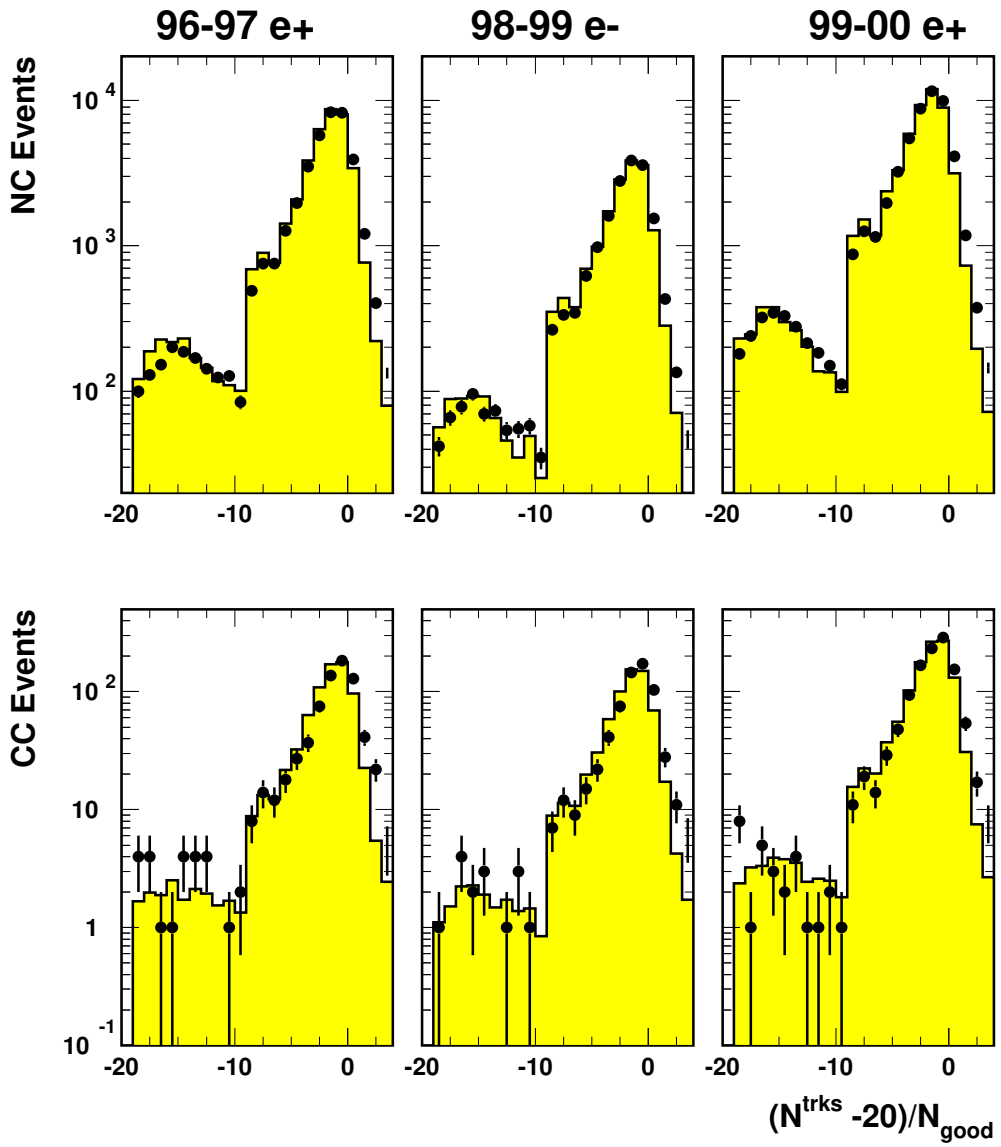

Figure 10.18: Comparison between MC and data for $\frac{N_{trks}-20}{N_{good}}$ in the NC (upper figures) and CC (lower figures) samples in the three data sets as denoted in the figure.

Run period	N_{data}^{NC}	N_{MC}^{NC}	N_{data}^{CC}	N_{MC}^{CC}
1996-1997	47321	47772	889	908
1998-1999	18047	18079	802	793
1999-2000	68347	68134	1474	1480

Table 10.5: The final number of events in the data and in MC in the NC and CC samples in the three data sets.

Run period	$\mathcal{L}$ (pb^{-1})	$\sin^2\theta_W$	stat. error
1996-1997 (e^+p)	38.6	0.232	0.023
1998-1999 (e^-p)	16.7	0.217	0.016
1999-2000 (e^+p)	60.8	0.228	0.017
average		0.227	0.013

Table 10.6: The determined values of $\sin^2\theta_W$ as obtained from the e^+p (1996-1997 and 1999-2000) and the e^-p (1998-1999) data.

10.6 Results

The NC to CC cross sections ratio, corrected for acceptance and resolution effects is calculated with the formula

$$R = \frac{N_{data}^{NC}}{N_{MC}^{NC}} \frac{N_{MC}^{CC}}{N_{data}^{CC}} \frac{\mathcal{L}_{\rm MC}^{\rm CC}}{\mathcal{L}_{\rm MC}^{\rm NC}} \frac{\sigma_{Theory}^{NC}}{\sigma_{Theory}^{CC}}\,, \tag{10.6}$$

where N_{data}^{NC} (N_{MC}^{NC}) is the number of NC events in data (MC), N_{data}^{CC} (N_{MC}^{CC})is the number of CC events in data (MC). The CC (NC) MC luminosity is $\mathcal{L}_{\rm MC}^{\rm CC}$ ($\mathcal{L}_{\rm MC}^{\rm NC}$), and the physical NC (CC) cross section is σ_{Theory}^{NC} (σ_{Theory}^{CC}). In this approach it is required that the MC properly describes the data.

Table 10.5 summarises the event statistics (N_{data}) for the various samples. For comparison, also shown are the expected number of events (N_{MC}) for $\sin^2\theta_W = 0.223$ and CTEQ-5D parameterisation.

In order to determine the value of $\sin^2\theta_W$, the theoretical expectation for R is calculate as a function of $\sin^2\theta_W$. The measured value of R determines the value of $\sin^2\theta_W$ in the data. The errors are calculated accordingly. This is shown schematically in Fig. 10.19, for the three samples. For each of the data samples, the value of $\sin^2\theta_W$ was extracted and the results are summarised in table 10.6.

The weighted average of the three results, also shown in table 10.6, is

$$\sin^2\theta_W = 0.227 \;\pm\; 0.013(stat)\; ^{+0.008}_{-0.009}(syst)\,, \tag{10.7}$$

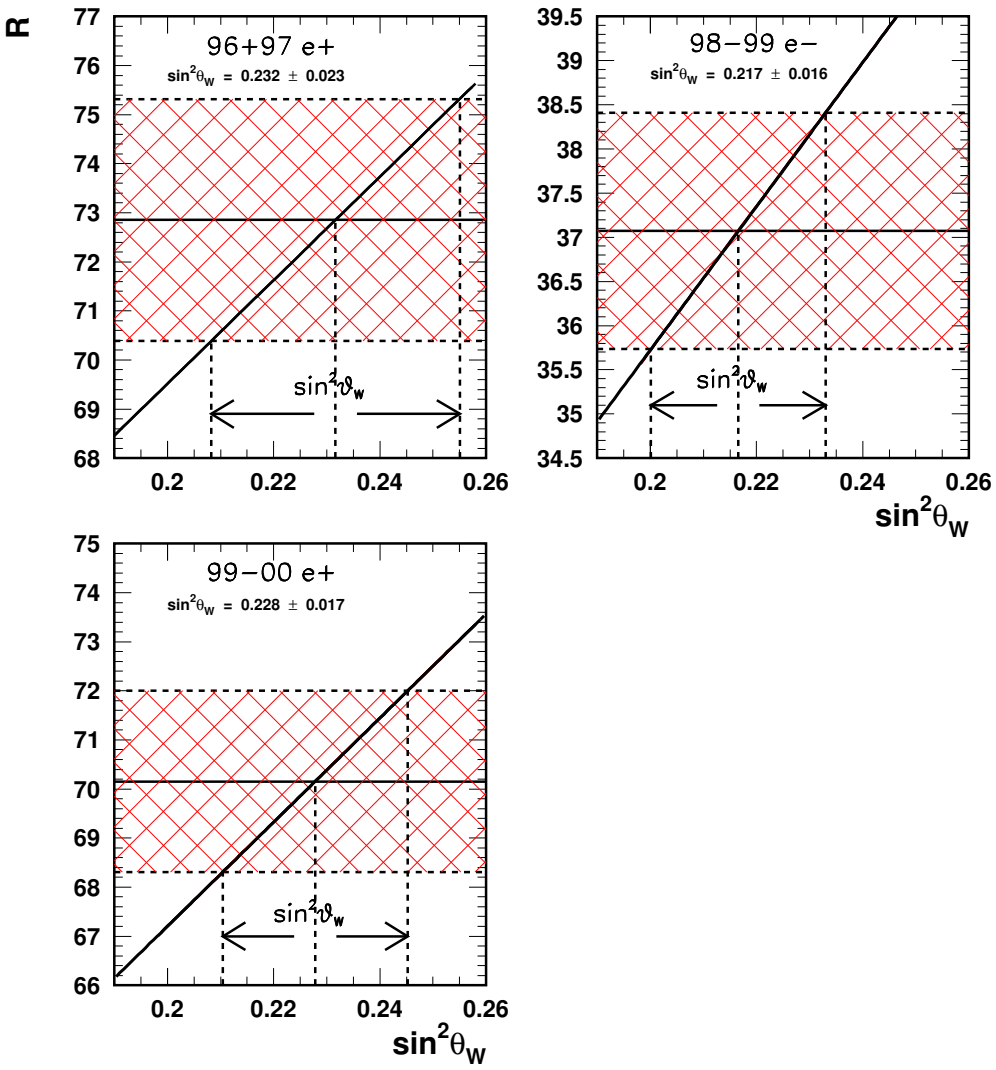

Figure 10.19: The expected ratio of integrated NC to CC cross section ratio, R, for $Q^2 > 200$ GeV^2 and the CTEQ5D parameterisation of parton distributions, as a function of $\sin^2\theta_W$, given for the experimental conditions relevant to the data sets, 1996-1997 (e^+p), 1998-1999 (e^-p), and 1999-2000 (e^+p). Also shown, as bands, are the results of the measurement with the statistical error.

where the sample with the highest luminosity was chosen as the sample to evaluate the systematic error on $\sin^2\theta_W$.

The value of $\sin^2\theta_W$ determined by probing the electroweak interactions at the highest scales ever achieved, is compatible with all previous measure-

ments and the world average for $\sin^2\theta_W$:

$$\sin^2\theta_W = 0.23120 \ \pm \ 0.00015\,, \tag{10.8}$$

and there is no indication of new physics, albeit the statistical significant of the measurement is limited.

Chapter 11

The $\frac{d}{u}$ ratio

11.1 Introduction

DIS experiments have played a crucial role in understanding the structure of the hadrons and in establishing QCD as the theory of strong interactions. The current knowledge of the PDFs is derived from the structure functions measured in these experiments. Precise measurements of the PDFs are needed for reliable predictions for processes involved in hadron-hadron colliders and searches for physics beyond the SM.

The high precision measurements of structure functions at HERA have been instrumental in establishing parton distributions at low x. The medium and high x region is presently, mainly constrained by fixed target experiments such as BCDMS [10], CCFR [43], E665 [12], and NMC [42]. The extraction of PDFs from structure function measurements suffers from uncertainties due to the lack of knowledge of the precise form of parton distributions [40].

The uncertainty of various PDFs is far from uniform. The best precision is obtained in the small/medium x region, but it is still rather poor towards the kinematic limit of large x. For example, there are no measurements of the d/u ratio at large x, as shown in Fig. 11.1, where various parameterisations of the d/u ratio are shown together with the origin of experimental constraints (or the lack of the latter).

In chapter 10, we extracted the value of $\sin^2\theta_W$, by measuring directly the NC to CC cross section ratio assuming that the PDFs are known. In this chapter, the NC to CC cross sections ratio in the e^+p interactions is used to extract the d/u at high x, assuming that all SM parameters are precisely known.

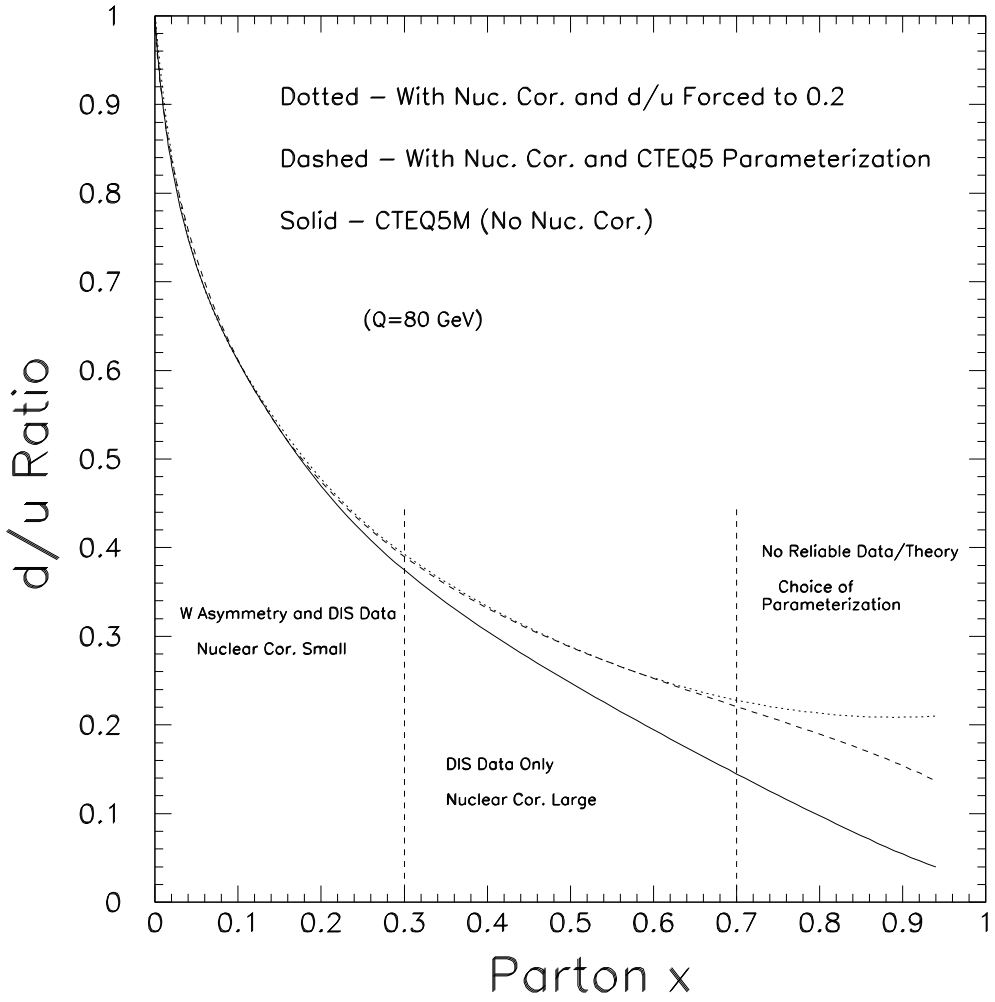

Figure 11.1: The $\frac{d}{u}$ ratio as a function of x for $Q^2 = 6400$ GeV^2. The solid (dashed) line corresponds to the parameterisation from CTEQ5M without (with) nuclear corrections. The dotted line represents the result with nuclear corrections and the $\frac{d}{u}$ ratio forced to be 0.2 at $x = 1$.

11.2 Assumption

For e^+p interactions and at $x > 0.35$, the NC cross section is dominated by the quarks d and u, while the CC cross section is dominated by the d quark. The double differential NC cross section at the Born level can be written as

$$\frac{d^2\sigma^{NC}}{dxdQ^2} = \frac{2\pi\alpha^2}{xQ^4}\left[Y_+F_2(x,Q^2) - Y_-xF_3(x,Q^2)\right] , \qquad (11.1)$$

with $Y_\pm = 1 \pm (1-y)^2$ and

$$\begin{aligned} F_2 &= A_u \cdot xu(x,Q^2) + A_d \cdot xd(x,Q^2)\,, & (11.2)\\ xF_3 &= B_u \cdot xu(x,Q^2) + B_d \cdot xd(x,Q^2)\,, & (11.3)\\ A_u &= \frac{1}{2}(A_u^L(Q^2) + A_u^R(Q^2))\,, & (11.4)\\ A_d &= \frac{1}{2}(A_d^L(Q^2) + A_d^R(Q^2))\,, & (11.5)\\ B_u &= \frac{1}{2}(B_u^L(Q^2) + B_u^R(Q^2))\,, & (11.6)\\ B_d &= \frac{1}{2}(B_d^L(Q^2) + B_d^R(Q^2))\,, & (11.7) \end{aligned}$$

where A and B were introduced in eq. (2.14) and are repeated for completeness. The double differential CC cross section at the Born level is

$$\frac{d^2\sigma^{CC}}{dxdQ^2} = \frac{G_\mu^2}{4\pi x}\frac{M_W^4}{(Q^2+M_W^2)^2}\left[Y_+ F_2^{CC}(x,Q^2) - Y_- xF_3^{CC}(x,Q^2)\right]\,, \qquad (11.8)$$

where the CC structure functions, $F_2^{CC}(x,Q^2)$ and $xF_3^{CC}(x,Q^2)$, are simply given by

$$\begin{aligned} F_2^{CC}(x,Q^2) &= xd(x,Q^2)\,, & (11.9)\\ xF_3^{CC}(x,Q^2) &= xd(x,Q^2)\,. & (11.10) \end{aligned}$$

In order to derive the dependence of the NC to CC cross section ratio on the d to u ratio, we introduce the following notation:

$$\begin{aligned} FF^{NC}(x,Q^2) &= \frac{2\pi\alpha^2}{xQ^4}\,, & (11.11)\\ FF^{CC}(x,Q^2) &= \frac{G_\mu^2}{4\pi x}\left(\frac{M_W^4}{(M_W^2+Q^2)^2}\right)(Y_+ - Y_-)\,, & (11.12)\\ ABU(Q^2) &= Y_+ A_u(Q^2) - Y_- B_u(Q^2)\,, & (11.13)\\ ABD(Q^2) &= Y_+ A_d(Q^2) - Y_- B_d(Q^2)\,. & (11.14) \end{aligned}$$

Then

$$R_{CC}^{NC}(x,Q^2) = FF_{CC}^{NC}(Q^2)\left[ABU(Q^2)\cdot\frac{u(x,Q^2)}{d(x,Q^2)} + ABD(Q^2)\right]\,, \qquad (11.15)$$

where

$$R_{CC}^{NC}(x,Q^2) \equiv \frac{\frac{d^2\sigma^{NC}}{dxdQ^2}(x,Q^2)}{\frac{d^2\sigma^{CC}}{dxdQ^2}(x,Q^2)}\,. \qquad (11.16)$$

F_{CC}^{NC} stands for

$$F_{CC}^{NC}(x,Q^2) \equiv \frac{FF^{NC}(x,Q^2)}{FF^{CC}(x,Q^2)}\,. \tag{11.17}$$

The measured value of R_{CC}^{NC}, $R_{CC}^{NC}(data)$, can be obtained by the following:

$$R_{CC}^{NC}(data)(x,Q^2) = \frac{N_{data}^{NC}}{N_{MC}^{NC}}\frac{N_{MC}^{CC}}{N_{data}^{CC}}R_{CC}^{NC}(x,Q^2)\,, \tag{11.18}$$

where N with a subscript/superscript stands for number of events in a particular bin $[x-\Delta x, x+\Delta x]$. In the region where the contribution of sea quarks is negligible, the ratio $\frac{d}{u}$ at a kinematic point (x_0, Q_0^2) is given by

$$\frac{d}{u}(x_0,Q_0^2) = \frac{ABU(Q_0^2)\cdot FF_{CC}^{NC}(x_0,Q_0^2)}{R_{CC}^{NC}(data)(x_0,Q_0^2) - ABD(Q_0^2)\cdot FF_{CC}^{NC}(x_0,Q_0^2)}\,. \tag{11.19}$$

11.3 Event selection

The data analysed in this chapter is based on the data collected with the ZEUS detector during the run period 1999-2000, with an equivalent integrated luminosity of 60.8 pb^{-1}. The NC and CC events in this analysis are selected the same way as described in chapter 10.

11.4 Kinematic region

The NC and CC events in the final samples are required to be in the following kinematic region

$$Q^2 > 1000 \text{ GeV}^2, \quad x > 0.35 \quad \text{and} \quad y < 0.9\,. \tag{11.20}$$

The region was selected to ensure that the contribution to the cross sections due to the sea quarks is negligible. Both NC and CC cross sections were calculated in two ways: once with the valence quarks and once with the valence-and-sea quarks. The resulting fraction of the cross section due to valence quarks contribution is shown in Fig. 11.2. The sea quarks contribution vanishes in the NC (CC) case at $x > 0.6$ ($x > 0.75$). Since no events with $x > 0.7$ are available in the ZEUS data, the measurements of the ratio $\frac{d}{u}$ are done at x values where the correction due to sea quarks is less than 10%. The cross sections are then corrected for the contribution from the sea quarks.

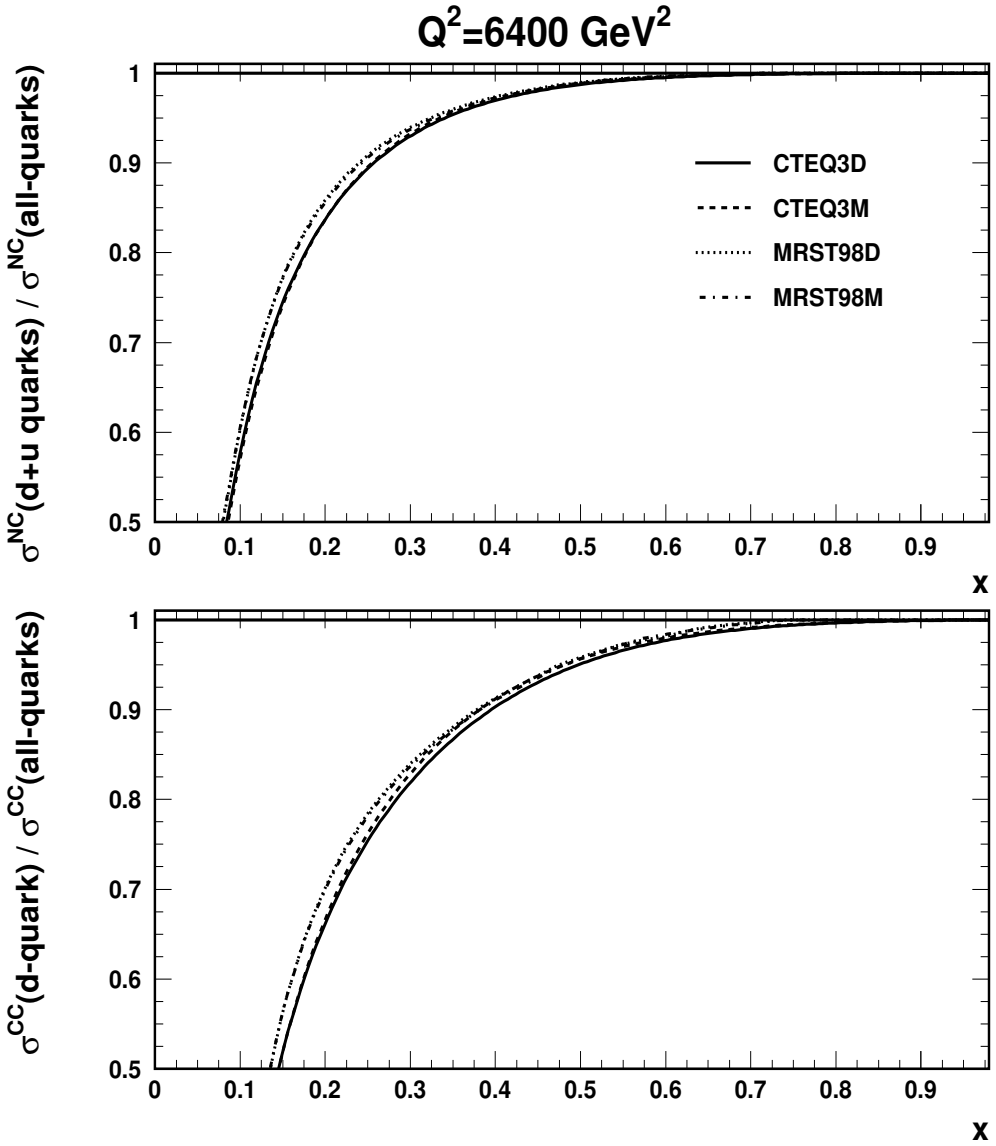

Figure 11.2: Upper plot: The fraction of the NC cross section due only to u and d quarks. Lower plot: The fraction of the CC cross section due only to d quarks.

11.5 Final samples

The final NC and CC samples contain events selected with cuts listed in Table 10.4 with the additional requirement of the particular kinematic region. In total, 287 NC events and 34 CC events were selected in the data. The

final events populate mainly the low γ_0 and high P_T region, i.e. high x and high Q^2 events, as shown in Fig. 11.3.

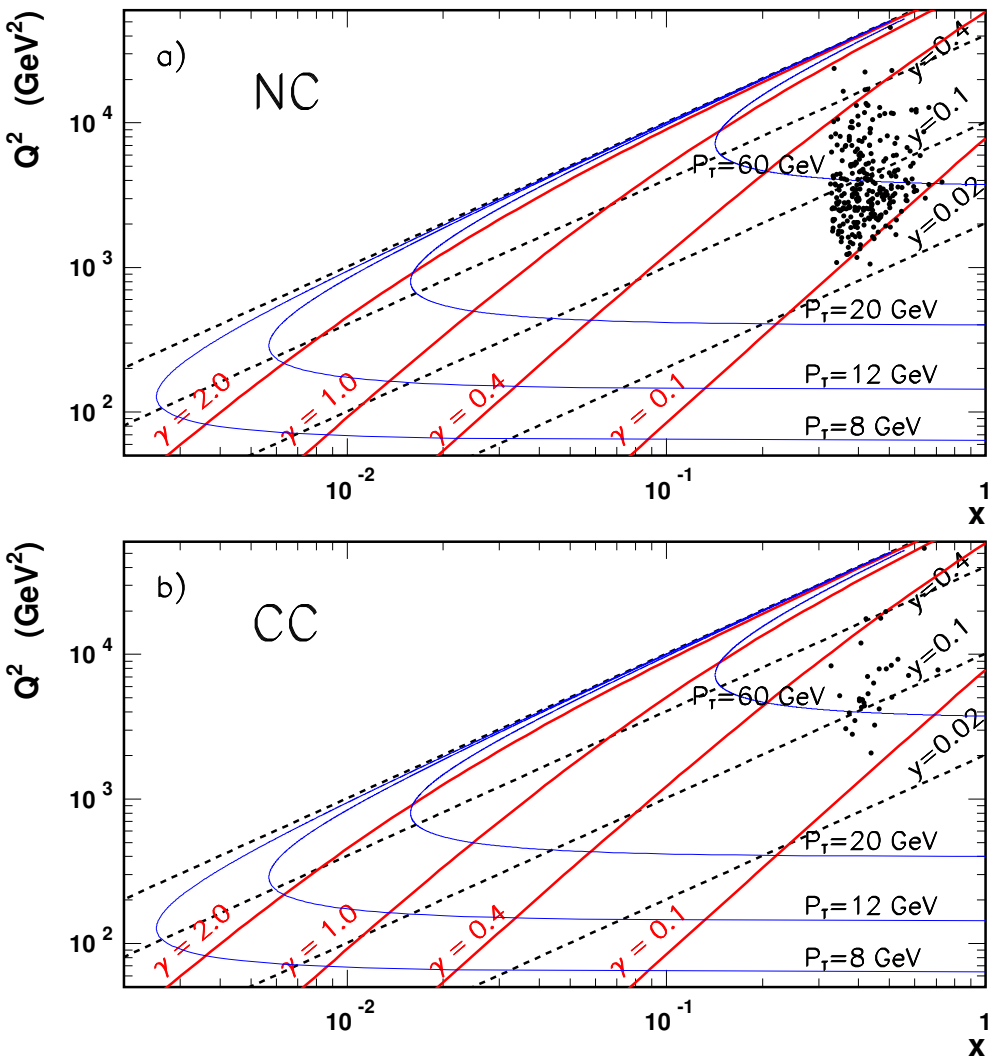

Figure 11.3: Fig. a) (b)): the kinematical phase-space in $Q^2 - x$ plane for the NC (CC) events, with iso-lines of y, P_T, and γ.

11.6 Monte Carlo and data comparison

In this section, the most relevant variables in this analysis are presented and a comparison between the MC expectations and the data is shown. This was

already presented in chapter 10 and repeated here in the specific kinematic region for completeness. In Fig. 11.4-11.6 the distributions of P_T, E_T, P_T/E_T, Q^2, x, and y are presented for the NC and CC final samples. The energy and the polar angle of the scattered electron in the final NC sample are shown in Fig. 11.7. As expected, the polar angle of the scattered electron in this sample is relatively large with relatively large energies. In general, the MC expectations reproduce well the data in all distributions.

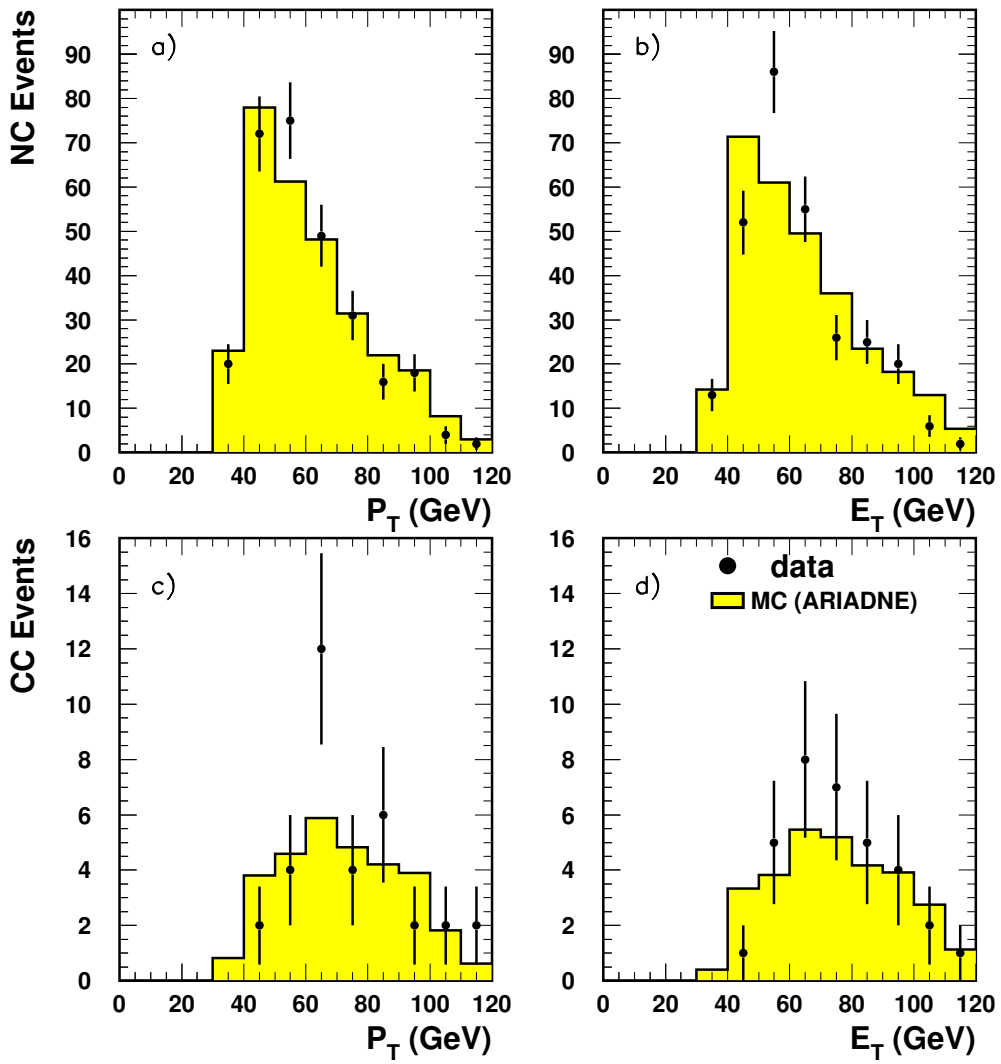

Figure 11.4: Upper: the P_T (a) and E_T (b) distribution for the final NC sample. Lower: the P_T (c) and E_T (d) distribution for the final CC sample.

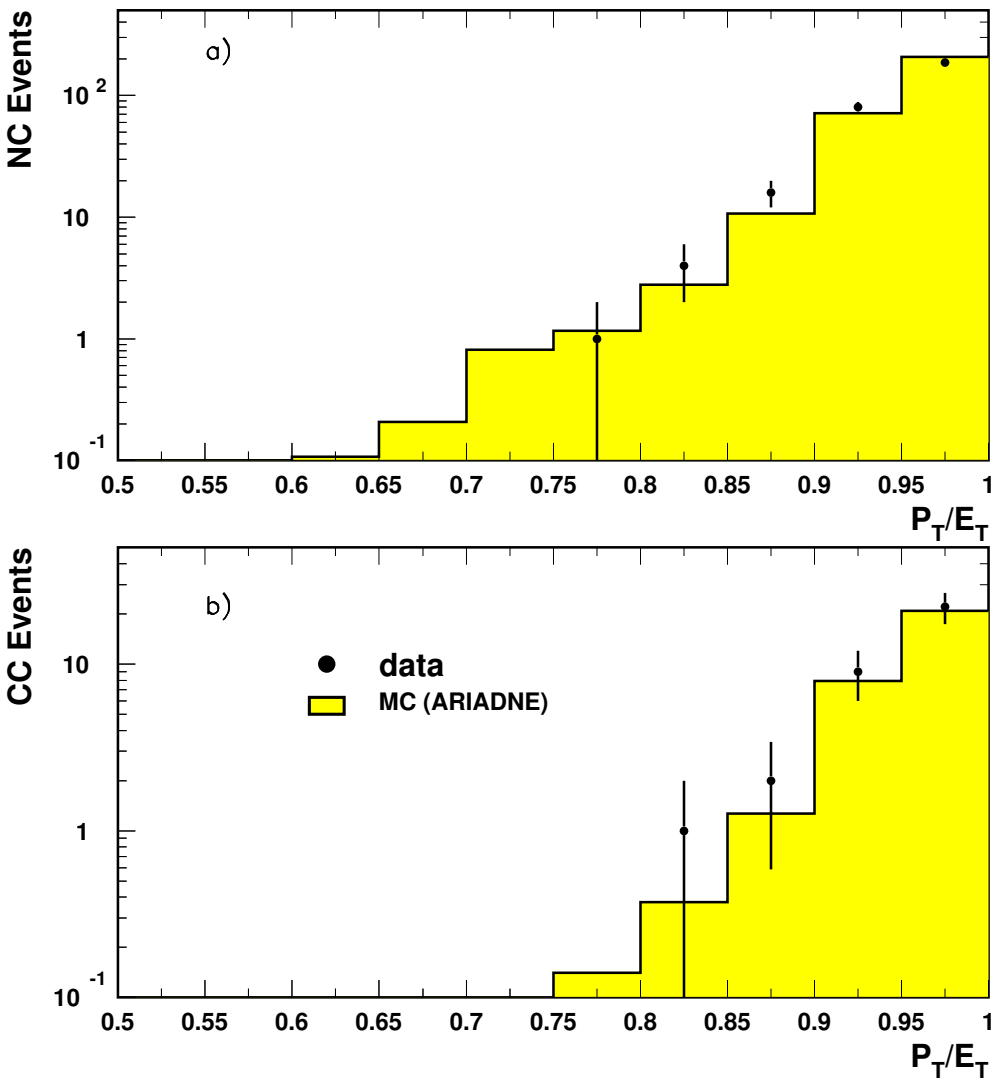

Figure 11.5: The $\frac{P_T}{E_T}$ distribution for the NC (a) and CC (b) final samples.

11.7 $\frac{d}{u}$ extraction

The ratio $\frac{d}{u}$ is extracted in three bins of x at $Q^2 = 6400$ GeV^2, as presented in Table 11.1. In the table, also the number of events in the data is compared to that expected from the MC. A good agreement is observed.

The extracted values of $\frac{d}{u}$ in the given bins are summarised in Table 11.2. For comparison, also given are the $\frac{d}{u}$ values for the CTEQ3D parameterisation. The errors quoted in this table are due to statistical uncertainties only.

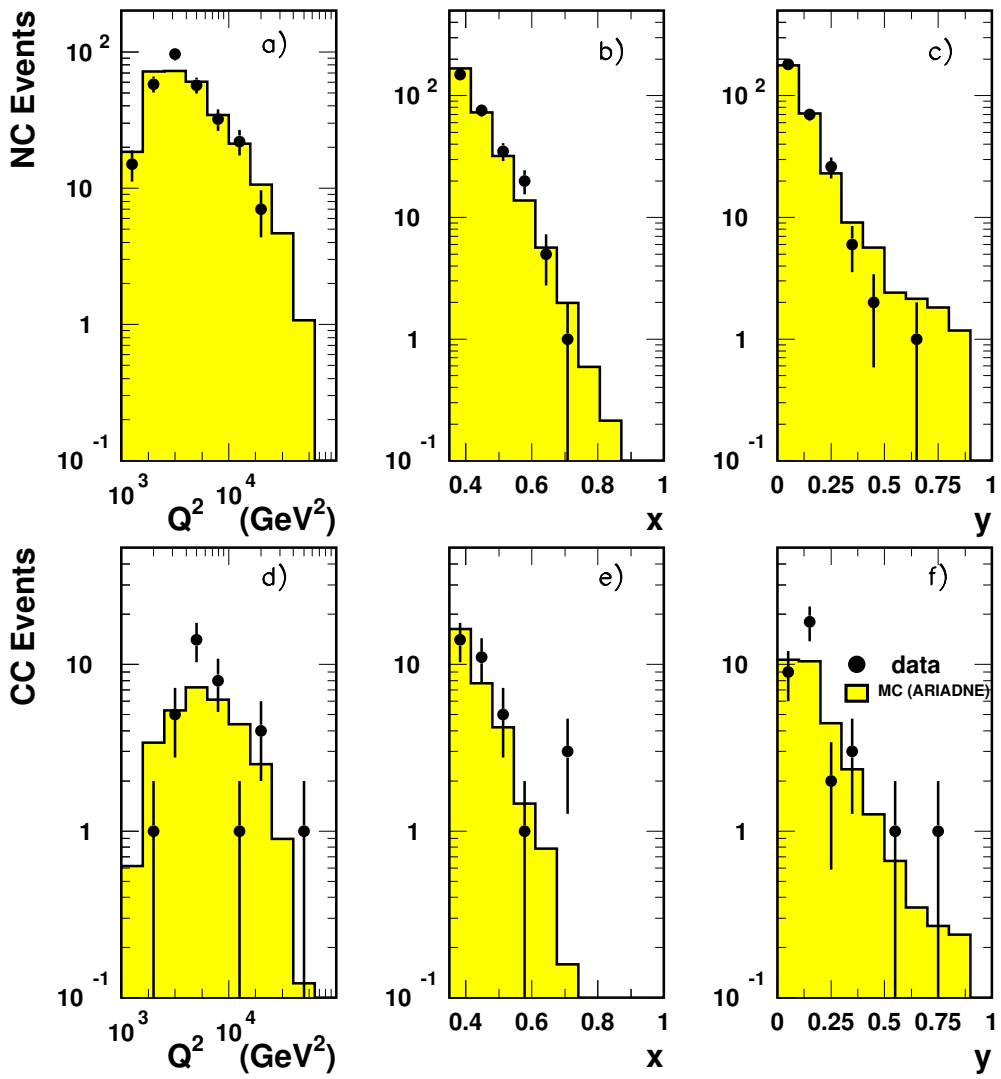

Figure 11.6: The kinematic variables, Q^2,x, and y distributions for NC sample are presented in Fig. a), b), and c), respectively. The corresponding distributions for the CC sample are presented in Fig. d), e), and f).

A good agreement between the extracted values and the expected ones is obtained. The results are shown in Fig. 11.8 where the extracted $\frac{d}{u}$ values are compared to several parameterisations. Within the present uncertainty, there is good agreement with the chosen parameterisations.

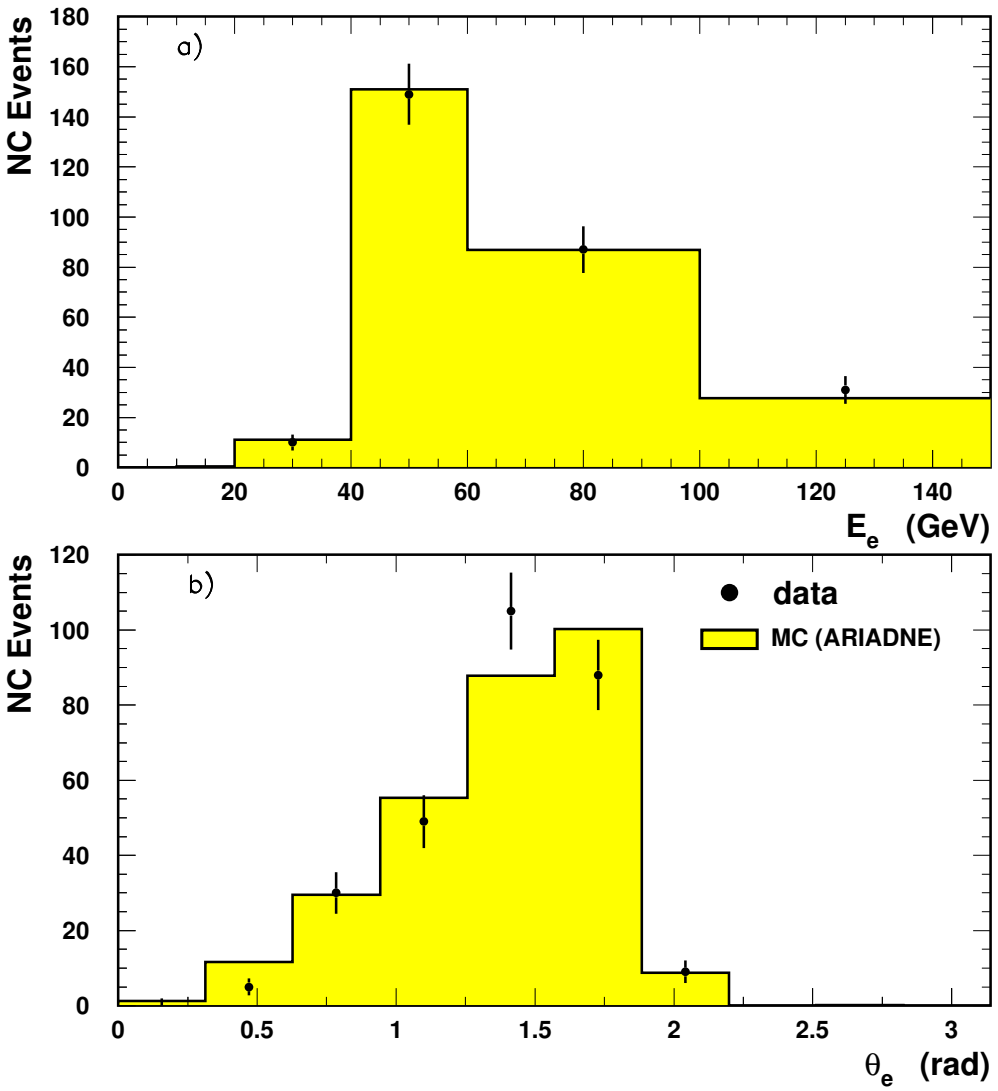

Figure 11.7: Fig. a) (b)): the energy and the the polar angle of the scattered electron for the final NC sample.

11.8 Outlook

This is the first determination of the $\frac{d}{u}$ ratio at high x and high Q^2 in ep interactions. The precision of this measurement is limited by the statistical uncertainty. HERA II is expected to deliver about 700 pb^{-1} before it will close down operation in summer 2007. This opens an opportunity to measure the $\frac{d}{u}$ ratio with more than ten times the statistics of this analysis. Therefore we expect to achieve a precision higher by a factor of three.

x-range	x_0	N_{data}^{NC}	N_{MC}^{NC}	N_{data}^{CC}	N_{MC}^{CC}
0.35-0.41	0.38	139	157.6	14	15.6
0.41-0.50	0.44	101	93.4	13	10.1
0.50-0.75	0.60	47	42	7	4.9

Table 11.1: Comparison of the data and MC events for NC and CC samples in three bins of x. Given in the table are the x-range, the bin centre (x_0), the number of NC data events (N_{data}^{NC}), the number of NC MC events (N_{MC}^{NC}), the number of CC data events (N_{data}^{CC}), and number of CC MC events (N_{MC}^{CC}).

x_0	$\frac{d}{u}$(extracted)	$\frac{d}{u}$(expected)
0.38	0.27 ± 0.08	0.27
0.44	0.28 ± 0.09	0.24
0.60	0.23 ± 0.10	0.18

Table 11.2: The extracted values of $\frac{d}{u}$ from the data, compared to the expectations using the CTEQ3D parameterisation, at the x-bin centre x_0.

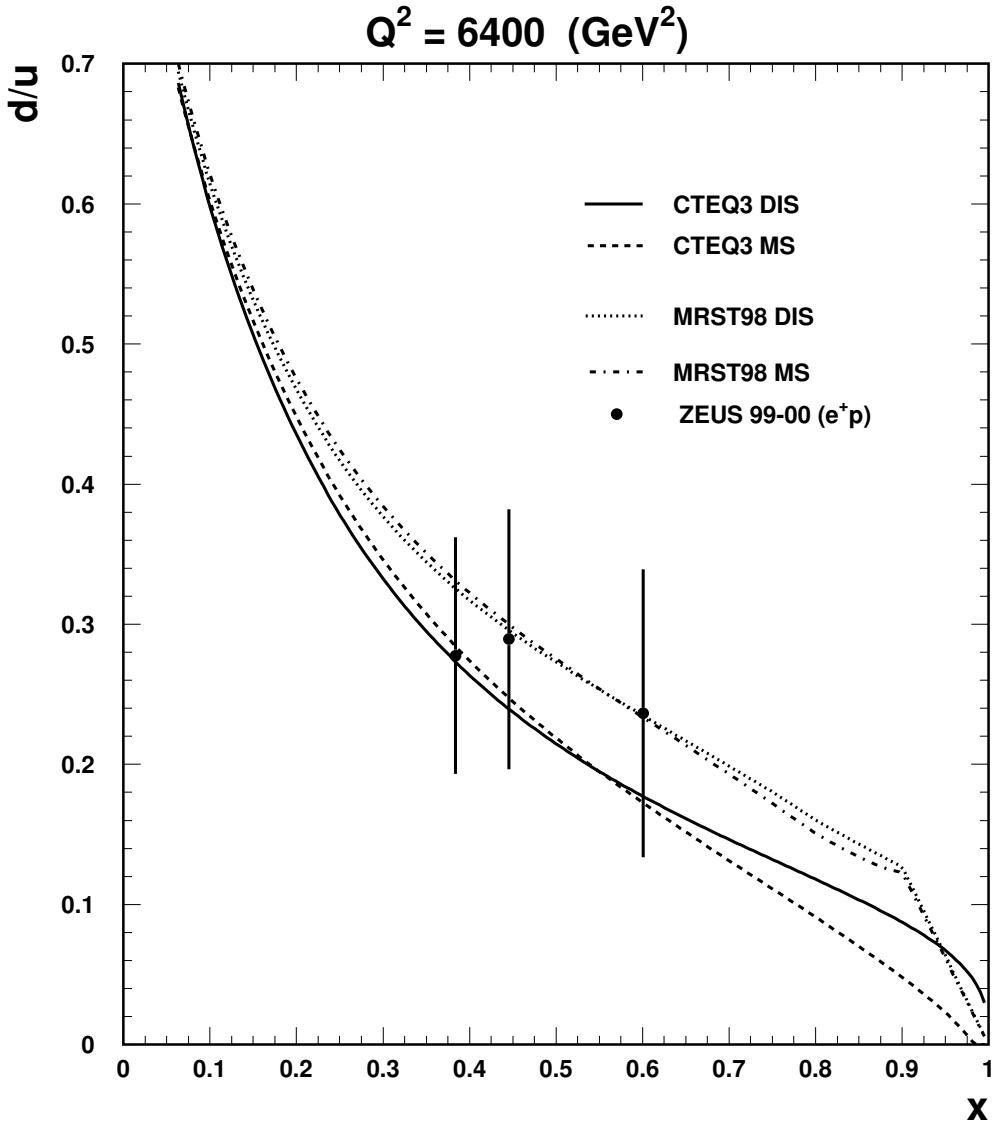

Figure 11.8: The ratio $\frac{d}{u}$ ratio as a function of x. The dots stand for the extracted $\frac{d}{u}$ using the 1999-2000 data, and the curves are the expectations for the parameterisations CTEQ3 DIS, CTEQ3 MS, MRST98 DIS, and MRST98 MS.

Appendix A

Figures for systematic uncertainties checks for charged current analysis

In Figs. A.1-A.12, a graphical representation of the systematic uncertainties (in percentage) for the LH and RH differential cross sections versus Q^2, x, and y are shown with respect to varying the high and low γ_0 selection cuts. In most checks and in most bins, the cross sections differ by only a few percents due to varying the selection cuts.

In Figs A.13-A.18, a graphical representation of the systematic uncertainties (in percentage) for the LH and RH differential cross sections versus the kinematic variables Q^2, x, and y are shown with respect to varying the calorimeter energy scale in the MC simulation. The largest effect in the cross section is up-to 5%.

In Fig A.19, the systematic uncertainty (in percentage) for the LH and RH differential cross sections due to replacing the ARIADNE MC with the MEPS one, is shown. The largest systematic effects in the cross section are up-to 5%.

Fig A.20 displays the P_T/E_T of the enriched photoproduction sample for LH and RH is shown with the χ^2 distributions for the parameters α and β. See sec 8.4 for further details.

Fig A.21 shows the systematic uncertainties in the differential cross sections due to the reweighting of the MC events to the ZEUS-S NLO PDFs. The largest systematic effect is obtained in the low Q^2, low x, and high y, and is about 7%.

In Fig A.22, the systematic uncertainties of the NLO QCD effects are shown. As expected, the largest effect is observed at high y values.

The summary of the systematic checks in the differential cross sections

are summarised in the Tables A.1-A.3.

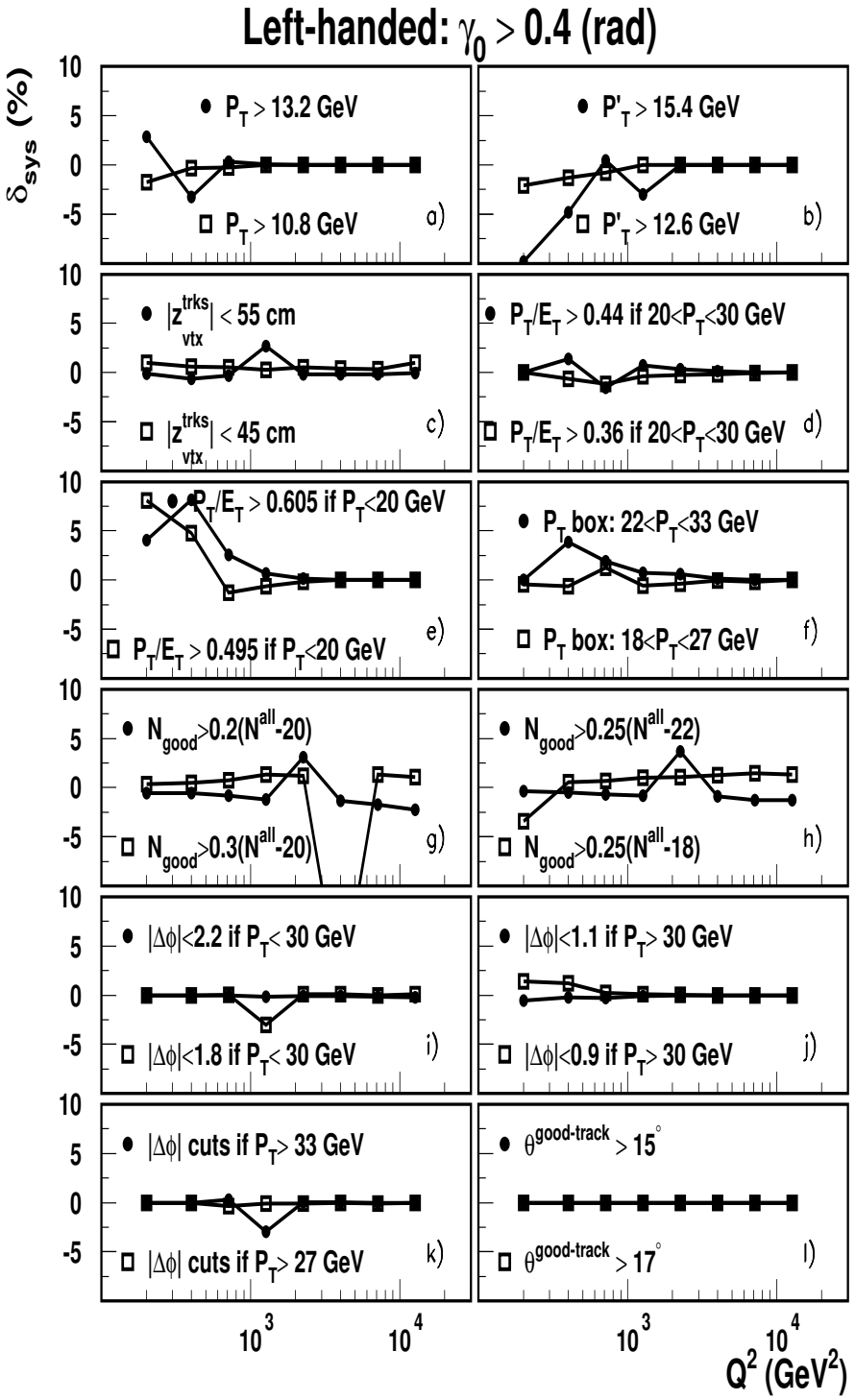

Figure A.1: The systematic uncertainties (in percentage) in the LH differential cross section versus Q^2 for varying the high γ_0 selection cuts.

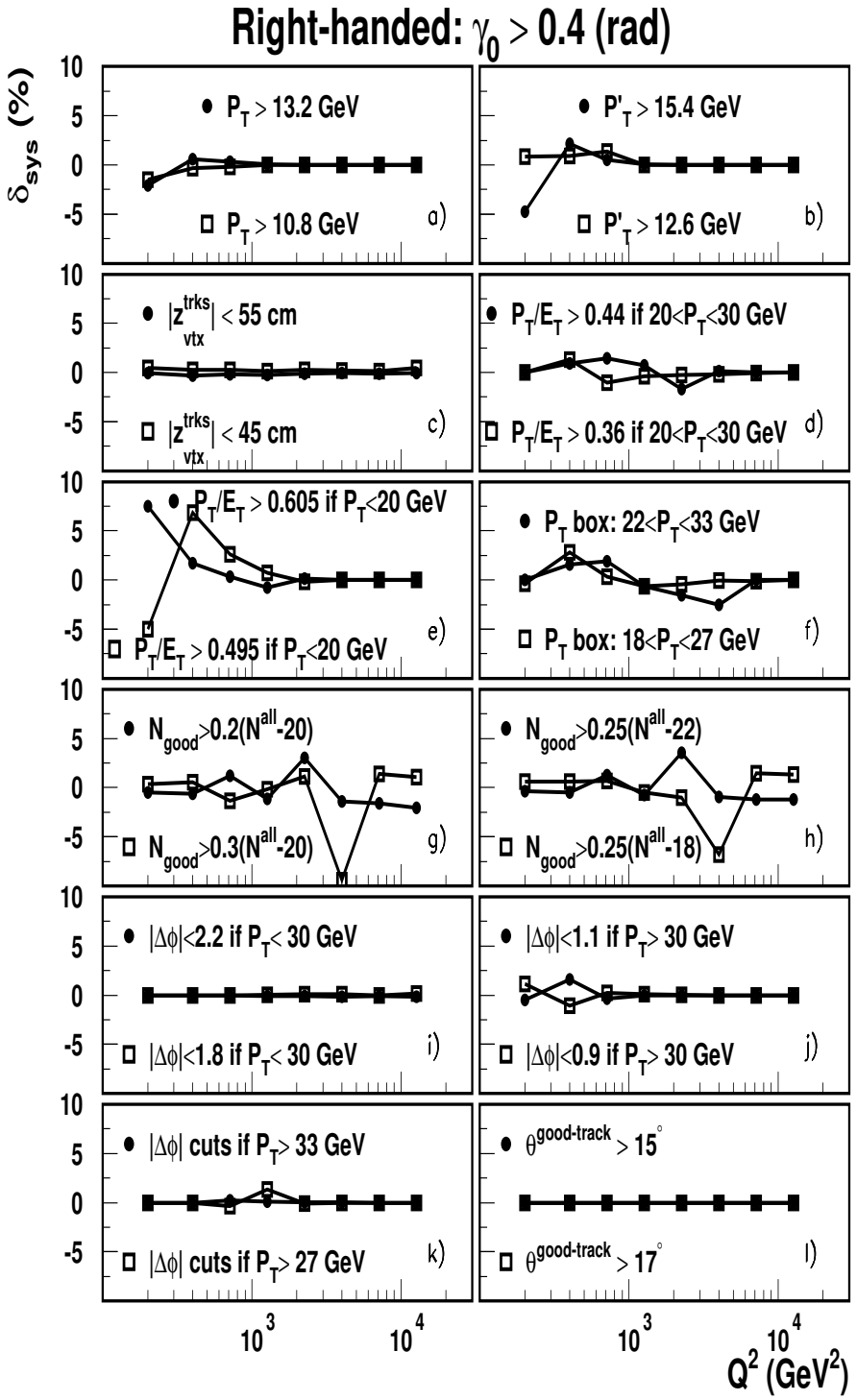

Figure A.2: The systematic uncertainties (in percentage) in the RH differential cross section versus Q^2 for varying the high γ_0 selection cuts.

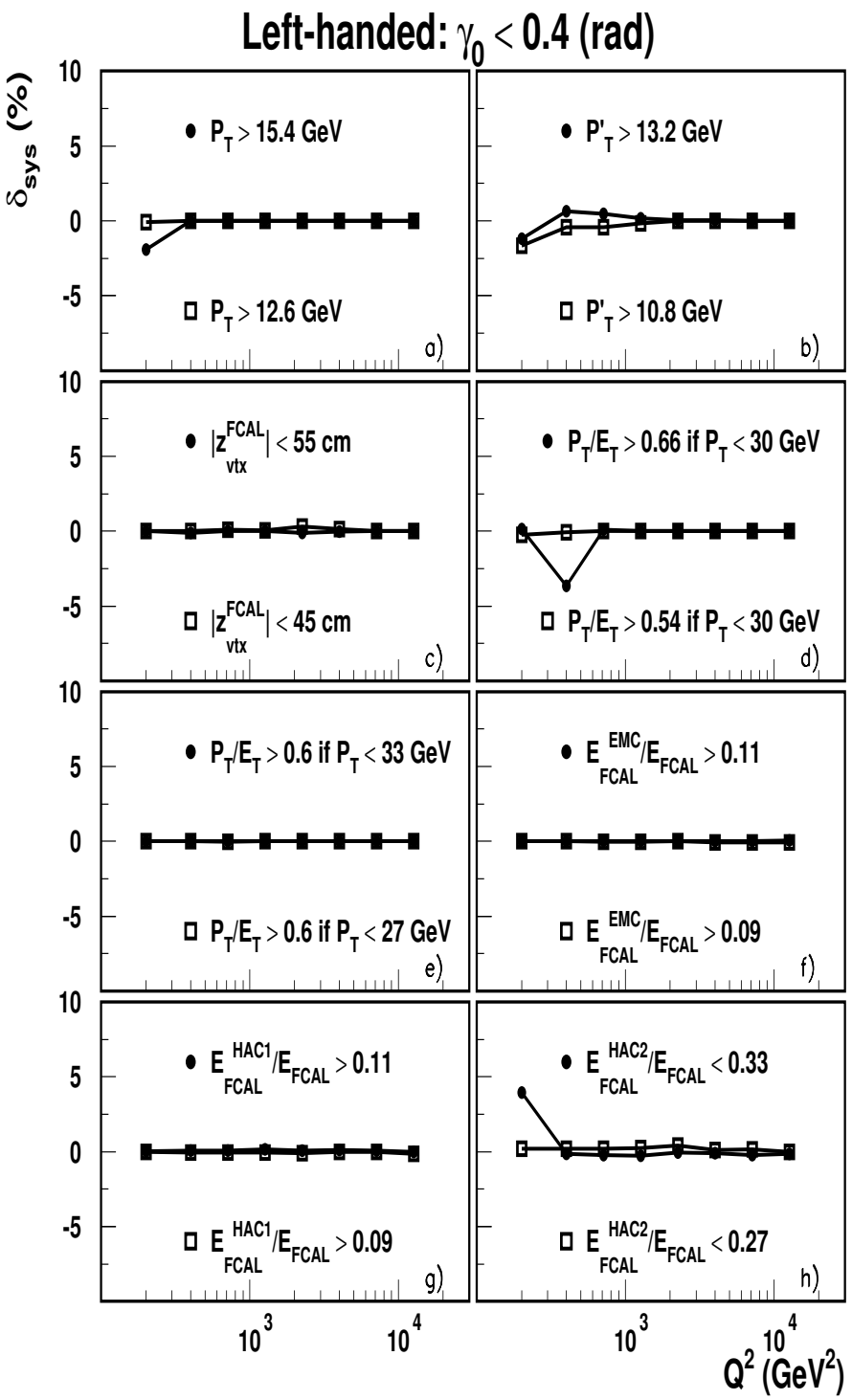

Figure A.3: The systematic uncertainties (in percentage) in the LH differential cross section versus Q^2 for varying the low γ_0 selection cuts.

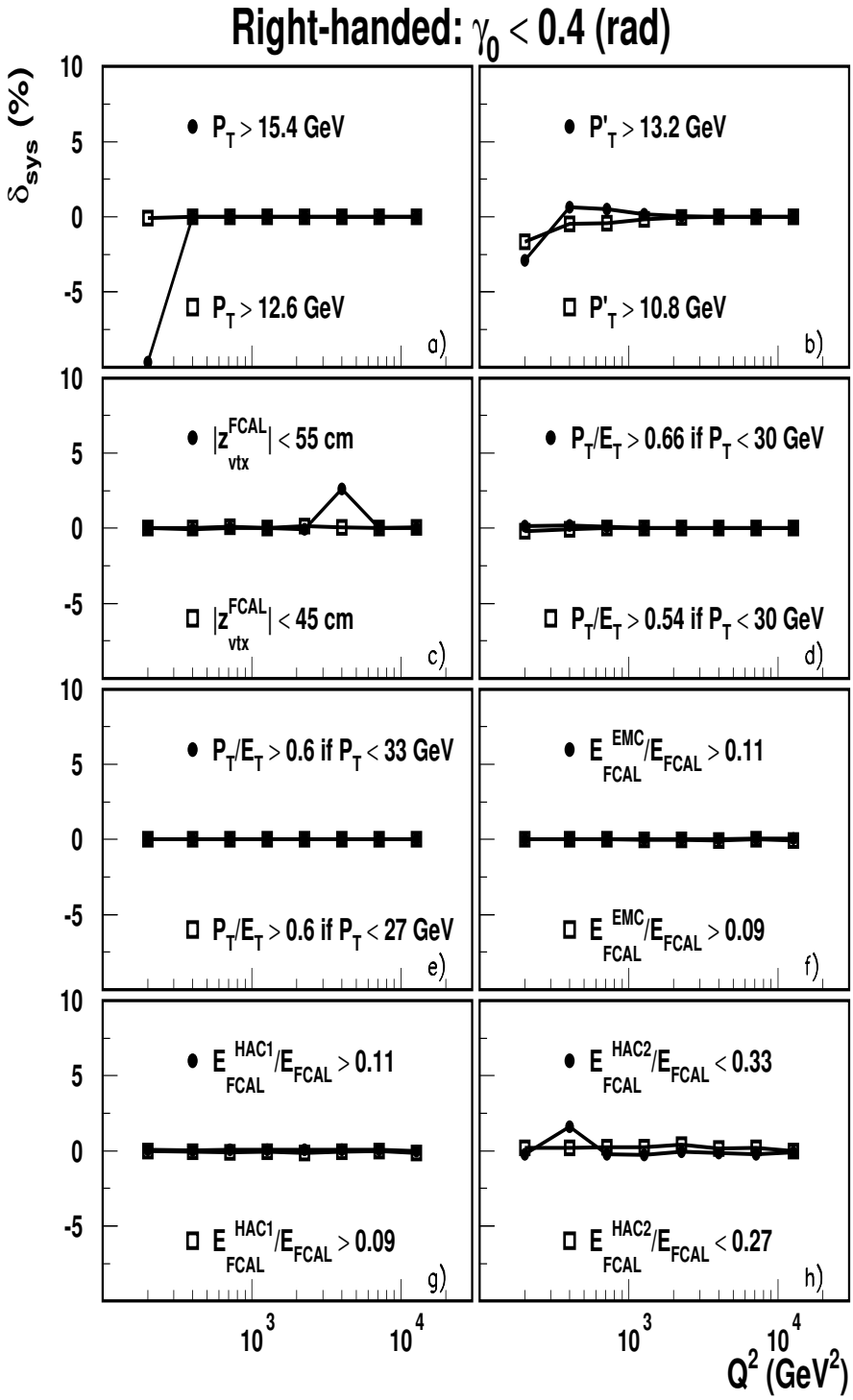

Figure A.4: The systematic uncertainties (in percentage) in the RH differential cross section versus Q^2 for varying the low γ_0 selection cuts.

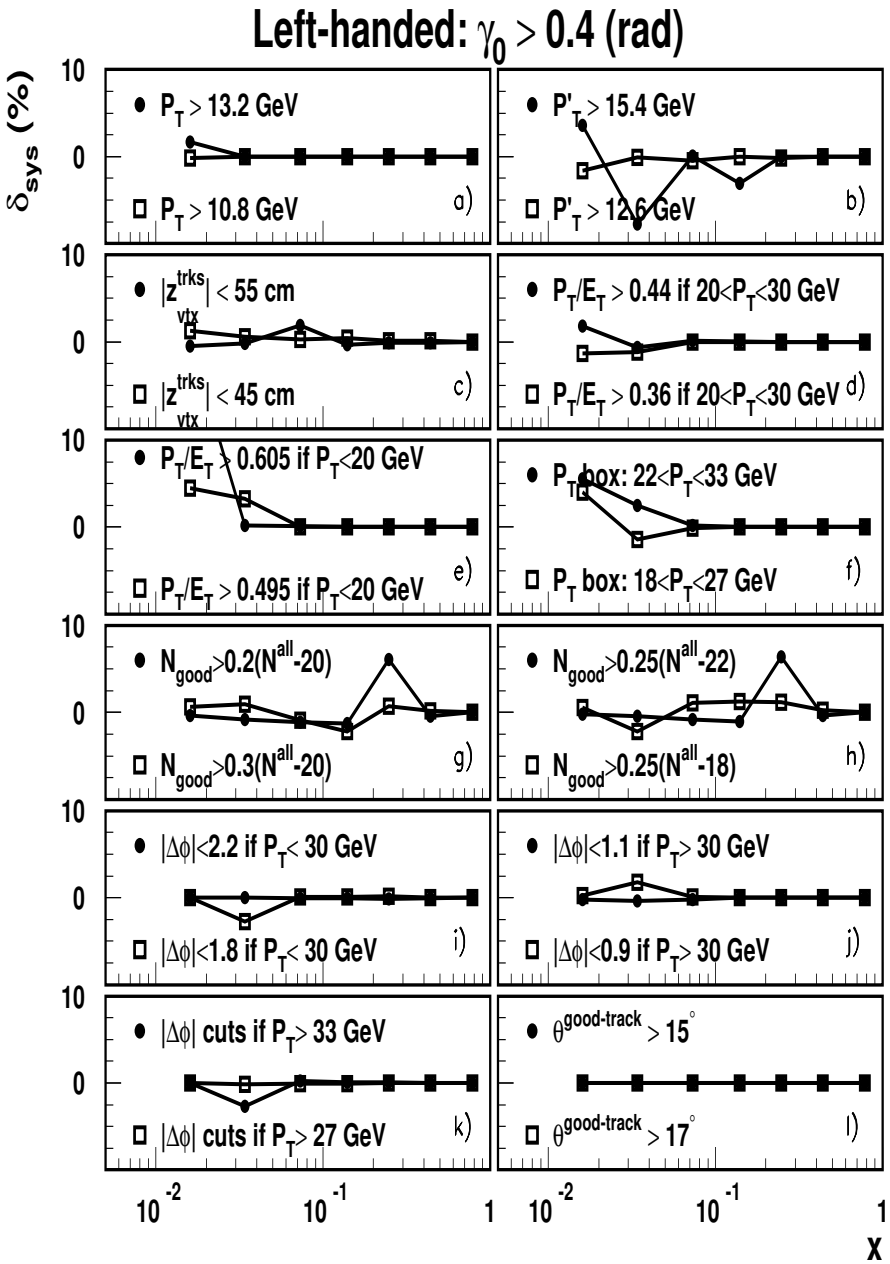

Figure A.5: The systematic uncertainties (in percentage) in the LH differential cross section versus x for varying the high γ_0 selection cuts.

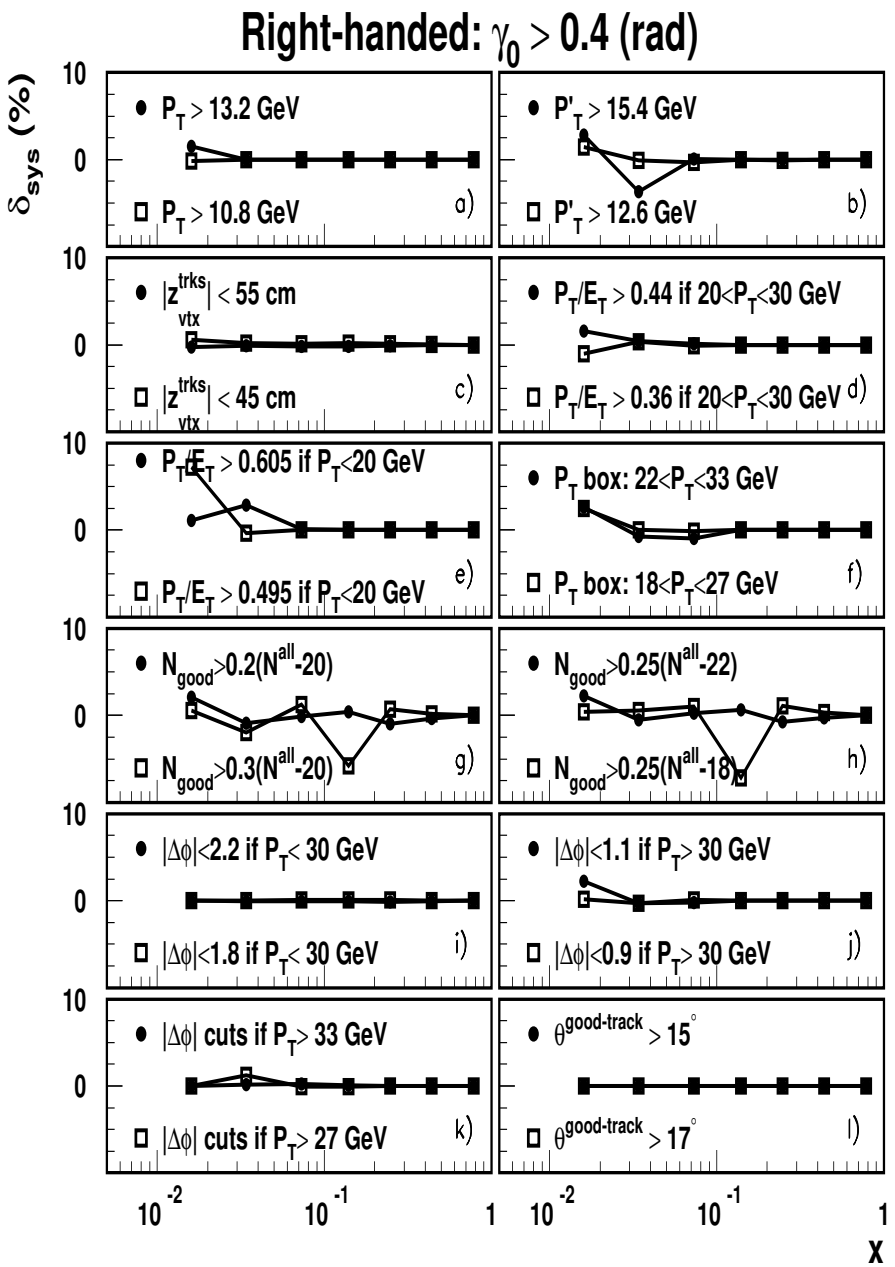

Figure A.6: The systematic uncertainties (in percentage) in the RH differential cross section versus x for varying the high γ_0 selection cuts.

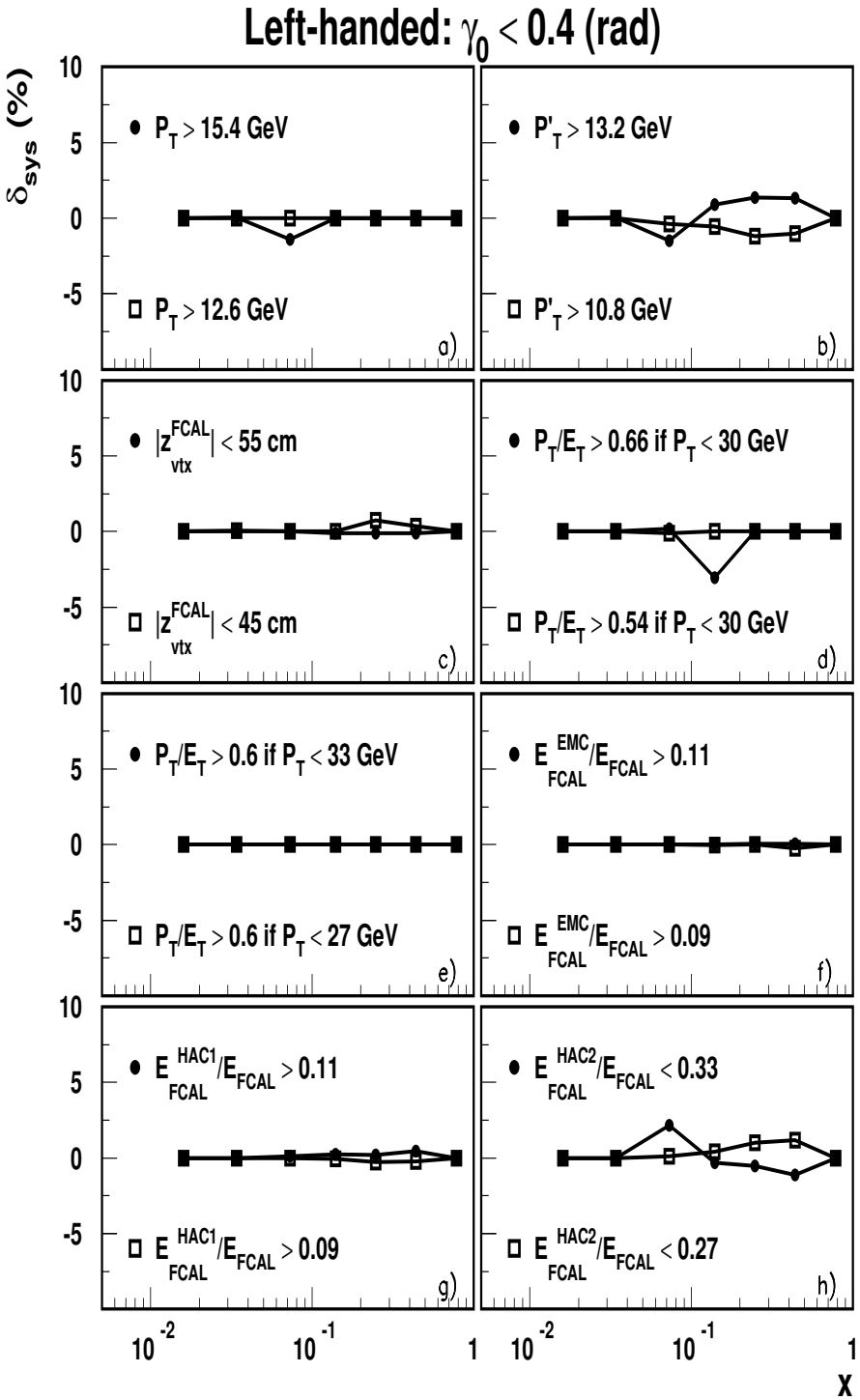

Figure A.7: The systematic uncertainties (in percentage) in the LH differential cross section versus x for varying the low γ_0 selection cuts.

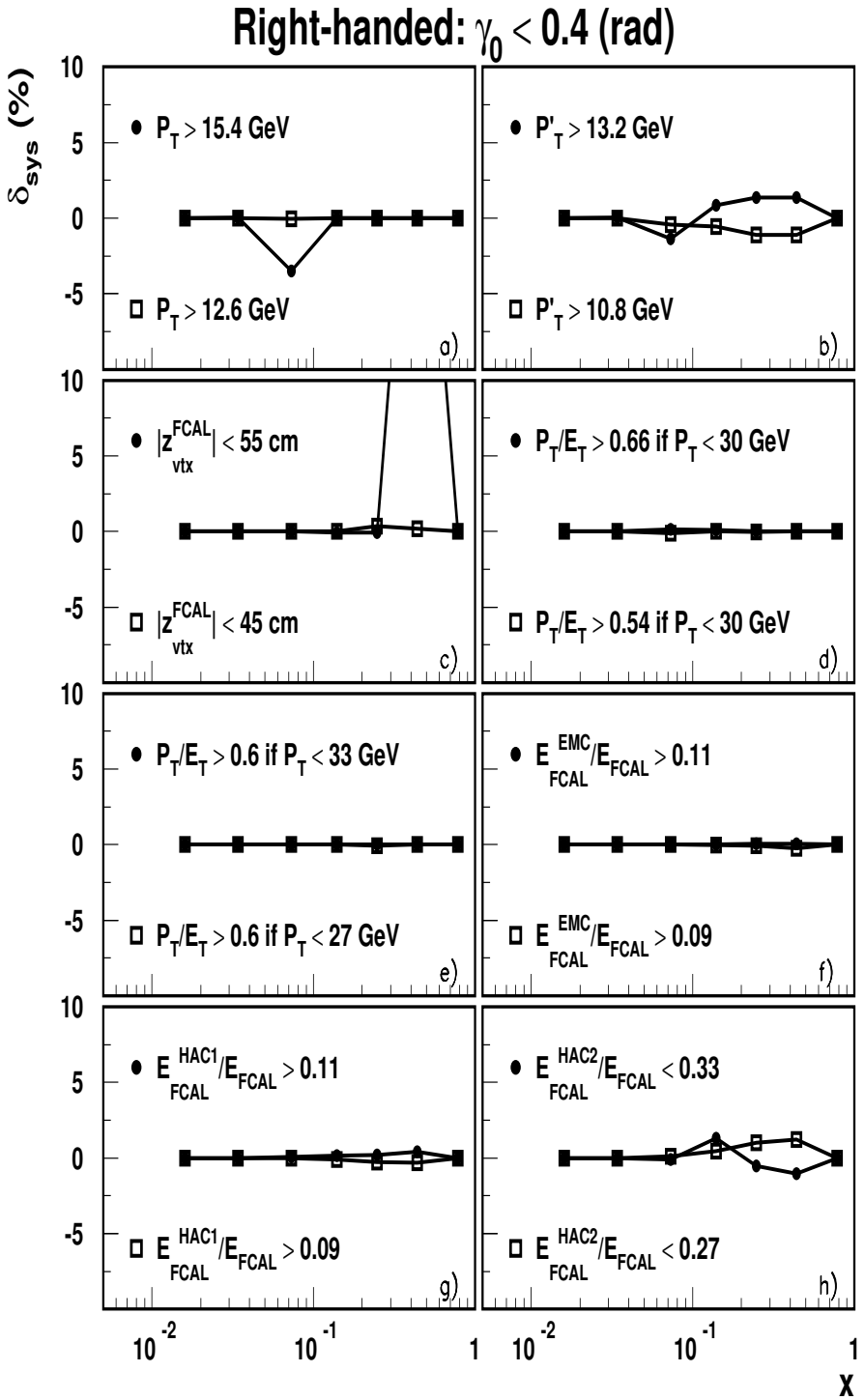

Figure A.8: The systematic uncertainties (in percentage) in the RH differential cross section versus x for varying the low γ_0 selection cuts.

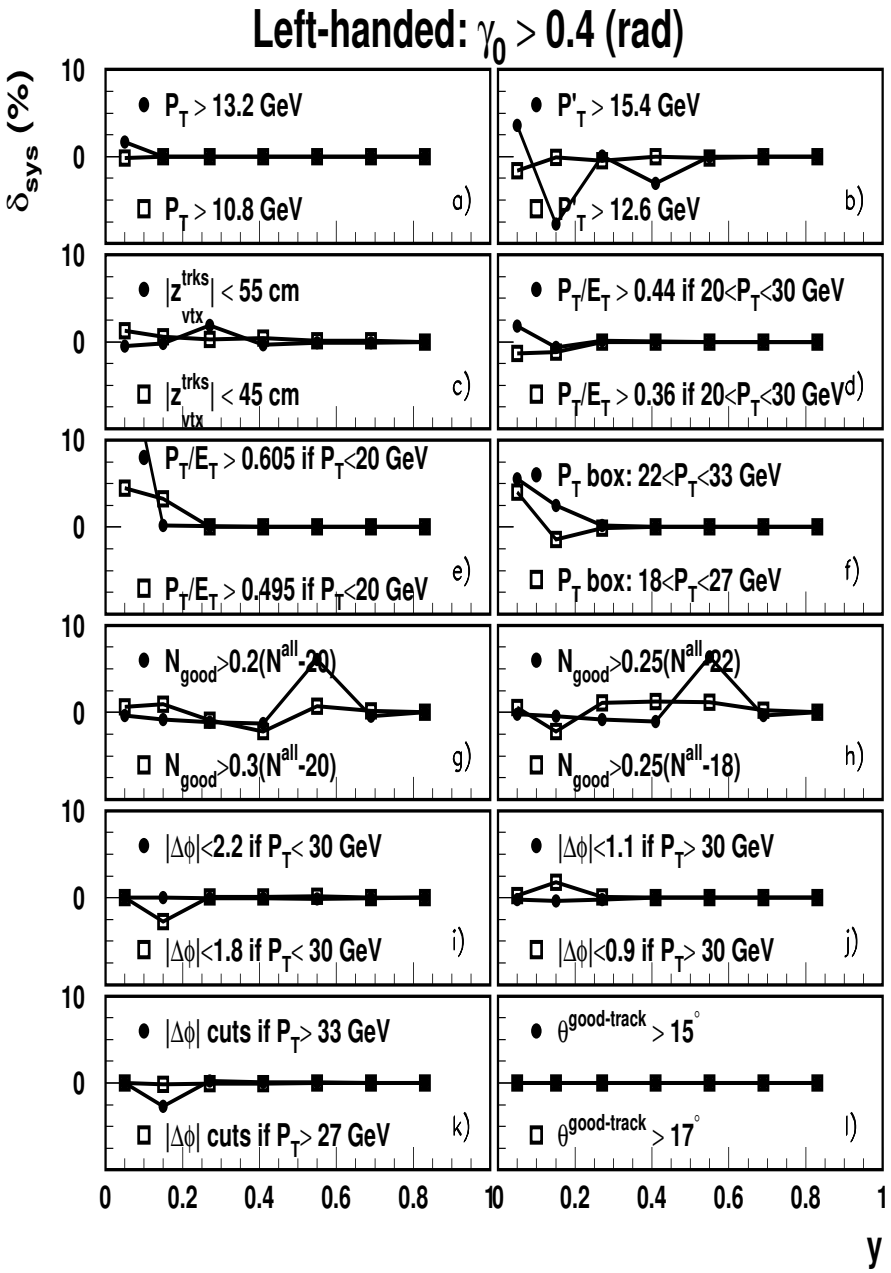

Figure A.9: The systematic uncertainties (in percentage) in the LH differential cross section versus y for varying the high γ_0 selection cuts.

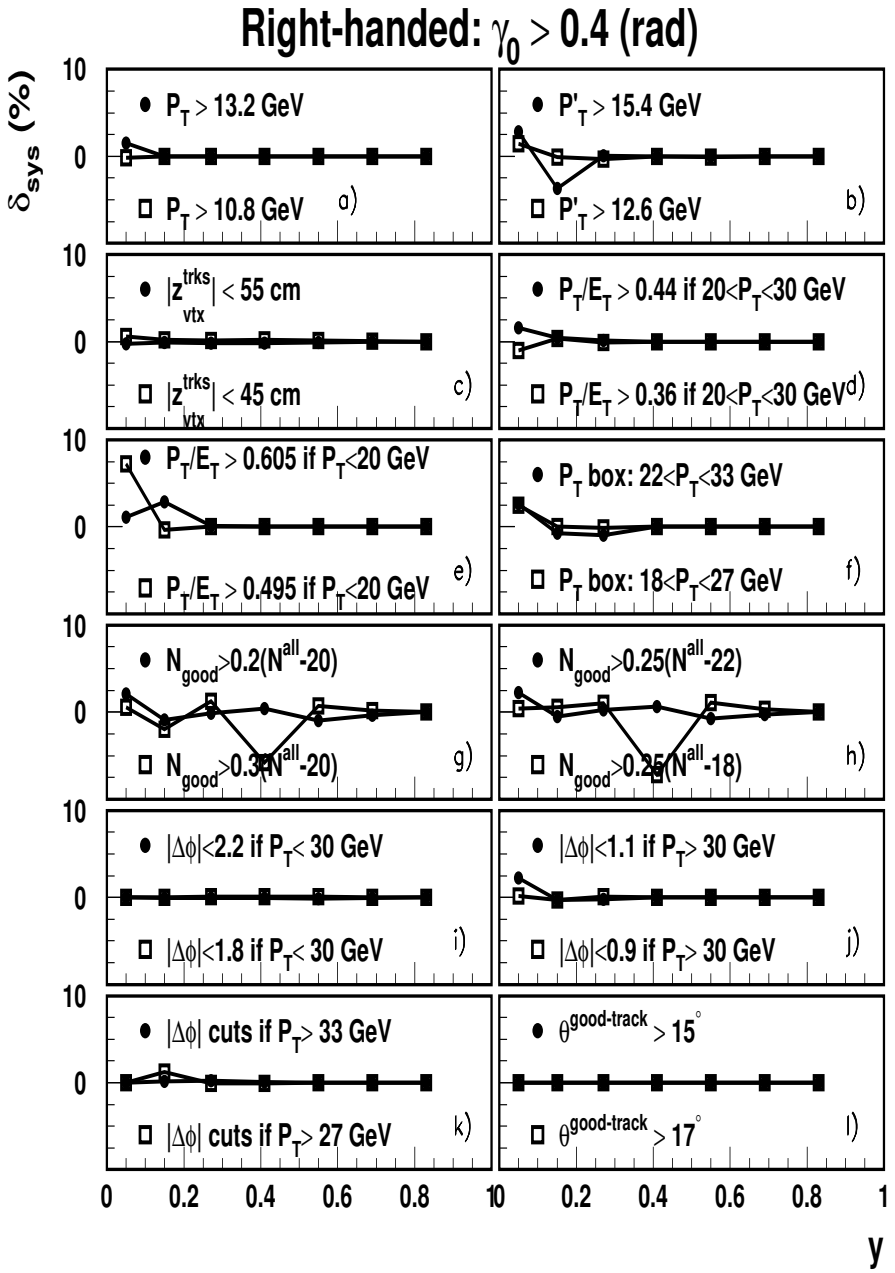

Figure A.10: The systematic uncertainties (in percentage) in the RH differential cross section versus y for varying the high γ_0 selection cuts.

Q^2 bin	$\delta^+_{LH}(\%)$	$\delta^-_{LH}(\%)$	$\delta^+_{RH}(\%)$	$\delta^-_{RH}(\%)$
$200. - 400.$	12.30	14.19	10.00	15.30
$400. - 711.$	11.65	10.54	10.02	7.70
$711. - 1265.$	6.47	7.55	6.79	7.20
$1265. - 2249.$	7.61	9.77	7.83	8.95
$2249. - 4000.$	8.18	7.01	7.86	7.40
$4000. - 7113.$	5.49	22.27	5.99	13.54
$7113. - 12649.$	5.84	6.13	5.93	6.09
$12649. - 22494.$	8.97	6.68	8.54	6.43
$22494. - 60000.$	–	–	–	–

Table A.1: Summary of the systematic errors for for the LH and RH $d\sigma/dQ^2$.

x bin	$\delta^+_{LH}(\%)$	$\delta^-_{LH}(\%)$	$\delta^+_{RH}(\%)$	$\delta^-_{RH}(\%)$
$0.010 - 0.022$	23.99	8.95	11.17	8.60
$0.022 - 0.046$	7.42	12.22	6.60	9.14
$0.046 - 0.100$	6.00	6.49	5.30	7.09
$0.100 - 0.178$	5.45	7.40	5.59	10.71
$0.178 - 0.316$	10.69	5.68	5.76	5.61
$0.316 - 0.562$	7.14	6.08	34.13	6.57
$0.562 - 1.000$	–	–	–	–

Table A.2: Summary of the systematic errors for for the LH and RH $d\sigma/dx$.

y bin	$\delta^+_{LH}(\%)$	$\delta^-_{LH}(\%)$	$\delta^+_{RH}(\%)$	$\delta^-_{RH}(\%)$
$0.000 - 0.100$	5.69	9.55	5.52	8.84
$0.100 - 0.200$	7.64	5.99	5.99	5.94
$0.200 - 0.340$	12.26	6.79	6.17	7.15
$0.340 - 0.480$	6.58	14.24	10.96	11.84
$0.480 - 0.620$	15.24	9.70	12.81	10.66
$0.620 - 0.760$	9.39	11.88	7.38	8.68
$0.760 - 0.900$	15.13	24.54	9.59	12.83

Table A.3: Summary of the systematic errors for for the LH and RH $d\sigma/dy$.

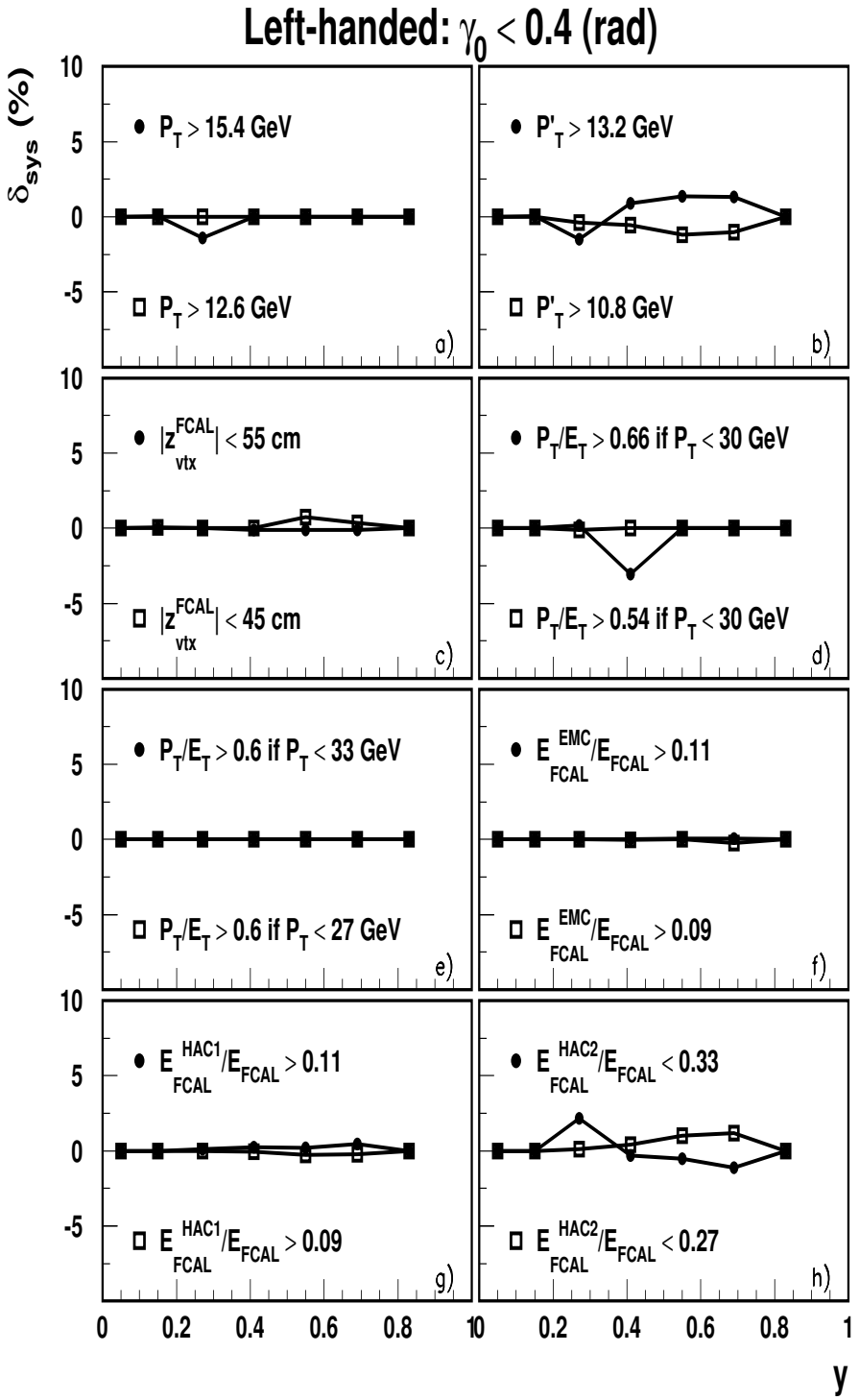

Figure A.11: The systematic uncertainties (in percentage) in the LH differential cross section versus y for varying the low γ_0 selection cuts.

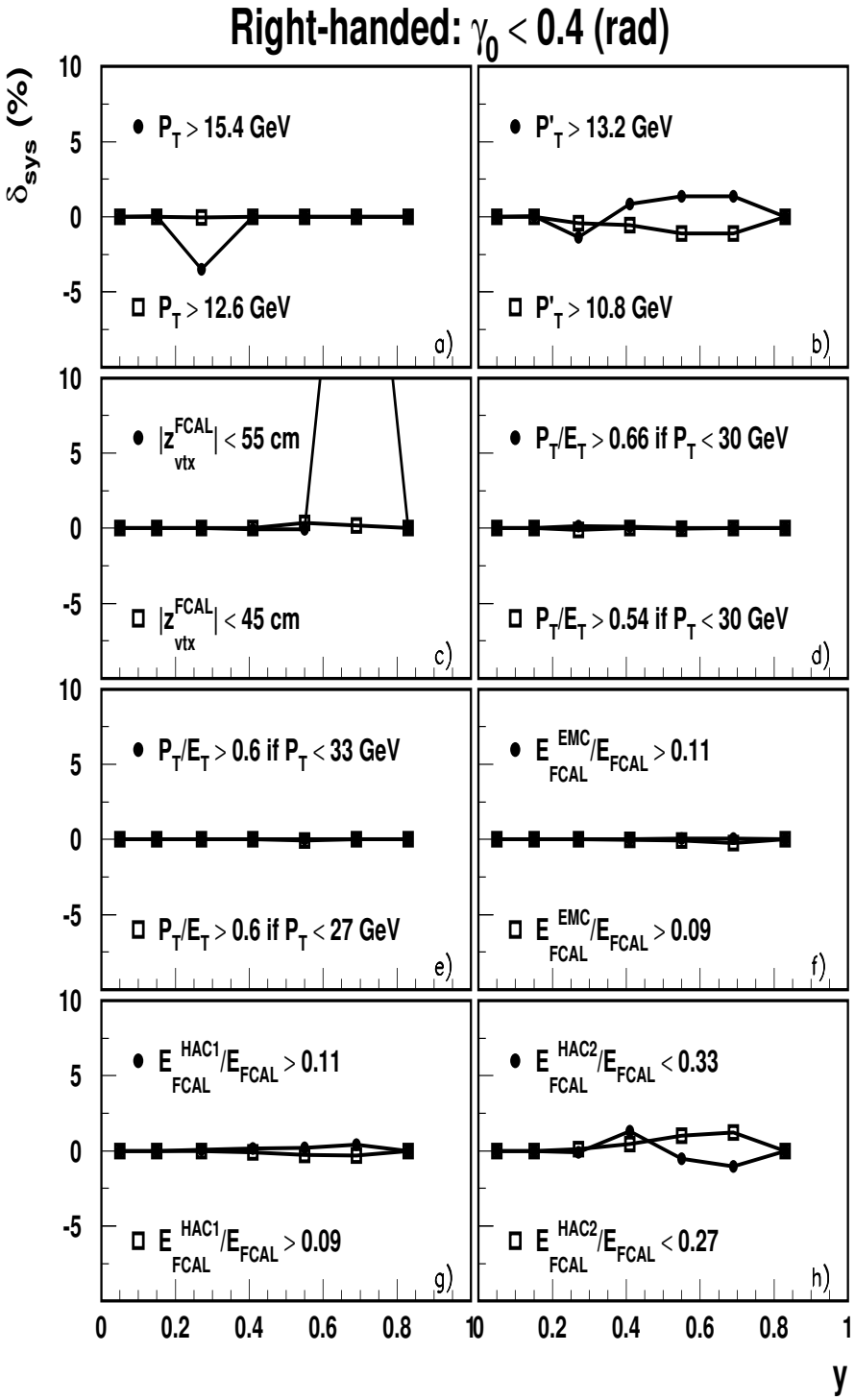

Figure A.12: The systematic uncertainties (in percentage) in the RH differential cross section versus y for varying the low γ_0 selection cuts.

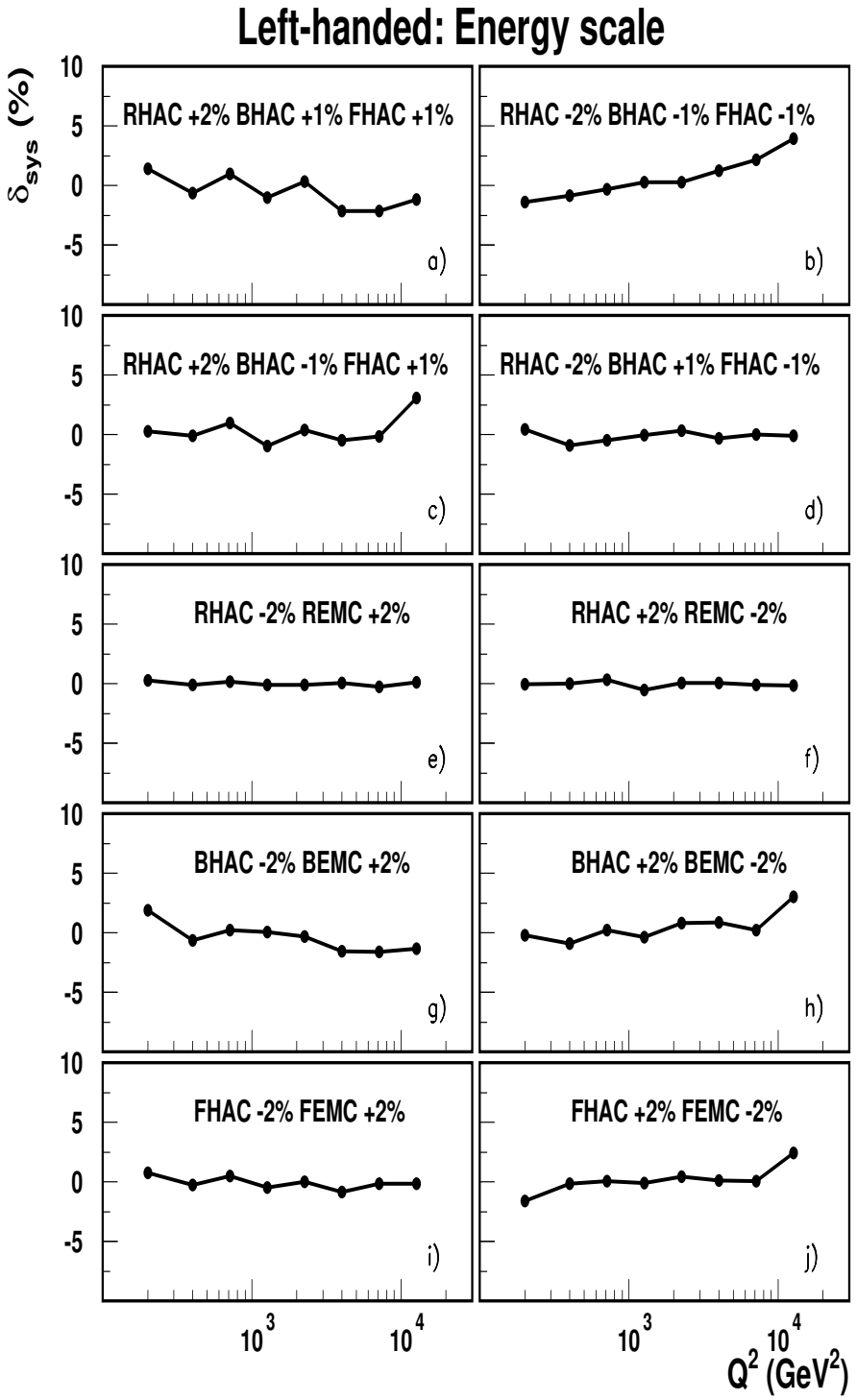

Figure A.13: The changes in the LH differential cross section versus Q^2 for the calorimeter energy scale checks.

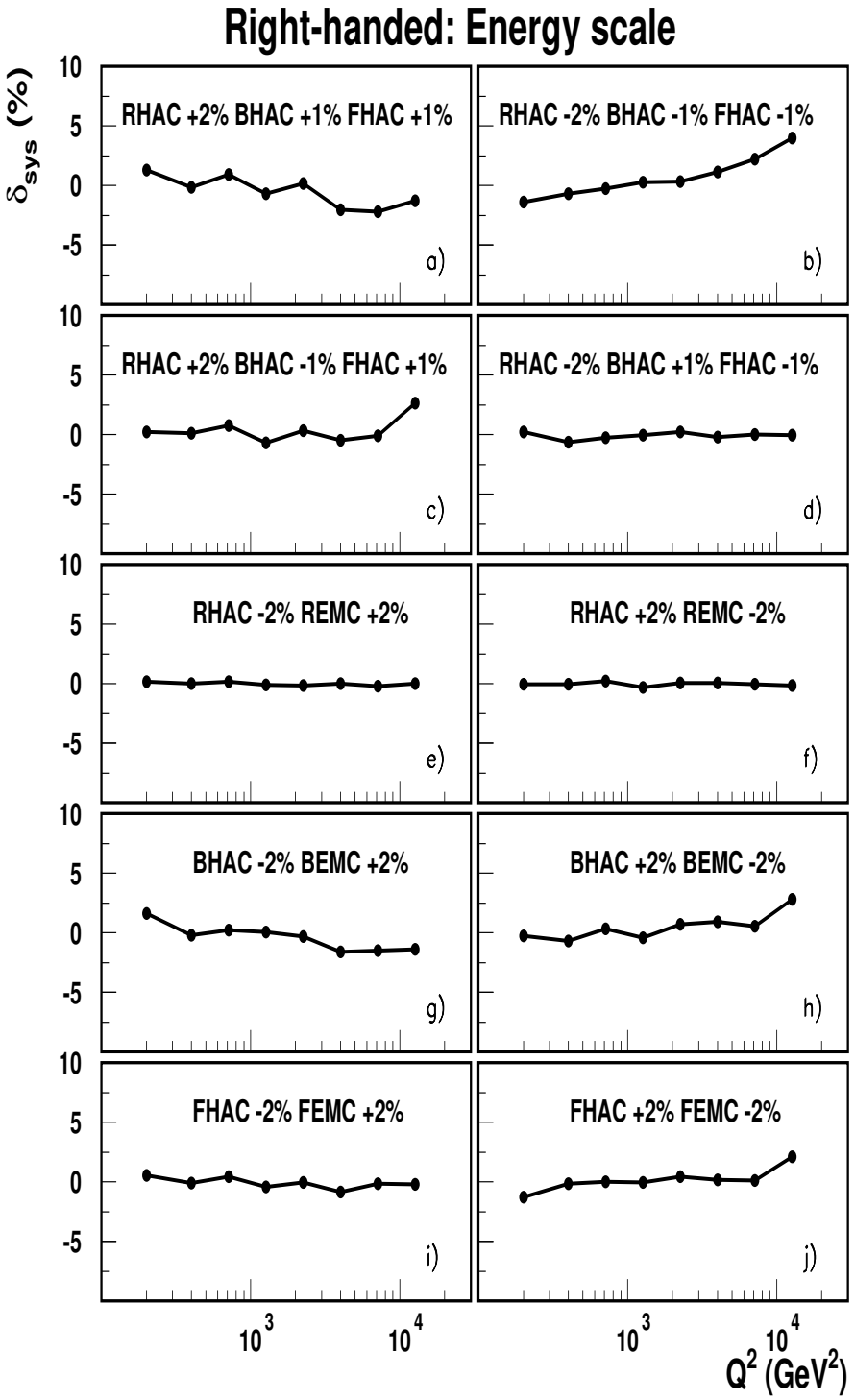

Figure A.14: The changes in the RH differential cross section versus Q^2 for the calorimeter energy scale checks.

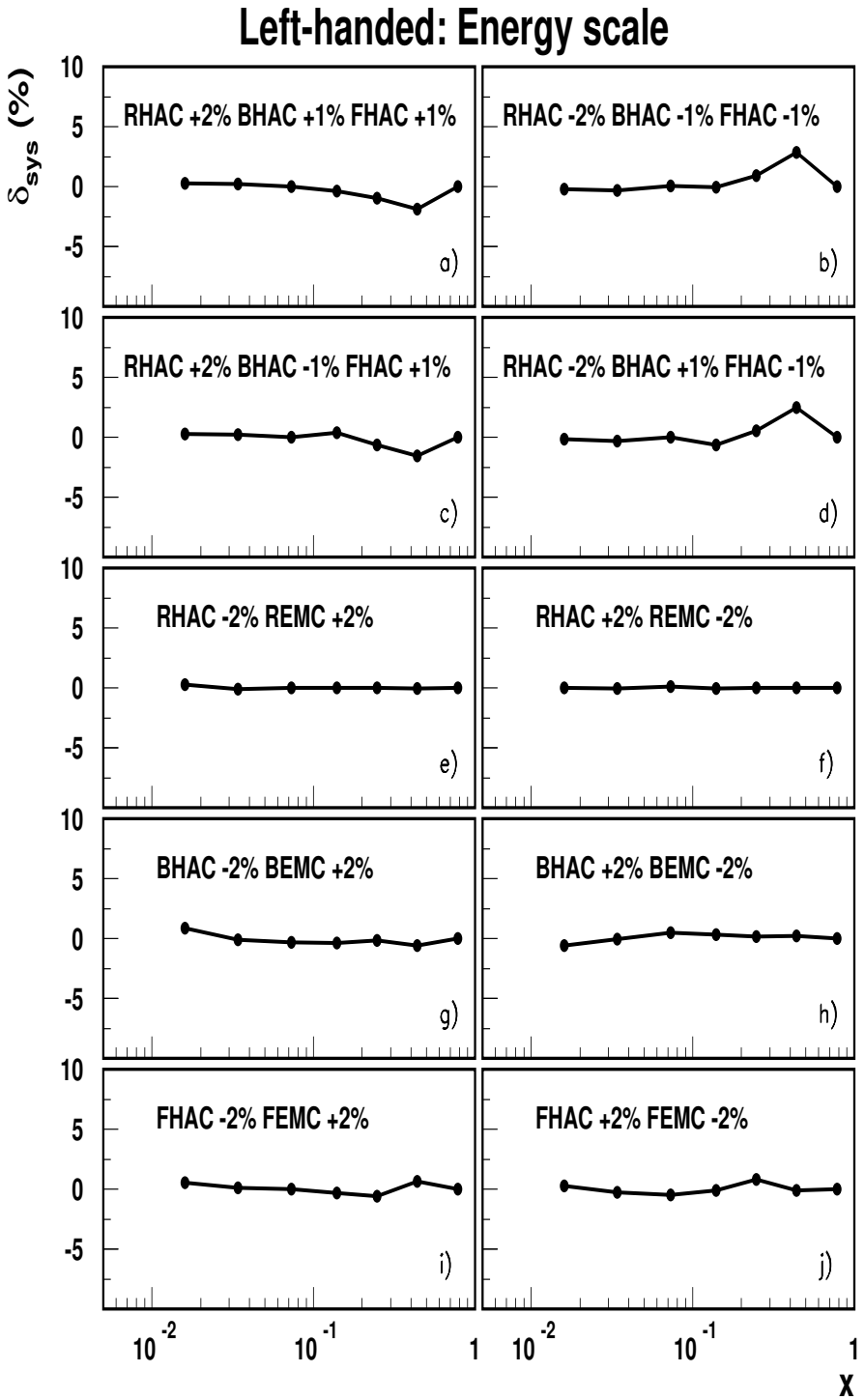

Figure A.15: The changes in the LH differential cross section versus x for the calorimeter energy scale checks.

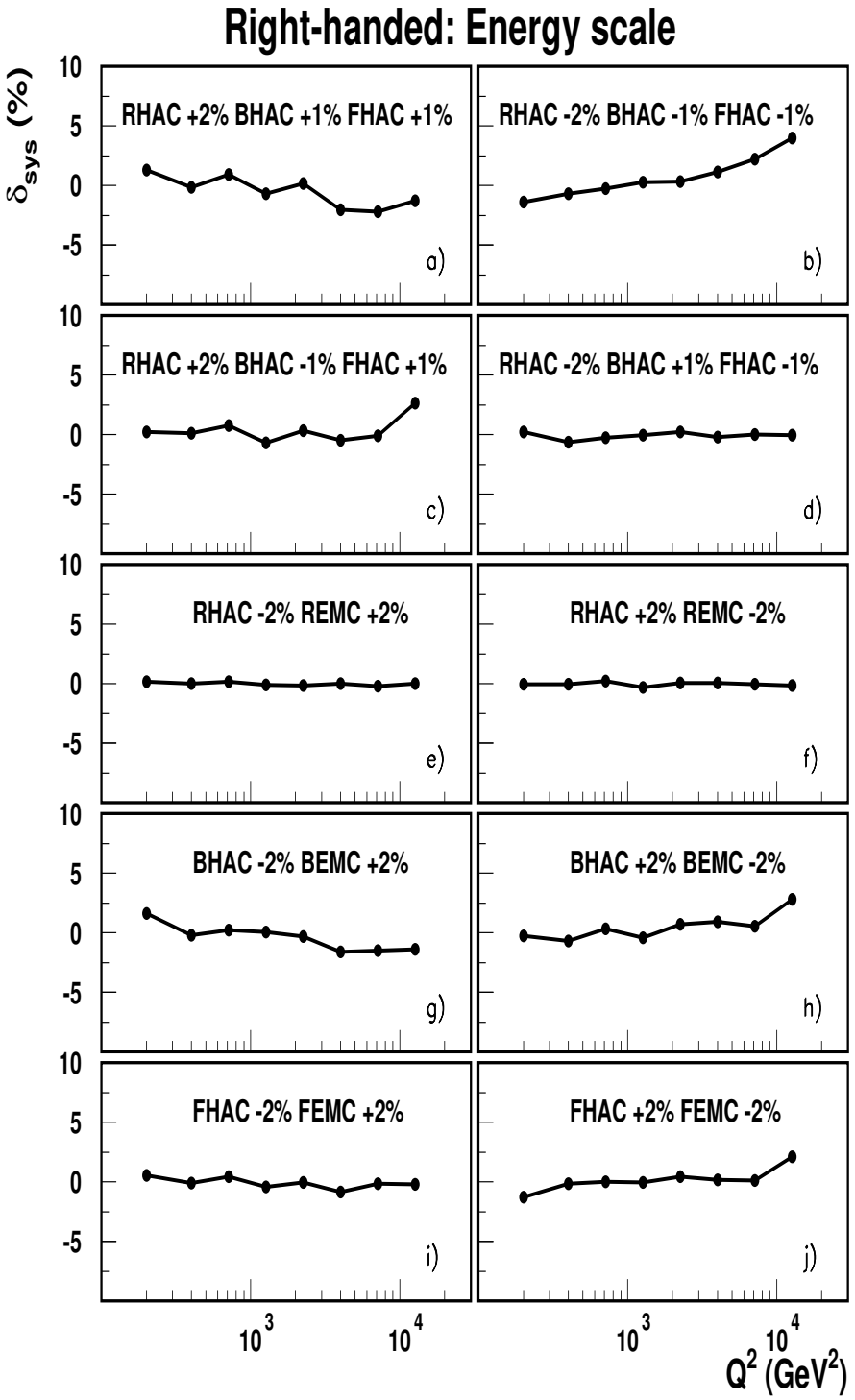

Figure A.16: The changes in the RH differential cross section versus x for the calorimeter energy scale checks.

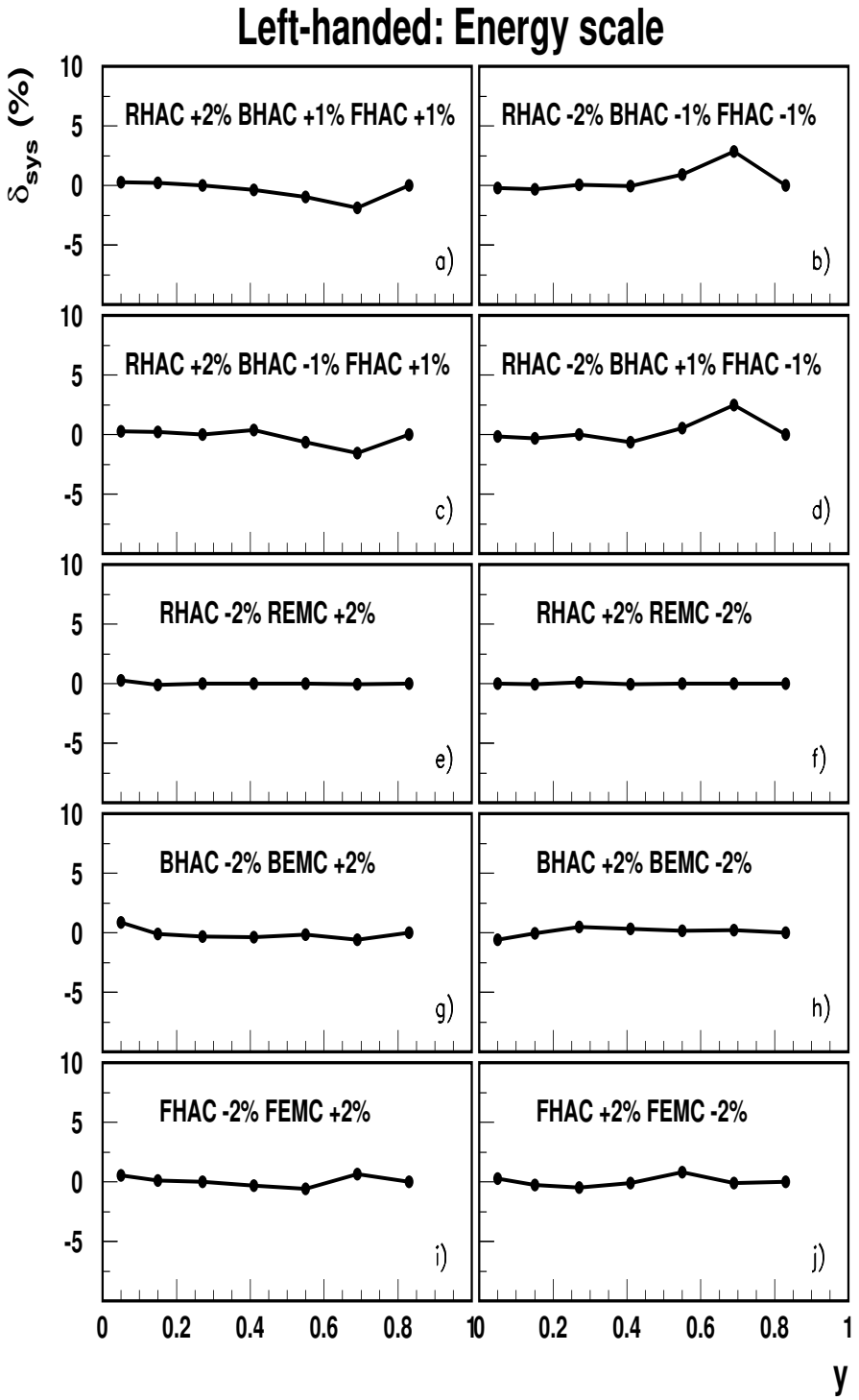

Figure A.17: The changes in the LH differential cross section versus y for the calorimeter energy scale checks.

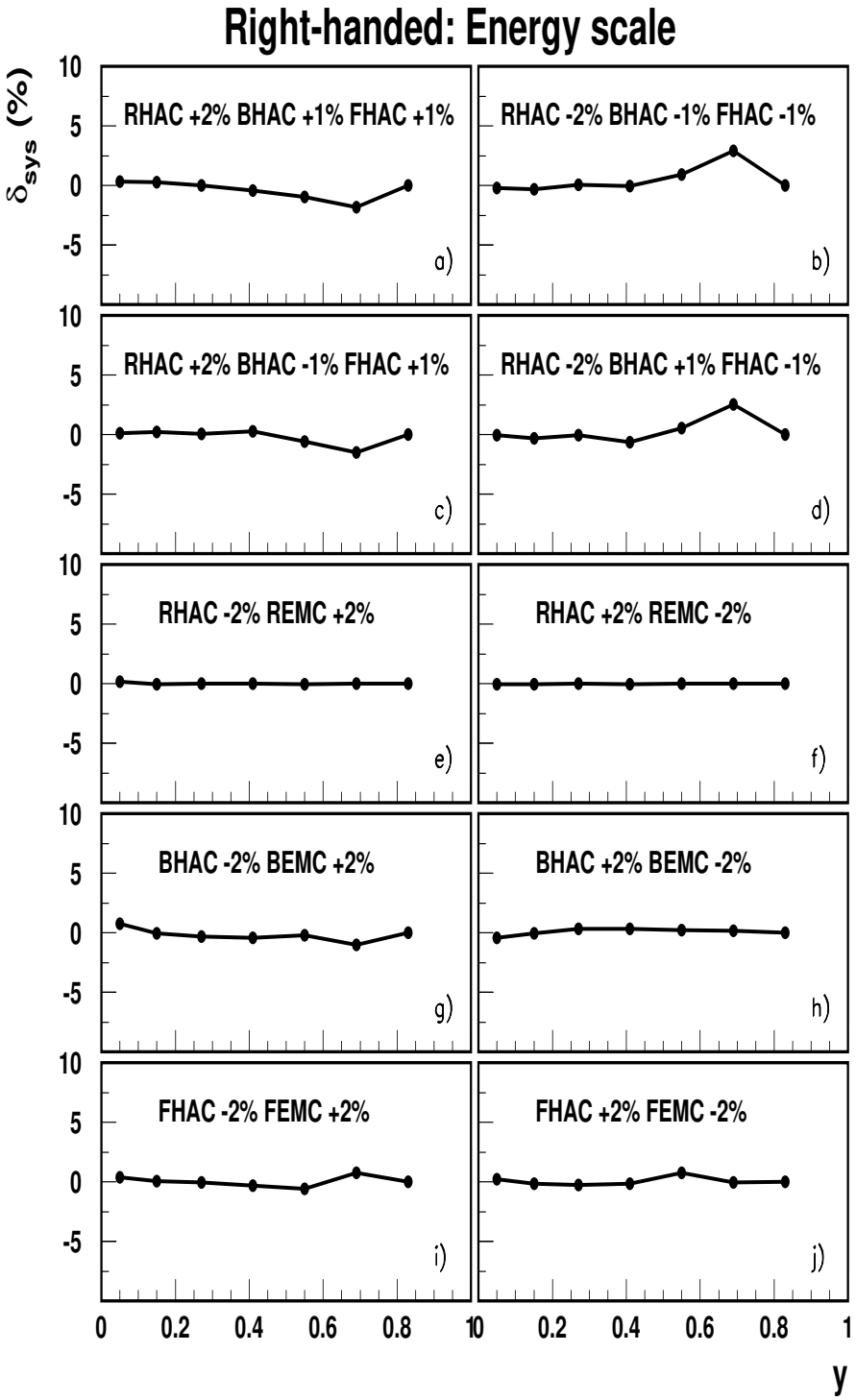

Figure A.18: The changes in the RH differential cross section versus y for the calorimeter energy scale checks.

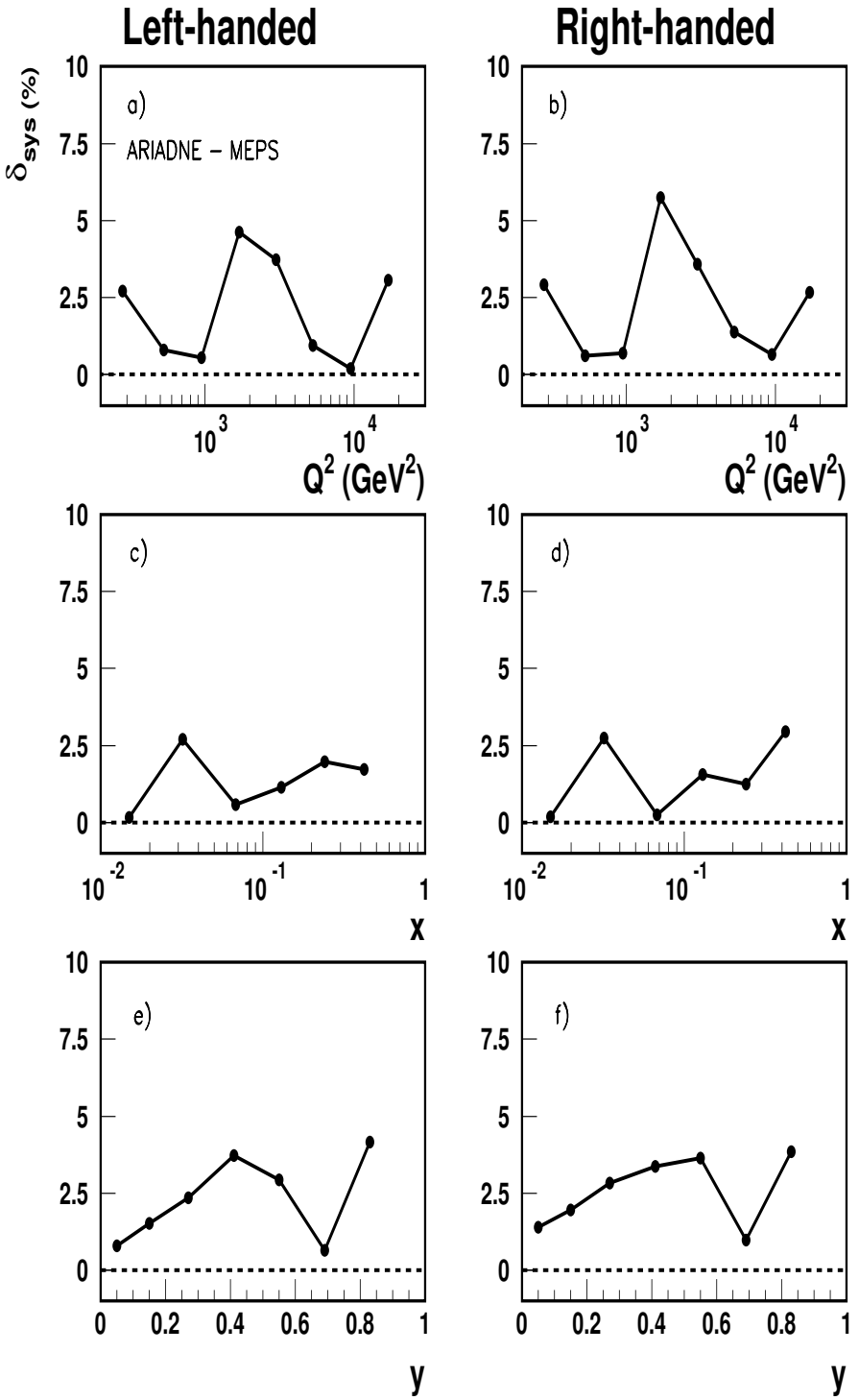

Figure A.19: The systematic contribution due to using the MEPS MC instead of ARIADNE to the differential cross section versus the kinematic variables, Q^2, x, and y, for LH (figures a, c, and e) and RH (figures b, d, and f).

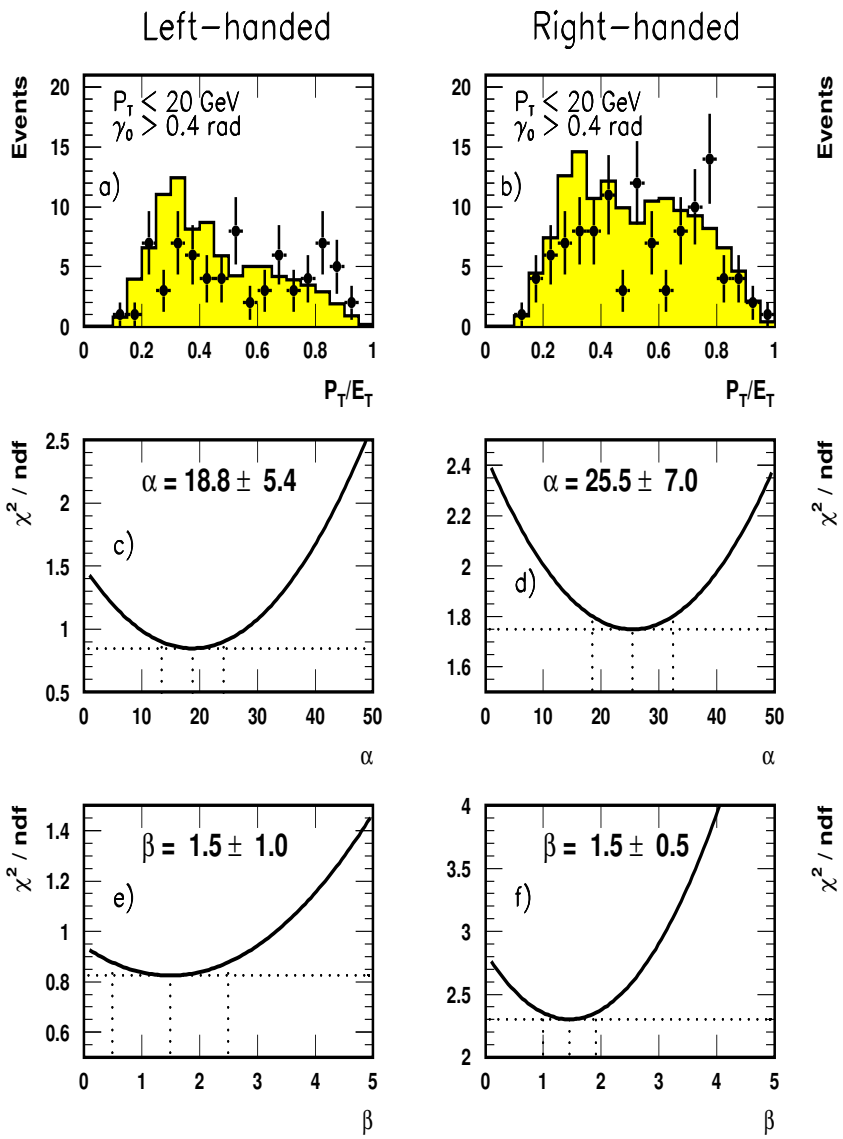

Figure A.20: The distribution of P_T/E_T for events with $\gamma_0 > 0.4$rad and $P_T < 20$GeV for LH (figure a)) and RH (figure b)) sample. The χ^2/ndf distributions versus the parameter α assuming fixed value for the parameter β are given for the LH and RH samples. (figures c) and d) respectively. The χ^2/ndf distributions versus the fit parameter β with fixed value for α for LH and RH samples are shown in figure e) and f), respectively.

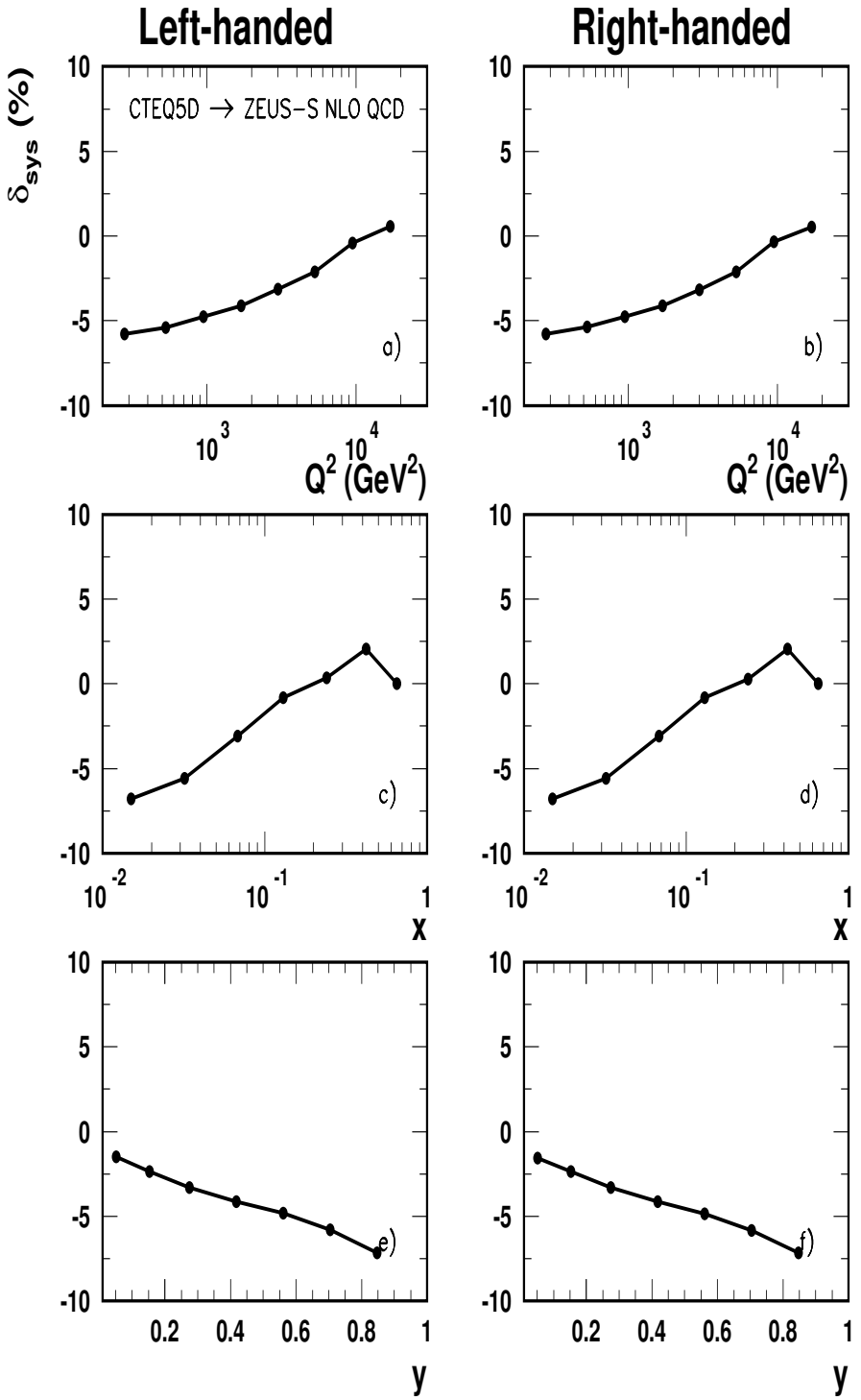

Figure A.21: The systematic uncertainty contribution in the LH and RH cross section (in percentage) measurements, versus the kinematic variables, due to reweighting the MC events which were generated with CTEQ5D to the ZEUS-S NLO QCD PDFs.

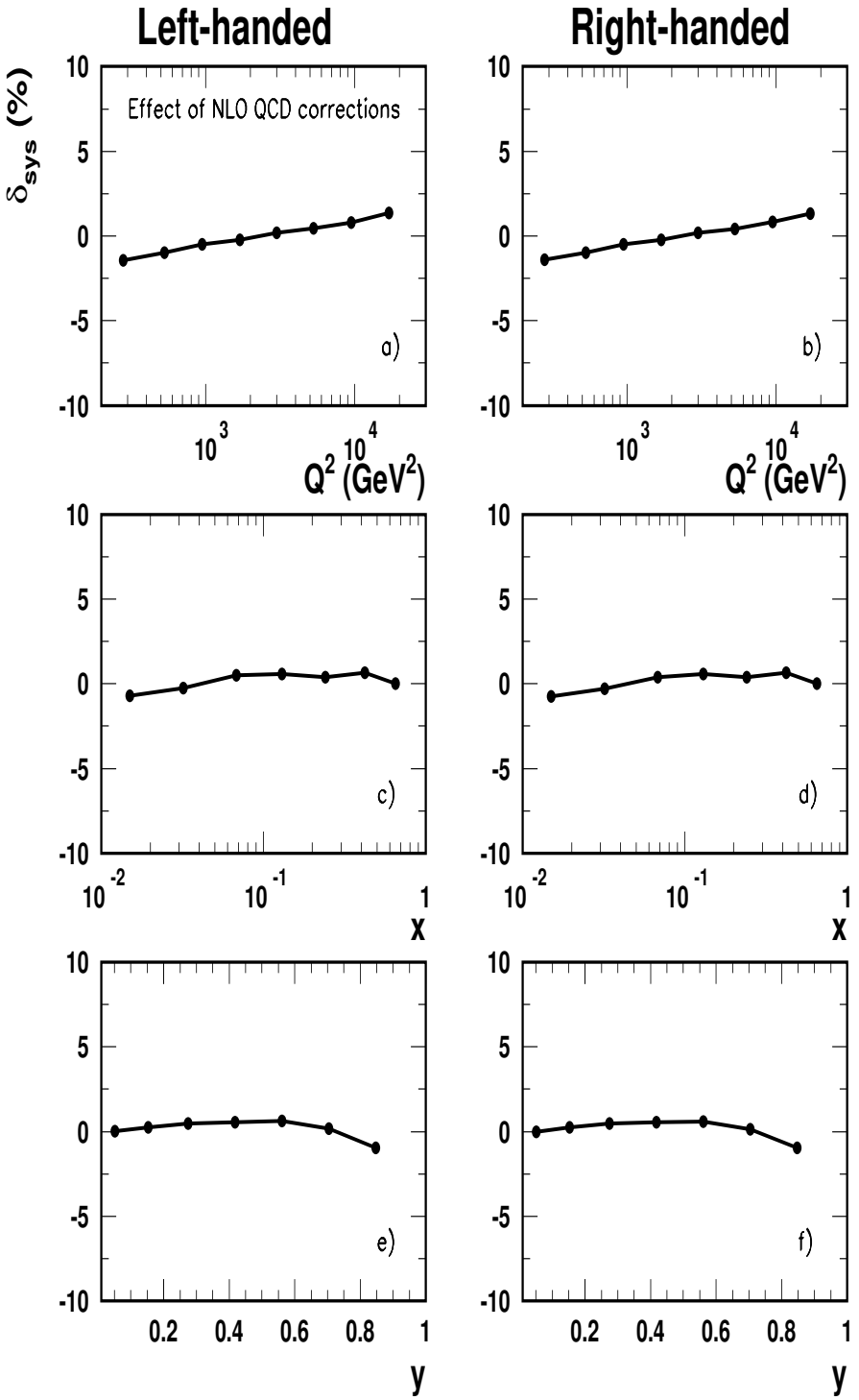

Figure A.22: The systematic uncertainty contributions (in percentage), to the cross section measurements due to the reweighting of the MC events to the NLO QCD corrections.

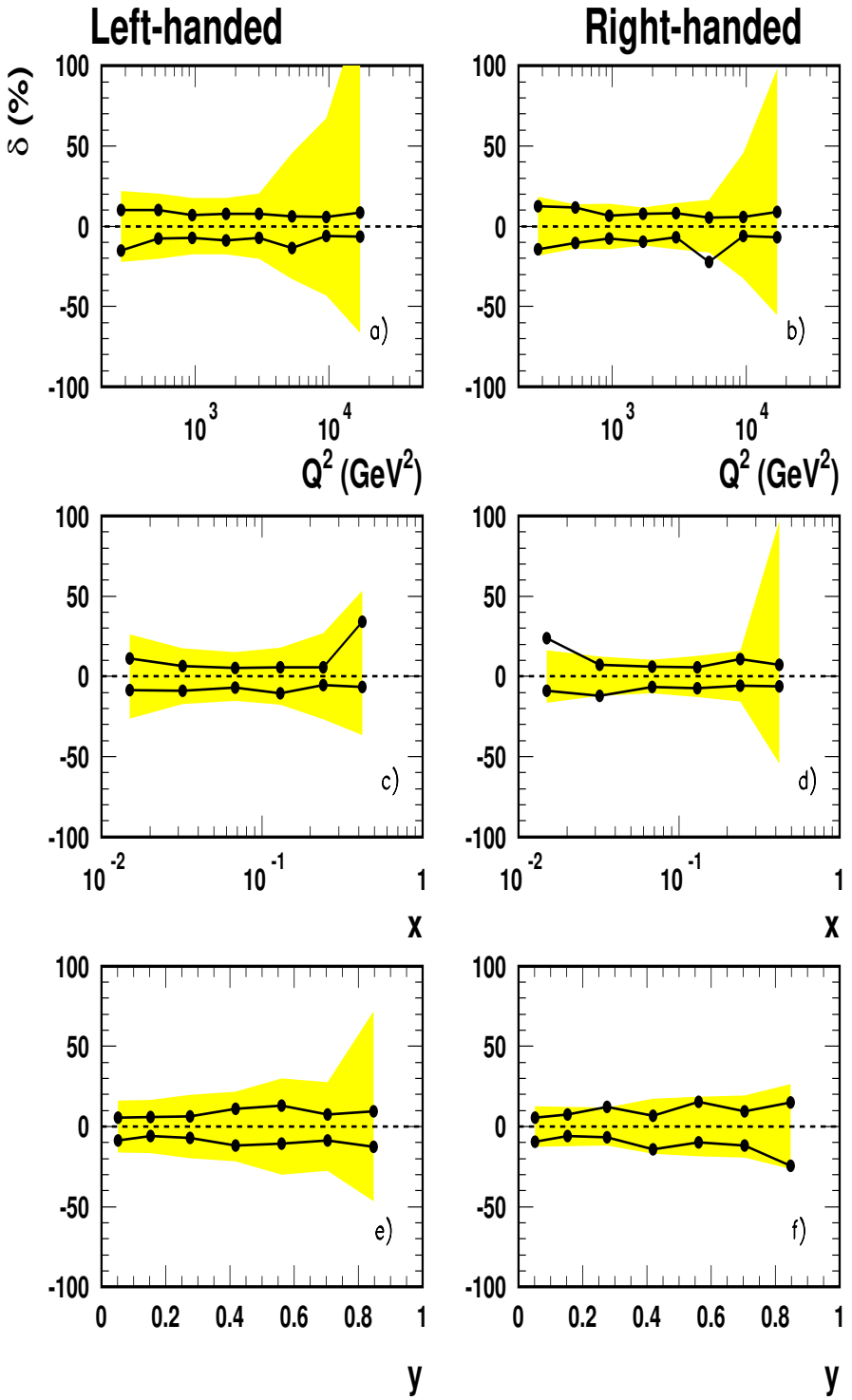

Figure A.23: The systematic uncertainties are compared with the statistical errors in the differential cross sections. The bands represent the statistical errors while the dots are the systematic errors.

Check	200 − 400	400 − 711	711 − 1265	1265 − 2249	2249 − 4000	4000 − 7113	7113 − 12649	12649 − 22494
2	2.8	-3.3	0.4	0.1	0.0	0.0	0.0	0.0
3	-1.7	-0.3	-0.3	0.0	0.0	0.0	0.0	0.0
4	-9.9	-4.8	0.4	-3.0	0.0	0.0	0.0	0.0
5	-2.1	-1.3	-0.8	0.0	0.0	0.0	0.0	0.0
6	-0.1	-0.6	-0.3	2.7	-0.2	-0.2	-0.2	0.0
7	1.0	0.6	0.5	0.3	0.5	0.4	0.3	1.0
8	0.0	1.4	-1.6	0.7	0.3	0.2	0.0	0.0
9	0.0	-0.6	-1.2	-0.4	-0.2	-0.2	-0.1	0.0
10	4.1	8.2	2.6	0.7	0.2	0.0	0.0	0.0
11	8.1	4.8	-1.3	-0.7	-0.2	0.0	0.0	0.0
12	0.0	3.9	1.9	0.7	0.6	0.1	0.0	0.0
13	-0.4	-0.6	1.2	-0.6	-0.4	-0.1	-0.2	0.0
14	-0.5	-0.6	-0.8	-1.2	3.1	-1.3	-1.7	-2.3
15	0.4	0.5	0.7	1.4	1.2	-21.3	1.3	1.1
16	-0.4	-0.5	-0.7	-0.8	3.7	-0.9	-1.3	-1.3
17	-3.4	0.6	0.7	1.0	1.1	1.3	1.5	1.3
18	0.0	0.0	0.0	-0.1	-0.1	-0.1	-0.2	-0.3
19	0.0	0.0	0.0	-3.0	0.1	0.1	0.0	0.1
20	-0.6	-0.2	-0.3	-0.1	-0.1	0.0	0.0	0.0
21	1.4	1.2	0.2	0.1	0.1	0.0	0.0	0.0
22	0.0	0.0	0.3	-2.9	0.1	0.1	0.0	0.0
23	0.0	0.0	-0.4	-0.1	-0.1	0.0	-0.1	0.0
24	0.0	0.0	0.0	0.0	0.0	0.0	0.0	0.0
25	0.0	0.0	0.0	0.0	0.0	0.0	0.0	0.0
26	-1.9	0.0	0.0	0.0	0.0	0.0	0.0	0.0
27	-0.1	0.0	0.0	0.0	0.0	0.0	0.0	0.0
28	-1.2	0.6	0.5	0.2	0.1	0.0	0.0	0.0
29	-1.7	-0.4	-0.4	-0.2	0.0	0.0	0.0	0.0
30	0.0	-0.1	0.0	0.0	-0.1	-0.1	0.0	0.0
31	0.0	0.0	0.1	0.0	0.3	0.1	0.0	0.0
32	0.1	-3.7	0.1	0.0	0.0	0.0	0.0	0.0
33	-0.2	-0.1	0.0	0.0	0.0	0.0	0.0	0.0
34	0.0	0.0	0.0	0.0	0.0	0.0	0.0	0.0
35	0.0	0.0	0.0	0.0	0.0	0.0	0.0	0.0
36	0.0	0.0	0.0	0.0	0.0	0.0	0.0	0.0
37	0.0	0.0	0.0	0.0	0.0	-0.1	-0.1	-0.1
38	0.0	0.1	0.1	0.1	0.1	0.1	0.1	0.0
39	0.0	-0.1	-0.1	0.0	-0.1	0.0	0.0	-0.1
40	4.0	-0.1	-0.2	-0.3	-0.1	-0.1	-0.2	-0.1
41	0.2	0.2	0.2	0.2	0.4	0.1	0.2	0.0
42	1.4	-0.6	1.0	-1.0	0.3	-2.2	-2.1	-1.1
43	-1.4	-0.8	-0.3	0.3	0.3	1.2	2.2	4.0
44	0.3	-0.1	1.0	-1.0	0.4	-0.5	-0.2	3.1
45	0.5	-0.9	-0.4	0.0	0.3	-0.3	0.0	-0.1
46	0.3	-0.1	0.2	-0.1	-0.1	0.1	-0.2	0.1
47	0.0	0.0	0.4	-0.5	0.1	0.1	-0.1	-0.1
48	1.9	-0.6	0.2	0.1	-0.3	-1.5	-1.6	-1.3
49	-0.2	-0.9	0.2	-0.4	0.8	0.9	0.2	3.0
50	0.8	-0.3	0.5	-0.5	0.0	-0.9	-0.2	-0.1
51	-1.6	-0.1	0.0	-0.1	0.5	0.1	0.1	2.4
52	2.7	0.8	0.6	4.6	3.7	0.9	0.2	3.0
53	-2.7	-0.8	-0.6	-4.6	-3.7	-0.9	-0.2	-3.1
54	-5.8	-5.4	-4.8	-4.1	-3.2	-2.1	-0.4	0.5
55	-1.4	-1.0	-0.5	-0.2	0.2	0.4	0.8	1.4
56	1.9	1.0	0.4	0.0	0.0	0.0	0.0	0.0
57	-1.9	-1.0	-0.4	0.0	0.0	0.0	0.0	0.0
58	0.3	0.3	-0.4	0.0	0.0	0.0	0.0	0.0
59	-0.3	-0.3	0.4	0.0	0.0	0.0	0.0	0.0
60	5.0	5.0	5.0	5.0	5.0	5.0	5.0	5.0
61	-5.0	-5.0	-5.0	-5.0	-5.0	-5.0	-5.0	-5.0
δ^+	12.3	11.6	6.5	7.6	8.2	5.5	5.8	9.0
δ^-	14.2	10.5	7.5	9.8	7.0	22.3	6.1	6.7

Table A.4: The systematic uncertainty contributions (in percentage) in the differential cross section versus Q^2, at $P = -40\%$.

Check	200 − 400	400 − 711	711 − 1265	1265 − 2249	2249 − 4000	4000 − 7113	7113 − 12649	12649 − 22494
2	-2.1	0.6	0.3	0.1	0.0	0.0	0.0	0.0
3	-1.5	-0.3	-0.2	0.0	0.0	0.0	0.0	0.0
4	-4.7	2.1	0.5	0.1	0.0	0.0	0.0	0.0
5	0.9	0.9	1.3	0.0	0.0	0.0	0.0	0.0
6	-0.1	-0.3	-0.2	-0.2	-0.1	-0.1	-0.1	0.0
7	0.4	0.3	0.3	0.1	0.2	0.2	0.1	0.5
8	0.0	0.9	1.4	0.7	-1.7	0.1	0.0	0.0
9	0.0	1.3	-1.0	-0.4	-0.3	-0.2	0.0	0.0
10	7.5	1.7	0.3	-0.8	0.1	0.0	0.0	0.0
11	-5.0	6.9	2.6	0.8	-0.2	0.0	0.0	0.0
12	0.0	1.6	1.9	-0.6	-1.5	-2.5	0.0	0.0
13	-0.4	2.8	0.3	-0.6	-0.5	-0.1	-0.1	0.0
14	-0.5	-0.6	1.2	-1.1	3.0	-1.4	-1.6	-2.0
15	0.4	0.5	-1.3	-0.2	1.1	-9.4	1.4	1.1
16	-0.4	-0.5	1.3	-0.8	3.6	-0.9	-1.2	-1.2
17	0.6	0.6	0.7	-0.5	-1.0	-6.8	1.5	1.3
18	0.0	0.0	0.0	-0.1	-0.1	-0.1	-0.1	-0.2
19	0.0	0.0	0.0	0.0	0.1	0.1	0.0	0.2
20	-0.5	1.6	-0.3	-0.1	-0.1	0.0	0.0	0.0
21	1.2	-1.1	0.3	0.1	0.1	0.0	0.0	0.0
22	0.0	0.0	0.3	0.1	0.0	0.1	0.0	0.0
23	0.0	0.0	-0.3	1.3	-0.1	0.0	0.0	0.0
24	0.0	0.0	0.0	0.0	0.0	0.0	0.0	0.0
25	0.0	0.0	0.0	0.0	0.0	0.0	0.0	0.0
26	-9.7	0.0	0.0	0.0	0.0	0.0	0.0	0.0
27	-0.1	0.0	0.0	0.0	0.0	0.0	0.0	0.0
28	-2.9	0.6	0.5	0.2	0.1	0.0	0.0	0.0
29	-1.6	-0.5	-0.4	-0.2	0.0	0.0	0.0	0.0
30	0.0	-0.1	0.0	0.0	-0.1	2.6	0.0	0.0
31	0.0	0.0	0.1	0.0	0.1	0.1	0.0	0.0
32	0.1	0.2	0.1	0.0	0.0	0.0	0.0	0.0
33	-0.2	-0.1	0.0	0.0	0.0	0.0	0.0	0.0
34	0.0	0.0	0.0	0.0	0.0	0.0	0.0	0.0
35	0.0	0.0	0.0	0.0	0.0	0.0	0.0	0.0
36	0.0	0.0	0.0	0.0	0.0	0.0	0.0	0.1
37	0.0	0.0	0.0	0.0	0.0	-0.1	0.0	-0.1
38	0.1	0.0	0.1	0.1	0.1	0.1	0.0	0.0
39	0.0	-0.1	-0.1	0.0	-0.2	-0.1	0.0	-0.2
40	-0.2	1.6	-0.3	-0.3	-0.1	-0.1	-0.2	-0.1
41	0.2	0.2	0.3	0.3	0.4	0.1	0.2	0.0
42	1.3	-0.1	0.9	-0.7	0.2	-2.0	-2.2	-1.2
43	-1.4	-0.7	-0.3	0.3	0.3	1.1	2.2	4.0
44	0.2	0.1	0.8	-0.7	0.4	-0.5	-0.1	2.7
45	0.2	-0.6	-0.3	0.0	0.2	-0.2	0.0	0.0
46	0.2	0.0	0.2	-0.1	-0.1	0.0	-0.2	0.0
47	0.0	0.0	0.3	-0.3	0.1	0.1	0.0	-0.1
48	1.6	-0.2	0.3	0.1	-0.3	-1.6	-1.5	-1.4
49	-0.3	-0.7	0.3	-0.4	0.7	0.9	0.5	2.8
50	0.5	-0.1	0.4	-0.4	0.0	-0.9	-0.1	-0.2
51	-1.3	-0.1	0.0	-0.1	0.4	0.2	0.1	2.1
52	2.9	0.6	0.7	5.8	3.6	1.4	0.6	2.7
53	-2.9	-0.6	-0.7	-5.7	-3.6	-1.4	-0.7	-2.7
54	-5.8	-5.4	-4.8	-4.1	-3.2	-2.1	-0.3	0.5
55	-1.4	-1.0	-0.5	-0.2	0.2	0.4	0.8	1.3
56	1.5	0.5	0.3	0.0	0.0	0.0	0.0	0.0
57	-1.5	-0.5	-0.3	0.0	0.0	0.0	0.0	0.0
58	0.1	0.0	-0.1	0.0	0.0	0.0	0.0	0.0
59	-0.1	-0.1	0.2	0.0	0.0	0.0	0.0	0.0
60	5.0	5.0	5.0	5.0	5.0	5.0	5.0	5.0
61	-5.0	-5.0	-5.0	-5.0	-5.0	-5.0	-5.0	-5.0
δ^+	10.0	10.0	6.8	7.8	7.9	6.0	5.9	8.5
δ^-	15.3	7.7	7.2	8.9	7.4	13.5	6.1	6.4

Table A.5: The systematic uncertainty contributions (in percentage) in the differential cross section versus Q^2, at $P = +32\%$.

Check	$0.01 - 0.022$	$0.022 - 0.046$	$0.046 - 0.1$	$0.1 - 0.178$	$0.178 - 0.316$	$0.316 - 0.562$
2	1.7	0.0	0.0	0.0	0.0	0.0
3	-0.2	0.0	0.0	0.0	0.0	0.0
4	3.6	-7.8	0.1	-3.1	0.0	0.0
5	-1.6	-0.1	-0.5	0.0	-0.1	0.0
6	-0.5	-0.2	1.9	-0.3	-0.1	-0.1
7	1.3	0.6	0.3	0.5	0.1	0.1
8	1.8	-0.6	0.1	0.0	0.0	0.0
9	-1.3	-1.2	0.0	0.0	0.0	0.0
10	21.4	0.2	0.1	0.0	0.0	0.0
11	4.5	3.3	0.0	0.0	0.0	0.0
12	5.5	2.5	0.2	0.0	0.0	0.0
13	4.0	-1.4	-0.1	0.0	0.0	0.0
14	-0.4	-0.8	-1.1	-1.3	6.1	-0.4
15	0.6	0.9	-0.9	-2.2	0.7	0.2
16	-0.2	-0.5	-0.8	-1.0	6.4	-0.3
17	0.6	-2.2	1.1	1.3	1.1	0.3
18	0.0	0.0	-0.1	-0.1	-0.1	-0.1
19	0.0	-2.8	0.1	0.1	0.1	0.0
20	-0.2	-0.4	-0.2	0.0	0.0	0.0
21	0.2	1.8	0.1	0.0	0.0	0.0
22	0.0	-2.7	0.2	0.1	0.1	0.0
23	0.0	-0.2	-0.1	-0.1	0.0	0.0
24	0.0	0.0	0.0	0.0	0.0	0.0
25	0.0	0.0	0.0	0.0	0.0	0.0
26	0.0	0.1	-1.4	0.0	0.0	0.0
27	0.0	0.0	0.0	0.0	0.0	0.0
28	0.0	0.1	-1.5	0.9	1.3	1.3
29	0.0	0.0	-0.4	-0.5	-1.2	-1.0
30	0.0	0.0	0.0	-0.1	-0.1	-0.1
31	0.0	0.1	0.0	0.0	0.7	0.4
32	0.0	0.0	0.2	-3.1	0.0	0.0
33	0.0	0.0	-0.1	0.0	0.0	0.0
34	0.0	0.0	0.0	0.0	0.0	0.0
35	0.0	0.0	0.0	0.0	0.0	0.0
36	0.0	0.0	0.0	0.0	0.1	0.1
37	0.0	0.0	0.0	0.0	0.0	-0.2
38	0.0	0.0	0.1	0.2	0.2	0.5
39	0.0	0.0	0.0	-0.1	-0.3	-0.2
40	0.0	0.0	2.2	-0.3	-0.5	-1.1
41	0.0	0.0	0.1	0.4	1.0	1.2
42	0.3	0.3	0.0	-0.3	-0.9	-1.8
43	-0.2	-0.3	0.1	0.0	0.9	2.8
44	0.3	0.2	0.0	0.4	-0.6	-1.5
45	-0.1	-0.3	0.0	-0.6	0.5	2.5
46	0.3	-0.1	0.0	0.0	0.0	0.0
47	0.0	-0.1	0.1	-0.1	0.0	0.0
48	0.9	-0.1	-0.3	-0.4	-0.1	-0.6
49	-0.6	-0.1	0.5	0.3	0.2	0.2
50	0.5	0.1	0.0	-0.3	-0.6	0.7
51	0.3	-0.3	-0.5	-0.1	0.8	-0.1
52	0.2	2.7	0.6	1.1	1.9	1.7
53	-0.1	-2.7	-0.5	-1.1	-1.9	-1.7
54	-6.8	-5.6	-3.1	-0.8	0.3	2.1
55	-0.7	-0.3	0.5	0.6	0.4	0.7
56	1.8	0.9	0.3	0.0	0.0	0.0
57	-1.8	-0.9	-0.2	0.0	0.0	0.0
58	0.6	-0.1	-0.1	0.0	0.0	0.0
59	-0.5	0.1	0.1	0.0	0.0	0.0
60	5.0	5.0	5.0	5.0	5.0	5.0
61	-5.0	-5.0	-5.0	-5.0	-5.0	-5.0
δ^+	24.0	7.4	6.0	5.5	10.7	7.1
δ^-	9.0	12.2	6.5	7.4	5.7	6.1

Table A.6: The systematic uncertainty contributions (in percentage) in the differential cross section versus x, at $P = -40\%$.

Check	$0.01 - 0.022$	$0.022 - 0.046$	$0.046 - 0.1$	$0.1 - 0.178$	$0.178 - 0.316$	$0.316 - 0.562$
2	1.6	0.0	0.0	0.0	0.0	0.0
3	-0.2	0.0	0.0	0.0	0.0	0.0
4	2.9	-3.7	0.1	0.0	0.0	0.0
5	1.4	-0.1	-0.3	0.0	-0.1	0.0
6	-0.2	-0.1	-0.2	-0.2	-0.1	0.0
7	0.6	0.2	0.2	0.2	0.1	0.0
8	1.6	0.4	0.1	0.0	0.0	0.0
9	-1.0	0.3	-0.1	0.0	0.0	0.0
10	1.1	2.9	0.1	0.0	0.0	0.0
11	7.3	-0.4	0.0	0.0	0.0	0.0
12	2.7	-0.7	-1.0	0.0	0.0	0.0
13	2.5	0.0	-0.1	0.0	0.0	0.0
14	2.1	-0.9	-0.1	0.4	-1.0	-0.4
15	0.5	-2.0	1.2	-5.8	0.7	0.2
16	2.3	-0.5	0.3	0.6	-0.8	-0.3
17	0.4	0.6	1.0	-7.2	1.1	0.3
18	0.0	0.0	-0.1	-0.1	-0.1	0.0
19	0.0	0.0	0.1	0.1	0.1	0.0
20	2.3	-0.3	-0.2	0.0	0.0	0.0
21	0.2	-0.3	0.1	0.0	0.0	0.0
22	0.0	0.1	0.2	0.1	0.0	0.0
23	0.0	1.2	-0.1	-0.1	0.0	0.0
24	0.0	0.0	0.0	0.0	0.0	0.0
25	0.0	0.0	0.0	0.0	0.0	0.0
26	0.0	0.1	-3.5	0.0	0.0	0.0
27	0.0	0.0	-0.1	0.0	0.0	0.0
28	0.0	0.1	-1.4	0.9	1.4	1.4
29	0.0	0.0	-0.4	-0.6	-1.1	-1.1
30	0.0	0.0	0.0	-0.1	-0.1	33.3
31	0.0	0.0	0.0	0.0	0.4	0.2
32	0.0	0.0	0.2	0.1	0.0	0.0
33	0.0	0.0	-0.1	0.0	-0.1	0.0
34	0.0	0.0	0.0	0.0	0.0	0.0
35	0.0	0.0	0.0	0.0	-0.1	0.0
36	0.0	0.0	0.0	0.0	0.1	0.0
37	0.0	0.0	0.0	0.0	-0.1	-0.2
38	0.0	0.0	0.1	0.2	0.2	0.4
39	0.0	0.0	0.0	-0.1	-0.3	-0.3
40	0.0	0.0	-0.1	1.3	-0.5	-1.0
41	0.0	0.0	0.1	0.4	1.0	1.2
42	0.3	0.3	0.0	-0.4	-1.0	-1.8
43	-0.2	-0.3	0.1	0.0	1.0	2.9
44	0.2	0.2	0.1	0.3	-0.6	-1.5
45	0.0	-0.3	-0.1	-0.6	0.6	2.5
46	0.2	-0.1	0.0	0.0	0.0	0.0
47	0.0	0.0	0.0	-0.1	0.0	0.0
48	0.8	0.0	-0.3	-0.4	-0.2	-1.0
49	-0.4	-0.1	0.4	0.3	0.2	0.2
50	0.4	0.1	-0.1	-0.3	-0.6	0.7
51	0.2	-0.2	-0.3	-0.1	0.8	0.0
52	0.2	2.8	0.3	1.6	1.2	2.9
53	-0.2	-2.7	-0.3	-1.6	-1.2	-3.0
54	-6.8	-5.6	-3.1	-0.8	0.3	2.1
55	-0.7	-0.3	0.4	0.6	0.4	0.7
56	0.8	0.5	0.1	0.0	0.0	0.0
57	-0.8	-0.5	-0.1	0.0	0.0	0.0
58	0.1	0.0	-0.1	0.0	0.0	0.0
59	-0.1	0.0	0.0	0.0	0.0	0.0
60	5.0	5.0	5.0	5.0	5.0	5.0
61	-5.0	-5.0	-5.0	-5.0	-5.0	-5.0
δ^+	11.2	6.6	5.3	5.6	5.8	34.1
δ^-	8.6	9.1	7.1	10.7	5.6	6.6

Table A.7: The systematic uncertainty contributions (in percentage) in the differential cross section versus x, at $P = +32\%$.

Check	$0. - 0.1$	$0.1 - 0.2$	$0.2 - 0.34$	$0.34 - 0.48$	$0.48 - 0.62$	$0.62 - 0.76$	$0.76 - 0.9$
2	0.0	0.4	1.7	-3.1	1.0	-6.3	3.0
3	0.0	0.0	-0.1	-1.2	-0.1	-0.5	-2.6
4	-6.7	-1.4	0.8	-3.7	-5.4	-3.8	2.6
5	-0.8	-0.1	-0.2	-0.4	-0.7	-0.7	-5.0
6	-0.2	-0.4	3.3	-0.3	-0.6	-0.1	0.0
7	0.0	0.6	0.6	0.7	0.4	0.9	0.7
8	0.0	0.8	0.4	-3.6	1.5	1.5	1.9
9	0.0	-0.1	-0.7	-0.8	-1.0	-1.0	-1.3
10	-0.9	3.1	4.9	-5.7	3.3	6.8	11.8
11	1.0	3.2	8.4	-4.1	11.7	-3.3	-6.0
12	0.1	1.2	1.1	1.6	2.4	2.2	2.9
13	-0.1	-0.8	2.3	-1.5	6.3	-3.6	-2.8
14	-0.3	1.4	-1.2	-1.0	-1.0	-0.8	-0.6
15	0.2	0.9	1.4	-3.6	1.0	1.6	-20.3
16	-0.4	1.7	-0.9	-0.6	-0.3	-0.2	-0.4
17	-1.9	1.1	1.2	0.7	0.6	1.0	0.3
18	0.0	-0.1	-0.2	-0.1	0.0	-0.2	-0.1
19	0.0	0.1	0.0	-4.6	0.0	0.1	0.1
20	-0.3	-0.3	-0.2	-0.1	0.0	-0.2	-0.3
21	0.9	0.8	0.1	0.1	0.2	0.4	0.1
22	0.1	0.2	0.1	-4.5	0.1	0.1	0.2
23	-0.1	-0.1	-0.1	-0.1	-0.1	-0.1	0.0
24	0.0	0.0	0.0	0.0	0.0	0.0	0.0
25	0.0	0.0	0.0	0.0	0.0	0.0	0.0
26	-1.1	0.0	0.0	0.0	0.0	0.0	0.0
27	-0.1	0.0	0.0	0.0	0.0	0.0	0.0
28	0.7	0.0	0.0	0.0	0.0	0.0	0.0
29	-2.1	0.0	0.0	0.0	0.0	0.0	0.0
30	-0.1	-0.1	0.0	0.0	0.0	0.0	0.0
31	0.2	0.2	0.0	0.0	0.0	0.0	0.0
32	-2.2	0.0	0.0	0.0	0.0	0.0	0.0
33	-0.2	0.0	0.0	0.0	0.0	0.0	0.0
34	0.0	0.0	0.0	0.0	0.0	0.0	0.0
35	0.0	0.0	0.0	0.0	0.0	0.0	0.0
36	0.1	0.0	0.0	0.0	0.0	0.0	0.0
37	0.0	0.0	0.0	0.0	0.0	0.0	0.0
38	0.3	0.1	0.0	0.0	0.0	0.0	0.0
39	-0.2	-0.1	0.0	0.0	0.0	0.0	0.0
40	1.7	-0.1	0.0	0.0	0.0	0.0	0.0
41	0.8	0.4	0.0	0.0	0.0	0.0	0.0
42	0.2	0.3	-0.8	0.0	-1.4	-0.1	-1.4
43	-0.6	0.0	-0.2	0.1	0.2	1.2	2.0
44	0.2	-0.1	-0.3	-0.3	0.4	1.1	2.4
45	-0.5	0.3	0.3	0.4	-1.6	-0.2	-2.2
46	0.0	0.1	0.0	0.1	0.2	-0.3	-0.2
47	0.0	0.0	0.0	-0.1	-0.3	-0.4	1.3
48	0.2	0.3	0.2	-0.1	-1.0	0.0	-2.8
49	-0.1	-0.2	0.0	-0.2	0.5	1.3	1.9
50	0.2	0.2	-0.4	-0.4	0.2	-0.5	0.0
51	-1.2	0.1	0.3	0.1	0.0	0.2	0.9
52	0.8	1.5	2.3	3.7	3.0	0.7	4.2
53	-0.8	-1.5	-2.4	-3.7	-2.9	-0.6	-4.2
54	-1.5	-2.3	-3.3	-4.1	-4.8	-5.8	-7.2
55	0.0	0.3	0.5	0.6	0.6	0.2	-1.0
56	0.7	0.5	0.6	0.2	0.6	0.4	0.9
57	-0.7	-0.5	-0.7	-0.2	-0.5	-0.4	-0.9
58	-0.2	0.0	-0.2	-0.5	0.2	0.7	1.7
59	0.2	0.0	0.1	0.5	-0.2	-0.7	-1.6
60	5.0	5.0	5.0	5.0	5.0	5.0	5.0
61	-5.0	-5.0	-5.0	-5.0	-5.0	-5.0	-5.0
δ^+	5.7	7.6	12.3	6.6	15.2	9.4	15.1
δ^-	9.6	6.0	6.8	14.2	9.7	11.9	24.5

Table A.8: The systematic uncertainty contributions (in percentage) in the differential cross section versus y, at $P = -40\%$.

Check	$0. - 0.1$	$0.1 - 0.2$	$0.2 - 0.34$	$0.34 - 0.48$	$0.48 - 0.62$	$0.62 - 0.76$	$0.76 - 0.9$
2	0.0	0.4	-1.2	1.4	-2.4	1.0	3.1
3	0.0	0.0	-0.1	-0.9	-0.1	-0.5	-2.1
4	-3.7	1.0	-0.6	0.9	2.4	2.9	2.7
5	-0.6	-0.1	1.2	-0.4	2.6	-0.8	4.3
6	-0.2	-0.2	-0.2	-0.1	-0.3	0.0	0.0
7	0.0	0.2	0.3	0.3	0.2	0.4	0.3
8	0.0	0.5	0.5	1.0	1.5	1.6	-5.1
9	0.0	-0.1	1.0	-0.7	-0.8	-1.1	-1.2
10	1.5	0.0	1.1	3.5	-3.6	2.1	1.2
11	-1.1	-0.5	0.6	4.7	9.7	0.1	0.6
12	0.1	0.9	-0.2	1.6	-4.8	2.3	-4.0
13	-0.1	0.7	0.1	4.2	1.2	-3.4	-2.9
14	-0.3	0.3	-1.2	1.9	2.3	-0.9	-0.7
15	0.2	0.8	-1.6	-7.7	-2.3	1.4	0.8
16	-0.4	0.5	-0.9	2.3	3.0	-0.2	-0.5
17	-1.0	-0.4	-0.2	-5.1	0.6	0.8	0.3
18	0.0	-0.1	-0.1	0.0	0.0	-0.1	0.0
19	0.0	0.1	0.0	0.1	0.0	0.1	0.0
20	-0.3	-0.3	-0.1	2.9	0.0	-0.2	-0.4
21	-0.9	0.6	0.1	0.0	0.2	0.3	0.1
22	0.0	0.2	0.1	0.1	0.0	0.1	0.2
23	-0.2	-0.1	-0.1	2.8	-0.1	-0.1	0.0
24	0.0	0.0	0.0	0.0	0.0	0.0	0.0
25	0.0	0.0	0.0	0.0	0.0	0.0	0.0
26	-4.9	0.0	0.0	0.0	0.0	0.0	0.0
27	-0.1	0.0	0.0	0.0	0.0	0.0	0.0
28	0.2	0.0	0.0	0.0	0.0	0.0	0.0
29	-2.1	0.0	0.0	0.0	0.0	0.0	0.0
30	-0.1	1.4	0.0	0.0	0.0	0.0	0.0
31	0.1	0.1	0.0	0.0	0.0	0.0	0.0
32	0.3	0.0	0.0	0.0	0.0	0.0	0.0
33	-0.3	0.0	0.0	0.0	0.0	0.0	0.0
34	0.0	0.0	0.0	0.0	0.0	0.0	0.0
35	-0.1	0.0	0.0	0.0	0.0	0.0	0.0
36	0.0	0.0	0.0	0.0	0.0	0.0	0.0
37	-0.1	0.0	0.0	0.0	0.0	0.0	0.0
38	0.3	0.1	0.0	0.0	0.0	0.0	0.0
39	-0.3	-0.1	0.0	0.0	0.0	0.0	0.0
40	0.7	-0.1	0.0	0.0	0.0	0.0	0.0
41	0.8	0.4	0.0	0.0	0.0	0.0	0.0
42	0.3	0.2	-0.3	0.1	-1.1	-0.1	-1.8
43	-0.6	0.0	-0.1	0.1	0.0	1.1	2.0
44	0.2	-0.1	-0.4	0.0	0.3	1.0	2.1
45	-0.6	0.3	0.4	0.4	-1.4	-0.3	-2.1
46	0.0	0.1	0.0	0.1	0.2	-0.3	-0.2
47	-0.1	0.0	0.1	0.0	-0.4	-0.4	1.4
48	0.2	0.2	0.2	0.1	-1.1	-0.1	-2.8
49	-0.2	-0.2	-0.1	0.0	0.6	1.2	1.9
50	0.2	0.2	-0.3	-0.3	0.1	-0.5	0.0
51	-1.0	0.1	0.3	0.1	0.0	0.2	0.5
52	1.4	2.0	2.8	3.4	3.6	1.0	3.9
53	-1.4	-2.0	-2.8	-3.4	-3.7	-1.0	-3.9
54	-1.6	-2.4	-3.3	-4.1	-4.9	-5.8	-7.2
55	0.0	0.3	0.5	0.5	0.6	0.1	-0.9
56	0.4	0.3	0.3	0.1	0.2	0.2	0.3
57	-0.5	-0.3	-0.3	-0.1	-0.2	-0.2	-0.3
58	-0.1	0.0	0.0	-0.1	0.0	0.2	0.2
59	0.0	0.0	0.0	0.1	0.0	-0.2	-0.2
60	5.0	5.0	5.0	5.0	5.0	5.0	5.0
61	-5.0	-5.0	-5.0	-5.0	-5.0	-5.0	-5.0
δ^+	5.5	6.0	6.2	11.0	12.8	7.4	9.6
δ^-	8.8	5.9	7.1	11.8	10.7	8.7	12.8

Table A.9: The systematic uncertainty contributions (in percentage) in the differential cross section versus y, at $P = +32\%$.

Check	$\delta_{sys}^{LH}(\%)$	$\delta_{sys}^{RH}(\%)$
2	−0.35	−0.05
3	−0.35	−0.26
4	−3.12	−0.05
5	−0.61	0.49
6	0.35	−0.16
7	0.52	0.23
8	0.13	0.35
9	−0.48	−0.09
10	1.86	0.82
11	2.21	1.29
12	1.25	−0.12
13	−0.04	0.35
14	−0.35	0.02
15	−0.35	−1.03
16	−0.04	0.30
17	0.26	−0.77
18	−0.09	−0.05
19	−0.61	0.05
20	−0.17	0.16
21	0.48	0.02
22	−0.56	0.09
23	−0.09	0.23
24	0.00	0.00
25	0.00	0.00
26	−0.39	−1.03
27	0.00	0.00
28	−0.09	−0.07
29	−0.39	−0.38
30	−0.04	0.30
31	0.09	0.05
32	−0.56	0.07

Check	$\delta_{sys}^{LH}(\%)$	$\delta_{sys}^{RH}(\%)$
33	−0.04	−0.02
34	0.00	0.00
35	0.00	0.00
36	0.00	0.02
37	−0.04	−0.02
38	0.09	0.07
39	−0.04	−0.05
40	0.43	0.14
41	0.22	0.26
42	−0.22	−0.14
43	0.00	0.02
44	0.09	0.07
45	−0.13	−0.12
46	0.00	0.02
47	−0.04	−0.02
48	−0.09	−0.07
49	0.09	0.12
50	−0.04	−0.05
51	−0.13	−0.05
52	0.17	0.49
53	−0.22	−0.49
54	0.26	0.26
55	−0.26	−0.26
56	0.48	0.23
57	−0.48	−0.23
58	0.00	0.00
59	0.00	0.00
60	4.99	5.00
61	−5.01	−5.00
δ^+	6.01	5.35
δ^-	6.14	5.33

Table A.10: The systematic uncertainty contributions (in percentage) in the RH differential cross section versus y.

Bibliography

[1] F. Halzen and Alan D. Martin. Quarks and leptons: An introductory course in modern particle physics. New York, Usa: Wiley (1984) 396p.

[2] S. L. Glashow. Partial symmetries of weak interactions. *Nucl. Phys.*, 22:579–588, 1961.

[3] Abdus Salam. Fundamental theory of matter: a survey of results and methods. International symposium on contemporary physics 7-28 Jun 1968, Trieste, Italy.

[4] Steven Weinberg. A model of leptons. *Phys. Rev. Lett.*, 19:1264–1266, 1967.

[5] Peter W. Higgs. Broken symmetries and the masses of gauge bosons. *Phys. Rev. Lett.*, 13:508–509, 1964.

[6] Peter W. Higgs. Spontaneous symmetry breakdown without massless bosons. *Phys. Rev.*, 145:1156–1163, 1966.

[7] F. Englert and R. Brout. Broken symmetry and the mass of gauge vector mesons. *Phys. Rev. Lett.*, 13:321–322, 1964.

[8] G. S. Guralnik, C. R. Hagen, and T. W. B. Kibble. Global conservation laws and massless particles. *Phys. Rev. Lett.*, 13:585–587, 1964.

[9] T. W. B. Kibble. Symmetry breaking in non-abelian gauge theories. *Phys. Rev.*, 155:1554–1561, 1967.

[10] A. C. Benvenuti et al. A high statistics measurement of the proton structure functions $F_2(x, Q^2)$ and r from deep inelastic muon scattering at high Q^2. *Phys. Lett.*, B223:485, 1989.

[11] M. Arneodo et al. Measurement of the proton and the deuteron structure functions, $F_2(p)$ and $F_2(d)$. *Phys. Lett.*, B364:107–115, 1995.

[12] M. R. Adams et al. Proton and deuteron structure functions in muon scattering at 470-GeV. *Phys. Rev.*, D54:3006–3056, 1996.

[13] J. P. Berge et al. A measurement of differential cross-sections and nucleon structure functions in charged current neutrino interactions on iron. *Z. Phys.*, C49:187–224, 1991.

[14] R. Blair et al. Measurement of the rate of increase of neutrino cross-sections with energy. *Phys. Rev. Lett.*, 51:343–346, 1983.

[15] E. Oltman et al. Nucleon structure functions from high-energy neutrino interactions. FNAL-616/701 experiment. *Z. Phys.*, C53:51–71, 1992.

[16] G. T. Jones et al. Determination of the ratio $R(v) = \frac{d(v)}{u(v)}$ of the valence quark distributions in the proton from neutrino and anti-neutrino reactions on hydrogen and deuterium. *Z. Phys.*, C62:601–607, 1994.

[17] T. Ahmed et al. First measurement of the charged current cross-section at HERA. *Phys. Lett.*, B324:241–248, 1994.

[18] S. Aid et al. Measurement of the e^+ and e^- induced charged current cross- sections at HERA. *Z. Phys.*, C67:565–576, 1995.

[19] S. Aid et al. Measurement of the Q^2 dependence of the charged and neutral current cross sections in $e^{\pm}p$ scattering at HERA. *Phys. Lett.*, B379:319–329, 1996.

[20] S. Aid et al. A search for selectrons and squarks at HERA. *Phys. Lett.*, B380:461–470, 1996.

[21] C. Adloff et al. A measurement of the proton structure function $F_2(x, Q^2)$ at low x and low Q^2 at HERA. *Nucl. Phys.*, B497:3–30, 1997.

[22] C. Adloff et al. Measurement of neutral and charged current cross sections in electron proton collisions at high Q^2. *Eur. Phys. J.*, C19:269–288, 2001.

[23] C. Adloff et al. Measurement and QCD analysis of neutral and charged current cross sections at HERA. *Eur. Phys. J.*, C30:1–32, 2003.

[24] M. Derrick et al. Measurement of charged and neutral current e^-p deep inelastic scattering cross-sections at high Q^2. *Phys. Rev. Lett.*, 75:1006–1011, 1995.

[25] M. Derrick et al. Measurement of the F_2 structure function in deep inelastic e^+p scattering using 1994 data from the ZEUS detector at HERA. *Z. Phys.*, C72:399–424, 1996.

[26] J. Breitweg et al. Measurement of dijet photoproduction at high transverse energies at HERA. *Eur. Phys. J.*, C11:35–50, 1999.

[27] J. Breitweg et al. Measurement of dijet production in neutral current deep inelastic scattering at high Q^2 and determination of α_s. *Phys. Lett.*, B507:70–88, 2001.

[28] S. Chekanov et al. Measurement of the neutral current cross section and F_2 structure function for deep inelastic e^+p scattering at HERA. *Eur. Phys. J.*, C21:443–471, 2001.

[29] S. Chekanov et al. Measurement of high Q^2 charged current cross sections in e^-p deep inelastic scattering at HERA. *Phys. Lett.*, B539:197–217, 2002.

[30] S. Chekanov et al. Measurement of high Q^2 charged current cross sections in e^+p deep inelastic scattering at HERA. *Eur. Phys. J.*, C32:1–16, 2003.

[31] S. Chekanov et al. Bottom photoproduction measured using decays into muons in dijet events in ep collisions at $\sqrt{s} = 318$ GeV. *Phys. Rev.*, D70:012008, 2004.

[32] E. Lohrmann and K. H. Mess. Remarks on the kinematics of ep collisions in HERA. DESY-HERA-83/08.

[33] V. N. Gribov and L. N. Lipatov. Deep inelastic ep scattering in perturbation theory. *Sov. J. Nucl. Phys.*, 15:438–450, 1972.

[34] V. N. Gribov and L. N. Lipatov. e^+e^- pair annihilation and deep inelastic ep scattering in perturbation theory. *Sov. J. Nucl. Phys.*, 15:675–684, 1972.

[35] Yuri L. Dokshitzer. Calculation of the structure functions for deep inelastic scattering and e^+e^- annihilation by perturbation theory in quantum chromodynamics. *Sov. Phys. JETP*, 46:641–653, 1977.

[36] Guido Altarelli and G. Parisi. Asymptotic freedom in parton language. *Nucl. Phys.*, B126:298, 1977.

[37] W. B. Atwood et al. Limits on parity violation in polarized electron scattering at 19.4-GeV. *Phys. Rev.*, D18:2223, 1978.

[38] C. Y. Prescott et al. Parity non-conservation in inelastic electron scattering. *Phys. Lett.*, B77:347–352, 1978.

[39] M. Vakili et al. Nuclear structure functions in the large x large Q^2 kinematic region in neutrino deep inelastic scattering. *Phys. Rev.*, D61:052003, 2000.

[40] Zhi-qing Zhang. Structure functions at large x. *J. Phys.*, G28:767–778, 2002.

[41] S. V. Chekanov and V. L. Morgunov. Selection and reconstruction of the top quarks in the all- hadronic decays at a linear collider. *Phys. Rev.*, D67:074011, 2003.

[42] M. Arneodo et al. Measurement of the proton and deuteron structure functions, $F_2(p)$ and $F_2(d)$, and of the ratio $\frac{\sigma_l}{\sigma_t}$. *Nucl. Phys.*, B483:3–43, 1997.

[43] W. G. Seligman et al. Improved determination of α_s from neutrino nucleon scattering. *Phys. Rev. Lett.*, 79:1213–1216, 1997.

[44] S. Kretzer, H. L. Lai, F. I. Olness, and W. K. Tung. CTEQ6 parton distributions with heavy quark mass effects. *Phys. Rev.*, D69:114005, 2004.

[45] W. J. Stirling, A. D. Martin, R. G. Roberts, and R. S. Thorne. MRST parton distributions. *AIP Conf. Proc.*, 747:16–21, 2005.

[46] P. D. Acton et al. A study of charged particle multiplicities in hadronic decays of the Z^0. *Z. Phys.*, C53:539–554, 1992.

[47] H. L. Lai et al. Improved parton distributions from global analysis of recent deep inelastic scattering and inclusive jet data. *Phys. Rev.*, D55:1280–1296, 1997.

[48] H. L. Lai et al. Global QCD analysis of parton structure of the nucleon: CTEQ5 parton distributions. *Eur. Phys. J.*, C12:375–392, 2000.

[49] HERA. A proposal for a large electron-proton colliding beam facility at DESY, DESY HERA 81-10 (unpublished).

[50] I. Abt et al. The H1 detector at HERA. *Nucl. Instrum. Meth.*, A386:310–347, 1997.

[51] ZEUS. The ZEUS detector, status report 1993, ed. U. Holm, DESY (1993) (unpublished).

[52] HERMES. Technical design report,DESY-PRC 93/06 MPIH-V20 1993 (unpublished).

[53] HERA-B. Status report, DESY-PRC-00-04 (2000) (unpublished).

[54] N. Harnew et al. Vertex triggering using time difference measurements in the ZEUS central tracking detector. *Nucl. Instrum. Meth.*, A279:290–296, 1989.

[55] B. Foster et al. The performance of the ZEUS central tracking detector z-by- timing electronics in a transputer based data acquisition system. *Nucl. Phys. Proc. Suppl.*, 32:181–188, 1993.

[56] B. Foster et al. The design and construction of the ZEUS central tracking detector. *Nucl. Instrum. Meth.*, A338:254–283, 1994.

[57] M. Derrick et al. Design and construction of the ZEUS barrel calorimeter. *Nucl. Instrum. Meth.*, A309:77–100, 1991.

[58] A. Andresen et al. Construction and beam test of the ZEUS forward and rear calorimeter. *Nucl. Instrum. Meth.*, A309:101–142, 1991.

[59] A. Caldwell et al. Design and implementation of a high precision readout system for the ZEUS calorimeter. *Nucl. Instrum. Meth.*, A321:356–364, 1992.

[60] A. Bernstein et al. Beam tests of the ZEUS barrel calorimeter. *Nucl. Instrum. Meth.*, A336:23–52, 1993.

[61] G. Abbiendi et al. The ZEUS barrel and rear muon detector. *Nucl. Instrum. Meth.*, A333:342–354, 1993.

[62] F. Arzarello et al. The ZEUS vertex and forward muon detectors readout electronics. *Nucl. Phys. Proc. Suppl.*, 32:506–512, 1998.

[63] M. Helbich et al. The spectrometer system for measuring zeus luminosity at hera. 2005.

[64] A. A. Sokolov and I. M. Ternov. On polarization and spin effects in the theory of synchrotron radiation. *Phys. Dokl.*, 8:1203–1205, 1964.

[65] D. P. Barber. Polarization at HERA: An introduction. In *Bad Lauterberg 1992, Proceedings, Harz-Seminar* 188-200.

[66] D. P. Barber et al. The HERA polarimeter and the first observation of electron spin polarization at HERA. *Nucl. Instrum. Meth.*, A329:79–111, 1993.

[67] V. N. Baier and Valery A. Khoze. Determination of the transverse polarization of high-energy electrons. *Sov. J. Nucl. Phys.*, 9:238–240, 1969.

[68] D. P. Barber. Polarized electron beams in storage rings. Prepared for 12th International Symposium on High-energy Spin Physics (SPIN 96), Amsterdam, Netherlands, 10-14 Sep 1996.

[69] M. Woods. The scanning compton polarimeter for the SLD experiment. 1996.

[70] I. Passchier et al. A compton backscattering polarimeter for measuring longitudinal electron polarization. *Nucl. Instrum. Meth.*, A414:446–458, 1998.

[71] W. A. Franklin et al. The MIT-bates compton polarimeter. *AIP Conf. Proc.*, 675:1058–1062, 2003.

[72] M. Beckmann et al. The longitudinal polarimeter at HERA. *Nucl. Instrum. Meth.*, A479:334–348, 2002.

[73] Bernard Leblond. Short pulse photoemission from a dispenser cathode under the 2nd, 3rd and 4th harmonics of a picosecond ND: YAG laser. *Nucl. Instrum. Meth.*, A317:365–372, 1992.

[74] E. N. Koffeman. A silicon micro vertex detector for the ZEUS experiment. *Nucl. Instrum. Meth.*, A453:89–92, 2000.

[75] D. Dannheim et al. Design and tests of the silicon sensors for the ZEUS micro vertex detector. *Nucl. Instrum. Meth.*, A505:663–682, 2003.

[76] A. Kwiatkowski, H. Spiesberger, and H. J. Mohring. Heracles: An event generator for e p interactions at HERA energies including radiative processes: Version 1.0. *Comp. Phys. Commun.*, 69:155–172, 1992.

[77] G. A. Schuler and H. Spiesberger. Django: The interface for the event generators HERACLES and LEPTO. In *Hamburg 1991, Proceedings, Physics at HERA, vol. 3* 1419-1432. (see HIGH ENERGY PHYSICS INDEX 30 (1992) No. 12988).

[78] Leif Lonnblad. ARIADNE version 4: A program for simulation of QCD cascades implementing the color dipole model. *Comput. Phys. Commun.*, 71:15–31, 1992.

[79] G. Ingelman, A. Edin, and J. Rathsman. LEPTO 6.5 - A Monte Carlo generator for deep inelastic lepton-nucleon scattering. *Comput. Phys. Commun.*, 101:108–134, 1997.

[80] D. E. Groom et al. Review of particle physics. *Eur. Phys. J.*, C15:1–878, 2000.

[81] J. Ferrando. Guide to funnel:The ZEUS Monte Carlo production facility (unpublished).

[82] G. Marchesini et al. HERWIG: A Monte Carlo event generator for simulating hadron emission reactions with interfering gluons. Version 5.1 - April 1991. *Comput. Phys. Commun.*, 67:465–508, 1992.

[83] A. D. Tapper. Measurement of charged current deep inelastic scattering cross sections using the ZEUS detector at HERA, Ph.D. thesis, University of London, 2001, DESY-THESIS-2001.

[84] Tetsuo Abe. GRAPE-dilepton (version 1.1): A generator for dilepton production in *ep* collisions. *Comput. Phys. Commun.*, 136:126–147, 2001.

[85] U. Baur, J. A. M. Vermaseren, and D. Zeppenfeld. Electroweak vector boson production in high-energy e p collisions. *Nucl. Phys.*, B375:3–44, 1992.

[86] R. Brun, F. Bruyant, M. Maire, A. C. McPherson, and P. Zanarini. GEANT3. CERN-DD/EE/84-1.

[87] U. Amaldi et al. Report from the study group on detectors for charged current events. In *Hamburg 1979, Proceedings, Study Of An E P Facility For Europe*, Hamburg 1979, 377-414.

[88] Gennady M. Briskin. Diffractive dissociation in *ep* deep inelastic scattering. DESY-THESIS-1998-036.

[89] J. Breitweg et al. Measurement of high Q^2 neutral-current e^+p deep inelastic scattering cross-sections at HERA. *Eur. Phys. J.*, C11:427–445, 1999.

[90] G. F. Hartner. VCTRAK briefing: program and math., ZEUS-Note 98-058.

[91] R. Pawlak. Vertex reconstruction from FCAL timing, ZEUS-Note 98-040.

[92] K. Nagano. Measurement of charged-current e^+p deep inelastic scattering cross sections at $\sqrt{s} = 300$ GeV, Ph.D. thesis, University of Tokyo, 1998.

[93] T. Fusayasu. Study of charged-current $e^{\pm}p$ deep inelastic scattering at $\sqrt{s} = 308$ GeV, Ph.D. thesis, University of Tokyo, 2001.

[94] S. Grijpink. Charged current cross section measurement at HERA, Ph.D. thesis, University of Amsterdam, 2004.

[95] J. Rautenberg. Measurement of high-Q^2 charged-current e^+p deep inelastic scattering at HERA, Ph.D. thesis, University of Bonn, Bonn-IR-2004-08.

[96] R. Sinkus and T. Voss. Particle identification with neural networks using a rotational invariant moment representation. *Nucl. Instrum. Meth.*, A391:360–368, 1997.

[97] O. Kind et al. A ROOT-based client-server event display for the ZEUS experiment. *ECONF*, C0303241:MOLT002, 2003.

[98] N. H. Brook et al. A comparison of deep inelastic scattering Monte Carlo event generators to HERA data. 1998.

[99] Amanda M. Cooper-Sarkar, R. C. E. Devenish, and A. De Roeck. Structure functions of the nucleon and their interpretation. *Int. J. Mod. Phys.*, A13:3385–3586, 1998.

[100] H. Abramowicz and A. Caldwell. Fits of $y(x)$ with errors on x and y, ZEUS-Note 04-008.

[101] F. James and M. Roos. 'MINUIT' A system for function minimization and analysis of the parameter errors and correlations. *Comput. Phys. Commun.*, 10:343–367, 1975.

[102] F. Cornet and R. Ruckl. Sensitivity of W' and Z' searches at HERA. Contributed to the DESY Workshop on Physics at HERA, Hamburg, Germany, Oct 12-14, 1987.

[103] S. Abachi et al. Search for right-handed W bosons and heavy W' in $p\bar{p}$ collisions at $\sqrt{s}$ =1.8 tev. *Phys. Rev. Lett.*, 76:3271–3276, 1996.

[104] F. Turkot et al. Proposal to measure proton - proton and proton - deuterium elastic and inelastic cross sections in the 0.4 TeV/c <= $p(inc)$ <= 1 TeV/c beam momentum range. FERMILAB-PROPOSAL-0681.

[105] M. Derrick et al. Study of charged-current e p interactions at $Q^2 > 200 -$ GeV^2 with the ZEUS detector at HERA. *Z. Phys.*, C72:47–64, 1996.

[106] Toichiro Kinoshita. The fine structure constant. *Rept. Prog. Phys.*, 59:1459–1492, 1996.

[107] Timo van Ritbergen and Robin G. Stuart. On the precise determination of the fermi coupling constant from the muon lifetime. *Nucl. Phys.*, B564:343–390, 2000.

[108] Martin W. Grunewald. Electroweak physics. ((c)) ((d)). *Nucl. Phys. Proc. Suppl.*, 117:280–297, 2003.

[109] The LEP collaborations. A combination of preliminary electroweak measurements and constraints on the standard model, *hep-ex/0312023.* 2003.

[110] M. Woods. Precise determination of the weak mixing angle from a measurement of A_{LR} in $(e^+e^- \to Z^0)$. Prepared for 11th International Symposium on High-energy Spin Physics and the 8th International Symposium on Polarization Phenomena in Nuclear Physics (SPIN 94), Bloomington, Indiana, 15-22 Sep 1994.

[111] G. P. Zeller et al. A precise determination of electroweak parameters in neutrino nucleon scattering. *Phys. Rev. Lett.*, 88:091802, 2002.

[112] Stefan Kretzer et al. The parton structure of the nucleon and precision determination of the Weinberg angle in neutrino scattering. *Phys. Rev. Lett.*, 93:041802, 2004.

[113] H. Spiesberger, M. Spira, and P. M. Zerwas. The standard model: Physical basis and scattering experiments, *hep-ph/0011255.* 2000.

[114] W. Hollik. Electroweak radiative corrections in deep inelastic electron - proton scattering. Presented at the NATO Advanced Research Workshop on Radiative Corrections : Results and Perspectives, Brighton, Eng., Jul 9-14, 1989.

[115] W. Hollik. Electroweak precision observables in the MSSM and global analyses of precision data, *hep-ph/9711489.* 1997.

[116] A. Dedes, A. B. Lahanas, and K. Tamvakis. The effective weak mixing angle in the MSSM. *Phys. Rev.*, D59:015019, 1999.

[117] Torbjorn Sjostrand. The LUND Monte Carlo for jet fragmentation and e^+e^- physics: JETSET version 6.2. *Comput. Phys. Commun.*, 39:347–407, 1986.

[118] Torbjorn Sjostrand and Mats Bengtsson. The LUND Monte Carlo for jet fragmentation and e^+e^- physics: JETSET version 6.3: An update. *Comput. Phys. Commun.*, 43:367, 1987.

[119] Torbjorn Sjostrand. High-energy physics event generation with PYTHIA 5.7 and JETSET 7.4. *Comput. Phys. Commun.*, 82:74–90, 1994.

[120] A. V. Sighem A. Kurse. MUFFINCUP- A wrapper for MUFFIN user manual and documenation, ZEUS-Note 98-025.

[121] S. Chekanov et al. Measurement of high Q^2 e^-p neutral current cross sections at HERA and the extraction of xF_3. *Eur. Phys. J.*, C28:175, 2003.

[122] A. Kappes. Measurement of $e^-p \to e^-X$ defferential cross sections at high Q^2 and of the structure function xF_3 with ZEUS at HERA, Ph.D. thesis, University of Bonn, Report BONN-IR-2001-16, 2001.

Acknowledgement

He who does not thank people does not thank god !

Supervisors

Only by chance did I joined the high energy physics group at the Tel Aviv University. But when I got in, I discovered myself very lucky working closely with Prof. **Halina Abramowicz** and Prof. **Aharon Levy** who became my supervisors in both my M.Sc. and Ph.D. theses. From the bottom of my heart, I would like to thank them for their help, teaching, patience and support. Thank you for this special relationship and friendship which reaches beyond the walls of the University.

People at Tel Aviv University

I would like to thank Dr. Sergey Kananov for constant interest in my work and much good advise; Dr. Zhenya Gurvich for finding time to solve all the computation problems we face; Prof. Samuel Dagan for the beautiful flat screen and good advice since my undergraduate studies; Prof. Danny Ashery for interesting physics and political discussions; Dr. Iuliana Cohen for good discussions, Prof. Evgeny Levin for clarifying the theory in simple words, Prof. Gideon Alexander for sharing his expertise in polarimetry, Prof. Asher Gotsman, Prof. Uri Maor and Prof. Yona Oren.

I had the pleasure of getting to know many graduate students, some of whom I collaborated closely and others were simply friends: Dr. Arik Kriesel whom I am happy to meet at SLAC soon, Mr. Avi Mitrani who has been a good and close friend since our undergraduate studies, Mr. Michael Groys, Mr. Ronen Ingbir-the best designer of presentations, Mr. Eyal Nevo, Mr. Ori Smith, Mr. Iftach Sadeh, Mr. Amir Stern, Mr. Erez Reinhertz-Aronis, Dr. Alon Markus, Dr. Michael Kroyter, Dr. Udi Fuchs, Dr. Meir Shimon, Dr. Eytan Katsav, Dr. Eran Naftali, Mr. Yiftach Lipkin. Many thanks to Mrs. Varda Bernstein for believing in my success.

People at DESY

I would like to thank Prof. Guenter Wolf for helping me in winning the Björn Wiik Fellowship , Dr. Uwe Schneekloth for good advise, Prof. Allen Caldwell for good guidance and advise, Prof. Stefan Schlenstedt for interesting discussion, Dr. Uta Stoesslein for her assistance in the polarimeter data, Dr. Bruce Straub for his constant willingness to help and good advise,

Prof. Wolfram Zeuner, Prof. Elisabetta Gallo, Mr. Krzysztof Wrona and Mr. Radek Kaczorowski.

I would like to thank the coordinators of the high Q^2 group: Dr. Katarzyna Wichmann, Dr. Alex Tapper, Dr. Enrico Tassi and Dr. Kunihiro Nagano. I appreciate very much the help and the fruitful discussion with Dr. Tapper while finalising the CC analysis. I like to thank Prof. Ken Long for his good advise when he coordinated the group. I would like to thank Dr. Mayuko Kataoka for the cooperation in the CC studies. My deep thanks to Dr. Julian Rautenberg for nice discussions and advise.

I had the pleasure to know Mr. Juraj Sutiak, Mr. Hiroshi Kaji, Mr. Volker Adler, Dr. James Ferrando, Dr. Alessandro Montanari, Dr. Dorian Kcira, Dr. Monica Vazquez, Dr. Amaya Lopez-Duran-Viani, Dr. Florian Geobel, Dr. Damir Lelas, Dr. Heuijin Lim, Mrs. Raquel Santamarta, Dr. John Loizides, Dr. Olaf Deppe, Mrs. Cathrin Schierholz and Mrs. Anja Deppe.

Family

My deep thanks to my wife, Diana, who did not stop encouraging me. She did the maximum to help me in my career and is ready to join me everywhere in the world. Thanks to my little son, Hasan, who brought joy and happiness to our life.

I am grateful to my parents, sisters and brothers for their love, support and encouragement, especially during my studies and my stays away from home. Thank you for understanding the last few months in which I was fully concentrated in finalising the thesis.

I would like to thank my parents-in-law for the warm relationship between us. Special thanks to my mother-in-law who found the time to visit us several times in Hamburg despite her duties. Thanks to my brother- and sister-in-law for loving and taking care of Hasan.

Foundations

This work was partially supported by: the Björn Wiik Laboratory Scholarship Programme at DESY, the MINERVA Foundation, the Israeli Science Foundation (ISF), and the Israeli Ministry of Science.

I was very privileged to have many wonderful friends who accompanied me during my studies. I would like to thank many others who are not mentioned here and whom I had the pleasure to know.

תקציר

בעזרת נתונים שנאספו בגלאי ZEUS במאיץ החלקיקים HERA במהלך שנת 2004, נחקרו חתך הפעולה של התהליך $ep \to \nu X$ (אינטראקציה מסוג Charged Current) בשני ערכי קיטוב של אלומת הפוזיטרונים (+32%, -40%). האקסטרפולציה של חתך הפעולה לקיטוב של -100%, אינו מורה על קיום הבוזון W המקוטב ימנית. תוצאה זו עולה בקנה אחד עם המודל הסטנדרטי.

בעזרת נתונים שנאספו במהלך השנים 2000 - 1996 ומתוך היחס של חתכי הפעולה של התהליכים $ep \to eX$ (אינטראקציה מסוג Neutral Current) ו- $ep \to \nu X$ נמצא הערך של הפרמטר $\sin^2 \theta_w$:

$$\sin^2 \theta_w = 0.227 \pm 0.013(stat)^{+0.008}_{-0.009}(syst)$$

ערך זה מתאים לערכים שנמדדו באינטראקציות אחרות.

בעזרת נתונים שנאספו במהלך 2000 – 1999 נמדד היחס בין הקווארק מסוג d לקווארק מסוג u בערכים גבוהים של x ו- Q^2. הערכים הנמדדים נמצאו בהתאמה עם פרמטריזציות שונות של צפיפות הפרטונים.

לזכר

מוחמד עבד אלראוף עסלייה

TEL AVIV UNIVERSITY
RAYMOND AND BEVERLY SACKLER
FACULTY OF EXACT SCIENCES
SCHOOL OF PHYSICS & ASTRONOMY

אוניברסיטת תל-אביב
הפקולטה למדעים מדוייקים
ע"ש ריימונד ובברלי סאקלר
בית הספר לפיסיקה ואסטרונומיה

זרם נייטרלי וזרם טעון באינטרקציות אלקטרון-פרוטון במאיץ HERA

חיבור זה הוגש כחלק מהדרישות לקבלת התואר
"דוקטור לפילוסופיה"- Ph.D. באוניברסיטת תל-אביב

ביה"ס לפיסיקה ולאסטרונומיה
החוג לאנרגיות גבוהות

על-ידי

ערפאת ג'בארין מוכתאר

העבודה הוכנה בהדרכתם של פרופ' ***הלינה אברמוביץ'*** ופרופ' ***אהרן לוי***

ינואר 2006